Fundamental understanding of high-energy-density Li-ion batteries and beyond : structure-property relationships and reaction chemistries

Wei Yin

Sorbonne Université

ED 397 – Physique et Chimie des Matériaux

Collège de France

Chaire de Chimie du Solide et de l'Energie

Fundamental understanding of high-energy-density Li-ion batteries and beyond: structure-property relationships and reaction chemistries

Wei YIN

Doctor thesis in Chemistry/Materials Science

Supervised by Jean-Marie TARASCON and Alexis GRIMAUD

To be presented and defended in public on 18 Octorber 2019 in front of the jury:

Dr. Fanny Bardé	Program manager, IMEC, Belgium	Referee
Prof. Betar M. Gallant	Assistant Professor, Massachusetts Institute of Technology	Referee
Prof. Mathieu Salanne	Professor, Sorbonne Université, Paris	Examiner
Prof. Ying Shirley Meng	Professor, University of California, San Diego	Examiner
Dr. Erik J. Berg	Associate senior lecturer, Uppsala University, Sweden	Examiner
Dr. Alexis Grimaud	CNRS researcher, Collège de France, Paris	Co-supervisor
Prof. Jean-Marie Tarascon	Professor, Collège de France, Paris	Supervisor

To my dear parents

and

to my dear sisters

Acknowledgements

First and foremost, I would like to express my sincerest gratitude to my supervisors Prof. Jean-Marie Tarascon and Dr. Alexis Grimaud. Their passion to science and availability to students will always be a source of inspiration and motivation for me. They are great mentors and I truly appreciate their professional guidance, scientific support and kind encouragement during the last four years.

I gratefully acknowledge the referees and examiners of my PhD committee Prof. Betar M. Gallant, Dr. Fanny Bardé, Prof. Mathieu Salanne, Prof. Ying Shirley Meng and Dr. Erik J. Berg for spending time reading my thesis, and for giving insightful comments and suggestions.

My appreciations also go to Dr. Florent Lepoivre for spending time during his thesis writing to answer my questions and to teach me how to play with the pressure cell at the beginning of my PhD, and to Dr. Daniel Alves Dalla Corte for sharing his expertise when designing the gas line and OEMS cells. It was a great pleasure to work with both of them. I learned from them that engineering can be elegant.

I would like to specially thank all the local and international collaborators for their technical supports and fruitful discussions: Dr. Daniel Alves Dalla and Dr. Arash Jamali for SEM imaging; Dr. Grégory Gachot for GC-MS measurements; Prof. Gwenaëlle Rousse for analyzing the synchrotron XRD and neutron powder diffraction patterns; Prof. Artem Abakumov for TEM studies; Dr. Leiting Zhang and Dr. Sigita Trabesinger for OEMS measurements; Dr. Antonella Iadecola for XAS experiments; Dr. Dominique Foix for XPS experiments and Dr. Domitille Giaume for ICP-OES experiments.

Throughout the four-year journey, I have worked with many talented and supportive colleagues. I sincerely appreciated the valuable discussions with Dr. Sathiya Mariyappan, Dr. Iban Azcarrate, Dr. Lukas Lutz, Mr. Nicolas Dubouis, Dr. Guochun Yan, Dr. Chunzhen Yang, Dr. Jiwei Ma, Dr. Gaurav Assat, Dr. Quentin Jacquet, Dr. Ronghuan Zhang, Dr. Forencia Marchini, Dr. Biao Li, and Dr. Jiaqiang Huang. I would like also to thank Mr. Thomas Marchandier for his help during the two-day XAS experiment at Soleil.

Specially, I would like to thank my office mates Ms. Laura albero blanquer, Dr. Forencia Marchini, Mr. Jean Vergnet, Mr. Thomas Dargon and Ms. Zeqi Zhou for creating such an enjoyable atmosphere, I cannot image better office mates than you. Many thanks to Dr. Vanessa Perreira Pimenta, Dr. Meiling Sun, Dr. Yan Duan, Dr. Biao Li, Dr. Jiaqiang Huang, Dr. Ronghuan Zhang, Dr. Chunzhen Yang, Dr. Guochun Yan, Dr. Qing Wang, Dr. Leiting Zhang, Dr. Yinghui Yin, Dr. Huijun Zhang, Dr. Yang Xia, and to my “hiking team” for the great time and moments we have shared.

Finally, I would like to express my utmost gratitude to my parents and my family for their patience and unconditional support.

Table of contents

Broader context and thesis outline

Broader context and thesis outline

For thousands of years, humankind has relied on fossil fuels to generate energy. The wide-scale use of fossil fuels, coal at first and petroleum later, to fire steam engines has enabled the first industrial revolution which marked a major turning point in history. In particular, the population began to experience an unprecedented growth, alike for the living standards that kept increasing. Nevertheless, despite of the critical role that fossil fuels have played in the development of most industrial nations, several practical problems related to the use of fossil fuels arise: i) fossil fuels are finite energy sources and take typically millions of years to be formed from natural process, the known viable reserves are being depleted much faster than new ones are being produced; ii) combustion of fossil fuels produce CO_2 which accounts for 75 % of the greenhouse gas (GHG) emissions and causes the global temperature to rise; iii) burning of fossil fuels also releases other air pollutants such as NO_2 and SO_2 which contribute to smog, acid rain and the formation of fine particulate matter; iv) radioactive elements, mainly uranium and thorium, are also released into the atmosphere from burning fossil fuels. More importantly, these global issues are becoming more serious than ever as the ever-rising energy consumption due to the overall population growth and prosperity increases (Figure 1). There is thus a strong need to transform the way we generate, distribute and use energy.

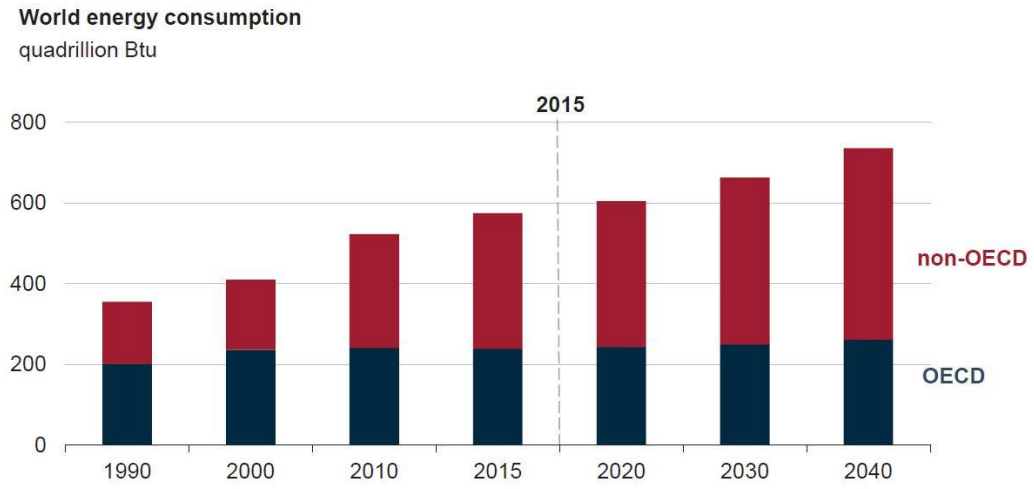

Figure 1 World energy consumption rises 28 % between 2015 and 2040 with most of the increases in energy demand coming from non-OECD (Organisation for Economic Co-operation and Development) countries. Adapted from: *IEA World Energy Outlook 2017*.[1]

Within this context, gradually shifting the world's energy sources from fossil fuels to lower-carbon fuels such as renewable energies (biofuels, geothermal, hydro, wind, solar sources, etc.) is considered to be a viable alternative to fulfil our energy demand with lower environment effects (Figure 2). To realize this global energy transition, several renewable technologies are being developed to broaden the access to more abundant and cleaner energy supplies. Despite renewable technologies have overcame various technological pitfalls, the major challenge resides in how to balance power supply and demand, with one example being how to tackle the intermittency issue caused by the fluctuations of wind and solar powered systems. Energy storage plays an important role in this balancing act and helps to ensure more flexible and steady power supply.

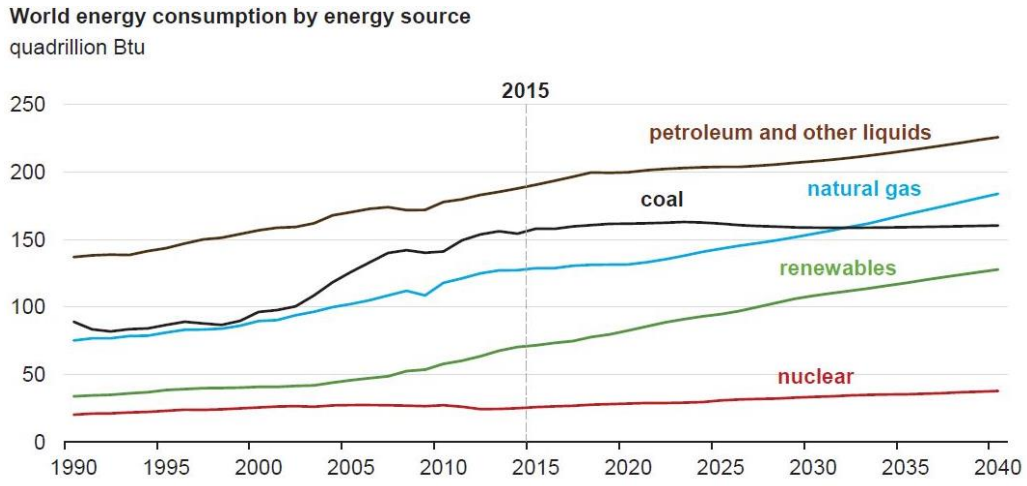

Figure 2 World energy consumption by energy source: energy sources shift gradually toward lower-carbon fuels such as renewables and natural gas, although fossil fuels (coal, petroleum and other liquids) continue to meet much of world's energy demand. Adapted from: *IEA World Energy Outlook 2017*.[1]

Energy storage technologies have continued to evolve over the last century, striving to meet the changing energy requirements and potential applications. These technologies can be broadly divided into four categories: mechanical, thermal, electromagnetic and chemical energy storage. Among them, chemical energy storage technologies, which can store and convert chemical energy into electricity, have experienced by far the greatest diversity of research and commercial products. So far, the prevailing chemical storage systems are batteries, especially those based on lithium-intercalation materials, i.e., Li-ion batteries. Although currently Li-ion batteries are the dominant power sources for portable electronic devices and are rapidly expanding into the electric vehicle

markets, they still do not compete with fossil fuels in terms of the energy storage capability. Therefore, the major challenge of today's battery research is to maximize the energy that can be stored in batteries. Towards this goal, intense research activities have been placed on continuously improving the electrochemical performance of the state-of-art Li-ion batteries while searching for new chemistries with potentially higher energy storage.

Outline of thesis

This thesis enrolls into the global push for designing batteries with better electrochemical performances and is parted between i) the fundamental understanding of the electrochemical-structural relationship in the state-of-art Li-rich layered oxides, seeking to unlock the full potential of Li-ion batteries at the material level, and ii) the investigation of the underlying reaction mechanisms for Li-CO_2 battery, an alternative to Li-ion battery which has the advantages of both energy storage and the conversion of the detrimental greenhouse gas CO_2 into value-added energy product like Li_2CO_3.

This work is thus divided into five chapters:

Chapter I start with a general introduction about the basic concepts of Lithium-based batteries and their energy limitation on the positive electrode side, prior to provide an overview of the research efforts that the battery community has made to pursue positive electrode materials with increased energy densities. Alternative battery chemistries that could potentially move beyond the energy-storage capability of Li-ion batteries will also be discussed.

Chapter II addresses the degradation phenomenon of Li-rich positive electrode materials via *in-situ* gas/pressure analyses. More specifically, rotating ring disk electrode voltammetry will be developed to monitor the irreversible O_2 release from Li-rich layered oxides on their initial charges. As a proof-of concept, the obtained results will be systematically compared with those obtained by two other well-established techniques, i.e., *in-situ* pressure cell and *online* electrochemical mass spectrometry. A general discussion concerning the pros and cons of these three pressure/gas analytical techniques will be also presented.

Based on the knowledge from the previous chapter about the structural instability of Li-rich layered oxides associated with oxygen redox, **Chapter III** explores deeper the dynamic structural change during the first electrochemical cycle in a practically important Li-rich positive electrode with a nominal formula of $Li_{1.2}Ni_{0.13}Mn_{0.54}Co_{0.13}O_2$. By cycling the material under various oxidative conditions as well as enlarging the discharge voltage window, we will demonstrate how the Li^+ extraction coupled with anionic oxidation will results in O_2 evolution, cation migration, and eventually a bulk phase densification. In addition, we will discuss how the cation migration progress upon cycling and how it will impact on the electrochemical properties. At last, we will reconsider in this chapter the origin of its undesirable first-cycle capacity loss.

Going beyond the horizon of Li-ion batteries, **Chapter IV** is specifically dedicated to a newly-born battery concept: Li-CO_2 batteries. The first part of this chapter will reveal how the electrolyte properties dictate the discharge processes of O_2-assisted Li-CO_2 batteries by controlling the superoxide intermediate. In the second part of this chapter, we will explore the potential use of quinone-based homogenous catalysts to promote the electrochemical reduction of CO_2 in "real" Li-CO_2 batteries. The practical potential of these two CO_2-battery systems will also be discussed.

The main results of this Ph.D. work will be summarized in **Chapter V**, their impacts and implications on further battery researches will be discussed along with the remaining questions.

Chapter I General introduction

Chapter I General introduction

I. 1 Basic concepts of Li-based batteries and insertion-type electrodes

I. 1. 1 Intercalation chemistry and the advent of Li battery

Intercalation chemistry refers to the reversible insertion of guest species into an open host structure with the maintenance of major structural features of the host. In 1970s, the discovery of highly reversible Li intercalation/de-intercalation in layered titanium disulfide, according to the reaction x Li + TiS_2 ↔ Li_xTiS_2, has enabled the birth of Li battery.[2,3] In a typical Li battery, two electrodes, the positive electrode and the negative electrode, are separated by an electrolyte (Figure I. 1a). The electrolyte allows the reversible shuttling of Li ions between the two electrodes while the external circuit allows for electron transport. The battery voltage (V) is determined by the equilibrium voltage difference between the positive electrode and the negative electrode, more specifically the difference between the Li chemical potentials in both electrodes (Equation I. 1).

$$V = -\frac{\mu_{Li}^{Cat} - \mu_{Li}^{An}}{e} \quad \text{(Equation I. 1)}$$

where μ_{Li}^{Cat} is the Li chemical potential of the cathode, and μ_{Li}^{An} is the Li chemical potential of the anode.

The energy storage capability of an electrode (Q) is defined as the specific capacity (Ah kg^{-1}), which is dependent on the number of Li ions that can be reversibly intercalated into the electrode without causing irreversible degradation of its structure (Equation I. 2)

$$Q = \frac{96485 * n(Li^+)}{3600 * M} \quad \text{(Equation I. 2)}$$

where $n(Li^+)$ is the number of Li ions, and M is the molecular weight of the electrode material.

The energy storage capability of a battery (E), termed as energy density (Wh L^{-1}) or specific energy (Wh kg^{-1}), is determined by the voltage (V) and the specific capacity (Q) of the positive electrode and the negative electrode (Equation I. 3)

$$E = Q * V \quad \text{(Equation I. 3)}$$

Therefore, since the first demonstration of Li battery, intensive research activities have been placed on screening/designing suitable materials for the two electrodes that would provide the highest battery voltage as well as the greatest energy density for the system. A brief historical review will be presented next regarding the developments of materials for Li batteries.

I. 1. 2 From Li battery to Li-ion battery

Starting with the negative electrode, metallic Li was first used owing to its high theoretical specific capacity (3860 mAh g^{-1} or 2061 mAh cm^{-3}) and lowest voltage (-3.04 V *vs* standard hydrogen electrode) as compared to all other candidates. In the late 1980s, Moli Energy commercialized the first Li battery using a MoS_2 positive electrode paired with excess metallic Li. However, soon this device had to be withdrawn from the market due to explosion hazards caused by uneven Li growth (dendrite) as Li was stripped/re-plated upon each charge/discharge. NEC and Mitsui have conducted reliability tests on over 500,000 Li metal batteries but failed to resolve the safety concern. Initial attempt to avoid the dendrite formation was thus made to substitute Li metal with LiAl alloy. However, such replacement would jeopardize the cycling performances of the battery because of large volume expansion associated with the alloying process.[4,5] The second approach to circumvent this safety issues aimed at replacing Li metal by another insertion-type material. Inherently safer than Li battery, this new concept is termed as Li-ion battery (or rocking-chair battery) (Figure I. 1b). Subsequently, with the discovery of low voltage and highly reversible Li intercalation/de-intercalation in carbonaceous material, Sony finally commercialized the first Li-ion battery in 1991. Carbon negative electrode, generally graphite, is still commonly used in today's commercial Li-ion batteries.

However, the capacity of carbon negative electrode is ~ 10 times less than that of Li metal (theoretical capacity of 372 mAh g^{-1} for graphite - LiC_6). This huge capacity difference is indeed an impetus for researchers to seek chemical or physical modifications for improving the carbon

negative electrode performances,[6,7] as well as to search for other promising carbon alternatives.[8,9] In parallel, intensive research activities have also been devoted to improve the understanding of Li metal chemistry via developing both characterization techniques[10,11] and Li dendrite growth theory[12,13], as well as to stabilize Li metal negative electrode through interface engineering and/or electrolyte engineering.[14-17]

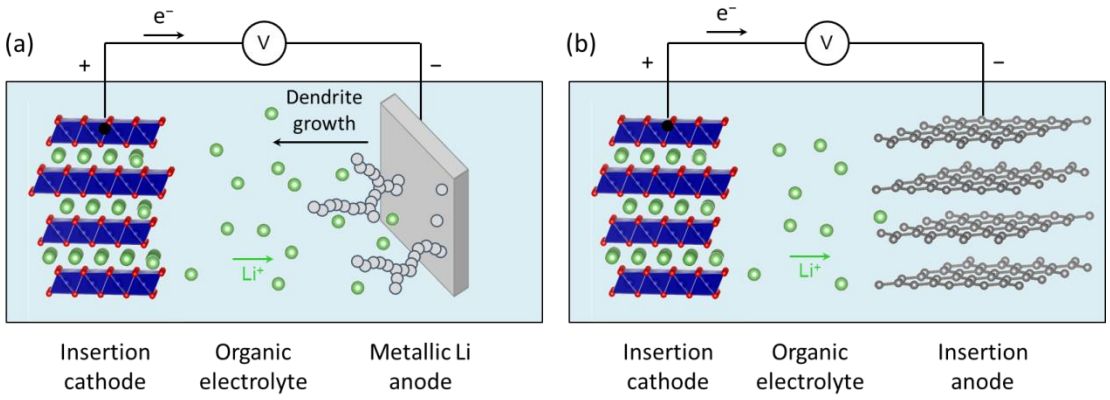

Figure I. 1 Two different Li-based batteries with negative electrodes of: (a) metallic Li and (b) insertion anode (graphite). Adapted from: *PhD thesis of Arnaud Perez, 2017.*

I. 1. 3 Positive electrode materials for Li-ion batteries and their energy limitation

Turning to the positive electrode side, it is worth firstly recalling that the positive electrode materials for Li batteries can be lithium free because of the use of Li metal negative electrode, while those for Li-ion batteries must act as the lithium source since the carbonaceous negative electrode contains no Li.

Soon after the discovery of TiS_2, layered oxide $LiCoO_2$ was introduced by Goodenough and coworkers as a new Li intercalation host.[18] Layered oxides have a higher intercalation potential than sulfides in general (Figure I. 2), owning to the more pronounced ionic character of 'M-O' bonds as compared to 'M-S' bonds. Research interests have thus quickly shifted from layered chalcogenides to oxides that are still widely used in today's Li-ion batteries. However, the drawback of $LiCoO_2$ is that only one-half of Li ions (corresponding to 150 mAh g^{-1} capacity) can be reversibly cycled without causing severe polarization and capacity loss (Figure I. 2d), owing to the abrupt structural

changes caused by the strong electrostatic repulsions of the negatively charged CoO_2 layers in Li_xCoO_2 ($0 \leq x \leq 0.5$).[19] More specially, on deep delithiation, the original O3 hexagonal phase converts to a hybridized O1-O3 hexagonal phase (also denoted as the H1-3 phase), where O represents octahedral sites, 3 is the stacking sequence of oxygen layers ABCABC and 1 is ABAB oxygen stacking sequence, as defined using the conventional nomenclature developed by Delmas and coworkers.[20] Meanwhile, gliding of the layers along with partial collapse of the O3 stacking as well as loss of oxygen further add up to the serious performances degradation of $LiCoO_2$ at high voltages and jeopardize its practical energy density.

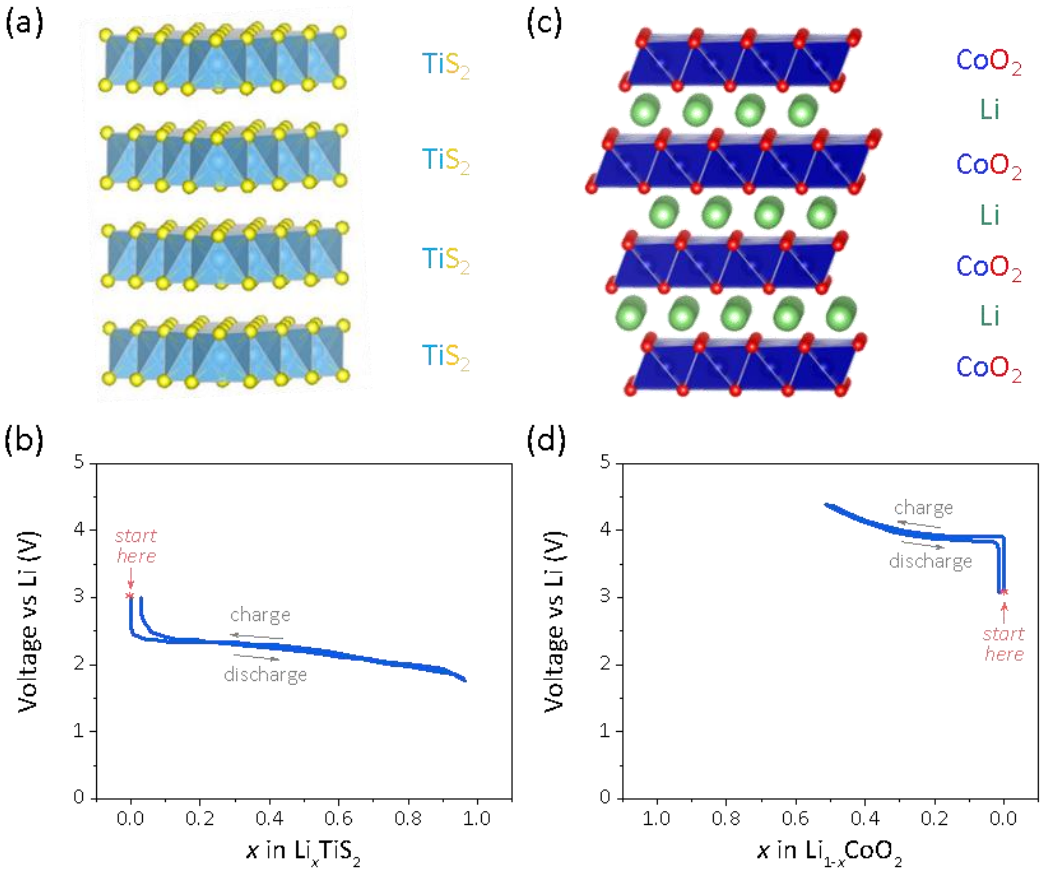

Figure I. 2 Crystal structure of TiS_2 (a) and $LiCoO_2$ (c). TiS_2 can insert 1 Li per formula unit at an average voltage of 2.2 V (b) and $LiCoO_2$ can release 0.5 Li per formula unit at an average voltage of 3.9 V (d). Adapted from: *PhD thesis of Gaurav Assat, 2018.*

Aware of the energy limitation of $LiCoO_2$, material scientists have embarked on a journey to improve the performances of positive electrode materials which currently limit the energy density of commercial Li-ion batteries. Various research directions were pursued: i) push the 0.5 Li^+ limit

of $LiCoO_2$ towards its theoretical capacity via chemical substitution, aiming to stabilize the layered framework; ii) further substitute transition metal with Li^+ (termed as Li-rich layered oxides) to increase the Li^+ content available for (de)intercalation; and iii) screen new intercalation-type positive electrodes and tailor their (de)intercalation voltage by selecting the electrochemical redox center. Directions i) and ii) target at improving the material capacity, while direction iii) focuses on increasing the material voltage.

Before going into more details in the next subchapter, let us first recall that, in addition to show a high voltage and be able to accommodate large number of Li^+ while maintaining its structural integrity, an ideal positive electrode should also possess a high electronic conductivity as well as fast Li ion diffusion, have low cost and toxicity, be chemically and thermally stable, be environmentally benign and easy to synthesize.

I. 2 Increase the energy density of positive electrode materials for Li-ion batteries

I. 2. 1 M/M' chemical substitution

To circumvent the capacity limitation of $LiCoO_2$ along with the high cost and ethical issues associated with the use of Co, the scientific community has initially attempted to replace Co with low-cost and more abundant transition metals such as Ni and Mn by ion exchange from α-$NaMnO_2$. However, isostructural $LiNiO_2$ is unable to compete with $LiCoO_2$ as it shows comparable capacity but lower (de)intercalation voltage, and was further overlooked because of its poor thermal stability in the delithiated form.[21,22] In contrast to the rhombohedral ($R\bar{3}m$) α-$NaFeO_2$ structure of $LiCoO_2$ and $LiNiO_2$, layered $LiMnO_2$ predominantly crystallizes in monoclinic (*C2/m*) unit cell with minor concentration of lithiated-spinel $Li_2Mn_2O_4$ ($F4_1/ddm$), and readily transforms into the spinel $LiMn_2O_4$ upon cycling.[23]

Mixed/partial substitution was then proposed to stabilize the layered structure as well as to tailor the (de)intercalation voltage. Numerous $LiMO_2$-type layered compounds were synthesized thereafter and can be broadly divided into binary $Li[MM']O_2$ and ternary $Li[MM'M'']O_2$ systems. Among them, the most practically important layered oxides for Li-ion batteries are $Li[Ni_xCo_yAl_z]O_2$

(NCA) and $Li[Ni_xMn_yCo_z]O_2$ (NMC) series. NCA can be intuitively viewed as a partial substitution of Ni by Co in $LiNiO_2$, together with a small amount of Al doping. Co helps to reduce the degree of Li/Ni disorder and effectively stabilizes the structure, while Al is electrochemically inactive but improves the thermal stability. Thanks to the synergistic effects of Co and Al co-substitution, $Li[Ni_{0.8}Co_{0.15}Al_{0.05}]O_2$ could achieve an attractive practical discharge capacity of ~ 200 mAh g^{-1} (Figure I. 3), and is widely used in today's electrical vehicles including Tesla Model S.[24,25] However, NCA suffers from capacity fading, particularly at high temperatures and at high current rates.

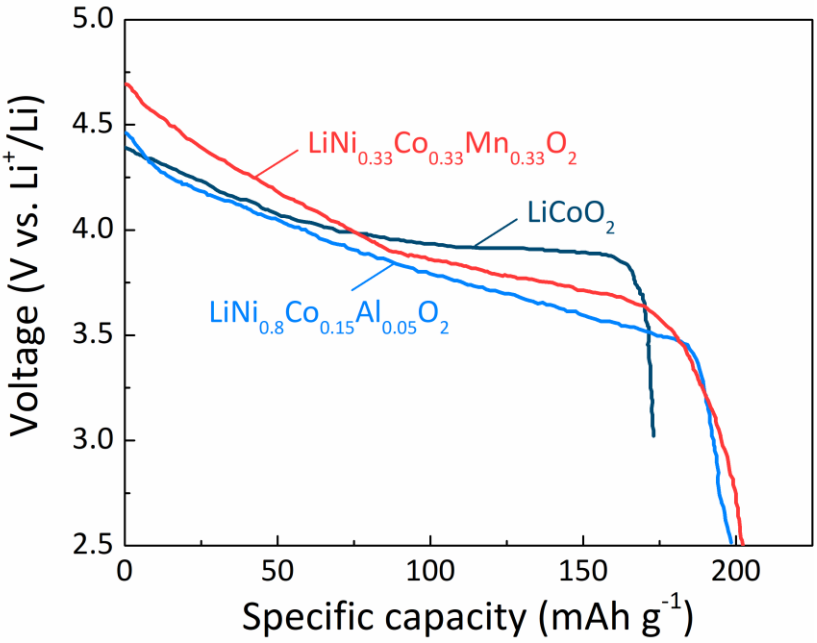

Figure I. 3 Typical discharge voltage profiles of different intercalation-type positive electrodes. Adapted from Nitta *et al.*[24]

Similarly, NMC series can be prepared by partially substituting Co with Ni and Mn in $LiCoO_2$ (Figure I. 4). In doing so, Ni provides the capacity, Co the structural stability and Mn the thermal stability,[26] and $Li[Ni_{1/3}Mn_{1/3}Co_{1/3}]O_2$ (also referred to as NMC 111) is found to deliver promising electrochemical performances with reversible capacity of ~ 200 mAh g^{-1} when charged up to 4.6 V (Figure I. 3) and is currently used in BMW i3, Chevy Bolt and the new Nissan Leaf. By steadily increasing the Ni content (decreasing the Co content), researchers further enhanced the capacity of NMC materials and prepared a series of Ni-rich NMCs termed as NMC 433, NMC 532, NMC 622 and NMC 811. However, raising the Ni-content result in penalties of reduced thermal

stability, safety issues owing to the release of O_2 and CO_2, along with poor capacity retention caused by the irreversible Li^+ loss associated with the progressive development of a surface film triggered by the fracturing of particles induced by large volumetric changes.[27-29] Extensive efforts seeking to mitigate these issues have been put into surface coating and modifications, morphology and mesostructured design, as well as electrolyte engineering.[30] Despite of the substantial progresses achieved so far, the most effective approach to further push the energy density of positive electrode materials towards their upper limits resides in playing with the chemical composition, as will be discussed next.

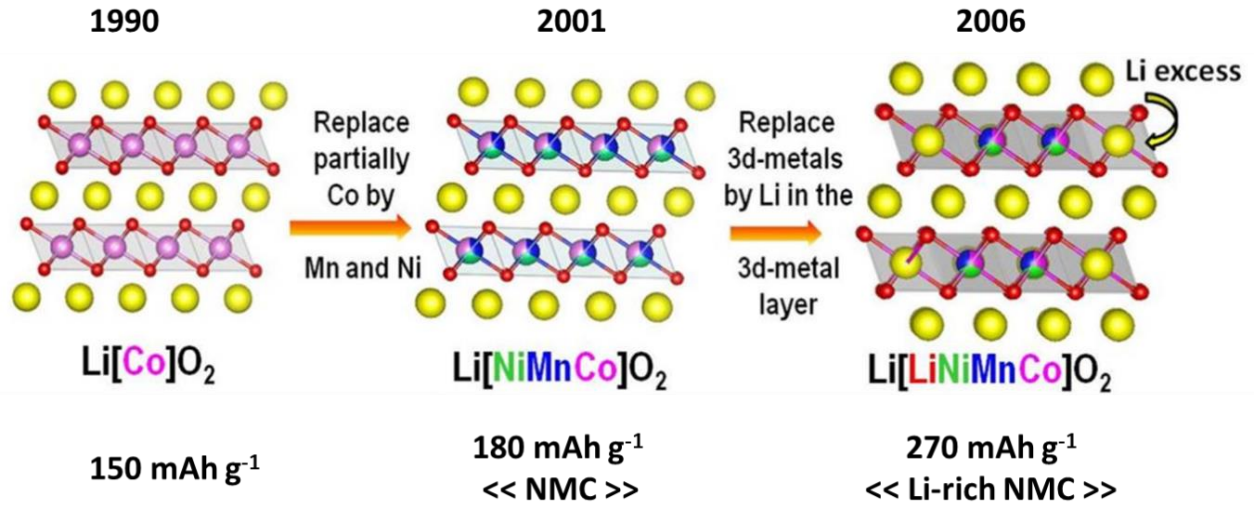

Figure I. 4 Push the capacity of layered oxide $LiCoO_2$ by 1) partially substitute Co (pink) with Ni (green) and Mn (blue) leading to the NMC phase and 2) further substitute with Li (yellow) to give Li-rich NMC phase. Adapted from Rozier *et al.*[31]

I. 2. 2 Li substitution and the participation of oxygen redox

In an attempt to achieve higher capacities than $LiMO_2$-type layered compounds, Li-rich Li_2MO_3-type materials (alternatively described as $Li[Li_{1/3}M_{2/3}]O_2$) with excess Li in the transition metal layers were also heavily investigated since late 1980s.[32-35] As expressed in their general formula, $Li[Li_{1/3}M_{2/3}]O_2$ and $LiMO_2$-type compounds share similar structures with one notable difference: all octahedral sites in the metal layers are occupied by M^{3+} cations in $LiMO_2$ structure, whereas one third of those sites are occupied by Li^+ and two third by M^{4+} in $Li[Li_{1/3}M_{2/3}]O_2$ structure. Pioneering works on $Li[Li_{1/3}M_{2/3}]O_2$-type materials involved the detection of

electrochemical activity in Li_2MnO_3 which is rather abnormal since the octahedral Mn^{4+} cannot be further oxdized to release Li^+ during charge.[36] Through acid-leaching, this unexpected electrochemical activity in Li_2MnO_3 was attributed to the Li_2O removal with "MnO_2-like" activation.[33] In parallel, binary phase $Li[Li_{(1/3-2x/3)}M_{(2/3-x/3)}M'_x]O_2$ prepared by partial transition metal substitution were also explored.[37-40] Among them, $Li[Li_{(1/3-2x/3)}Mn_{(2/3-x/3)}Ni_x]O_2$ with x = ¼ delivers reversible capacities of nearly 230 mAh g^{-1} (corresponding to almost 1 Li per formula unit) when charged up to 4.8 V.[41] The improved capacity obtained for $Li[Li_{(1/3-2x/3)}\ Mn_{(2/3-x/3)}Ni_x]O_2$ when compared to classical layered oxides created an impetus for further exploration of these Li-rich phases, before to eventually lead to the discovery of $Li[Li_xNi_yMn_zCo_{(1-x-y-z)}]O_2$ (also termed as Li-rich NMC) that could offer staggering discharge capacities of more than 270 mAh g^{-1} (Figure I. 4),[34,42,43] a high value which cannot be explained by the conventional view of transition metal redox. Markable differences are also observed in the voltage-composition profiles of Li-rich layered compounds. Typically, Li-rich oxides exhibit a two-step staircase charge voltage profile with a long high-voltage plateau (ca. 4.5 V) followed by a sloping S-shaped voltage profile on discharge. This S-shape profile pertains on subsequent cycles, and differs from classsical Li-stoichiometric oxides whose charge and discharge voltage-composition profiles mirror each other nicely.

Such high capacities and the unusual long charge plateau were initially explained by the Li-driven activation of oxygen redox (simultanous removal of Li^+ and oxidation of lattice O^{2-} to O_2, also referred to as Li_2MnO_3 activation) based on Rietveld refinement and further demonstrated with *in-situ* differential electrochemical mass spectrometry (DEMS).[41,44,45] However, controversies arise as the onset of O_2 evolution does not exactly match with the beginning of the high-voltage plateau.[46] Furthermore, quantitative gas analysis reveals that the amount of released O_2 (amount of O^{2-} oxidation) is far too little to be responsible for the capacity obtained during the high-voltage plateau (the detected O_2 amount can only account for ~ 6.4 mAh g^{-1} of charge capacity, which is negligible compared to the overall extra charge capacity of ~ 200 mAh g^{-1} (the part of capacity that cannot be explained by cationic redox)).[47] Finally, a global "bulk-shell model" was suggested in order to rationalize the oxygen redox mechanisms: reversible oxygen redox ($2n\ O^{2-} \leftrightarrow (O_2)^{n-} + 2n\ e^-$ (n < 2)) in the bulk which explains the superior reversible capacities obtained with these Li-rich type materials and irreversible oxygen release at the near-surface region ($2\ O^{2-} \rightarrow O_2 + 2\ e^-$).[47-50] Aware of the diffculty of establishing the oxygen redox mechanism in the complex Li-rich NMC systems which include three cationic redox centers (Ni^{2+}, Mn^{4+}, Co^{3+}), Tarascon and co-workers

designed a model system $Li_2Ru_{1-y}Sn_yO_3$ which is isostructural with Li-rich NMCs but with only one single cationic redox center Ru^{4+}, and demonstrated direct evidence on the formation of $(O_2)^{n-}$ species ($n < 2$).[51] This observation confirmed the aforementioned speculation of reversible participation of oxygen redox in Li-rich oxides, and unambiguously explained their high capacities as arising from cumulative cationic ($M^{n+} \leftrightarrow M^{(n+1)+} + e^-$) and anionic ($2n\ O^{2-} \leftrightarrow (O_2)^{n-} + 2n\ e^-$($n < 2$)) redox processes. Years later, the reversible participation of lattice oxygen redox in Li-rich NMC was also experimentally proved using ^{18}O-labelled *online* electrochemical mass spectrometry by quantifying the amount of latticed oxygen released as O_2 and CO_2.[46]

Through intensive experimental and theoretical studies, it is now generally understood that the origin of oxygen redox in Li-rich layered oxides is the O (2*p*) lone-pair states which are close enough to the Fermi level to be oxidized.[52-54] Those lone-pair states are preferentially formed for the Li-O-Li configurations in which the Li (1*s*) orbitals of Li^+ from both the transition metal and Li layers cannot overlap with O (2*p*) orbitals. This explains well the different redox mechanisms observed for conventional and for Li-rich layered oxides. Indeed, for conventional $LiMO_2$ layered oxides, each oxygen ions are coordinated by three transition metal ions so that all the O (2*p*) orbitals overlap with transition metal *d* orbitals, leading to zero O (2*p*) lone-pair state. Accordingly, their electrochemical reactions are dominated by cationic redox. Note that although the presence of excess Li^+ in transition metal layers plays an important role in activating oxygen redox activity, it is not an essential requirement as O (2*p*) lone-pair states also occur in environments containning Mg^{2+} (stemming from Mg^{2+} 3*s* interaction with O 2*p*) or cationic vacancies. This fact explains the reversible participation of oxygen redox in Na-based layered oxides without Na excess such as $Na_{2/3}Mg_{0.28}Mn_{0.72}O_2$ and $Na_{4/7}[\square_{1/7}Mn^{6/7}]O_2$ ($\square$ being Mn vaccancy).[55,56]

Increasing the O/M (or Li/M) ratio thus offers the opportunity to push the oxygen redox capacity by increasing the number of O (2*p*) lone-pair states. Following this strategy, Tarascon and co-workers reported a Li_3IrO_4 phase which could reversibly uptake and release 3.5 Li^+ per iridium ion, the highest value ever reported among all the intercalation-type positive electrode materials. In this phase, two Li^+ could be reversibly (de)intercalated from Li_3IrO_4 with the sole participation of oxygen redox, while the remaining insertion of 1.5 Li^+ into Li_3IrO_4 is counter-balanced by the reduction of Ir^{5+}.[57] Nevertheless, the large oxygen gas release and structural amorphization observed at highly charged states of $Li_{3-x}IrO_4$ clearly suggest that, pushing the oxygen redox

activity in Li-rich materials comes with the risk of increasing the structural instability. Several approaches have thereafter been suggested to stabilize the oxygen network including chemical substitutions,[58] increasing M-O bond covalency,[59] and altering the dimensinaltiy of the the M-O network.[60] Also worth mentioning is a recent theoretical work which propose that the charge-transfer gap (Δ_{CT}) of Li-rich layered oxides and the number of holes per oxygen (h^0) can serve as descriptors to quantify the achievable oxygen redox capacity on charge and its reversibility on discharge.[61]

Overall, the discovery of reversible oxygen redox activity in Li-rich oxides is appealing as it provides an opportunity to raise the energy limit of current positive electrode materials by combing cationic and anionic redox processes within the same compound. In those compounds, oxygen can effectivly serve as an extra electron source when more Li^+ needs to be extracted than the transition metal redox center can offer. Moreover, the demonstration of oxygen redox in 4*d* and 5*d* transition metal-based Li-rich oxides opens a wide playground for material scientists to design new high-capacity electrodes including a new class of cation-disordered oxides,[58] and to bring new understanding about the oxygen redox process. Nevertheless, the extra capacity offered by the oxygen redox activity generally associated with structural instabilities (i.e., irreversible O_2 gas loss (further addressed in Chapter II), cation migrations (further explored in Chapter III)), and unfavorable electrochemical properties (i.e., large first cycle irreversibility, voltage decay and capacity fading upon cycling).

I. 2. 3 Positive electrode materials with elevated (de)intercalation voltage

Given the Equation I. 3, an alternative approach to enhance the energy density of Li-ion batteries is to increase the output cell voltage without compromising the specific capacity. Since the potential of graphite negative electrode commonly used in modern Li-ion battery is less than 0.25 V *vs* Li^+/Li (for Li_yC_6, $0.1 < y < 1$), the cell voltage is obviously dictated by the Li^+ (de)intercalation potential of the positive electrodes.

Other than playing with the transition metal redox center (e.g., slightly higher operation potential can be obtained by moving from Ni^{3+}/Ni^{4+} to Co^{3+}/Co^{4+} redox couple), the redox potential of positive electrodes can be alternatively tuned by using more electronegative anions or anionic ligands. Along this line, moving from transition metal sulfides to transition metal oxides would be

advantageous as already discussed in Chapter I. 1. 3. Further replacing oxygen ions with polyanion units $(XO_4)^{n-}$(X = S, P, Si, etc.) lead to the discovery of a class of poly-anion compounds with higher (de)intercalation voltage. The strong covalent bonding within the poly-anion units reduces the separation between the bonding and antibonding orbitals, shifting the antibonding orbitals, which are pinned at the Fermi level and responsible for the electrochemical activity of the material, to lower energy thereby increasing the (de)intercalation voltage (the so-called "inductive effect").[62,63] Following this strategy, introducing fluorine as the anion to form M-F bond would further raise the (de)intercalation voltage by lowering the energy of the antibonding *d*-orbital of the transition metal.[64] Despite offering the potential to extend the (de)intercalation voltage up to 5 V and even beyond,[65] researches dedicated to poly-anion compounds are now leveling off because of the energy and the power penalties associated with their heavy formula weight, poor electronic/ionic conductivity and low packing density.

For a material with a given chemical composition, its (de)intercalation voltage can be tuned by playing with the crystal structure, introducing defects or changing the local chemical environment. As the Li^+ (de)intercalation in electrode materials involves simultaneous addition (removal) of lithium ions and electrons, the redox voltage of electrode materials is directly related with the energy required to add (remove) lithium ions into (from) the host crystal lattice and to add (remove) electrons into (from) the *d* orbitals of the transition metals. Different positions in a given crystal structure exhibit different Li^+ (de)intercalation voltage depending on their site energy, i.e., the main component of the Gibbs free energy, defined as the enthalpy change during Li^+ (de)intercalation. For instance, in spinel $Li_xMn_2O_4$, Li^+ ions are intercalated into smaller tetrahedral sites at 4.3 V ($x \leq 1$) and bigger octahedral sites at 3.1 V ($x \geq 1$), despite of operating on the same Mn^{3+}/Mn^{4+} redox couple within the spinel framework.[66] Introducing disorder of atomic arrangement can also affect the (de)intercalation voltage. For example, spinel $LiNi_{0.5}Mn_{1.5}O_4$ with the disordered face-centered $Fd\bar{3}m$ structure exhibits lower de-intercalation voltage than that of $LiNi_{0.5}Mn_{1.5}O_4$ with ordered primitive simple cubic structure ($P4332$) (i.e., 4.69 V and 4.75 V compared to 4.74 V and 4.77 V).[67] Up to now, the most successful high-voltage cathode material is the Ni-doped Mn spinel $LiNi_{0.5}Mn_{1.5}O_4$ showing an operation voltage in the range of 4.7 – 4.8 V with reasonable cyclability even at high rate.[68] Although $LiNi_{0.5}Mn_{1.5}O_4$-based spinel materials cannot compete with Li-rich layered oxides in terms of energy density because of their moderate capacities, they hold

promise for high-power applications due to fast Li^+ diffusion enabled by the interconnected diffusion channels in their 3D structures.

Nevertheless, the practical application of these $LiNi_{0.5}Mn_{1.5}O_4$-based spinel electrodes poses severe challenges to the electrochemical stability of electrolytes against oxidation as their operation voltages entirely or partially exceed the electrochemical window of the commonly used organic electrolytes. Major issues are associated with the electrode/electrolyte interface where electrolyte (both solvent and salt) decomposition is promoted by high-valence transition metals in the charged electrodes, resulting in the surface dissolution of transition metals, inter-reaction of bulk electrolyte components, "electrochemical dialogues" between positive and negative electrodes, and corrosion of other cell components (e.g. aluminum current collector).[69-72] Additionally, the effect of these parasitic reactions becomes even more severe at elevated temperatures and in full cell configuration where the Li^+ content is limited. Mastering the surface/interface chemistry of $LiNi_{0.5}Mn_{1.5}O_4$ is therefore critical for its successful commercialization. Various approaches have been explored to stabilize the electrode/electrolyte interface, including i) modifying the crystal chemistry through cationic or anionic substitution;[68] ii) surface treatment;[73] iii) designing novel electrolytes that are intrinsically more stable such as ionic liquids, polymer and inorganic solid electrolytes;[74] iv) introducing electrolyte additives aiming to form a thin but robust protective layer on the electrode surface;[75] v) adding HF scavenger (HF is generated from the hydrolysis reaction of $LiPF_6$ salt and is responsible for most of the aforementioned parasitic reactions);[76] vi) developing new lithium salts that can potentially overcome the two shortcomings of the stellar salt $LiPF_6$ (i.e., chemical and thermal instability);[77] and vii) applying concentrated electrolytes (electrolytes with high salt/solvent ratio) with improved oxidative stability.[78]

I. 3 Searching for new chemistries with potentially higher energy storage

Despite all the outstanding developments achieved so far for the Li-ion battery technology, their energy storage capability based on intercalation chemistry is insufficient for the long-term needs of modern society. This mismatch spurred intensive researches on alternative chemistries holding the potential to surpass the energy limitations of Li-ion batteries, among which several representatives will be introduced next.

I. 3. 1 Conversion chemistry

In contrast to intercalation chemistry, conversion chemistry involves the cleavage and formation of new chemical bonds during Li^+ insertion/extraction. So far two types of conversion reactions have been identified for Li chemistries:

Type I : $MX_z + y\ Li^0 \leftrightarrow M^0 + z\ Li_{(y/z)}X$

Type II: $y\ Li^0 + X^0 \leftrightarrow Li_yX$

where M are typically transition metal cations and X are anions.

Type I conversion reactions, in contrary to classical intercalation reactions that are often limited to 1 e^- per transition metal, can offer 2 e^- or even more per transition metal, therefore enabling staggering capacities. Moreover, their redox potentials can be tuned by playing with the electronegativity of anions and transition metals (e.g., the redox potential ranges from 0.4 to above 3.0 V as moving from covalent phosphides to ionic fluorides), hence offering the opportunity to use those conversion electrodes as both positive and negative electrodes. The concept of "conversion reaction" was considered as a breakthrough but still remains a laboratory curiosity because of its intrinsic drawbacks: i) the formation of metal nanoparticles actively decompose the $Li_{(y/z)}X$ matrix in which they are embedded; ii) the strong structural re-organization during phase transformation induces large volume change and iii) the existence of large voltage hysteresis. Moreover, being lithium-free compounds, MX_z require an additional chemical lithiation step prior to be used as positive electrodes. Along that line, worth mentioning is a recent work which address this limitation by blending nano-sized MnO with LiF that function as a Li source.[79] The MnO-LiF composite is activated at high potentials (~ 4.5 V) to form a new Mn-O-F-like surface that can reversibly uptake/release Li^+ ($LiF + Mn^{II}O \leftrightarrow Li^+ + e^- + Mn^{III}O–F$). Such "surface conversion reaction" has the merit of maintaining the high-valence states of transition metals (M^{II}/M^{III}) as they are housed by the anions on both charge (by O^{2-} and F^-) and discharge states (by O^{2-}), hence maintaining the operation cell voltage. Although this work opens a new route to design positive electrodes, cautions must be exercised in the role of LiF and side reactions brought by the use of nanocomposites (increased exposure surface), as suggested by Tarascon and coworkers, without LiF, the

electrochemical activation of MnO to Mn-O-F-like phase can equally occur via the decomposition of $LiPF_6$ salt.[80]

Type II conversion reaction is also quoted as "chemical transformation reaction" because it involves the transformation of one single phase into another single phase. Typical examples include the lithiation of chalcogens and halogens (i.e., S, Se, Te, Br, I). Amongst the lithiation of S (referred as Li-S battery) has been studied the most because of its greater specific energy, since S is light element and one S atom can accept two electrons (uptake two Li^+) to form lithium sulfide ($2\ Li^+ + 2\ e^- + S \leftrightarrow Li_2S$), amounting to a theoretical capacity one magnitude higher than that of transition-metal oxide at the expense of a lower operating voltage (ca. 2.15 V). Moreover, being the fifth most abundant element on earth, S has a cost advantage. On the negative side, the S/Li_2S conversion reaction is accompanied by a large volume change of about 80 %. In addition, the poor electrical conductivity of S and Li_2S necessitates the incorporation of conducting additives (e.g., carbon) to construct composite S electrode, which markedly compromises the volumetric energy density. Another major issue is associated with the soluble intermediate polysulfides (Li_2S_x) generated at the positive electrode during the discharge. Those Li_2S_x species diffuse to the negative electrode (i.e., metallic lithium) where they are chemically reduced to lower polysulfides or insoluble Li_2S_2 and Li_2S, giving rise to the so-called "shuttle" effect which induces the loss of active material, impedance build-up and capacity fading. Several approaches have been suggested to tackle the dissolution of polysulfides: i) play with surface chemistry or solvation properties of electrolytes aiming to promote the chemical interactions between the host material and the dissolved polysulfides; ii) design smart electrode architectures to allow encapsulation of polysulfides, iii) utilize polymer or solid electrolytes instead of liquid ones to physically separate the two electrodes; and iV) introduce electrolyte additives, such as the "magic" $LiNO_3$, to enhance the passivation of metallic lithium. Although the battery community has witnessed in the last four decades Li-S battery with greatly improved electrochemical performance and fundamental understanding, step-changes are awaited in many aspects before Li–S chemistry can be successfully employed in practical systems: i) accommodating the large volume expansion and contraction on full S/Li_2S conversion; ii) realizing high-S-loading electrode with reasonable conductivity to ensure both the energy density and power rate; iii) controlled Li_2S deposition/dissolution and iV) improving the metallic lithium electrode, a task that has in common with Li battery as introduced in Chapter I.1 whist with an additional requirement in its chemical stability against polysulfides.

Another important class of type-II conversion reaction is the O_2/Li_2O_2 conversion in Li-O_2 battery with a high theoretical specific energy rivals that of gasoline. Because gaseous oxygen is involved in the electrochemical reaction enlisting a solid-gas-solution reaction, Li-O_2 batteries possess intrinsically different merits and challenges, which will be introduced in the next subchapter.

I. 3. 2 Li-O_2 battery

Li-O_2 batteries can operate under both aprotic and aqueous conditions, respectively forming Li_2O_2 ($2\ Li + O_2 \leftrightarrow Li_2O_2$) and LiOH ($4\ Li + O_2 + 2\ H_2O \leftrightarrow 4\ LiOH$) as the final discharge product. Their cell configurations and working principles are depicted in Figure I. 5. In both cases, metallic Li is used as the negative electrode, O_2 gas as the reactant along with a porous carbon matrix as the positive electrode to accommodate the discharge product. Because water readily reacts with metallic Li, a Li conducting while electronic insulating layer or a polymer membrane must be incorporated into the aqueous system to protect Li. During discharge, the metallic Li negative electrode is oxidized to release Li^+ into the electrolyte. At the positive electrode, the reactant (O_2) undergoes reduction before to combine with Li^+ to form lithium peroxide (Li_2O_2) in non-aqueous system; or to produce LiOH in aqueous system since water also participates in the reaction. The reverse reactions are expected to occur on charge. Nevertheless, the decomposition of Li_2O_2 or LiOH is unfavorable due to the difficulty of off-stoichiometric $Li_{2-x}O_2$ formation or O-H bond cleavage, jeopardizing the reversibility and cyclability of the system. Because of the more complex cell-design required for aqueous system and safety concerns, more attention has been paid to non-aqueous system until a publication from Grey and coworker in 2015 revived interests and debates in the aqueous systems.[81]

At this stage, it is clear that the alluring theoretical energy density of Li-O_2 battery (3436 Wh L^{-1}) arises from three aspects: i) metallic Li which offers the highest specific energy is used as the negative electrode; ii) the reactant O_2 gas is not contained within the system but comes from the atmosphere; iii) the energy storage product Li_2O_2 (or LiOH) has a much lower molecular weight to electron ratio than typical intercalation transition metal oxides used in Li-ion batteries (i.e., 23 g/(mol*e^-) for Li_2O_2 and 24 g/(mol*e^-) for LiOH *versus* 98 g/(mol*e^-) for $LiCoO_2$, amounting to specific energy of 3505 Wh Kg^{-1} and 3582 Wh Kg^{-1} for aprotic and aqueous Li-O_2 batteries, and 387 Wh Kg^{-1} for Li-ion batteries). However, the practically accessible specific energy of Li-O_2

batteries is less attractive for two reasons: i) the utilization of oxygen-containing pressure vessel or oxygen-selective membrane is mandatory in order to cycle under pure O_2 atmosphere, which will inevitably jeopardize the energy density and increase the cost at the system level; ii) the loss of electronic conductivity as arising from the deposition of insulating discharge products onto the electrode surface.

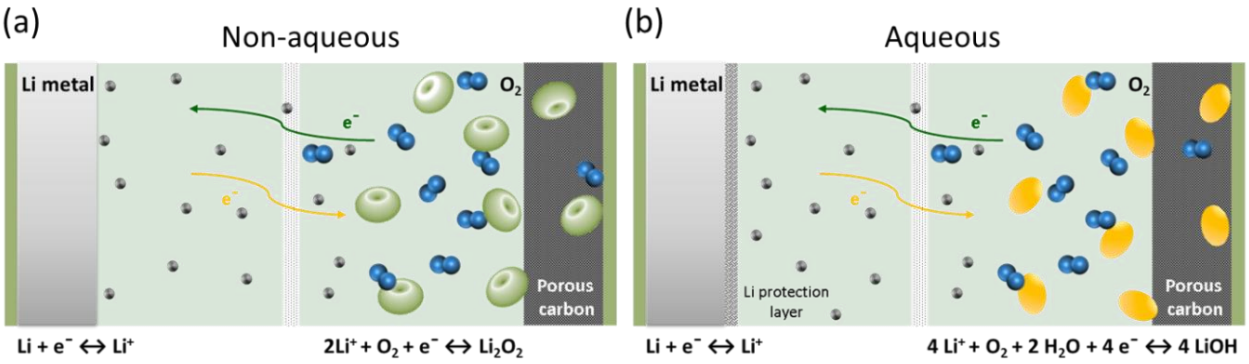

Figure I. 5 Schematic illustration of (a) non-aqueous and (b) aqueous Li-O_2 batteries. Note that the yellow arrow indicates the discharge process, whereas the green arrow indicates the charge process.

To overcome the challenges at the positive electrode, essentially one needs to understand the electrochemical mechanisms of O_2 reduction in Li^+-containing non-aqueous electrolytes. Now it is well understood that the first step involves the one electron reduction of O_2 and the subsequent combination with Li^+ to form LiO_2 as the intermediate ($Li^+ + e^- + O_2 \rightarrow LiO_2$). Successively, two different reaction paths have been envisioned: i) LiO_2 adsorbed on the electrode surface (denoted as LiO_2^*) to be converted into Li_2O_2 via a second-electron reduction ($LiO_2^* + e^- + Li^+ \rightarrow Li_2O_2$), the so-called "surface mechanism" or ii) LiO_2 dissolved in the electrolyte (referred to $LiO_{2(sol)}$) where it undergoes a disproportionation reaction ($2\ LiO_{2(sol)} \rightarrow Li_2O_2 + O_2$), also known as "solution mechanism" (Figure I. 6).[82] Notably, these two mechanisms lead to a marked difference in the morphologies of discharge products: surface mechanism generally induces film-like Li_2O_2 on the electrode surface, whereas solution mechanism results in a precipitation of toroidal-shape Li_2O_2 particles. The morphology difference also suggests that the solution mechanism is more desirable than the surface mechanism for maximizing the discharge capacity and the energy density: the formation of insulating Li_2O_2 film on the electrode surface rapidly increases the charge-transfer resistance thereby causes early cell death,[83] whereas the solution-mediated growth of large toroidal

particles generally leads to larger discharge capacity. Because the competition between the surface and the solution mechanism depends on the equilibrium between LiO_2^* and $LiO_{2(sol)}$, increasing the solubility of LiO_2 should offer opportunities to boost the discharge performance of Li-O_2 batteries. Researchers have suggested several strategies to enhance the solubility of LiO_2 so as to promote the solution-driven growth of Li_2O_2 including i) selecting electrolyte solvents with higher Gutmann donor number[82] or acceptor number;[84] ii) utilizing salt anions with increased Li^+ solvation strength;[85] iii) using protic additives;[86] or iv) facet-engineering of the positive electrode.[87]

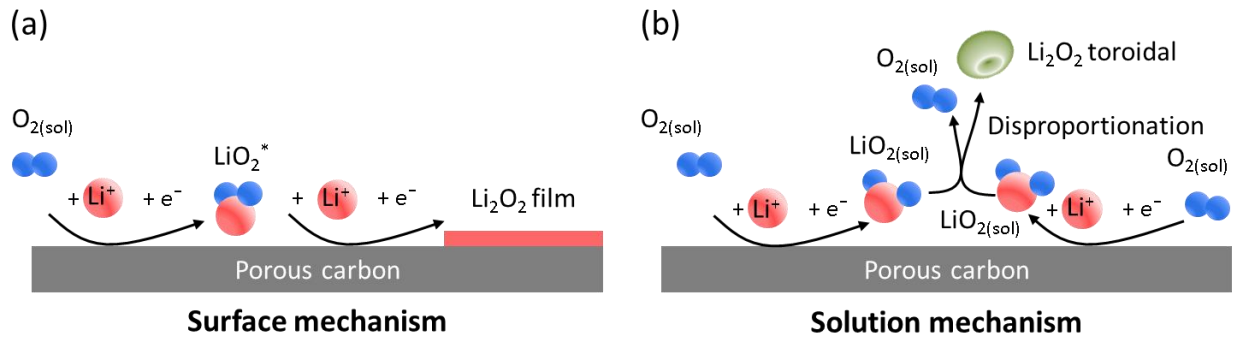

Figure I. 6 Schematic illustration of O_2 reduction in Li^+-containing non-aqueous electrolytes following (a) the surface and (b) the solution mechanism.

Although the solution mechanism alleviates the surface passivation of positive electrode and improves the discharge capacities of Li-O_2 batteries, the electrolytes and additives that support this mechanism also introduce additional parasitic reactions. For instance, strongly solvating solvents are often more vulnerable to nucleophilic attack or proton abstraction by the reactive $LiO_{2(sol)}$ intermediate.[88] Further exploration is thus needed to reach an optimized combination between solvating properties and stability. Alternatively, worth mentioning is the use of a molecular additive, named 2, 5-di-tert-butyl-1,4-benzoquinone (DBBQ), which can promote solution-phase discharge in weakly solvating electrolytes that are more stable towards $LiO_{2(sol)}$.[89] This work dodges the "double-edge sword" (high capacity but poor stability) and provides a new route to enable the solution growth of Li_2O_2.

The decomposition reaction of Li_2O_2 during charge is another critical issue. As Li_2O_2 is a poor electronic conductor with a large band gap of ~ 5 eV, a huge overpotential (0.5 ~ 1.3 V) is typically observed on charge due to the sluggish electron transport. The situation is even worse for the Li_2O_2 particles that are away from the electrode surface, for instance, those formed via solution

mechanism. Charging at high potentials not only undermines the round-trip efficiency, but also causes carbon corrosion and electrolyte decomposition. Therefore, controlling the defect chemistry of Li_2O_2 emerged as a potential strategy to improve the electronic conductivity in bulk Li_2O_2 including doping,[90] creating off-stoichiometric (O-rich) $Li_{2-x}O_2$[91] and Li_2O_2 with surface/grain boundaries.[92] Along that line, tuning the crystal structure of Li_2O_2 through heterogeneous catalysts like noble metal palladium was shown to lower the charge potential via the formation of amorphous Li_2O_2 which has a better electronic conductivity than crystalline Li_2O_2.[93,94] Nevertheless, caution must be exercised in this strategy since the use of metallic particles also promotes the degradation of organic electrolytes. Adding soluble catalysts (denoted as redox mediators hereinafter) to the electrolyte that shuttle electrons between "distant" Li_2O_2 particles and the electrode surface has been heavily explored as an alternative strategy to facilitate the Li_2O_2 oxidation. The fascinating aspect of this approach is that the use of a redox mediator shifts the Li_2O_2 oxidation from an electrochemical pathway to a chemical pathway such that the battery will be charged at the redox potential of the redox mediator, bypassing the high over-potential resulted from the electron transfer limitation in bulky Li_2O_2 particles (Figure I. 7). Nevertheless, this intriguing approach has not yet led to a breakthrough because of four considerations: i) the chemical stability of redox mediators themselves, ii) degradation of other cell components induced by redox mediators, iii) once oxidized, redox mediators might diffuse to the negative electrode (metallic Li) side, rather than diffuse to a Li_2O_2 particle, creating an electron shuttle between the negative and the positive electrode, iv) other insulating side products deposited on the electrode surface block the oxidation of redox mediators.

Overall, as compared to the discharge process, the charge of Li-O_2 batteries is more problematic and less understood. Several key puzzling questions still remain unanswered: i) what is the charge transfer mechanism in Li_2O_2? ii) what is the origin for the differences in the shape of the charge voltage profiles? and more importantly, 3) what is the decomposition reaction mechanism of Li_2O_2?

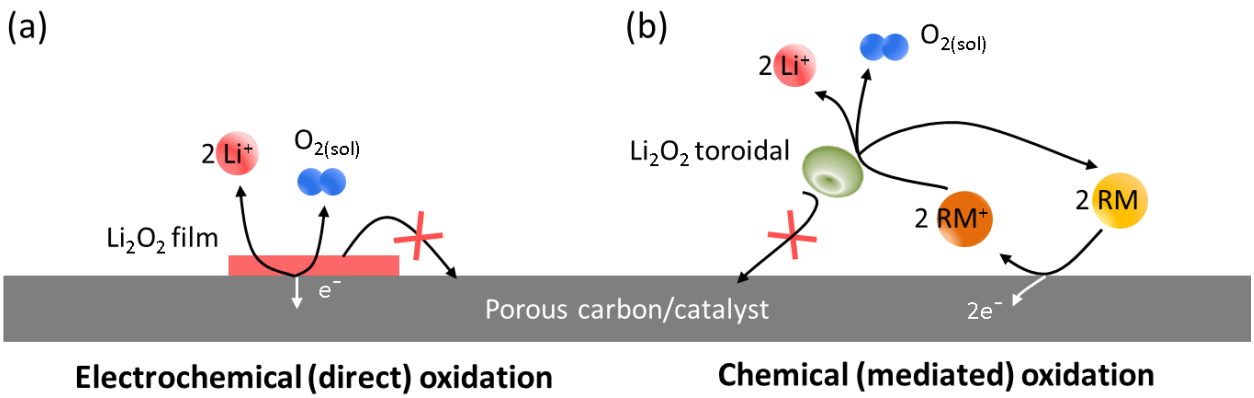

Figure I. 7 Schematic illustration of (a) direct electrochemical Li_2O_2 oxidation and (b) chemical Li_2O_2 oxidation mediated by redox mediators. Red "X" mark shows that Li_2O_2 particles deposited away from the electrode surface fails to be oxidized because they are electronically isolated from the electrode surface.

The last, and perhaps the most significant challenge, pertains to understand how the constituents of ambient air affect the Li-O_2 electrochemistry. Ideally, in a Li-O_2 battery, O_2 can be fed directly from ambient air with a filtering system to ensure the removal of all other air components. Nevertheless, such approach induces penalties on the energy density which significantly drops from 3436 Wh L^{-1} at the material level to 411 Wh L^{-1} at the system level.[95] Even worse is that, practical-wise, trace amount of ambient impurities are inevitable. Amongst two common impurities, CO_2 and H_2O will be considered in the following paragraphs.

The effects of H_2O in Li-O_2 electrochemistry are very complex and seem to vary with H_2O concentration, electrolytes and additives. Several possibilities were suggested in pioneering works: i) small amount of H_2O promotes LiO_2 dissolution, leading to the formation of toroid Li_2O_2 through the solution-mediated mechanism and therefore the increase of discharge capacity;[86] ii) H_2O slows down the nucleation rate of Li_2O_2 on the electrode surface and thereby triggers the solution mechanism;[96] iii) increasing the acidity of H_2O by specific catalysts like lithium iodide leads to the formation of LiOH as the dominating discharge product instead of Li_2O_2;[81,97] iv) H_2O modifies the discharge intermediate from superoxide to hydrosuperoxide;[98] and v) H_2O stabilizes the redox mediators in their reduced form, shifting the discharge potential to higher values.[99] In addition, the presence of H_2O also induces more parasitic reactions: i) H_2O degrades metallic Li negative electrode; ii) H_2O may chemically react with Li_2O_2 to give LiOH that can hardly decompose during

charge; and iii) the stabilization of nucleophilic LiO_2 species by H_2O induces proton/hydrogen abstraction from non-aqueous solvents, undermining the solvent stability.[88] Overall, how the addition of H_2O will modify the morphology, the nucleation rate, the formation pathway and even the chemical nature of discharge products are still open questions. Unlike for the discharge process, so far little is known about the effect of H_2O on the charge process.

Equally important is to understand the influence of CO_2 contamination in Li-O_2 batteries. Coupled galvanostatic charge/discharge measurements and density function theory (DFT) calculations suggest that, even a low concentration of CO_2 (1 %) could effectively blocks the nucleation sites of Li_2O_2 and alters its shape and growth directions due to Li_2CO_3 formation, resulting in an increased discharge capacity at the expense of a raise in charge potentials.[100] Apart from increasing the charge over-potential thus undermining the round-trip efficiency, the presence of Li_2CO_3 as discharge product deteriorates the rechargeability of Li-O_2 batteries in another three aspects: i) the portion of Li_2CO_3 which fails to be decomposed on subsequent charges concentrates at the electrode surface leading to early cell death; ii) other cell components (i.e., porous carbon, binder, solvents, salts…) are likely unstable at the very high charge potentials induced by the high Li_2CO_3 concentration on the electrode surface; and iii) the decomposition of Li_2CO_3 releases reactive superoxide radicals ($2\ Li_2CO_3 \rightarrow 2\ CO_2 + 4\ Li^+ + O_2^{\bullet -} + 3\ e^-$) which are detrimental for the stability of organic solvents.[101] Moreover, CO_2 was shown to react with $O_2^{\bullet -}$ in Li^+-containing non-aqueous electrolytes to form Li_2CO_3 via an electrochemical pathway.[102] This potential reaction pathway further underscores the importance of examining how the discharge reactions and the final discharge products will be altered by the existence of CO_2. This question will be addressed more in detail in Chaper IV.

In light of the severe energy inefficiency associated with the phase change between solid Li_2O_2 and gaseous O_2, solid-phase conversion ($Li_2O(s) \leftrightarrow Li_2O_2(s) \leftrightarrow LiO_2(s)$) avoiding O_2 gas uptake and release was alternatively explored with nanolithia composite electrodes.[103,104] Because the reaction proceeds via the redox of light element oxygen akin to Li-O_2 battery, this $Li_2O/Li_2O_2/LiO_2$ chemistry preserves the merit of high energy storage (1000 Wh kg^{-1}) while significantly reduces the charge overpotential from 0.5 ~ 1.3 V to ~ 0.24 V. Nevertheless, further studies are awaited to overcome the critic barrier for advancing this new energy storage system: i) the low electrochemical activity and poor electronic conductivity of Li_2O; ii) possible O_2 gas release

on further oxidation due to the metastability of the delithiated Li_2O; and iii) parastic reactions associated with LiO_2 which readily reacts with organic electrolytes, as often observed in Li-O_2 batteries. Transition metal doping and the use of nanosized electrode were adopted to promote this electrochemical reactions.[105] In parallel, an internal charge shuttle may be incorporated to maintain the charge voltage below the thermodynamic potential for O_2 to be evolved from Li_2O_2 (i.e., 2.96 V), offering the chance to prevent O_2 gas evolution.[104]

I. 4 Conclusions

The energy density of Li-ion batteries has been tripled since their initial commercialization (from 80 Wh kg^{-1} in 1991 (Sony) to 250 Wh kg^{-1} in 2017 (Tesla)), thanks to the continuous improvement of the layered oxide chemistry ($LiCoO_2$) via chemical substitutions. In the recent years, we have seen the emergence of Li-rich layered oxides showing oxygen redox activity aside from the conventional cationic one, with great potential for application. Indeed, oxygen redox is an intriguing concept to move beyond the outlook of the classical positive electrode materials. In order to explore the full potential of this concept, it is crucial whilst challenging to maximize the reversible anionic redox participation while maintaining the structural integrity especially at high state of charge. Tridimensional structures should be advantageous over layered structures in this regards.[60] On the other hand, most of the Li-rich oxides reported so far contain heavy and expensive 4*d* or 5*d* transition metal ions such as Nb, Mo, Ru and Ir, hence designing oxygen redox based positive electrodes with light and cost-effective 3*d* transition metals would be beneficial practical-wise.

In parallel, numerous new chemistries are actively pursued hoping to surpass the energy limit of conventional Li-ion intercalation chemistry. Marked improvements have been achieved regarding the fundamental understanding of the charge/discharge mechanisms, the interfacial chemistry/electrochemistry and critical parasitic reactions. Interesting concepts/strategies continue to emerge but are often accompanied with new challenges. Overall, each chemistry newly proposed has its own distinct technical challenges to overcome and fundamental questions to answer. It is so far unclear whether or when any of those new battery technologies will reach mass commercialization. Nevertheless, even if their practical applications may not be witnessed in the near future, investigating those different whist relevant battery systems has been a rich learning

playground. Notably, it leads to a better understanding about how to stabilize the reactive intermediates via playing with solvation-desolvation kinetics so as to elaborate the desired reaction pathway.

Chapter II Monitor the oxygen release at high potentials in Li-rich layered oxides

Chapter II Monitor the oxygen release at high potentials in Li-rich layered oxides

II. 1 Background and motivation

As mentioned in Chapter I, the recent discovery of anionic redox has effectively unlocked the energy storage limitation of positive electrode materials, which was previously believed to be pinned by the transition metal cations (how much their oxidation state can change). Despite the fact that combined redox activity of cations (transition metals) and anion (oxygen) can push the positive electrode capacity well beyond what the sole cationic redox can offer,[26,43] most of these Li-rich layered oxides studied so far exhibit irreversible O_2 gas release when charged to high potentials, the extent of which depends on the nature of the material (chemical composition, band structure, surface chemistry, dimensions, etc.).[44,57,106] Combined experimental and theoretical calculations have shown that such lattice oxygen loss which deteriorates the materials' performances (irreversibility, parasitic surface reactions, voltage fade, and safety) is unfortunately the largest for the 3*d* metals which present the greatest interest practical-wise.[46,51-54,59] Aware of these limitations, and searching for high-energy-density, cost-competitive and stable positive electrode materials, intense research activities have therefore been devoted to the *operando* detection and reliable quantification of possible O_2 evolution.[107-111] The direct probe of O_2 gas release is of special significance not only to provide insights about the irreversible part of anionic redox activities, but also to help in understanding the origins of bulk structure reorganization, surface morphology change as well as battery performance deterioration.[28,47,50,106,112-115]

A straightforward approach to probe the gas evolution phenomenon is to employ *operando* gas/pressure analytical techniques which can directly analyze the gaseous products formed during cycling. When this work was started, two of such techniques have been heavily implemented in the battery field. The first one is the differential (or *online*) electrochemical mass spectrometry, also termed as DEMS (or OEMS), which allows the identification and quantification of various gaseous species evolved/consumed upon battery operation. This technique has been extensively used in Li-O_2 battery research to quantify O_2 consumption/evolution,[116-118] and has been implemented in Li-ion battery field to follow the gas evolution caused by the degradation of battery components since

1990s (salt, electrolyte, positive electrode material, negative electrode material…).[119-124] Despite OEMS providing valuable insights toward the complex electrochemical processes occurring upon battery cycling, the disadvantages related to the utilization of OEMS are nested in its complexity, high cost and sensitive operation, which currently hamper its day-to-day use. Such limitations have led to the development of another technique termed as *in-situ* pressure cell, which can be easily implemented to enable long-time gas monitoring.[125-127] However, the main drawback of this rather user-friendly approach being that it only measures the pressure change, and thus does not allow for determining the nature of the evolved gases. These limitations naturally motivate us to search for simple and accurate alternate that can be used to rapidly screen new positive electrode materials regarding their electrochemical stability against O_2 release.

Within this context, the rotating ring disk electrode (RRDE) voltammetry has caught our attention. RRDE is an electrochemical technique which offer unique opportunity to investigate the short-lived intermediates generated in steady-state measurements.[128-130] Benefiting from the laminar electrolyte flow created by the mechanical rotation and the existence of double concentric working electrodes (the disk and the ring electrode) separated by a non-conductive barrier, intermediates generated at the disk electrode can be swept across the surrounding ring electrode along with the electrolyte flow, and be electrochemically observed (detected) at the ring. In fact, this concept has much in common with the "generation-collection" experiments in scanning electrochemical microscopy (SECM).[131] If the intermediate is stable in the transit time (i.e., the average time required for the intermediate to traverse the gap between the disk and the ring electrode, which is a function of the gap distance and the rotation rate), then the collection efficiency given by the ratio of the disk current and the ring current is only a function of the geometry of the electrode. Giving RRDE experiments in which the ring electrode is maintained at a sufficient positive (negative) potential such that any intermediate reaching the ring is rapidly oxidized (reduced), knowledge about species produced at the disk electrode surface can be obtained by simply measuring the magnitude of the ring currents. Therefore, since its first introduction in 1958 by Alexander Frumkin,[130] RRDE has been widely applied to study the reaction kinetics and transport properties for the oxygen reduction reaction (ORR) relevant to metal-air batteries and proton exchange membrane (PEM) fuel cell,[132-138] as well as to probe the intermediates of lithium-sulfur redox reactions,[139] to study the manganese dissolution of spinel-based positive electrodes,[140] to survey the dissolution of metal ions during the corrosion processes,[141,142] and to determine the faradaic

efficiency of oxygen evolution reaction (OER) electrocatalysts for water splitting, [143,144] among other usages.

In this chapter, we will describe our methodology of using RRDE voltammetry to monitor the O_2 release phenomenon in positive electrode materials.[145] To this end, two families of well-studied Li-based layered oxides (Li-stoichiometric and Li-rich NMCs as well as $Li_2Ru_{1-y}Ti_yO_3$ phases) were chosen for initial evaluation. As a proof-of-concept, the results obtained by our RRDE method will be further compared with those obtained by the existing pressure/gas analysis techniques (*in-situ* pressure cell and OEMS). Lastly, the merits as well as the limitations of this new RRDE approach for O_2 gas detection will be evaluated, and an outlook on its future optimization and possible extension will be provided.

We will start in the next section with a brief description of the three gas analysis techniques used in this work: *in-situ* pressure cell, OEMS and the newly proposed RRDE voltammetry.

II. 2 Description of the *in-situ* gas analysis techniques

II. 2. 1 *In-situ* pressure cell

Figure II. 1a presents a photo as well as a corresponding schematic of the *in-situ* pressure cell developed in our laboratory by Dr. F. Lepoivre and employed throughout this thesis. The pressure cell is derived from the Swagelok-type cell, and is composed of a gas reservoir of 9.7 cm^3, a gas outlet/inlet that can be connected to the gas filling station (a schematic of the gas filling station is given in Appendix Figure A. 1. 1) for purging/refilling the cell with desired gases, together with a pressure sensor which measures the pressure evolution inside the cell. More detailed descriptions can be found in the Ph.D. work of Dr. F. Lepoivre.[146] Figure II. 1b presents the pressure (blue solid line) and voltage profile (black solid line) typically measured by *in-situ* pressure cell, from which the specific voltage where the cell starts to degas and the quantity of the evolved gas can be deduced.

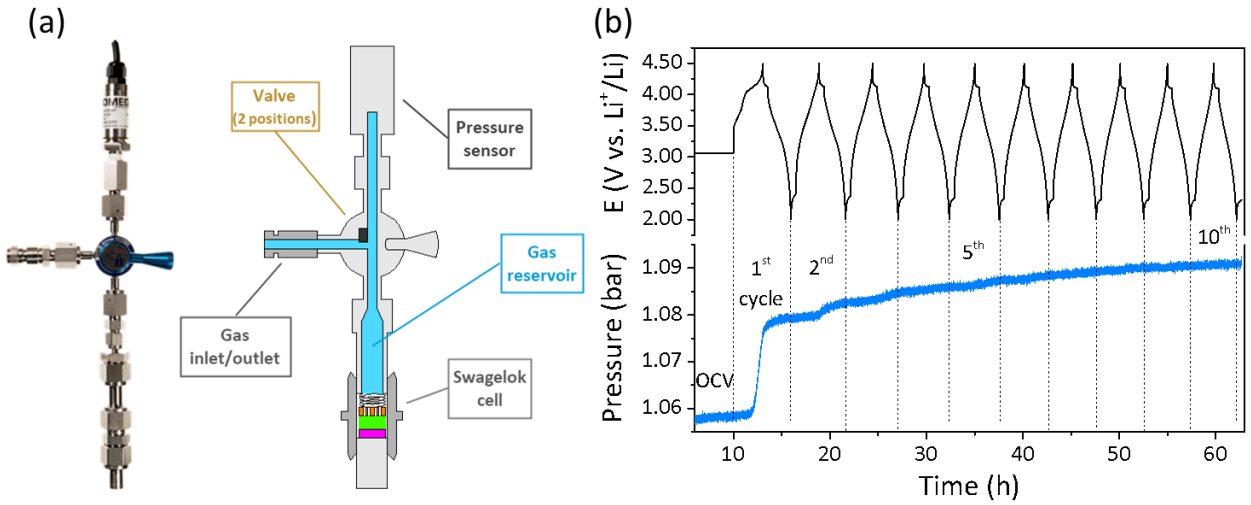

Figure II. 1 (a) Photograph (left side) and schematic (right side) of the *in-situ* pressure cell. Adapted from: *Ph.D. thesis of Florent Lepoivre, 2016.* (b) A representative *in-situ* pressure profile during the cycling of a $Li_2Ru_{0.75}Ti_{0.25}O_3$ half-cell.

II. 2. 2 *Online* electrochemical mass spectrometry

Online electrochemical mass spectrometry (OEMS) is composed of an electrochemical cell with both a vacuum system and a quadrupole mass spectrometer which analyzes the volatile species sampled in the head space of the electrochemical cell.[118,147] Figure A. 1. 2 in Appendix shows a schematic view of the whole OEMS system used in this work, which is a closed system allowing for the continuous gas sampling from the electrochemical cell to the mass spectrometer (MS) through a thin capillary. More detailed description of the system can be found in Appendix section A. 1. 2. Figure II. 2 present the electrochemical cell used for the OEMS experiments. The cell is derived from the *in-situ* pressure cell with one single modification: the quick connector for gas inlet/outlet in the pressure cell has been replaced by a Swagelok adaptor which can be connected to either a connector to the inlet capillary of MS or to the gas filling station.

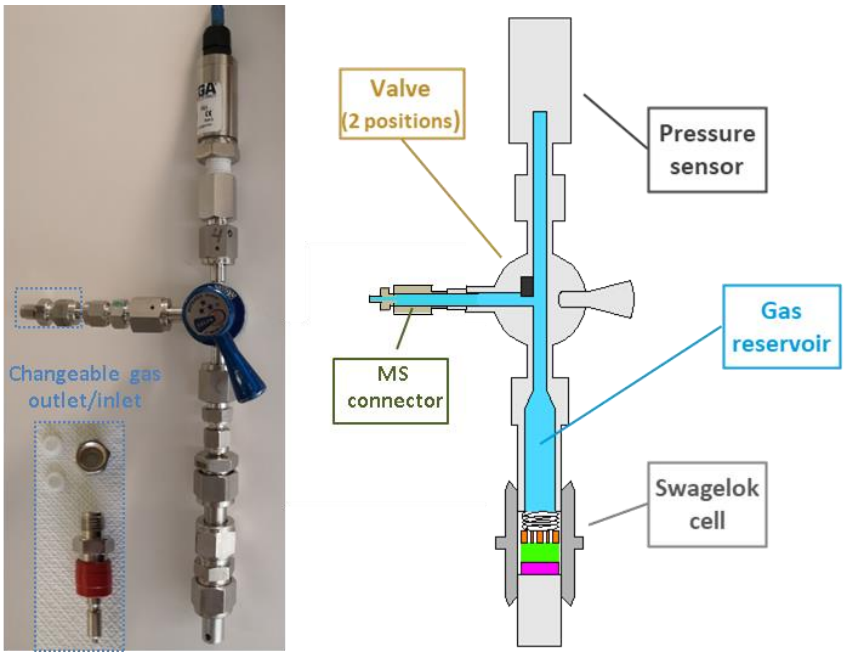

Figure II. 2 Picture (left side) and schematic (right side) of the electrochemical cell dedicated to the closed OEMS system.

II. 2. 3 Rotating ring disk electrode voltammetry

As illustrated in Figure II. 3a, RRDE tip is constructed by embedding in the cylindrical insulator (polytetrafluoroethylene (PTFE) is typically used owing to its great chemical stability and inertness) a central disk electrode and a surrounding ring electrode. Depending on the target usage, different materials and sizes can be selected for the electrodes as well as the insulator. Platinum ring is chosen in this work due to its remarkable catalytic activity for oxygen reduction reaction, as witnessed in the fields of Li-O_2 battery and fuel cell.[148,149] The disk and the ring electrode are electrically separated by an insulating barrier (a PTFE U-cup as marked with blue arrow in Figure II. 3a). The RRDE experiments are carried out with a bipotentiostat, which controls independently the potentials of the disk and the ring electrode with respect to the reference electrode and measures separately the current going through each electrode (Figures II. 3b & 4). The RRDE tip is also connected with a motor controller through a shaft which allows for rotating both the two electrodes at the same rate (Figure II. 4). A schematic of the whole RRDE system together with a four-electrode electrochemical cell is presented in Figure II. 4 and more details about the set-up can be found in Appendix Section A. 2. 1.

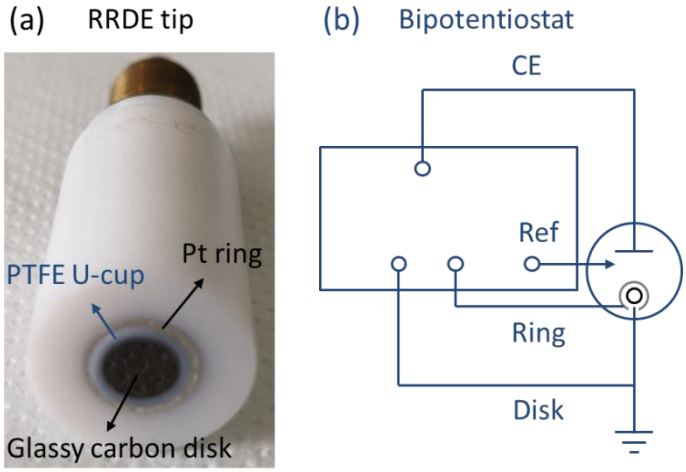

Figure II. 3 (a) Picture of the RRDE tip used in this work and (b) block diagram of the bipotentiostat (CE stand for counter electrode, Ref stands for reference electrode), adapted from *Bard et al.*[150]

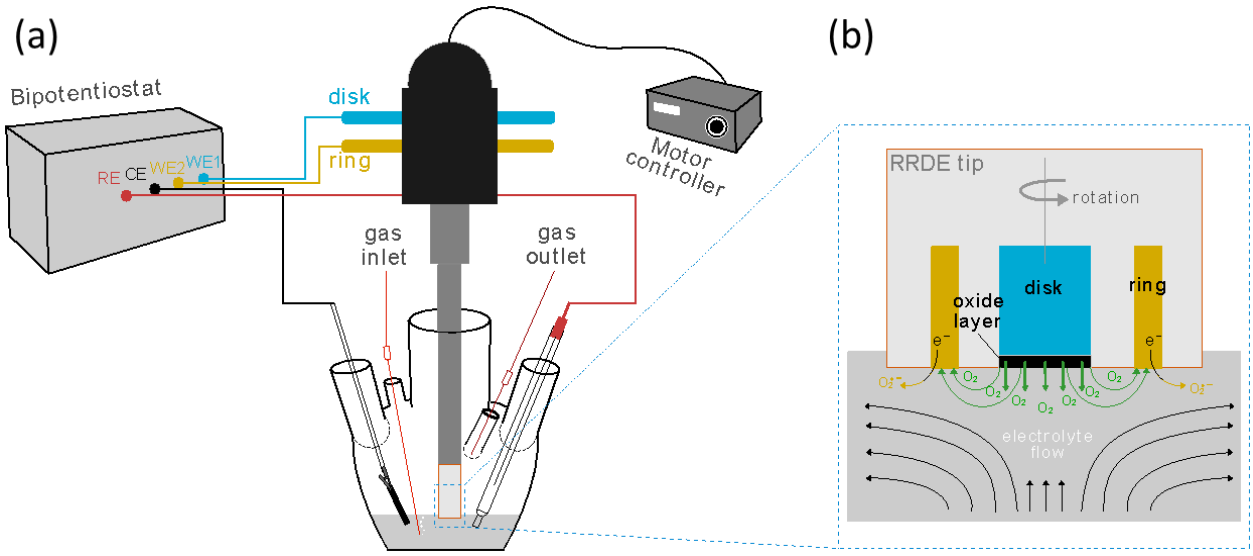

Figure II. 4 (a) Schematic of RRDE system and the four-electrode cell configuration, WE1, WE2, CE and RE stand for working electrode 1 (disk electrode), working electrode 2 (ring electrode), counter electrode and reference electrode, respectively. (b) A magnified view of the RRDE tip and its near-electrolyte region depicts the transport and redox processes occurring in the RRDE system designed to assess the O_2 release phenomenon in Li-rich layered oxides.

In this work, we are interested in studying the O_2 gas generation from Li-rich layered oxides. To this end, the oxides of interest were firstly deposited onto the disk electrode and linear scan

voltammetry, cyclic voltammetry or galvanostatic techniques were performed to charge the oxides until high potentials where O_2 gas release likely occurs. Simultaneously, the ring electrode is maintained at a sufficiently negative potential for oxygen generated at the disc electrode to be rapidly reduced. To determine the required ring potential, we performed initial oxygen reduction measurements in LP30 electrolyte (1 M $LiPF_6$ dissolved in 1:1 *v/v* Ethylene carbonate/Dimethyl carbonate) with platinum rotating disk electrode at a rotation speed of 1600 rpm (Figure II. 5a). The gradual decrease in current densities observed after 2.4 V *vs* Li^+/Li shown that further increasing the overpotential would drastically decrease the active catalytic sites owing to surface passivation by Li_2O_2 (the ultimate O_2 reduction product in Li^+-containing electrolytes).

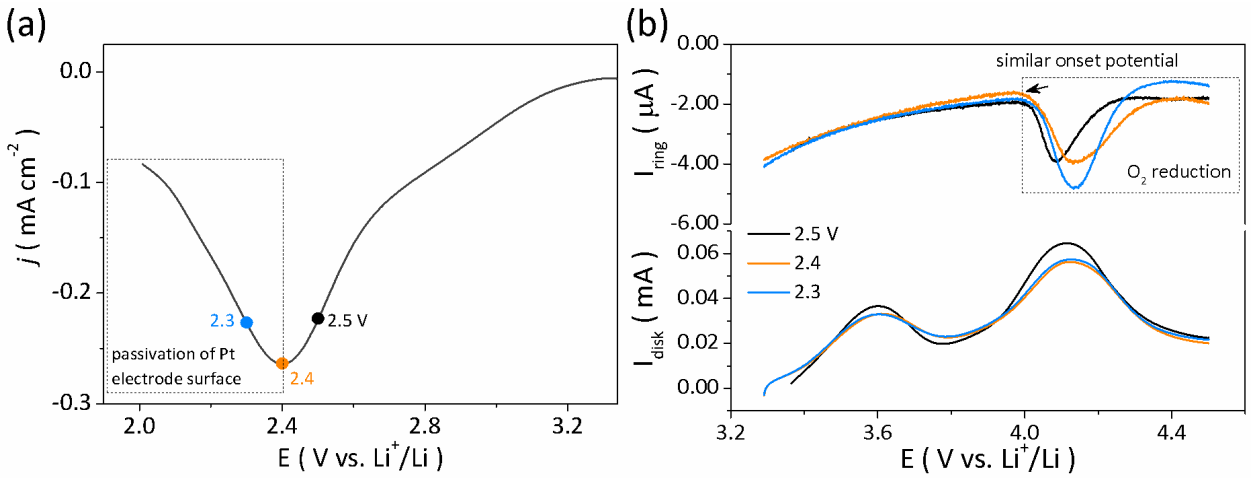

Figure II. 5 (a) Potentiodynamic O_2 reduction current densities on a platinum rotating disk electrode at a rotation speed of 1600 rpm in LP30 electrolyte with a scan rate of 10 mV s^{-1}. Note that the dashed square indicates that the current density decreases as the overpotential increases, owing to the passivation of Pt electrode surface. (b) RRDE profiles obtained with $Li_2Ru_{0.5}Ti_{0.5}O_3$ at a rotation speed of 1600 rpm in LP30 electrolyte by holding the ring electrode at different potentials: 2.3 V (blue curve), 2.4 V (yellow curve), and 2.5 V (black curve). Linear scan voltammetry was applied at the disk electrode to delithiate $Li_2Ru_{0.5}Ti_{0.5}O_3$. Note that the dashed square marks the increase of reductive currents due to O_2 reduction. The black arrow reveals that similar onset potential is obtained for O_2 reduction, irrespective of the applied ring potential.

We then performed preliminary RRDE measurements with a Li-rich compound which known to release O_2, namely $Li_2Ru_{0.5}Ti_{0.5}O_3$, by holding the ring at various potentials (2.3 V, 2.4 V and 2.5V), similar onset potential were observed for O_2 reduction (detection) irrespective of the

applied ring potential (Figure II. 5b). Therefore, the ring potential was selected to be 2.5 V *vs* Li^+/Li, a value that is sufficient to allow for O_2 reduction (detection) while relatively positive to minimize reductive parasitic reactions. Note that all the results reported in this work were at least duplicated two times but not corrected for the background ring current, the magnitude of which being typically less than 3 μA. The background ring currents show a tendency to decrease as the concentration of residual oxygen and/or impurity in the electrolyte decreases.

II. 3 Results and discussion

Despite the fact that combining cationic (transition metals) and anionic (oxygen) redox activity can enhance the capacity well beyond what the sole cationic redox can offer with capacities exceeding 280 mAh g^{-1} for $Li_{1.2}Ni_{0.13}Mn_{0.54}Co_{0.13}O_2$ (Li-rich NMC) as compared to solely 180 mAh g^{-1} for $LiNi_{1/3}Mn_{1/3}Co_{1/3}O_2$,[26,43] classical $Li(Ni_xMn_yCo_z)O_2$ denoted as NMC which are presently used in commercial Li-ion batteries do not show O_2 gas release upon oxidation in contrast to the Li-rich phases.[28,44,46,107,108,124] As a proof of concept to demonstrate the usage of RRDE for O_2 gas detection, we therefore decided to firstly investigate these two NMC phases: the stoichiometric $LiNi_{1/3}Mn_{1/3}Co_{1/3}O_2$ (NMC 111) and $Li_{1.2}Ni_{0.13}Mn_{0.54}Co_{0.13}O_2$ (Li-rich NMC).

Figures II. 6a & 6b present their voltage and internal pressure change as a function of capacity. The cell with Li-rich NMC displays a discernable increase of pressure during the high-voltage charging plateau (from *a* to *b*) followed by a rapid pressure growth (from *b* to the end of charge) (bottom panel in Figure II. 6a). The two different pressure increments (from *a* to *b*, and from *b* to the end of charge) during the charge period indicate the presence of at least two different phenomena governing the release of gases, which will be further discussed below. Unlike for Li-rich NMC, only a minor increase of the pressure was measured for NMC111 throughout the charge (from *f*, bottom panel in Figure II. 6b), suggesting negligible gas evolution. In order to discern the chemical nature of the evolved gases, OEMS measurements were further carried out. Figures II. 6c & 6d show the OEMS data obtained with NMC 111 and Li-rich NMC during their first charges followed by an open circuit voltage (OCV) step for 0.5 h. Note that only O_2 and CO_2 are considered here as they represent for the major constitutes of the sampled volatile species. Starting with the Li-rich NMC (Figure II. 6c), the evolution of O_2 was measured only after the high-voltage charging plateau (starting from *d*). Unlike for O_2, the CO_2 evolution starts at the beginning of the

high-voltage charging plateau (from *c*), before to dramatically increase at the end of charge simultaneously with the evolution of O_2 (from *d*). These results are in good agreement with previous reports.[47] Moreover, they explain the results previously obtained by pressure analysis (Figure II. 6a) with the initial slight increase of pressure (from *a* to *b*) originating solely from CO_2 evolution, while both O_2 and CO_2 evolutions contribute to the second rapid pressure build-up (from *b* to the end of charge). In the case of NMC 111 cell (Figure II. 6d), CO_2 was the only detected gas, accounting for the minor pressure build-up previously observed in pressure cell, whereas no O_2 evolution was observed during both the charge and OCV period.

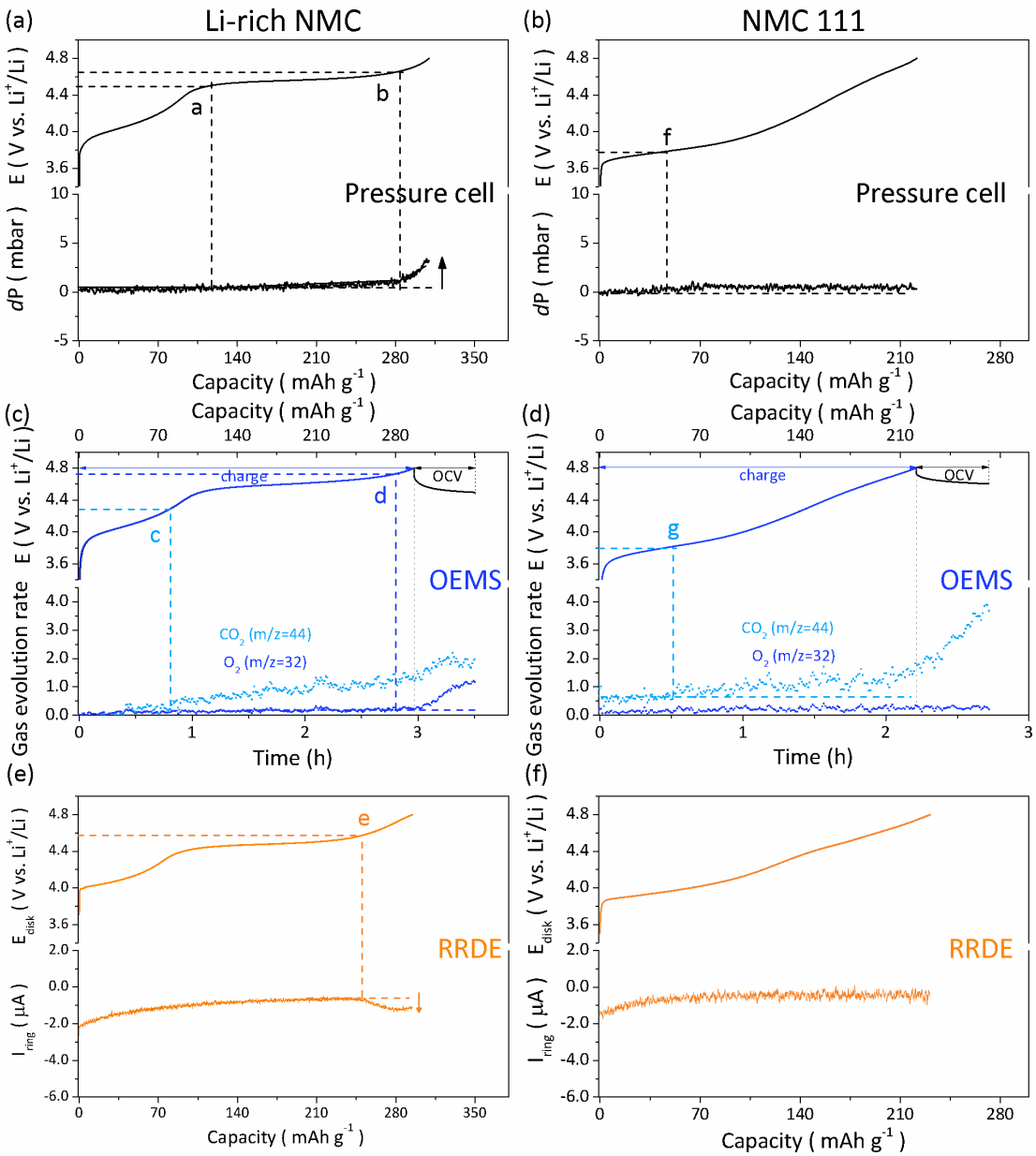

Figures II. 6 Galvanostatic charge curves (top panels) and their respective pressure change (bottom panels) for Li-rich NMC (a) and NMC 111 (b) in *in-situ* pressure cells. Potential (top panels) and gas evolution rate (bottom panels) as a function of time (and capacity) for Li-rich NMC (c) and NMC 111 (d) measured by OEMS. RRDE profiles measured for Li-rich NMC (e) and NMC 111 (f) in LP30 electrolyte. Top panels present the galvanostatic charge curves obtained in the disk electrode. Bottom panels illustrate their corresponding ring current response. All the cells are charged at a current rate of 0.3 C to 4.8 V *vs* Li^+/Li. Gas evolution onsets are defined by dash lines labeled from *a* to *g* as guide for the eye.

Knowing that O_2 is evolved at the end of charge for Li-rich NMC but not for NMC 111, RRDE measurements were then performed for both materials. The respective voltage-capacity profiles are presented in Figures II. 6e & 6f (top panels) and are in agreement with those obtained with pressure and OEMS cells. Turning to the ring current, an increase of the reduction current was measured for Li-rich NMC close to the end of charge (from *e*, Figure II. 6e), alike the potential at which O_2 release was previously detected by OEMS and pressure measurements. In contrast, no such cathodic current increase was observed (bottom panel in Figure II. 6f) for NMC 111 in agreement with the absence of O_2 release as deduced from OEMS. The obvious correlation of the cathodic current increase and the oxygen evolution for Li-rich NMC, as well as the absence of cathodic current increase and oxygen release for NMC 111, allows us to attribute the increase of reduction current to the electrochemical reduction of O_2 evolved from Li-rich NMC. Since the evolution of O_2 is accompanied by the evolution of CO_2, as shown by our OEMS measurement with Li-rich NMC (Figure II. 6c), the effect of CO_2 generation on the detection of O_2 at the ring electrode was then considered. As previously mentioned, the release of CO_2 begins for Li-rich NMC at an earlier stage of the charge (before the plateau, from *c*, Figure II. 6c) compared to the onset potential for O_2 generation (after the plateau, from *d*, Figure II. 6c). However, an increase of the reduction current was only recorded, at the ring electrode, after the plateau (from *e*, Figure II. 6e) where O_2 starts to release. Therefore, one can conclude that RRDE specifically detects O_2 while being silent to CO_2 when holding the ring potential at 2.5 V *vs* Li^+/Li. This conclusion is further supported by performing RRDE measurements with a mixture of NMC 111 and Li_2CO_3 (Li_2CO_3 is known to evolve CO_2 but not O_2 within the charge potential range)[101,151] where no modification for the ring current response is observed compared to pure NMC 111 (Figure II. 7). Bearing in mind that the ring electrode detects every soluble product that could be reduced/oxidized at the ring potential (impurities, dissolved metal ions from oxides and/or counter electrodes, electrolyte degradation products, etc.), we then evaluate whether species other than O_2 could contribute to the increase of the cathodic ring current upon charging Li-rich NMC. By measuring bare and Csp-loaded glassy carbon disk electrodes in cyclic voltammetry mode up to 4.8 V *vs* Li^+/Li, no increase of the reduction current was observed at the ring electrode (Figure II. 8). Therefore, the detection of species originating from the carbon additive, binder and/or direct electrolyte oxidation could be excluded. Finally, to demonstrate the versatility of the proposed RRDE method for O_2 detection, linear scan voltammetry mode was also applied at the disk electrode instead of galvanostatic charging, giving a good agreement between RRDE and pressure cell measurements (Figure A. 2. 3).

Hence, by comparing with *in-situ* pressure and OEMS measurements, we could demonstrate that the RRDE method can indeed selectively detect O_2 generated from Li-rich NMC.

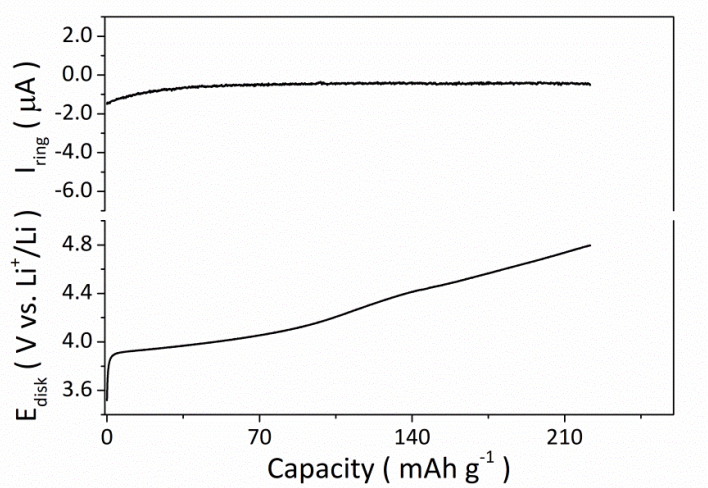

Figures II. 7 RRDE profile for 95 % NMC 111 + 5 % Li_2CO_3 measured at 1600 rpm in LP30 electrolyte. The bottom panel presents the galvanostatic charge curve obtained in the disk electrode at a current rate of 0.3 C to 4.8 V *vs* Li^+/Li and the top panel illustrates its corresponding ring current response.

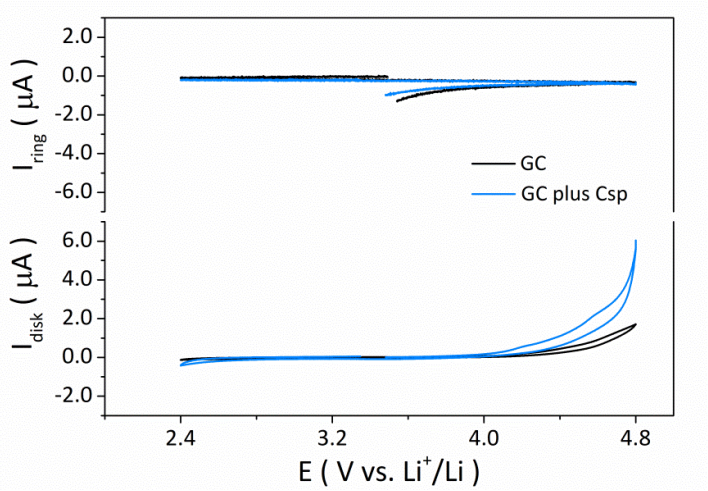

Figures II. 8 RRDE profiles on bare (yellow line) and Csp-casted (blue line) glassy carbon disk electrodes cycled at a scan rate of 0.5 mV s^{-1} between 2.4 and 4.8 V *vs* Li^+/Li.

To assess if the RRDE method can be utilized to detect oxygen release for other Li-rich compounds, we further extended our work to the Li_2MO_3 family,[51,152,153] with a special attention

paid to the $Li_2Ru_{1-y}Ti_yO_3$ series which was previously shown to evolve O_2 at high potentials.[154] Applying the same methodology, we first monitored with *in-situ* pressure cell the gas release upon charging $Li_2Ru_{0.5}Ti_{0.5}O_3$ (Figure II. 9a). A slight increase of the internal cell pressure was recorded at the beginning of the high-voltage charging plateau (from *a* to *b*, Figure II. 9a), followed by a rapid growth (from *b* to the end of charge). Subsequently, OEMS measurements show that the evolution of CO_2 begins at around 4.0 V *vs* Li^+/Li (line *c*, Figure II. 9b), which correlates well with the onset of pressure increase detected by pressure cell (line *a*, Figure II. 9a). Thereafter, O_2 is found to evolve at a relatively higher rate in comparison to the CO_2 evolution (from *d*, Figure II. 9b). In conclusion, upon charging $Li_2Ru_{0.5}Ti_{0.5}O_3$, CO_2 first evolves resulting in a small pressure increase, then O_2 evolution turns on at a higher rate accompanied with the evolution of CO_2 gas leading to a rapid growth of pressure. Now switching to the RRDE technique (Figure II. 9c), an increase of the cathodic current was recorded at the ring electrode (from *e*, bottom panel), similarly to Li-rich NMC phase. The onset of this ring current increase (~ 4.0 V *vs* Li^+/Li) is in good agreement with the onset of O_2 evolution measured by OEMS (~ 4.06 V *vs* Li^+/Li), which indicates that O_2 is evolved from $Li_2Ru_{0.5}Ti_{0.5}O_3$ and is detected at the ring electrode via its electrochemical reduction. It is worth mentioning that the capacity obtained in charge with the RRDE technique was ~ 20% smaller compared to that obtained with pressure and OEMS cells. This can be explained by the different cell configurations and by the fact that a small portion of the oxide remains inactive due to the lack of stacking pressure in RRDE set-up. Unlike for $Li_2Ru_{0.5}Ti_{0.5}O_3$, similar capacities were obtained for NMCs materials by RRDE, pressure and OEMS cells, suggesting their better electronic conductivity as compared to the $Li_2Ru_{1-y}Ti_yO_3$ series.

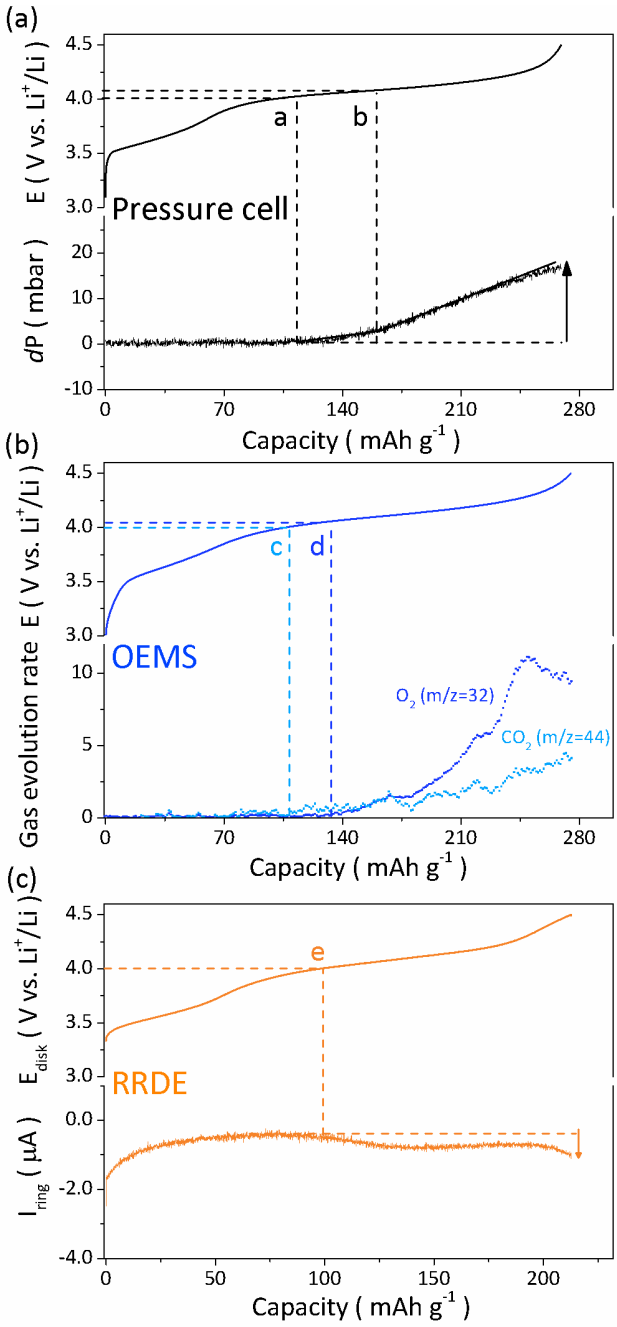

Figures II. 9 (a) Galvanostatic charge curve (top panel) and its respective pressure change (bottom panel) for $Li_2Ru_{0.5}Ti_{0.5}O_3$ in *in-situ* pressure cell. (b) Potential (top panel) and gas evolution rate (bottom panel) as a function of capacity for $Li_2Ru_{0.5}Ti_{0.5}O_3$ measured by OEMS. (c) RRDE profiles for $Li_2Ru_{0.5}Ti_{0.5}O_3$ measured in LP30 electrolyte. Top panel shows the galvanostatic charge curve obtained in the disk electrode. Bottom panel illustrates its corresponding ring current response. All the cells are charged at a current rate of 0.3 C to 4.5 V *vs* Li^+/Li. Gas evolution onsets are defined by dash lines labeled from *a* to *e* as guide for the eye.

The effect of titanium substitution in $Li_2Ru_{1-y}Ti_yO_3$ series on O_2 evolution was then studied by measuring $Li_2Ru_{0.75}Ti_{0.25}O_3$. As seen in Figures II. 10a & 10b, the evolution of O_2 begins at around 4.1 V *vs* Li^+/Li (line *d*), leading to a rapid growth in internal cell pressure (from *b* to the end of charge). As expected, an increase of ring reduction current was recorded by RRDE at this potential (from *e*, Figure II. 10c), indicating the reduction (detection) of O_2. This result clearly confirms that the proposed RRDE method is capable of probing the release of O_2 in various Li-rich materials. Finally, we could demonstrate the reproducibility of these results by performing repetitive RRDE experiments with both $Li_2Ru_{0.75}Ti_{0.25}O_3$ and $Li_2Ru_{0.5}Ti_{0.5}O_3$ phases. As seen in Figure A. 2. 4**,** nearly identical disk electrochemical performances (showing the charge of the oxide) and ring current responses (corresponding to the detection of O_2) were obtained.

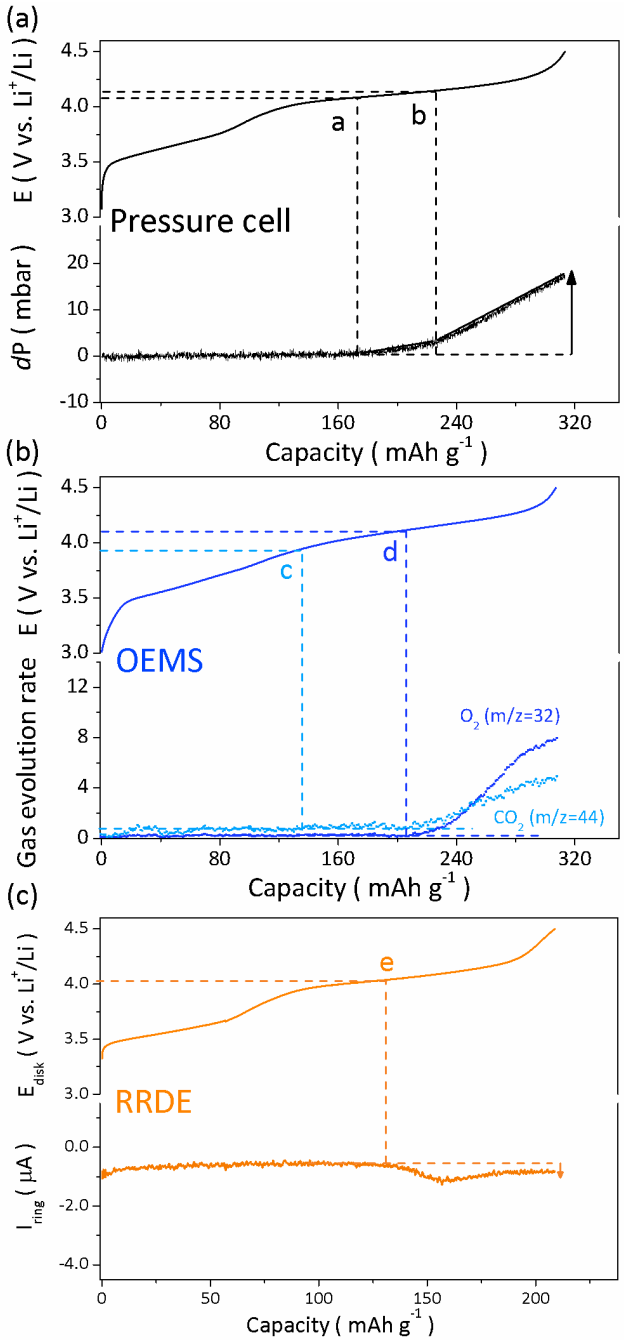

Figures II. 10 (a) Galvanostatic charge curve (top panel) and its respective pressure change (bottom panel) for $Li_2Ru_{0.75}Ti_{0.25}O_3$ in *in-situ* pressure cell. (b) Potential (top panel) and gas evolution rate (bottom panel) as a function of capacity for $Li_2Ru_{0.75}Ti_{0.25}O_3$ measured by OEMS. (c) RRDE profiles for $Li_2Ru_{0.75}Ti_{0.25}O_3$ measured in LP30 electrolyte. Top panel shows the galvanostatic charge curve obtained in the disk electrode. Bottom panel illustrates its corresponding ring current response. All the cells are charged at a current rate of 0.3 C to 4.5 V *vs* Li^+/Li. Gas evolution onsets are defined by dash lines labeled from *a* to *e* as guide for the eye.

At this stage of the study, the sensitivity of the RRDE technique is worth discussing. As seen in Figures II. 11, when using the same amount of active material for pressure analysis as for the RRDE study (~ 100 µg), the pressure measured upon charging $Li_2Ru_{0.75}Ti_{0.25}O_3$ remained nearly constant when using a scan rate of 0.5 mV s^{-1} (green curve) or 1.0 mV s^{-1} (blue curve). Only when a slower scan rate was applied (0.1 mV s^{-1}, red curve) to allow longer time for gas accumulation in the headspace and most likely larger amount of O_2 gas release, a pressure increase was then recorded. In fact, the mass loading of active materials used for pressure analyses and OEMS experiments were respectively ≈ 70 and 130 times greater than that used for the RRDE measurements. The capability of RRDE method in detecting O_2 at a significant lower mass loading (lower O_2 concentrations) suggests a better sensitivity. Therefore, the proposed RRDE method can be expected to be a useful tool for studying materials from which relatively smaller amount of O_2 is released, which may be below the detection limit of the pressure analysis or OEMS measurement. We should note that all the results reported herein were not normalized to the loading of active materials, therefore the magnitude of pressure build-up, O_2 mass spectrometry signal and ring currents increment should not be considered for quantitative comparison or sensitivity indicators.

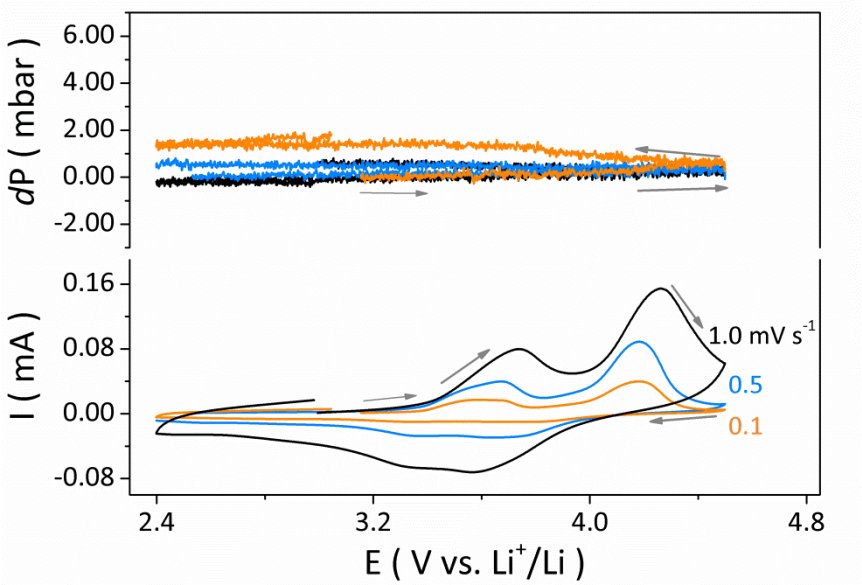

Figures II. 11 Cyclic voltammograms (bottom panels) recorded in *in-situ* pressure cells at various scan rates: 0.1 mV s^{-1} (yellow line), 0.5 mV s^{-1} (black line), and 1.0 mV s^{-1} (blue line) cycled between 2.4 and 4.5 V *vs* Li^+/Li and their respective pressure changes (top panels) for $Li_2Ru_{0.75}Ti_{0.25}O_3$ with the same mass loading of active material as used in RRDE measurements.

To further evaluate the potential use of RRDE for accurately determining the state of charge at which oxygen is released from Li-rich compounds, cyclic voltammetry experiments were carried out for $Li_2Ru_{0.75}Ti_{0.25}O_3$ at various scan rates using both pressure cell and the RRDE set-up. During the RRDE tests, the onset potential for O_2 release was constantly determined at ~ 4.03 V *vs* Li^+/Li at every scan rate (Figure II. 12a), while for pressure measurements the measured onset potentials for gas release vary with the scan rates (Figure II. 12b).

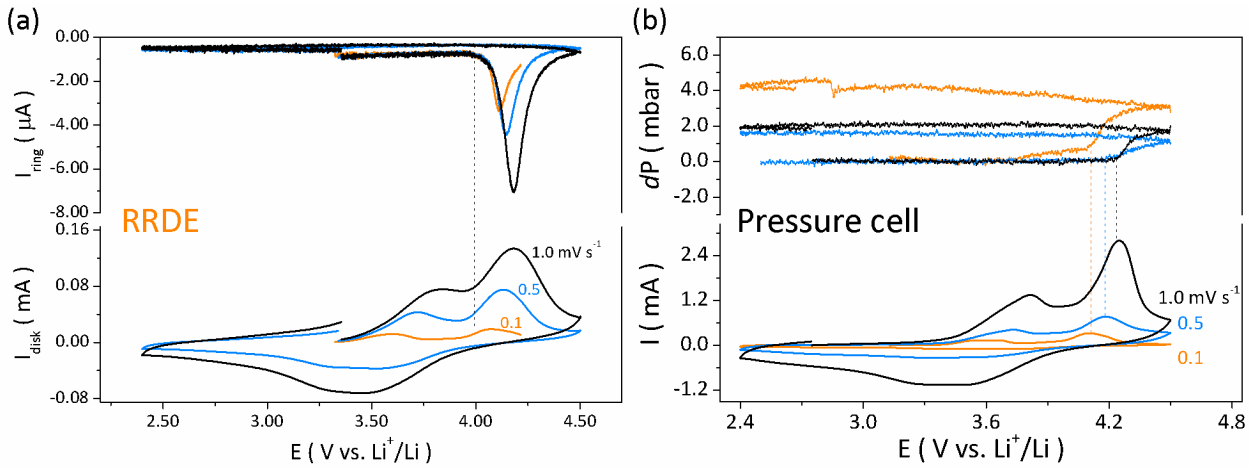

Figures II. 12 Comparison of RRDE profiles (a) and *in-situ* pressure analysis (b) for $Li_2Ru_{0.75}Ti_{0.25}O_3$ recorded at various scan rates: 0.1 mV s^{-1} (yellow line), 0.5 mV s^{-1} (blue line), and 1.0 mV s^{-1} (black line). The cyclic voltammograms are presented in the bottom panels and their respective ring current response (a) and pressure change (b) are shown in the top panels.

This different behavior is in fact not surprising when considering the different working principles of these two techniques. In pressure measurements, the gaseous species generated at the electrode must first diffuse through the electrolyte and accumulate in the headspace of the electrochemical cell before being detected by the pressure sensor. Unlike for pressure measurements, with the RRDE setup, the transport of O_2 is controlled by the convection movement, i.e. the laminar electrolyte flow created by mechanical rotation, which is faster than the diffusion of O_2 in electrolytes. Aside from the faster O_2 transportation rate in RRDE set-up, the unique ring-disk geometry also provides a shorter O_2 transport length than in a pressure cell. Besides, the sensitivity of pressure measurement (and also OEMS) is jeopardized by the amount of gas dissolved into the electrolyte as well as the dead volume of the electrochemical cell, which is not the case for RRDE method where O_2 can be detected once it is generated at the disk electrode surface and swept

outwards the ring electrode. In addition, pressure cell and OEMS measure both the gas released from the material itself and the gases resulted from electrode surface reactions (e.g., electrolyte reactions at the electrode surface), RRDE can minimize the contribution of the latter and more selectively detect O_2 released from the material by shortening the time needed for detection. Considering all the pros and cons, we could conclude that RRDE is a complementary technique to the *in-situ* pressure cell and the OEMS, and can be employed to accurately determine the onset potential for oxygen release.

After demonstrating that RRDE is capable to detect the oxygen loss from Li-rich compounds during their initial charges, the electrochemical behavior for $Li_2Ru_{0.5}Ti_{0.5}O_3$ and $Li_2Ru_{0.75}Ti_{0.25}O_3$ compounds during the second voltammetric cycles were recorded (Figure II. 13). The results reveal a very limited increase of the ring currents arising from the reduction of O_2 generated on the surface of these two compounds, which is consistent with the small irreversibility previously observed during galvanostatic cycling after the first charge.[154]

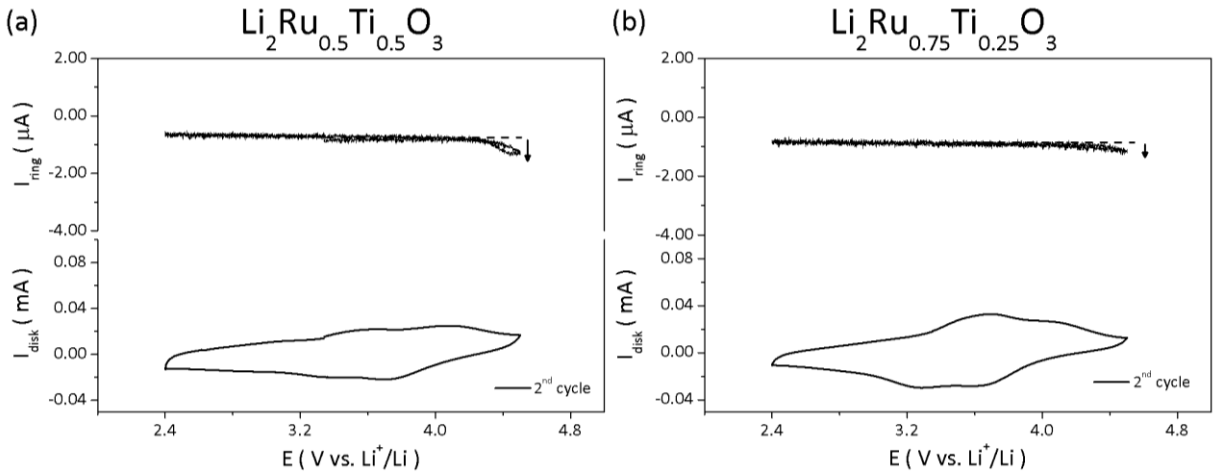

Figures II. 13 RRDE profiles for $Li_2Ru_{0.5}Ti_{0.5}O_3$ (a) and $Li_2Ru_{0.75}Ti_{0.25}O_3$ (b) during their second cycles at a scan rate of 0.5 mV s^{-1}, with the cyclic voltammograms presented in the bottom panels and their respective ring current evolution shown in the top panels.

The question then comes to the quantitative analysis of the amounts of O_2 generated from the Li-rich materials which can theoretically be deduced from the integration of the cathodic ring current increase. Comparing the results obtained for $Li_2Ru_{0.5}Ti_{0.5}O_3$ (Figure II. 14a) and $Li_2Ru_{0.75}Ti_{0.25}O_3$ (Figure II. 14b), the quantity of O_2 released from $Li_2Ru_{0.5}Ti_{0.5}O_3$ was calculated to

be larger than that from $Li_2Ru_{0.75}Ti_{0.25}O_3$ (1.036 % and 0.62 % loss of the total oxygen content for $Li_2Ru_{0.5}Ti_{0.5}O_3$ and $Li_2Ru_{0.75}Ti_{0.25}O_3$, respectively, see Appendix Section A. 2. 3 for detailed calculation). This trend correlates well with the electrochemical performance for which a greater irreversibility was observed during the first cycle with increased titanium substitution in the $Li_2Ru_{1-x}Ti_xO_3$ series.[154] However, discrepancy arises when comparing their final compositions after the initial charge calculated based on RRDE and pressure measurements. For $Li_2Ru_{0.5}Ti_{0.5}O_3$, a composition of $Li_{0.65}Ru_{0.5}Ti_{0.5}O_{2.74}$ was obtained from the pressure increase by assuming that all the detected gas is oxygen, whereas a composition of $LiRu_{0.5}Ti_{0.5}O_{2.97}$ is calculated from the RRDE results assuming a collection efficiency of 25 % (Table A. 2. 1). Even though the contribution from other gas components such as CO_2 to the pressure evolution has not been taken into account, the expected value for oxygen loss measured by RRDE should be higher since O_2 is the main gas evolved upon charging $Li_2Ru_{0.5}Ti_{0.5}O_3$, as deduced from OEMS measurements (Figure II. 9b). Such discrepancy could likely arise from the lower collection efficiency for O_2 at the ring electrode compared to the theoretical value given by the geometrical parameters of the RRDE tip (25.05 % ± 0.15 with the geometry used in this study). Indeed, this theoretical value is only achieved for soluble species such as ferrocene (Figure A. 2. 2), while for dissolved gas like O_2, limitations associated with a limited O_2 solubility in the supporting electrolytes as well as possible bubble formation from the evolved O_2, as discussed elsewhere,[143,155] can significantly lower the O_2 detection efficiency. Besides, a precise quantification of the amount of released oxygen is further complexed by the fact that small errors in the ring current and the mass loading can lead to a relatively large deviation. This is especially true considering the small amounts of active materials used for the RRDE measurements. Therefore, we believe that the amounts of O_2 measured from the ring current increase can be used for qualitative comparison among different materials, but caution must be exercised when implement such comparison. The values obtained by RRDE should be complemented by other techniques such as OEMS and/or pressure cells for quantification purposes.

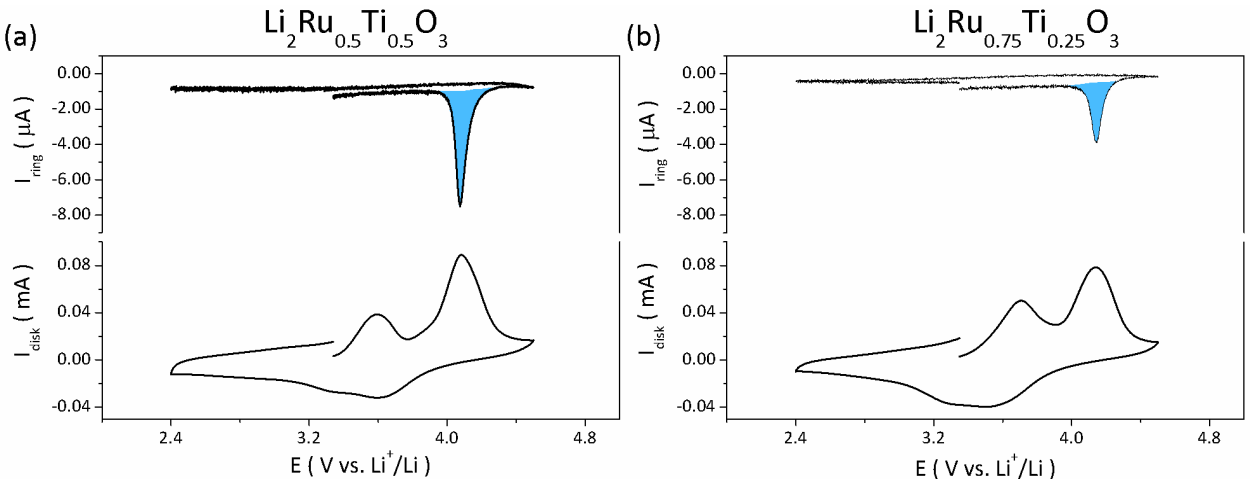

Figures II. 14 Comparison of RRDE profiles for $Li_2Ru_{0.5}Ti_{0.5}O_3$ (a) and $Li_2Ru_{0.75}Ti_{0.25}O_3$ (b) recorded at a scan rate of 0.5 mV s^{-1} with the cyclic voltammograms presented in the bottom panels and their respective ring current evolution shown in the top panels. The blue shaded area in the top panels represents the increment of cathodic ring current due to the reduction of detected O_2.

II. 4 Chapter conclusion and outlook

In this chapter, we propose the utilization of rotating ring disc electrode (RRDE) voltammetry for identifying the O_2 gas release phenomenon in Li-rich layered oxides. This simple method includes two sequential steps: (i) the deposition of the oxides of interest onto the disk electrode surface via a drop-casting method; (ii) application at the disk electrode of a standard electrochemical technique (i.e., linear scan voltammetry, cyclic voltammetry or galvanostatic cycling) to control the delithiation/lithiation of the oxides, while concomitantly maintaining the ring electrode at a potential which oxygen reduction reaction could effectively takes place. By rotating the whole electrode assembly, O_2 gas released from the oxides can reach and be electrochemically detected (reduced) in the ring electrode. We have validated the proposed methodology by conducting RRDE measurements using various Li-rich layered oxides and found that our results nicely compare with those obtained by OEMS and *in-situ* pressure cell. Through this comparative study, we could demonstrated that RRDE i) selectively detect oxygen while being silent to other species potentially generated at high potentials, ii) show better sensitivity and reliability than the aforementioned techniques allowing for the detection of O_2 at relatively lower concentrations, iii) enable a precise determination of the onset potential for O_2 gas release, and 4) can be used to

rapidly screen the O_2 release phenomena in a wide variety of new materials owing to its wide-spread in the fields of batteries and electrocatalysis. We believe that the proposed RRDE approach which offers high sensitivity while being fast and simple could greatly help to advance the understanding of oxygen redox processes and promote the design of new oxygen-redox-based materials. However, caution must be exercised when tentatively quantifying with RRDE the amount of O_2 generated from the materials. Overall, the RRDE method comes as a valuable complement to the existing pressure/gas analysis techniques which usually do not allow for either quickly screening multiple materials (i.e., OEMS) or for specifically detecting O_2 (i.e., *in-situ* pressure cell).

In principle, one can expect this proposed method to be extended to detect other soluble species or other type of gases such as CO_2. To this end, the selection of the adequate ring electrode will be crucial since it should selectively reduce or oxidize the target gas or species of interest (e.g., copper ring for CO_2 detection) without jeopardizing the electrochemical/chemical stability of the whole system. Another possible extension of this method is to modify the operation mode of RRDE voltammetry. This approach is helpful to screen a series of products formed at the disk electrode upon charging the oxides to certain potentials by using the ring potential as an indicator.

Chapter III Revisiting the structural evolutions and electrochemical properties in the first cycle of Li-rich NMC

Chapter III Revisiting the structural evolutions and electrochemical properties in the first cycle of Li-rich NMC

III. 1 Background and motivation

As mentioned in Chapter I, Li-rich layered oxides represent one of the few leading candidates for achieving greater energy storage. Their archetypical composition $Li_{1.2}Ni_{0.13}Mn_{0.54}Co_{0.13}O_2$ (Li-rich NMC) delivers capacities as high as ~ 300 mAh g^{-1} due to the cumulative contribution of both transition metal and oxygen redox.[46,156] However, extra capacities offered by oxygen redox come with practical drawbacks, such as voltage fade, large voltage hysteresis, and poor rate capability. Although quite remarkable progresses have been made in exploring the underlying science governing these Li-rich materials, we are far from reaching a sufficient understanding for their practical applications. Thus the need persists for revisiting Li-rich NMC with a fresh perspective on a few remaining questions that, despite intense discussions, have not reached a consensus.

Specifically, one of the questions is: what are the mechanistic details of the staircase *vs* S-shape potential evolution between the first charge and discharge? The origin of this voltage profile change remains ill understood, but shall be deeply rooted in the irreversible structural change during the first charge and/or the inherently different charge/discharge reaction paths. To address this question, the feasibility of eliminating structural disorder and restoring cation ordering, thereby recovering the staircase charge profile and voltage, by simply heating a discharged sample is of paramount importance,[112] since it highlights how the cation disordering which is triggered during the first charge, more specifically, during the high voltage plateau at which the anionic-redox takes place, impacts on the various aspects of the electrochemical performances of Li-rich phases. Going deeper into this question, Yu *et al.* have recently showed the appearance of a core-shell structure within particles at potentials greater than 4.4 V (during and above the high voltage plateau) using X-ray fingerprint associated with an additional Bragger peak next to the (003) one belonging to the main phase.[157] This peak was proposed to be associated with a disordered-spinel structure, growing at the surface of the particle, which reversibly converts back to a rocksalt one upon lithiation. Nevertheless, doubts regarding the nature of this new structure still remain because long-range

techniques like X-ray diffraction (XRD) should be "blind" to surface structures of ≈ 2 - 3 nanometers.[49] Indeed, Meng and co-workers suggested the formation of a second layered phase in the high voltage region.[158-160] Unfortunately, difficulties reside in unambiguously solving the structure of this new phase because two independent phases may be present while only one extra peak is clearly observed in the whole pattern. Moreover, neither the dynamics of this phase conversion was studied nor any means to promote it was proposed.

The second question, which naturally arises, is: why do Li-rich NMCs display larger first-cycle irreversibility (~ 25 %) as compared to classical insertion materials? Early works proposed irreversible oxygen loss,[46,47] the migration of transition metals into lithium vacancies,[48,161] and the formation of a surface spinel phase[158] to be responsible for the first-cycle irreversible capacity. In addition, Shunmugasundaram *et al.* shown that "Li-rich oxides" containing metal site vacancies in the transition metal layer ($Li[\square_q M_{(1-q)}]O_2$, M being a combination of Ni, Mn, and Co,) exhibit very low irreversible capacity (~ 6.5 %), as a potential consequence of enhanced atomic diffusion provided by vacancies.[162] It is most likely that the first-cycle irreversible capacity has multi-fact origins, namely a combination of irreversible oxygen loss, oxidative electrolyte decomposition, solid electrolyte interface formation, kinetic limitation, inactive domain, etc. Nevertheless, the irreversible capacity caused by the sluggish lithium diffusion which might be recovered at elevated temperature, at slower C-rates, or by applying a constant voltage step alike what has been suggested for classical layered oxides, namely $LiNi_{1/3}Mn_{1/3}Co_{1/3}O_2$[163] and $LiNi_{0.8}Mn_{0.1}Co_{0.1}O_2$,[164] should be differentiate from the capacity loss arising from irreversible processes. Only this complete understanding can pave the way to effectively mitigate the large first-cycle irreversibility.

Therefore, we decided to revisit the electrochemical-structural relationship of $Li_{1.2}Ni_{0.13}Mn_{0.54}Co_{0.13}O_2$ under severe oxidative-reductive conditions. Firstly, we show the feasibility to stabilize for the first time, the aforementioned new phase by pushing the high-voltage oxidation, entailing the possibility of detailed structural characterization using an arsenal of techniques like transmission electron microscopy (TEM), synchrotron XRD and neutron powder diffraction (NPD). We also revealed the underlying origins of the new phase formation and its impacts on electrochemical properties. Secondly, we demonstrated that a major part (~ 70 %) of the first-cycle capacity loss is induced by kinetic limitation, and can be recovered by applying a constant potential step at ~ 2.0 V. Thirdly, we showed that the oxygen redox activity on charge triggers an extra low voltage electrochemical activity, which has never been reported before. In the

end of the chapter, we further discuss these findings by putting them into the context of a vast number of literature reports on this topic, and providing a more holistic comprehension of the electrochemical-driven structural evolution in Li-rich NMC materials.

III. 2 Results and discussion

III. 2. 1 Phase transition and O_2 release on deep oxidation

A pure $Li_{1.2}Ni_{0.13}Mn_{0.54}Co_{0.13}O_2$ phase, as deduced from Rietveld refinement of the synchrotron XRD pattern (Figure III. 1 and Table III. 1), was prepared by combined co-precipitation and solid state synthesis.[43]

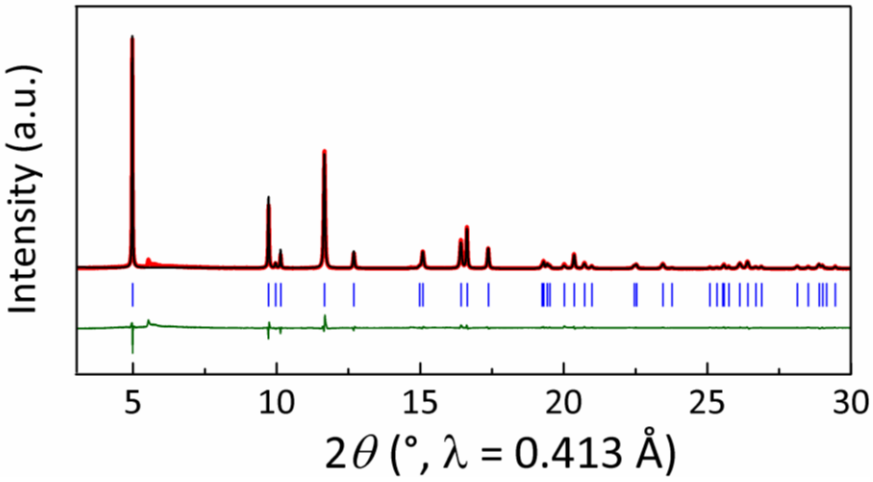

Figure III. 1 Rietveld refinement of the synchrotron XRD pattern of the pristine $Li_{1.2}Ni_{0.13}Mn_{0.54}Co_{0.13}O_2$ phase**.** The red line, black line and bottom green line represent the observed, calculated XRD patterns and the difference, respectively. Vertical blue tick bars mark the Bragg positions in the $R\bar{3}m$ space group.

Table III. 1 Crystallographic data and atomic positions for the pristine $Li_{1.2}Ni_{0.13}Mn_{0.54}Co_{0.13}O_2$ phase as determined from Rietveld refinement of the synchrotron XRD pattern.

Pristine Li-rich NMC phase ($O3 - Li_{1.2}Ni_{0.13}Mn_{0.54}Co_{0.13}O_2$)						
Space group: $R\bar{3}m$	a (Å)		b (Å)	c (Å)		V (Å^3)
SXRD	2.85396(2)		2.85396(2)	14.25381(15)		100.545(2)
χ^2 = 9.09, Bragg R-factor = 5.49 %						
Atom	Site	x/a	y/b	z/c	Occupancy	B_{iso} (Å^2)
Li	3a	0	0	0	1	0.54(7)
Ni/Mn/ Co/Li	3b	0	0	0.5	0.13/0.54/ 0.13/0.20	0.132(8)
O	6c	0	0	0.24105(8)	1	0.351(18)

Electrochemical tests were made in Swagelok cells against metallic lithium. As typically reported for this material,[43] the voltage-composition curves exhibit a two-step first-charge profile that converts into a sloping S-shaped one on the following discharge. Afterwards, the S-shape voltage profile is maintained, which is however tainted by capacity decay and voltage fade (Figure III. 2).

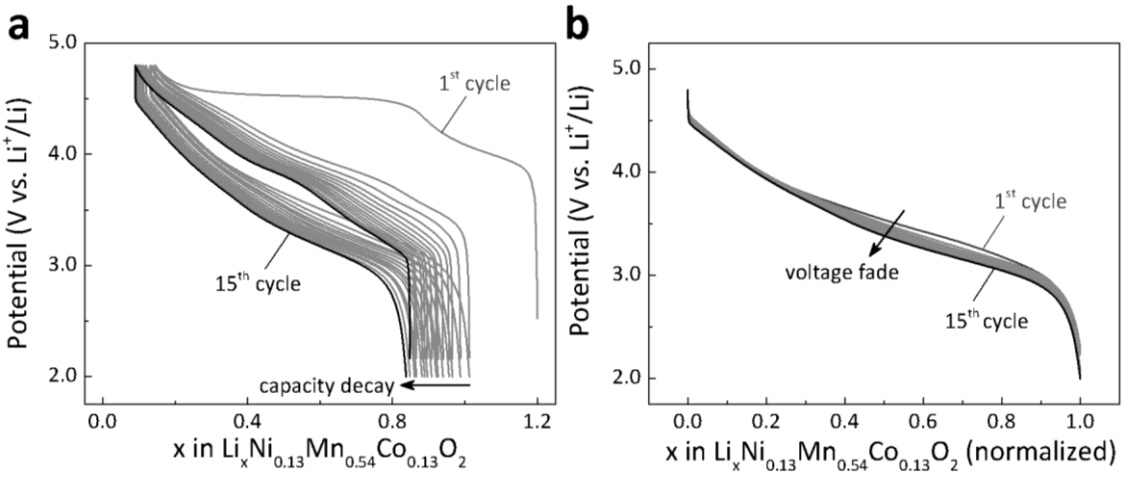

Figure III. 2 (a) Potential-composition curves of $Li_{1.2}Ni_{0.13}Mn_{0.54}Co_{0.13}O_2$ cycled within a potential window of 4.8 - 2.0 V at a current rate of C/5. (b) Normalized discharge curves of Li-rich NMC cycled within a potential window of 4.8 - 2.0 V at a current rate of C/5, i.e., the Li content (x) were normalized such that the maximum Li content in each discharge is taken as unity (x = 1.01 and 0.84 are taken as unity for the first and fifteenth cycle, respectively.)

Since the first-cycle voltage profile significantly differs from those for the subsequent cycles, suggesting that structure rearrangements mainly occur during the first electrochemical cycle, especially during the first charge. Therefore, as an initial step in revisiting this topic, we explored the structural evolution during the first charge under various oxidative conditions. For that purpose, two *in-situ* XRD cells were charged at C/3 to 4.8 V and to 4.6 V, respectively, followed with an open circuit voltage (OCV) step for 10 h. As shown in Figure III. 3, after charging to 4.8 V, in accordance with previous reports,[46,48,165] a shoulder peak starts to appear at the high-angle side of the original (003) peak (denoted hereinafter phase A), indicative of the growth of a new phase (denoted hereinafter phase A'). Interestingly, no appearance of phase A' was observed when the charge cutoff voltage was limited at 4.6 V. It is worth noting that the phase A → A' transition only appears during the OCV period when intentionally charging the cells at a relatively fast current rate (i.e., C/3), suggesting the slow kinetics for such phase transition.

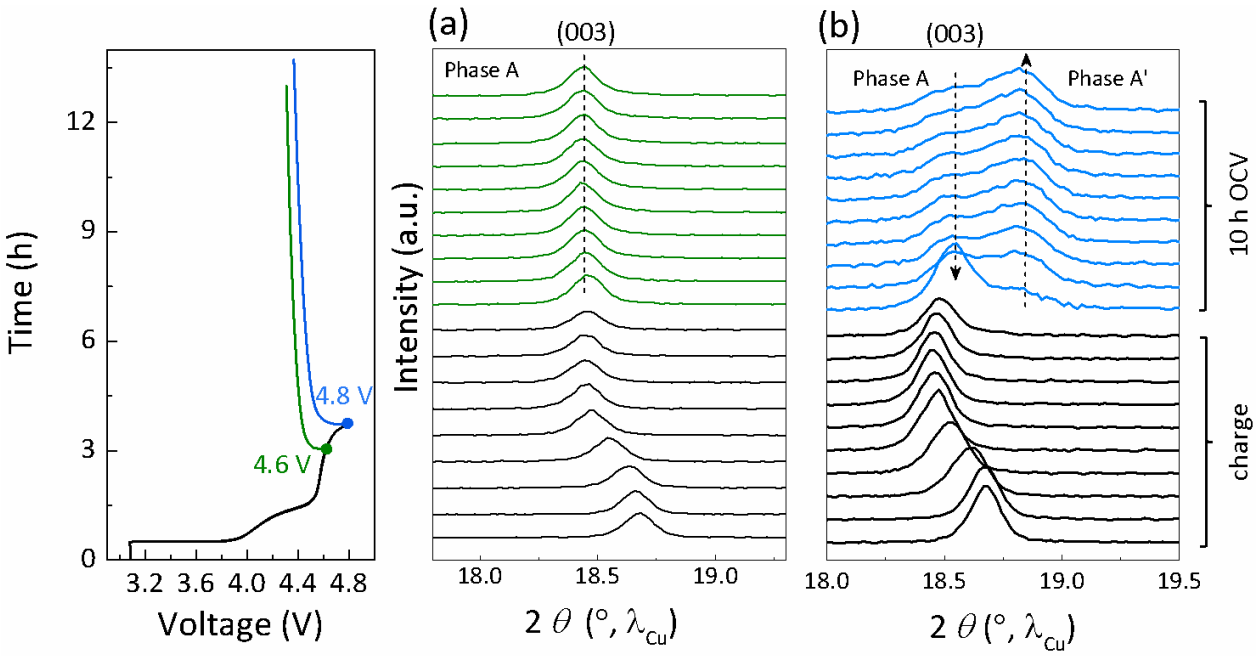

Figure III. 3 *In-situ* XRD study of the first-charge of $Li_{1.2}Ni_{0.13}Mn_{0.54}Co_{0.13}O_2$ to 4.6 V (a) and 4.8 V (b), followed with an OCV step for 10 h. Note that only the (003) Bragg peak is shown because it represents the major change of the whole XRD pattern. Dash line in panel (a) suggests that only phase A is formed after 4.6 V charge. On the contrary, a new phase A' is grown at the expense of phase A on further charging to 4.8 V, as indicated by the dashed arrows in panel (b).

In light of the observation that a new phase A' is formed on charging $Li_{1.2}Ni_{0.13}Mn_{0.54}Co_{0.13}O_2$ to higher voltage (4.8 V), we continued to push the material to higher oxidation state by clamping the voltage at 4.8 V for 5 h. Notably, the phase A' grows at the expense of the original phase A, and eventually becomes a single phase (Figure III. 4). This result clearly indicates that the newly formed phase A' is a bulk rather than a surface structure, in contrast with previous literatures which interpreted it as either a disordered-spinel or a densified surface layer.[48,157]

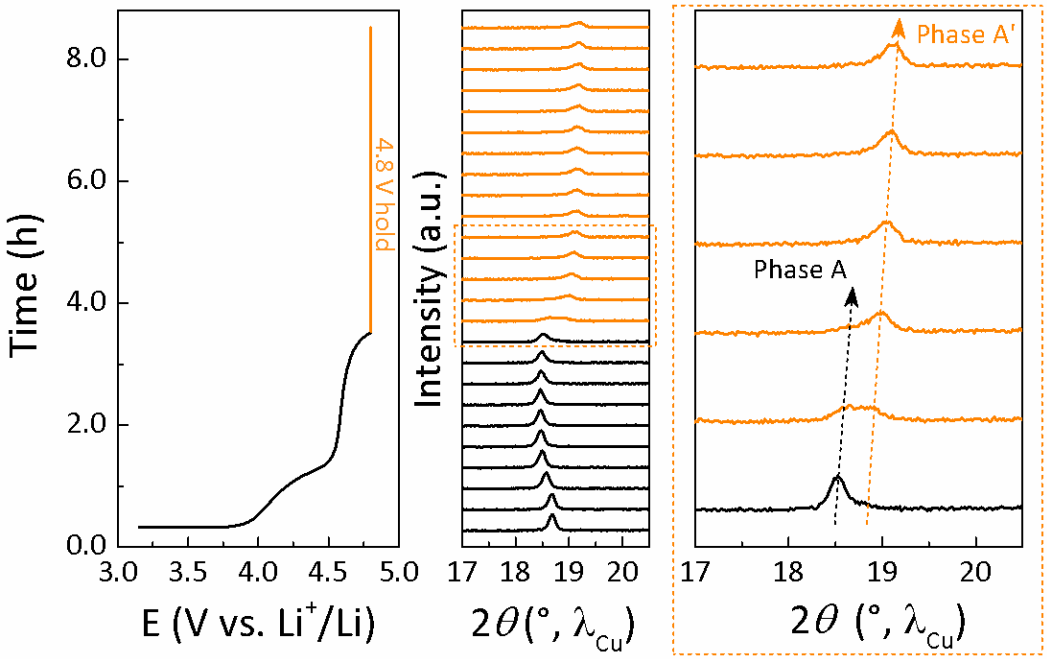

Figure III. 4 *In-situ* XRD study of the first-charge of $Li_{1.2}Ni_{0.13}Mn_{0.54}Co_{0.13}O_2$ to 4.8 V at C/3, followed with a constant voltage (CV) hold for 5 h. Dashed square reveals that the phase A gradually transform into phase A' during the voltage holding at 4.8 V.

Before understanding more about the structure of phase A', we first considered the physical origins of such phase A → A' transition. *In-situ* and *ex-situ* XRD studies clearly shown that the oxidation state of the material matters (Figures III. 3 & 4 and A. 3. 1). More specifically, the removal of more Li^+ creates more Li vacancies and further destabilizes the material's structure, hence facilitating the phase transition. In addition, O_2 loss from the material is known to occur during the first charge of Li-rich materials, creating oxygen vacancies and causing structure rearrangements.[44,45,49,166,167] Therefore, to explore the gas release of $Li_{1.2}Ni_{0.13}Mn_{0.54}Co_{0.13}O_2$ under various oxidative conditions, OEMS measurements were carried out by Dr. L. Zhang at Paul Scherrer Institut (PSI), Switzerland. The onset of O_2 release is located at ca. 4.6 V (Figures III. 5b and A. 3. 2), where the phase transition also starts to appear. Furthermore, either an OCV step or a CV hold was tentatively applied after charging to 4.8 V, since *in-situ* XRD demonstrated that within this time period phase A → A' transition occurs (Figures III. 3 & 4). Notably, O_2 continues to evolve after entering the OCV step and the CV hold, with its evolution rate being larger for the latter case, ending with total amounts of 751 µmol g^{-1} and 383.4 µmol g^{-1} respectively for cells charged with additional CV and OCV steps, as compared to 269.5 µmol g^{-1} for the cell directly

switched to discharge (Table III. 2). The additional O_2 evolution during OCV, i.e., when no charge is passed, has several possible origins: i) the delay between the O_2 evolution from the material and its detection in the mass spectrometer; ii) the kinetic hindrance related to the O_2 diffusion across the van der Waals gap; iii) structure rearrangement of the material or iv) chemical reactions (e.g., disproportionation) of the released oxidized oxygen species (O^{n-}, $0 < n < 2$) that are still unknown in their chemical nature. Nevertheless, the O_2 evolution quickly stops in the cell which directly switched to discharge, demonstrating that the additional O_2 release cannot be explained by the former two possibilities. Overall, OEMS combined with *in-situ* XRD results show that the growth of phase A' solely occurs after the onset of O_2 release, and is always accompanied by O_2 release during OCV and CV period, suggesting that the O_2 release and the phase A → A' transition are strongly correlated.

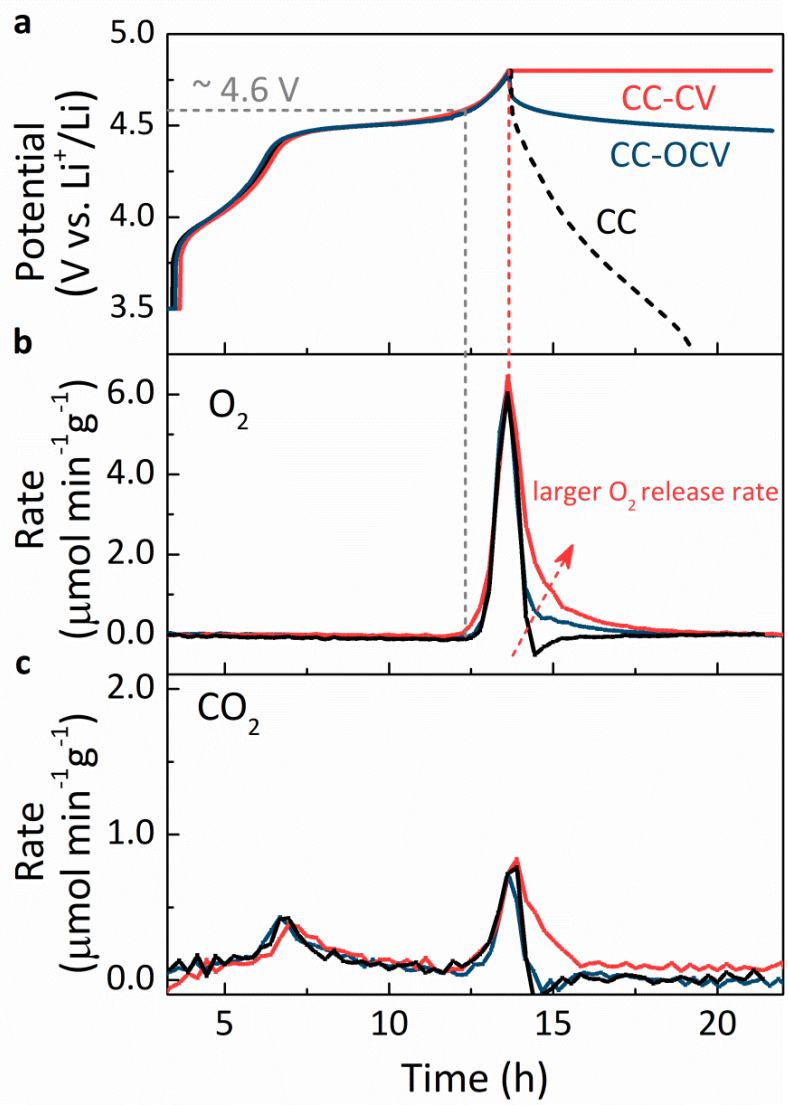

Figure III. 5 OEMS gas analysis during the first constant current (CC) charge of $Li_{1.2}Ni_{0.13}Mn_{0.54}Co_{0.13}O_2$ followed by a CC discharge (black lines), an OCV step (blue lines) and a CV hold at 4.8 V (red lines). O_2 (m/z = 32) and CO_2 (m/z = 44) ion currents were recorded and then converted to gas evolution rates. (a) The voltage *vs* time curves (note that the curves are superimposed up to the 4.8 V charge cutoff voltage indicating a good reproducibility of the OEMS cells, and the dash black line illustrates partially the subsequent discharge for the sake of comparison) and the evolved rates of O_2 (b) and CO_2 (c) in the units of µmol $min^{-1}g^{-1}$ with colors quoted the same as in panel (a). The grey dash line indicates the onset of O_2 evolution. The red line marks the 4.8 V cutoff voltage of the CC charge. The red dash arrow reveals that larger O_2 evolution rate was observed in the CC - CV charged cell.

Regarding the CO_2 evolution, it begins at ca. 4.2 V followed by a second release which coincides with the onset of O_2 evolution at ca. 4.6 V (Figure III. 5c). It is generally recognized that the first CO_2 evolution corresponds to the decomposition of surface Li_2CO_3 contaminants, while the second CO_2 evolution may have multiple contributions, ranging from continued Li_2CO_3 decomposition, reactive oxidized oxygen species attacking carbonate electrolyte, and high-voltage-driven electrolyte decomposition, etc.[111,168-170] A notable larger rate for the second CO_2 evolution was observed during the CV hold as compare to the OCV step and CC discharge, suggesting possible electrochemically-driven oxidation of the electrolyte.

Further quantitatively exploiting the gas evolution in the CC-CV charged cell, we estimated the total extraction of O atom from the material by 1) only considering the recorded O_2 amounts, and 2) assuming that CO_2 evolved at high voltages (denoted as high V CO_2) also comes from the released O_2 reacting with electrolyte, as suggested by Strehle *et al.*[47] We could deduce a maximum loss of ~ 0.15 O per formula unit (Table III. 2). This value, combined with the Li, Co, Ni and Mn contents obtained by the inductively coupled plasma – optical emission spectrometry (ICP-OES) measurements, leads to a theoretical chemical composition of $Li_{0.05}Ni_{0.13}Mn_{0.54}Co_{0.13}O_{1.85}$ for the A' phase.

Table III. 2 Estimation of the O content in charged $Li_{1.2}Ni_{0.13}Mn_{0.54}Co_{0.13}O_2$ phases. The evolved O_2 and CO_2 amounts are deduced from the same cells presented in Figure III. 5 based on the ion currents recorded respectively for m/z = 32 and m/z = 44.

	O_2 amount ($\mu mol\ g^{-1}$)	CO_2 amount (high V, $\mu mol\ g^{-1}$)	y in Li_xTMO_y (considering O_2)	y in Li_xTMO_y (considering O_2 + high V CO_2)
CC	269.5	45.8	1.95	1.95
CC-OCV	383.4	40.7	1.93	1.93
CC-CV	751	126	1.87	1.85

III. 2. 2 Detailed structural characterization of phase A'

Next, the structure of the A' phase was determined by combined transmission electron microscopy (TEM), synchrotron XRD and NPD.

TEM data were collected by Dr. A. Abakumov at EMAT, Belgium. The electron diffraction (ED) patterns reflect that the majority of the A' phase crystallizes in the O3 $R\bar{3}m$ structure (Figure III. 6b). The [010] ED pattern demonstrates reflection splitting along the **c*** direction, which is the typical signature of the mirror-twinned O3 $R\bar{3}m$ structure with the (001) twin plane (Figures III. 6b and 7). The nanosized twinned domains are evident in the low magnification high-angle annular dark-field scanning transmission electron microscopy (HAADF-STEM) image (Figure III. 6b). Besides sharp reflections of the O3 structure, diffuse spots are present in the [010] ED pattern of the A' phase at the positions characteristic of the O1 structure (marked with vertical arrowheads in Figure III. 6b). In contrast to the pristine Li-rich NMC sample,[43] the $[\bar{1}10]$ ED pattern of the A' phase shows only very faint diffuse intensity lines from the "honeycomb" Li-TM ordering (marked with horizontal arrowheads in Figure III. 6b), indicating that this ordering is largely suppressed. This justifies the validity of the simple O3 $R\bar{3}m$ structure model used for further Rietveld refinement of the A' structure.

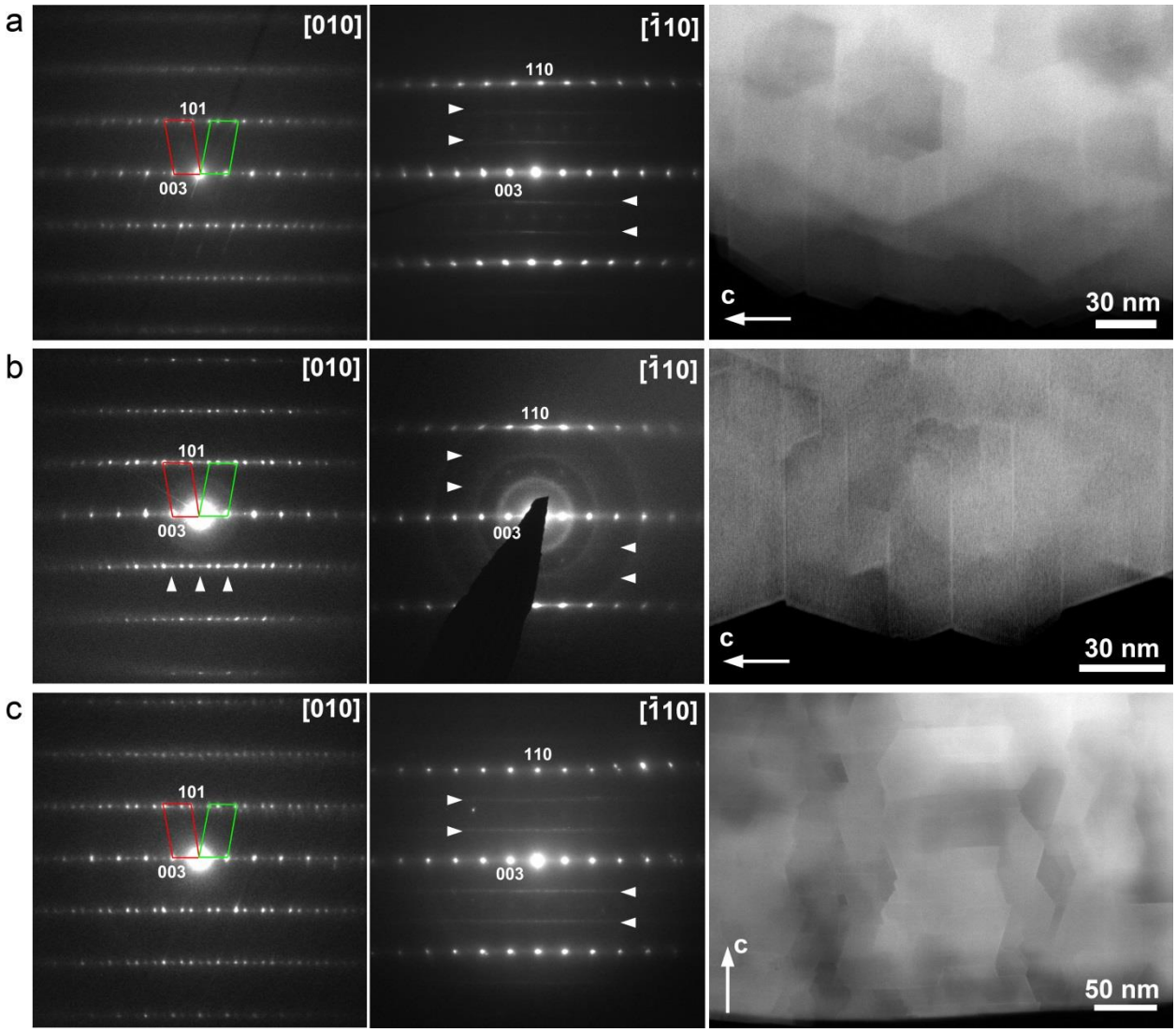

Figure III. 6 Electron diffraction (ED) patterns and low magnification HAADF-STEM images of Li-rich NMC charged to 4.6 V (**a,** the A phase), 4.8 V (**b**, with 8 h constant voltage holding to form the pure A' phase) and discharged to 2.0 V (**c**). The ED patterns are indexed with the O3 $R\bar{3}m$ structure. Note the reflection splitting in the *h*0*l*, $h \neq 3n$ reciprocal lattice rows in all [010] ED patterns which is caused by mirror twinning of the O3 $R\bar{3}m$ structure with the (001) twin plane (Figure III. 7). The primitive reciprocal unit cells of two twinned variants are outlined in red and green in the [010] ED patterns. Twinned domains with few tens of nanometers in thickness along the *c*-axis are clearly visible in low magnification HAADF-STEM images for all three states of charge. Extra spots elongated along the **c*** axis appear between the pairs of bright reflections of the O3 structure in the [010] ED pattern of the A' phase (**b**, marked with vertical arrowheads). These reflections originate from thin domains of the O1 structure, as evidenced with the HAADF-

STEM images in Figure III. 8**.** [$\bar{1}$10] ED pattern of the A phase (**a**) reveals faint diffuse intensity lines (marked with horizontal arrowheads) from residual short-range "honeycomb" Li-M ordering. These diffuse intensity lines become almost invisible in the [$\bar{1}$10] ED pattern of the A' phase (**b**) indicating significant suppression of the "honeycomb" Li-M ordering, but regain their brightness after discharge to 2.0 V (**c**) due to restoration of this ordering. Weak spots between diffuse intensity lines in the [$\bar{1}$10] ED patterns of Li-rich NMC charged to 4.6 V (**a**) and 4.8 V (**b**) come from the near-surface M cation ordering analyzed in Figure III. 9.

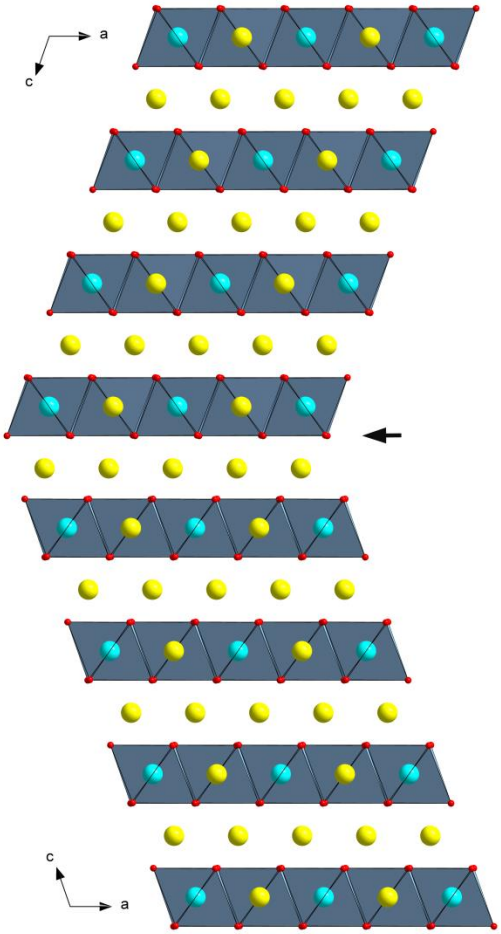

Figure III. 7 Tentative model of twins in the O3 $R\bar{3}m$ structure. Two twinned domains viewed along [010] possess mirror-related orientation of the *c*-axis. At the twin plane the "cubic" *ccp* close packing of the O atoms is interrupted by a single "hexagonal" *h* layer (marked with an arrow). The M cations, Li cations and O atoms are shown as cyan, yellow and red spheres, respectively. The MO_6 octahedra are shaded.

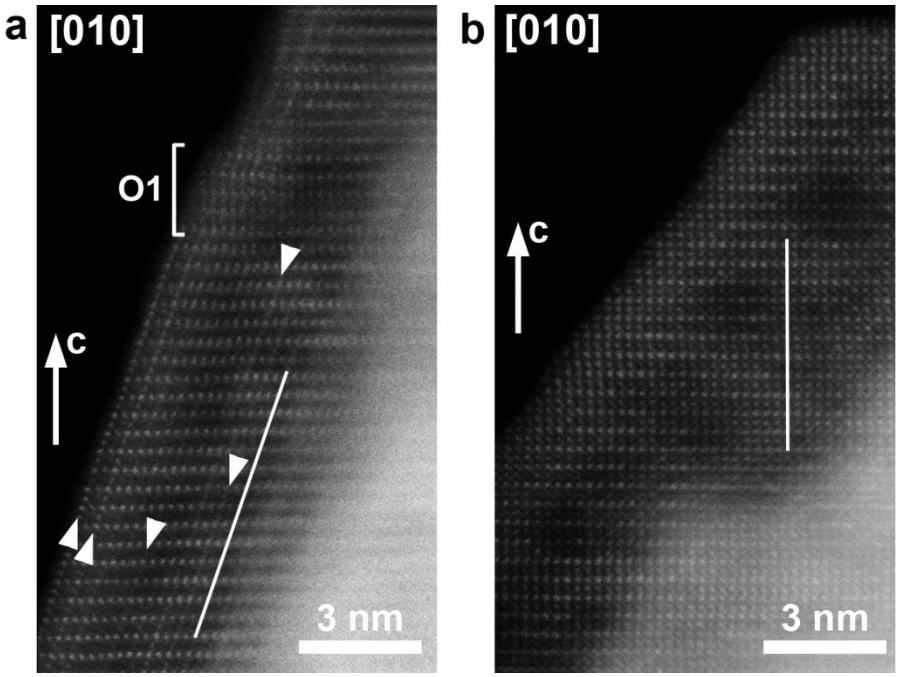

Figure III. 8 Local structure of the A' phase viewed with [010] HAADF-STEM images. **a,** The near-surface O3 structure: the M layers are horizontally being traced with the rows of bright dots of the M cationic columns. The "cubic" stacking sequence is evidenced with cumulative lateral shift of the $Li_{1-x}M_{2+x}$ layers (marked with a sloped line). The migration of the M cations to the octahedral interlayer sites is visible as a nucleation of the $\{10\bar{2}\}$-oriented TM-cation layer at ~ 60^{o} to the {001}-oriented $Li_{1-x}M_{2+x}$ layers (marked with arrowheads). Thin lamella of the O1 phase is marked with a bracket. **b,** The near-surface structure of an extended O1 domain: the "hexagonal" stacking sequence is evidenced by absence of the lateral displacements of the $Li_{1-x}M_{2+x}$ layers (marked with a vertical line). The migration of the M cations to the interlayer octahedral sites is very pronounced seen by appearance of extra rows of dots between the $Li_{1-x}M_{2+x}$ layers (look brighter).

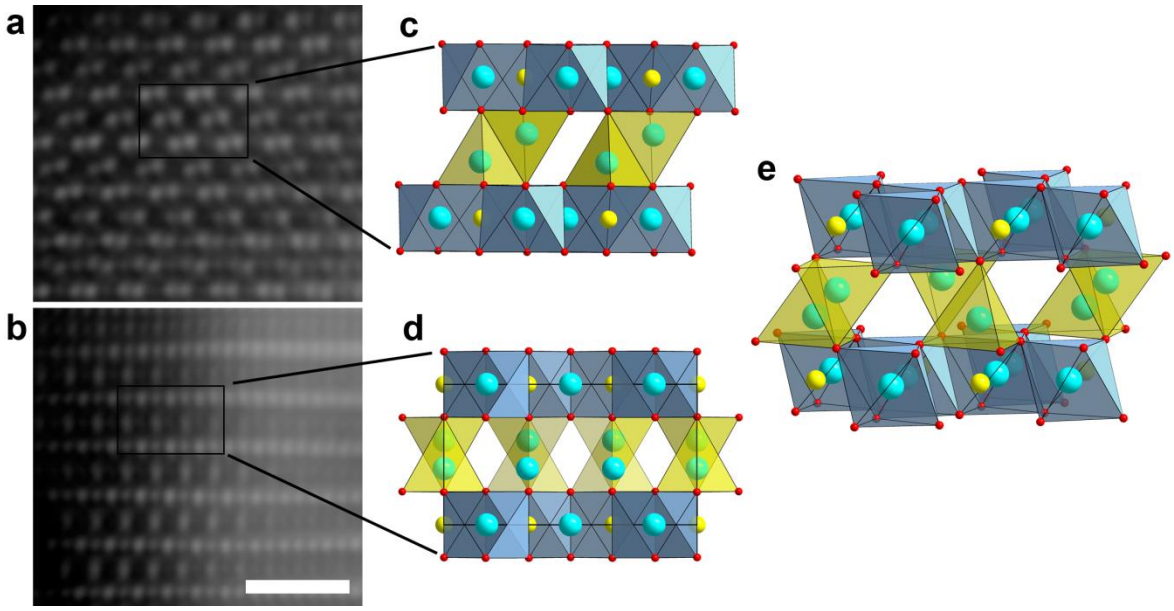

Figure III. 9 Near-surface locally ordered states in the A' phase. **a, b,** HAADF-STEM images of the ordering of M cations in the tetrahedral interstices between the M layers with pertaining "honeycomb" M cation ordering (the scale bar is of 1 nm). **c, d,** Projected structures corresponding to the cationic positions in the HAADF-STEM images **a** and **b**, respectively. The M cations, Li cations and O atoms are shown as cyan, yellow and red spheres. **e,** The projected structures, in fact, correspond to the same 3D structural arrangements viewed at different directions rotated by 60°. Note that the tetrahedral interstices are linked by common edge and cannot be occupied simultaneously.

Rietveld refinements of synchrotron X-ray and neutron diffraction patterns were performed by Dr. G. Rousse at Sorbonne Université, France. In agreement with the ED data, the synchrotron XRD pattern can be indexed in an O3 $R\bar{3}m$ structure with lattice parameters of a = 2.84194(11) Å, c = 13.9722(14) Å (Table III. 3), As the distribution of five species with different scattering factors (Li, Ni, Mn, Co and cation vacancy) among two crystallographic positions of the $R\bar{3}m$ structure cannot be distinguished uniquely, combined neutron/synchrotron Rietveld refinement was carried out with the oxygen composition and Li content fixed to $Li_{0.05}MO_{1.85}$ formula (as deduced from ICP-OES for Li content and OEMS for O content), and assuming that only one of the three transition metal (TM) cations may migrate. Indeed, neutron diffraction provides a unique contrast between Mn (b_{Mn} = - 3.73 fm), Ni (b_{Ni} = 10.3 fm) and Co (b_{Co} = 2.49 fm). The total occupancy of each TM cation was imposed to the one expected from the pristine chemical formula. The best fit, shown in Figure III. 10 with corresponding crystallographic parameters reported in Table III. 3, was

obtained by populating the vacant Li 3*a* sites with ~ 0.079(2) Mn, hence a chemical cationic composition $[Li_0Mn_{0.08}][Li_{0.05}Ni_{0.13}Mn_{0.46}Co_{0.13}]O_{1.85}$, where square brackets refer to atoms in the octahedral 3*a* and 3*b* sites of the $R\bar{3}m$ structure, respectively. The migration of TM into octahedral lithium site was also supported by difference-Fourier mapping (Figure A. 3. 3). Note that the Mn migration to the vacant octahedral sites in the Li layers has already been experimentally observed and theoretically proposed.[171-174] However, one should note that there are two possible interpretations of such a refinement. The first one corresponds to the above-written chemical formula and involves the presence of oxygen vacancies and an under-coordination of metals. The second interpretation is to rewrite the chemical formula as $[Li_0Mn_{0.08}][Li_{0.05}Ni_{0.14}Mn_{0.50}Co_{0.14}]O_2$. This corresponds to an O3 structure without any oxygen vacancies but "densified", because the TM/O ratio has increased compared to the pristine $Li_{1.2}Ni_{0.13}Mn_{0.54}Co_{0.13}O_2$ (0.43 for A' phase; 0.40 for pristine phase). The second interpretation is in full agreement with the fact that the unit cell volume of the A' phase is smaller compared to the pristine phase (97.730(11) $Å^3$ for A' phase; 100.545(2) $Å^3$ for pristine phase), because of the shortening of the *c* lattice parameter (from 14.25381(15) Å for the pristine phase to 13.9722(14) Å for the A' phase). These results clearly indicate that "densification" is not a surface but rather a bulk effect. Lastly, it is worth mentioning that the *c*/*a* aspect ratio in the A' phase is very close to (but different from) that of an ideal cubic lattice ($c/a = 4\sqrt{3}/\sqrt{2}$), which can explain why this phase may have been previously misinterpreted as a spinel cubic phase in literatures.

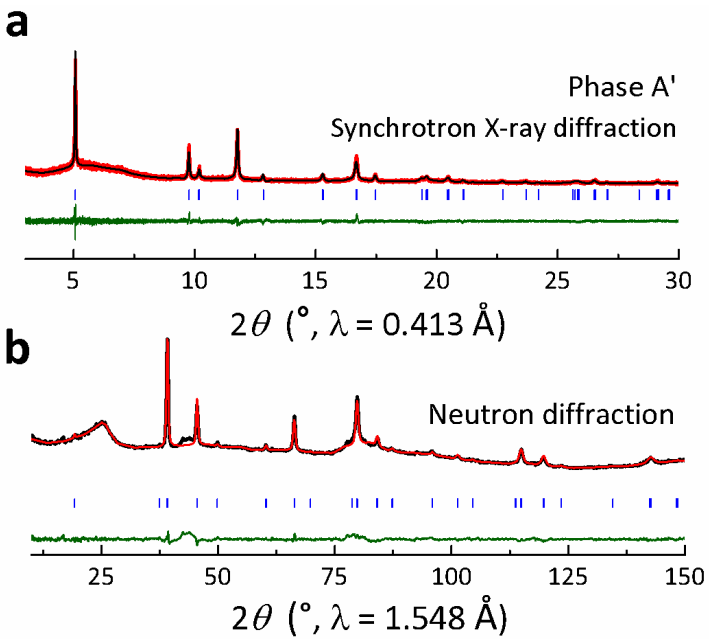

Figure III. 10 Rietveld refinement of synchrotron (a) and neutron (b) powder diffraction for A' phase.

Table III. 3 Crystallographic data and atomic positions of the phase A' determined from Rietveld refinements of the combined synchrotron and neutron powder diffraction patterns.

CC-8 h CV charged Li-rich NMC phase (Phase A': O3 – $Li_{0.05}Ni_{0.14}Mn_{0.58}Co_{0.14}O_2$)						
Space group: $R\bar{3}m$		a (Å)		b (Å)	c (Å)	V (Å^3)
SXRD NPD		2.84194(11) 2.8297(6)		2.84194(11) 2.8297(6)	13.9722(14) 13.878(7)	97.730(11) 96.24(6)
χ^2 = 5.1, Bragg R-factor = 14.5 % (SXRD), Bragg R-factor = 21.3 % (NPD)						
Atom	Site	*x/a*	*y/b*	z/c	Occupancy	B_{iso} (Å^2)
Mn	3*a*	0	0	0	0.083(2)	0.38(3)
Ni/Mn/ Co/Li	3*b*	0	0	0.5	0.14/0.499(2)/ 0.14/0.056	0.38(3)
O	6*c*	0	0	0.2422(2)	1	1.75(4)

To enforce this structural analysis, we further performed atomic-resolution HAADF-STEM and annular bright-field scanning transmission electron microscopy (ABF-STEM) imaging. The

[010] HAADF-STEM image (Figure III. 8a) reflect the prevailing O3-type stacking of the TM layers, albeit with thin domains of the O1-type stacking spanning over just few unit cells. More extended O1 domains are also observed, as evidenced in Figure III. 8b. In the O3 structure, the layered ordering of the TM cations is violated by the TM cation migration to the vacant Li sites appearing as a nucleation of the $\{10\bar{2}\}$-oriented TM-cation layer at ~ 60^{o} to the {001}-oriented $Li_{1-x}TM_{2+x}$ layers. The O1 domains demonstrate more pronounced occupation of the octahedral interstices by the TM cations. The most remarkable picture of the structural inhomogeneity of the A' phase related to TM migration is visualized with the $[\bar{1}10]$ HAADF-STEM image (Figure III. 11a). First inhomogeneity is related to the "honeycomb" Li-M ordering which pertains only in part of the $Li_{1-x}M_{2+x}$ layers whereas the layers with suppressed "honeycomb" ordering are frequently present (both variants are marked with arrowheads in Figure III. 11a). Significant M cation migration occurs over whole > 15 nm distance from the surface demonstrating a variety of local ordering, where the M cations occupy either octahedral Li sites or tetrahedral interstices (illustrated with inserts in Figure III. 11a). The enlarged images of this local ordering are provided in Figures III. 9 and A. 3. 4, along with tentative distribution of cations among the tetrahedral and octahedral sites. These locally ordered sequences, which also manifest themselves in reciprocal space as very faint reflections between the diffuse intensity lines in the $[\bar{1}10]$ ED pattern (Figure III. 6b), can be considered as a prerequisite to the formation of the spinel-type structure. Hence we conclude that the A' phase preferentially adopts the O3-type structure with M cation partially migrating to the empty octahedral or tetrahedral sites at the surface as well as in the interior parts of the crystallites causing bulk densification. This migration is associated with the formation of the A' phase and it is substantially reversible as comparatively illustrated with the $[\bar{1}10]$ HAADF-STEM images of Li-rich NMC charged to 4.6 V (the A phase), 4.8 V (the A' phase) and discharged to 2.0 V (Figure III. 11b, 11c & 11d, respectively).

Overall, the TEM observations corroborate the Rietveld refinement results. Hence we conclude that the A' phase preferentially adopts the O3-type structure with TM cation partially migrating to the empty octahedral sites in the interior parts of the crystallites causing bulk densification, whereas the "honeycomb" Li-TM ordering maintains in the near-surface region along with TM cations migrate into both octahedral and tetrahedral interlayer site (Figure III. 12).

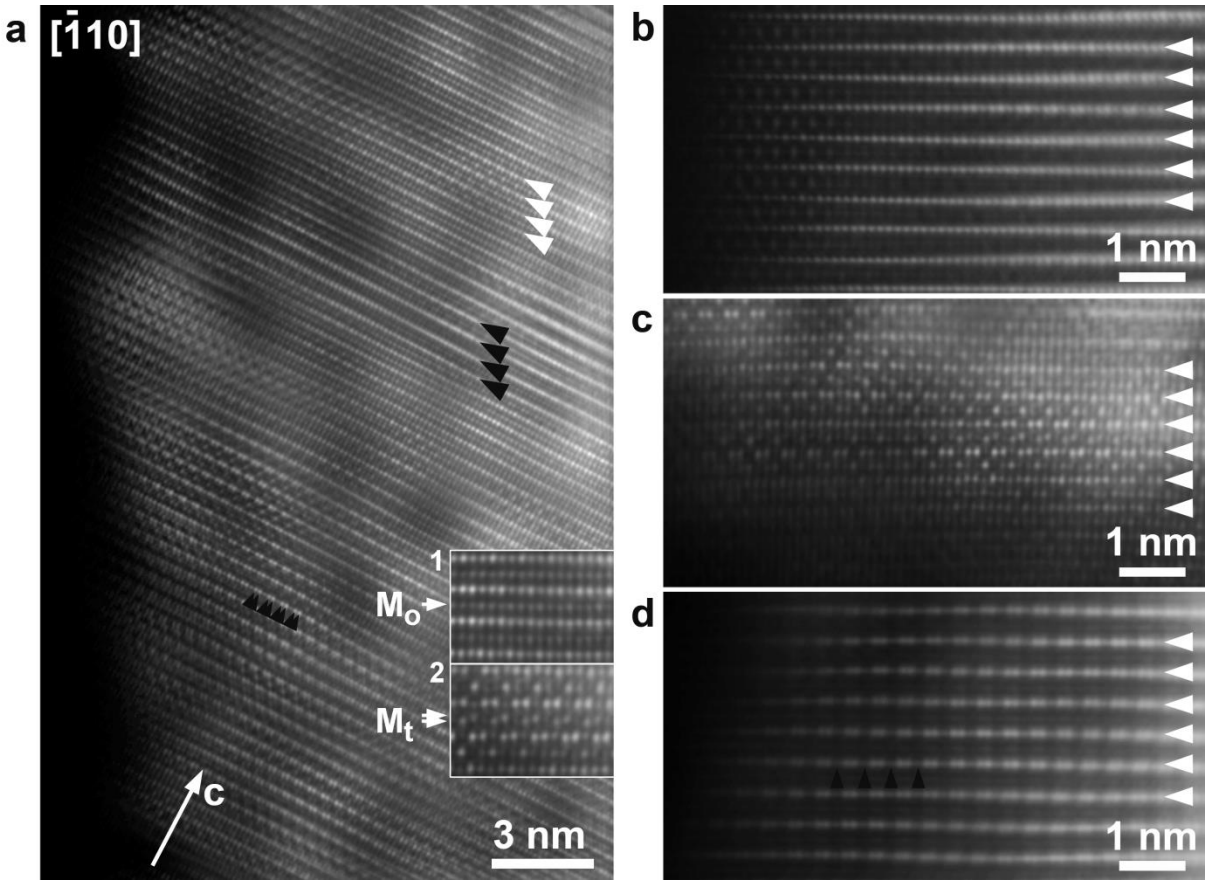

Figure III. 11 Local structures of Li-rich NMCs viewed with HAADF-STEM images. a, Overview [$\bar{1}$10] HAADF-STEM image showing structural inhomogeneity of the A' phase. The $Li_{1-x}M_{2+x}$ layers are visible as rows of brighter dots perpendicular to the *c*-axis. "Honeycomb" Li-M ordering is visualized by pairs of bright dots with ~ 0.14 nm interdot separation (such as marked with pairs of small black arrowheads). The $Li_{1-x}M_{2+x}$ layers with pertaining "honeycomb" ordering (such as marked with large white arrowheads) alternate with the layers where this ordering is largely suppressed (such as marked with large black arrowheads). The interlayer spaces demonstrate pronounced HAADF intensity indicating migration of the M cations to either octahedral sites M_o (see insert 1) or to the tetrahedral interstices M_t (see insert 2, see Figure III. 9 for atomic position assignment). This migration occurs at the near-surface region as well at > 15 nm away from the surface. Near-surface [$\bar{1}$10] HAADF-STEM images of Li-rich NMC charged to 4.6 V (**b,** the A phase), 4.8 V (**c**, the A' phase) and discharged to 2.0 V (**d**). The M cation migration sets in at very thin 1-2 nm surface layer in the A phase, then it becomes very pronounced in the A' phase and finally gets almost fully suppressed after 2.0 V discharge. The "honeycomb" Li-M ordering is largely restored in the discharged phase as demonstrated by the pattern of the bright dot

pairs, but some disorder still remains indicated by residual intensity between the dot pairs (marked with black arrowheads in **c**).

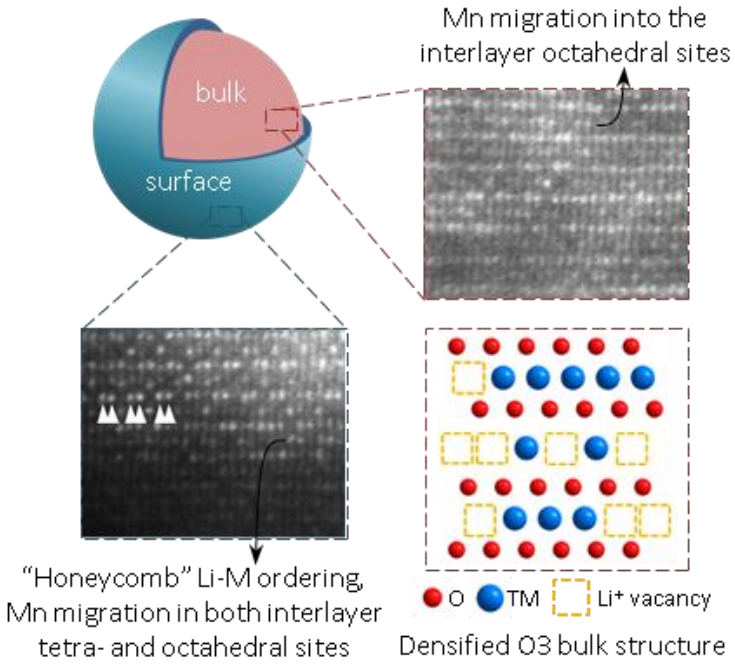

Figure III. 12 Schematic of the bulk and surface structure of the newly formed A' phase along with the illustrative atomic-resolution HAADF-STEM images.

III. 2. 3 The impact of phase transition on the electrochemical properties

Next, we continued to explore how the phase transition impacts the electrochemical behavior for this Li-rich phase. As previously demonstrated in the subchapter III. 2. 1, following the 4.8 V charge, phase A → A' transition starts to occur after entering the OCV period, and gradually becomes a single phase A' with CV hold. Therefore, we tentatively cycled three identical $Li_{1.2}Ni_{0.13}Mn_{0.54}Co_{0.13}O_2$/Li cells between 4.8 V and 2.0 V, but with different first charge protocols: one cell was directly switched to discharge (denoted as CC, black curve) with phase A forming at the end of the first charge, whereas either an intermediate OCV step for 120 h (blue line, denoted as CC - OCV) or CV hold for 8 h (red line, denoted as CC - CV) was imposed to the other two cells to trigger the formation of phase A'. Figure III. 13 compare the first charge-discharge voltage curves, and Figure III. 14 compare the retention for the average discharge voltage and the discharge capacity upon cycling. Notably, phase A' exhibits a larger first-cycle irreversible capacity and an

initial voltage drop as compare to phase A (Figure III. 13), whilst upon cycling, the persistence of the voltage decay and capacity fading (Figure III. 14).

From an electrochemical perspective, the initial voltage drop can be explained by the reduction of transition metal ions (Co and Ni) during OCV or CV step, as revealed by *ex-situ* X-ray absorption spectroscopy (XAS) measurements (Figure III. 15). The observed capacity drop after imposing the OCV or CV step is closely associated with the gradual phase A → A' transition. More specifically, the contraction of TM layers and the growing Mn occupation in the octahedral Li sites upon A → A' phase transition certainly would cause a kinetic hindrance in Li^+ intercalation. In addition, the formation of phase A' is accompanied with O_2 release, which are known to induce particle cracking that could also contribute to the performance deterioration.

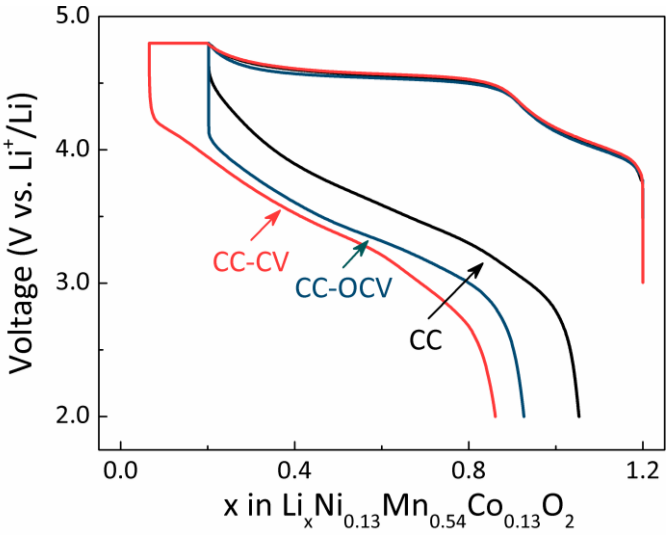

Figure III. 13 The first charge-discharge voltage curves of $Li_{1.2}Ni_{0.13}Mn_{0.54}Co_{0.13}O_2$ cycled with different protocols. One cell was charged to 4.8 V and then directly discharged to 2.0 V, denoted as CC (black line), whereas an intermediate OCV step for 120 h (blue line, denoted as CC - OCV) or CV hold for 8 h (red line, denoted as CC - CV) was respectively imposed to the other two cells. All the cells were cycled at C/3.

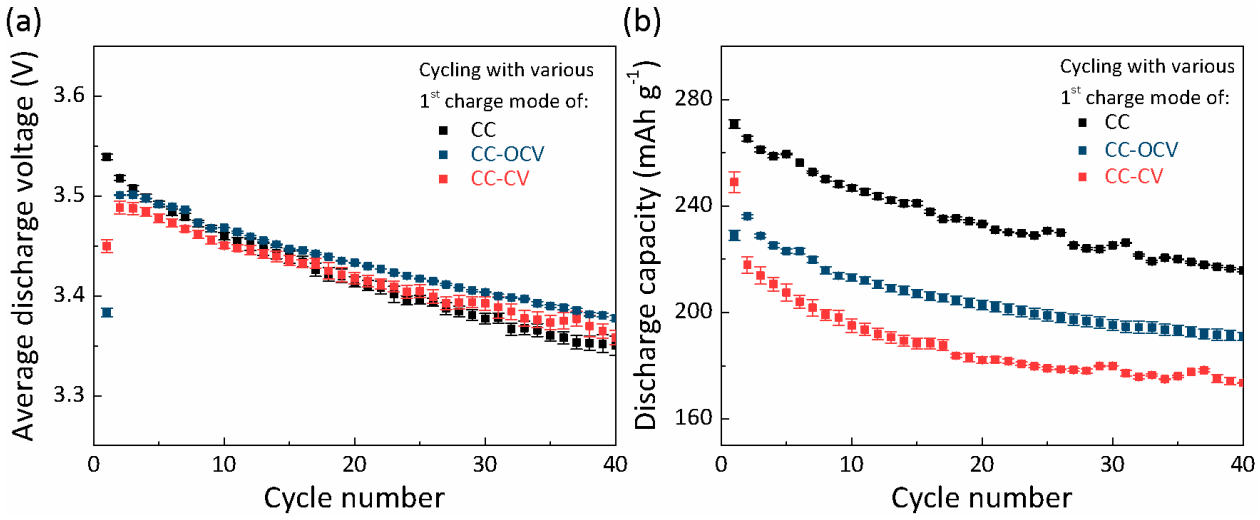

Figure III. 14 Retention profiles of the average discharge voltage (a) and the discharge capacity (b) of $Li_{1.2}Ni_{0.13}Mn_{0.54}Co_{0.13}O_2$ cycled between 4.8 and 2.0 V with different first-charge protocol: CC (black line), CC - OCV (blue line) and CC - CV (red line). Error bars represent standard deviation of two cells.

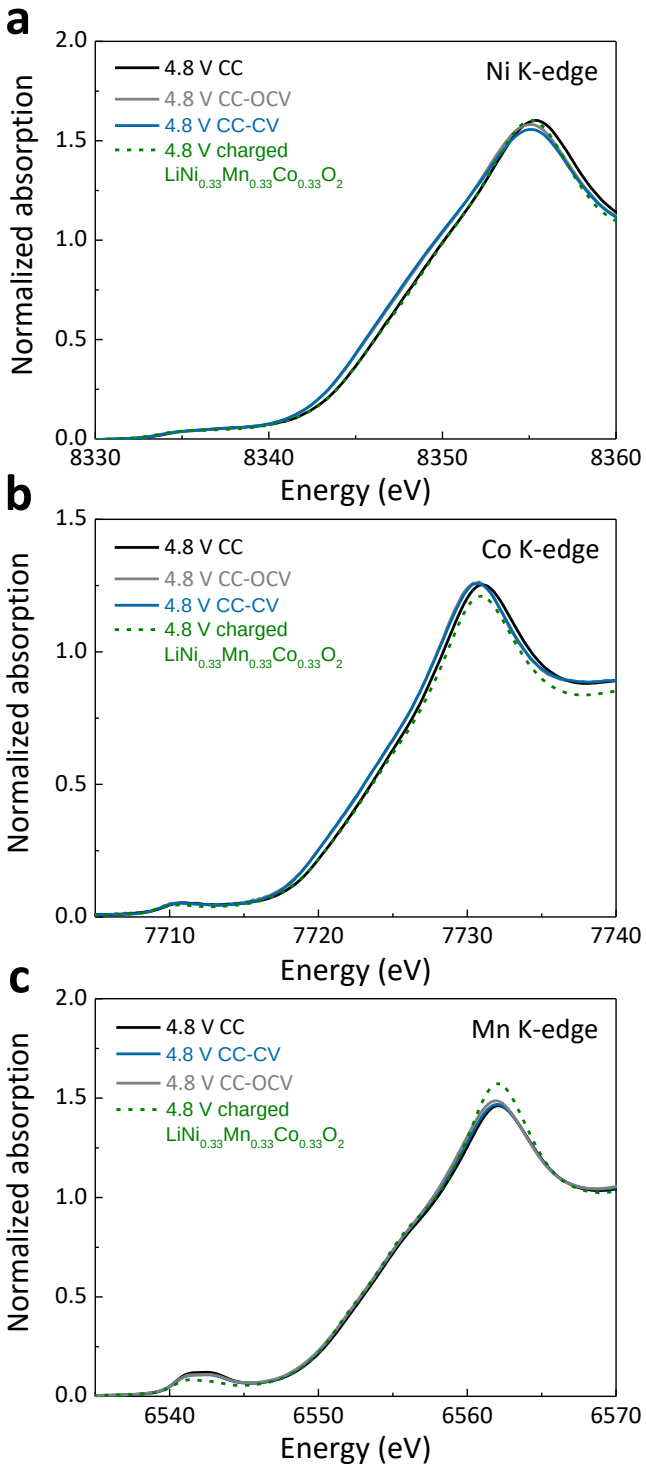

Figure III. 15 Normalized XANES spectra at the (a) Ni K-edge, (b) Co K-edge and (c) Mn K-edge for Li-rich NMC samples which were charged to 4.8 V (black line), and charged to 4.8 V with an additional OCV step (grey line) or CV hold (blue line) for 5 h. The spectra for $LiNi_{0.33}Mn_{0.33}Co_{0.33}O_2$ collected at 4.8 V charge state are given as references.

III. 2. 4 Mn migration triggered by oxygen redox and its consequence of extra low-voltage electrochemical activities

As previously discussed, phase A' forming under harsh oxidizing condition enlists Mn migration, we further investigated the influence of depth of charge on the Mn migration. For that, we prepared several $Li_{1.2}Ni_{0.13}Mn_{0.54}Co_{0.13}O_2$/Li cells that were electrochemically oxidized till Δx = 0.4, 0.6, 0.8, and 1.0 followed by 120 h OCV (Δx refers to the amount of Li^+ removal on charge or the amount of Li^+ insertion on discharge), prior to sampling the electrodes for *ex-situ* synchrotron X-ray diffraction measurements. By employing the same Rietveld methodology as before, we could deduce that while the Δx = 0.4 charged sample shows no Mn migration in interlayer octahedral sites (defined as δ in $[Li_{1.0-\Delta x}Mn_{\delta}][Li_{0.2}Ni_{0.13}Mn_{0.54-\delta}Co_{0.13}]O_2$), a progressive increase of Mn migration (δ) was observed with increasing Δx from 0.6 up to 1.0 (Figure III. 16a). Interestingly, further maintaining the Δx = 1.0 charged sample at 4.8 V for 8 hours to obtain the A' phase did not change the amount of Mn migration (δ) within the accuracy of this method, but slightly decreased the *c* parameter from 14.2058(4) Å to 13.9722(14) Å (Tables III. 3 & A. 3. 1). This is consistent with the decrease in Li^+ content from 0.02 (for Δx = 1.0 charged sample) to 0.005 (for CC - 8 h CV charged sample) according to ICP-OES, which leads to less charged oxygen ions thereby weaker oxygen-oxygen repulsion. In parallel, X-ray photoemission spectroscopy (XPS) measurements were carried out for the various charged samples to determine the fraction of oxygen involved in the anionic redox process (Figure III. 16c). To no surprise, this fraction increases with increasing Δx alike the degree of Mn migration (δ), hence, implying their correlation. In contrast, note that neither Mn migration (δ) or the percentage of oxidized oxygen correlated with O_2 release (Figure III. 16).

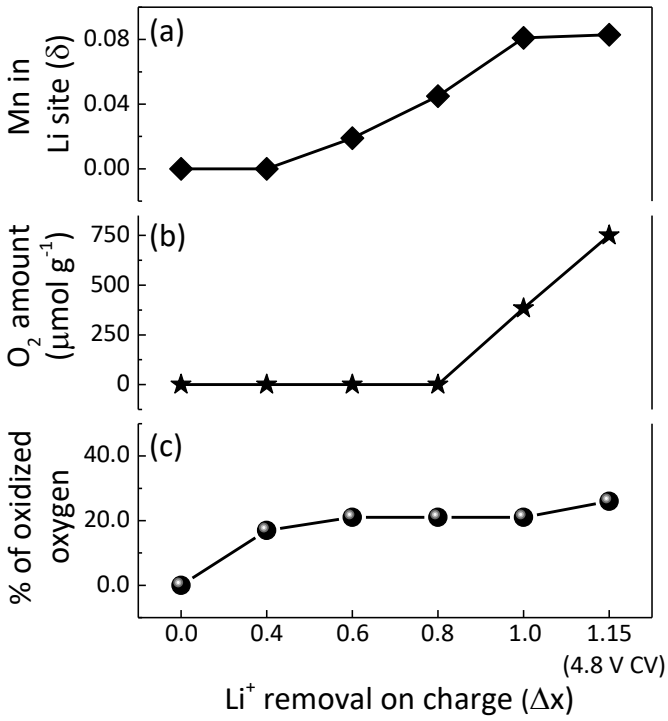

Figure III. 16 (a) Mn migration in interlayer octahedral Li sites (δ) deduced from Rietveld refinement of synchrotron XRD patterns collected for the various charged samples with the amount of Li^+ removal (Δx) ranging from 0.0 (pristine), 0.4, 0.6, 0.8, 1.0 to 1.15 (with 4.8 V CV hold for 8 h). (b) The amount of released O_2 quantified by OEMS, and (c) the percentage of oxidized oxygen (define as $O^{n-}/(O^{n-}+O^{2-})$ quantified from XPS are plotted as a function of Δx.

Besides exploring the harsh oxidizing conditions, we next investigated the effect of harsh reducing conditions on the electrochemical signatures of Li-rich NMC. At first, we fixed the discharge cut-off potential to 2.0 V and monitored the effect of state of charge on the subsequent discharge profile by opening the charge potential window stepwise (i.e., increasing Δx from 0.4 to 1.0 in steps of 0.2, the same as in the *ex-situ* synchrotron XRD study). We observed that the S-shape discharge profiles become more pronounced, when the charge voltage reaches the high-voltage plateau (Figure III. 17). Simultaneously, the degree of hysteresis and the amplitude of irreversible capacity were found to increase with deeper oxidation on charge (inset in Figure III. 17).

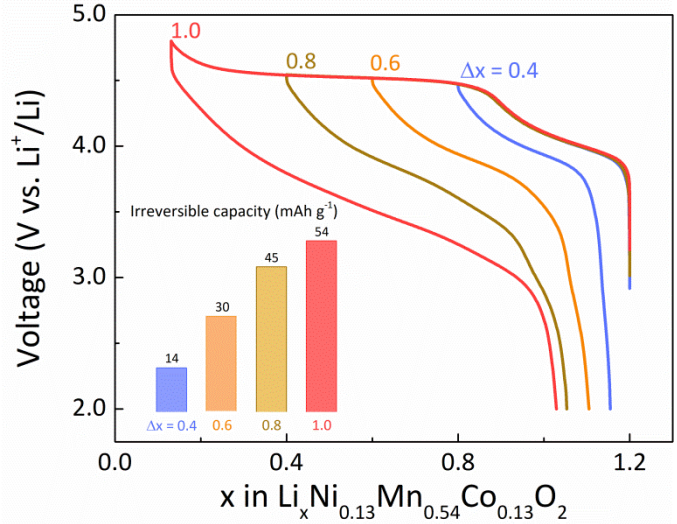

Figure III. 17 Voltage-composition profiles of $Li_{1.2}Ni_{0.13}Mn_{0.54}Co_{0.13}O_2$ obtained by varying the Li^+ removal on charge (Δx) from 0.4 (purple line), 0.6 (orange line), 0.8 (dark yellow line), to 1.0 (red line), while fixing the discharge cutoff voltage at 2.0 V. The inset shows the corresponding irreversible capacity observed in discharge.

Nevertheless, when the cells were further discharged to 1.2 V, totally unexpected is the gradual appearance of extra redox activities located within 1.5 ~ 1.2 V, whose capacity increases with increasing Δx on charge (Figures III. 18a and 18b). Strikingly, these extra capacities are not present when the cell was directly started on reduction (Δx = 0.0) or when the charge was limited to the cationic domain (Δx = 0.4). This suggests a straightforward correlation between the extra capacities and the extent of the anionic redox process. A possible explanation could be rooted in the Mn-migration (δ) which is triggered during the charge once the anionic activity becomes part of the oxidation process. To check this hypothesis, we revisited the Rietveld refinements of the synchrotron XRD patterns collected for the various charged samples with Δx = 0.4, 0.6, 0.8, and 1.0 (Figure A. 3. 7 and Tables A. 3. 1 ~ A. 3. 4), using the $R\bar{3}m$ space group and the same methodology as before. The refinements indicate Mn-migration (δ), appears only when charging to the anionic redox region, and progressively builds up with increasing state of charge. Moreover, no Mn-migration is observed when the charge is limited to the cationic redox (Δx = 0.4), akin to the pristine phase (Δx = 0.0) (Figure III. 16a). Rietveld refinement of the synchrotron XRD pattern collected at 2.0 V discharged state after charging up to Δx = 1.0 shows that such Mn-migration can only be partially restored upon discharging to 2.0 V, since Mn migration (δ) of ~ 0.0349(4) still

remains for a sample that was charged to 4.8 V and then discharged to 2.0 V (Figure A. 3. 8 and Table A. 3. 5). From ED patterns and HAADF-STEM analysis of this discharged phase, we could deduce that the microstructure of $Li_{1.2}Ni_{0.13}Mn_{0.54}Co_{0.13}O_2$ is largely restored (Figure III. 6c). Hence, such a discharged phase, which slightly deviates from the pristine one, is denoted as P' hereinafter. Altogether, these results suggest a robust correlation between the appearance of low-voltage redox activity and the Mn-migration induced by anionic redox, which is to some extent irreversible.

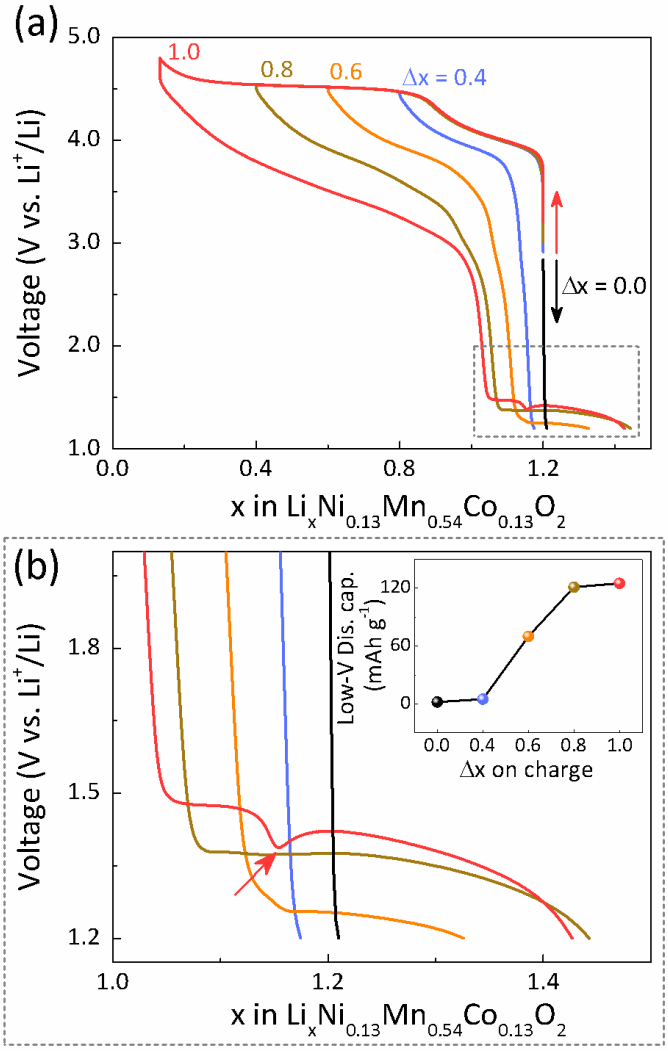

Figure III. 18 (a) Voltage-composition profiles of $Li_{1.2}Ni_{0.13}Mn_{0.54}Co_{0.13}O_2$ obtained by varying Δx on charge from 0.0 (pristine, black line), 0.4 (purple line), 0.6 (orange line), 0.8 (dark yellow line), to 1.0 (red line) whilst fixing the discharge cutoff voltage at 1.2 V. The dashed grey square indicates the gradual appearance of extra low-voltage (2.0 – 1.2 V) electrochemical activities on pushing the extent of charge to trigger anionic redox. (b) A magnified view of the voltage-composition profiles in low-voltage region (also marked with dashed grey square in panel a). The red arrow indicates the voltage overshooting point in the discharge process after charging up to Δx = 1.0. The inset shows the amount of low-voltage discharge capacities as a function of Δx. Note that the colors in panel (b) are quoted the same as in panel (a).

Further scrutinizing the low-potential capacity region (below 2.0 V), enlists two different domains separated by a voltage overshooting (marked by a red arrow in Figure III. 18b) which is

usually reminiscent of the nucleation-growth process of a new phase. To confirm this point, a $Li_{1.2}Ni_{0.13}Mn_{0.54}Co_{0.13}O_2$/Li *in-situ* XRD cell was charged to 4.8 V and then discharged to 3.0 V, prior to collecting XRD patterns, while the discharge was pushed down to 1.2 V (Figure III. 19). We observed a continuous initial shift of the P' phase reflections (i.e., (003) reflection shifts toward higher angles, whereas (111) and (131) reflections shift toward lower angles) with some decreasing in intensity until near the voltage overshoot (~ 1.4 V), indicating a solid solution transformation process. Then upon further increasing in *x*, some reflections disappear at the expense of new ones that remain broad until becoming a single reflection, indicative of a new phase (denoted hereinafter as P"), when the voltage reaches 1.2 V.

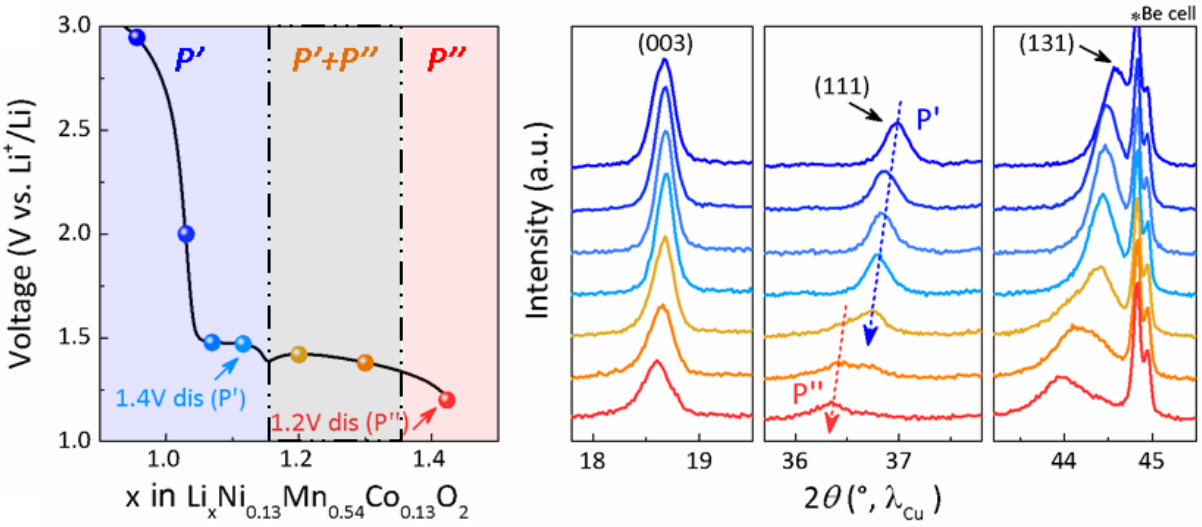

Figure III. 19 Structural evolutions during the low-voltage discharge process within 3.0 V – 1.2 V. (a) Selective galvanostaic discharge curve (left side), and selective regions ((003), (111) and (131) reflections) of the corresponding *in-situ* XRD patterns (right side) collected upon discharging $Li_{1.2}Ni_{0.13}Mn_{0.54}Co_{0.13}O_2$ from 3.0 V down to 1.2 V, after charging to 4.8 V and discharging to 3.0 V (see results for the complete discharge in Figure A. 3. 10). Note that the dashed blue arrow marks the evolution of phase P' and the dashed red arrow indicates the growth of phase P", respectively.

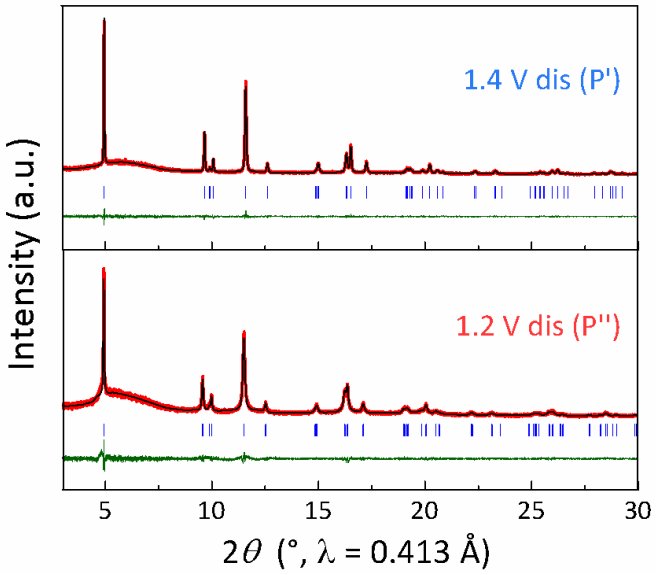

Figure III. 20 Rietveld refinements of the synchrotron XRD patterns for the samples collected after 1.4 V (phase P') and 1.2 V (phase P") discharge. The red line, black line and bottom green line represent the observed, calculated XRD patterns and the difference, respectively. Vertical blue tick bars mark the Bragg positions in the $R\bar{3}m$ space group.

Owing to the width of these reflections, we have collected high-resolution synchrotron XRD patterns on powders recovered from cells that have been discharged respectively to 1.4 V (phase P') and 1.2 V (phase P") (Figure III. 20). Rietveld refinements indicate that both phases remain in the $R\bar{3}m$ space group with smaller lattice parameters for the P' phase (a = 2.87386(2) Å, c = 14.3442(2) Å, V = 102.598(2) Å^3, Table A. 3. 6) as opposed to the larger values for the P" phase (a = 2.90026(5) Å, c = 14.3783(5) Å, V = 104.739(4) Å^3, Table A. 3. 7). The amount of Mn-migration (δ) was determined to be 0.057(2) for the P' phase and 0.085(2) for the P" phase, respectively (Figure III. 21). The increase in lattice parameters is consistent with the uptake of Li^+ upon reduction to 1.2 V ($Li_{1.14}Ni_{0.13}Mn_{0.54}Co_{0.13}O_{1.95}$ for the phase P' and $Li_{1.44}Ni_{0.13}Mn_{0.54}Co_{0.13}O_{1.95}$ for the phase P", as deduced by ICP-OES for Li content and OEMS for O content), but not clarifying the location of these extra Li^+ within the structure. Previous studies have shown that $LiNiO_2$ upon reduction can uptake one more Li^+ leading to the Li_2NiO_2 structure, having all the Li^+ in the tetrahedral sites[175,176]. Therefore, we can postulate, at this stage, that our 1.2 V discharged sample (P" phase) could contain some Li^+ in the tetrahedral sites. This hypothesis is also consistent with the fact that all the octahedral sites are fully occupied in the $Li_{1.2}Ni_{0.13}Mn_{0.54}Co_{0.13}O_2$ phase, in another words, only the

tetrahedral sites are available to accommodate additional Li^+ when the lithium content exceeds that in the pristine phase. However, Li_2NiO_2 has a 1T structure (space group $P\bar{3}m1$) with ABAB oxygen stacking sequence, whereas P" phase shares the same O3 structure, i.e., the same ABCABC oxygen stacking sequence, as the pristine $Li_{1.2}Ni_{0.13}Mn_{0.54}Co_{0.13}O_2$. Therefore, another puzzle concerns why the overlithiation of P' phase to P" phase does not induce an O3 to 1T phase transition. Since considerable amount of Mn (~ 0.057(2)) migrate to the interlayer octahedral sites in the phase P', we believe that these migrated Mn ions serve as "pillar" to stabilize the structure, preventing the rearrangement of oxygen sublattice. This argument is also in good agreement with previous report, showing that $Li_{1.2}Cr_{0.4}Mn_{0.4}O_2$ phase with Cr migration in the interlayer octahedral sites could retain its original *ccp* oxygen stacking during overlithiation.[177,178]

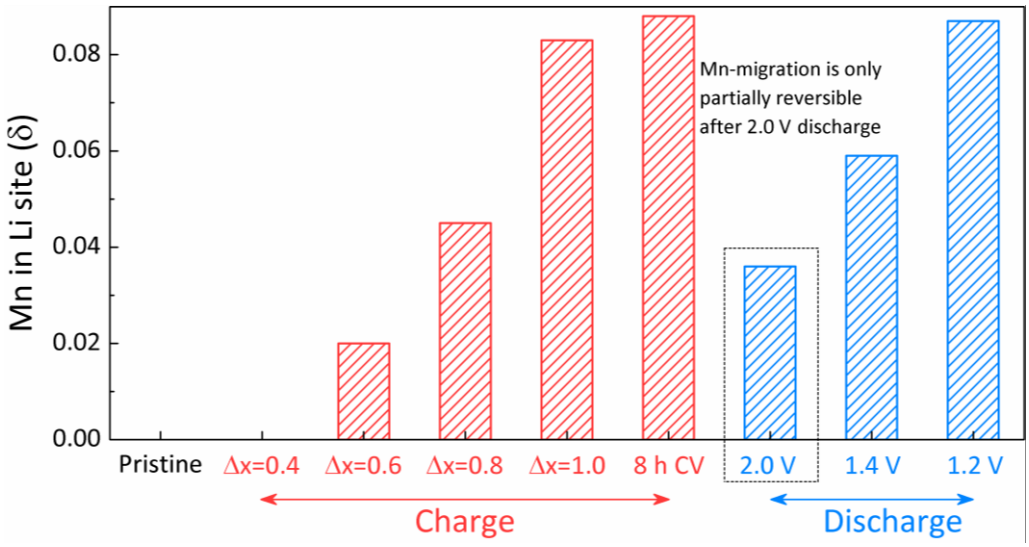

Figure III. 21 Evolution of Mn migration (δ) in the interlayer octahedral Li sites during the first charge-discharge of $Li_{1.2}Ni_{0.13}Mn_{0.54}Co_{0.13}O_2$.

To further verify our proposed mechanism that the Mn-migration associated with the oxygen redox is responsible for the uptake of additional Li^+ at low-voltage, we carried out a heat treatment study of phase P'. This study is inspired by the previous report from A. Singer *et al.*, showing that annealing the cycled Li-rich oxide material at its discharged state can recover the voltage, and restore the superstructure peak which is reminiscent of the "honeycomb" Li-TM ordering within the $LiTM_2$ layers.[112] One $Li_{1.2}Ni_{0.13}Mn_{0.54}Co_{0.13}O_2$/Li cell was charged to 4.6 V and then discharged to 2.0 V, prior to collect, and anneal the sample at the discharged state under Ar atmosphere at 250 ℃ for 1 h. Indeed, the superstructure has been partially recovered after the

annealing, in agreement with the previous literature (Figure III. 22). More importantly, Rietveld refinements of the synchrotron XRD patterns reveal that the degree of Mn migration (δ) has been decreased from 0.038(2) to nearly zero (0.007(2)) after annealing (Figure III. 23 and Tables A. 3. 8 & A. 3. 9).

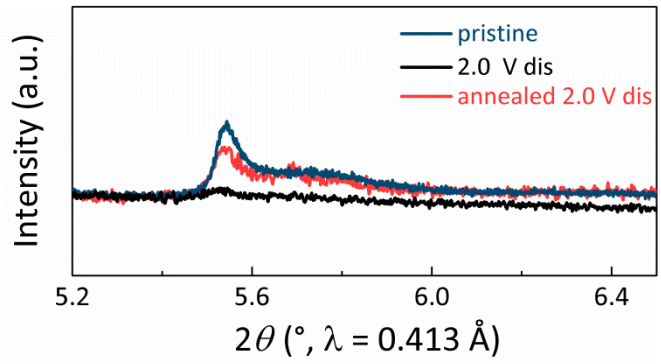

Figure III. 22 Comparison of the superstructure peak in the pristine (marine line), the sample collected at 2.0 V discharged state after 4.6 V charge before (denoted as "2.0 V dis", black line) and after annealing (denoted as "annealed 2.0 V dis", red line).

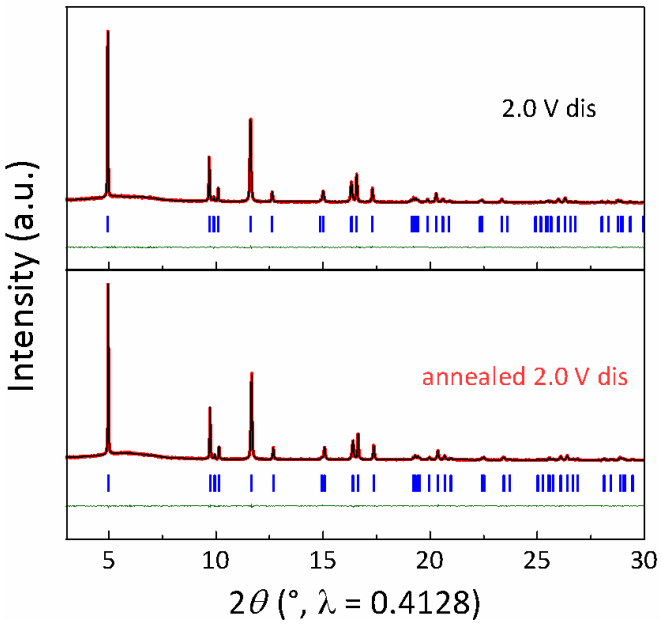

Figure III. 23 Rietveld refinements of the synchrotron XRD patterns of the sample collected at 2.0 V discharged state after 4.6 V charge before and after annealing**.** The red line, black line and bottom green line represent the observed, calculated XRD patterns and the difference, respectively. Vertical blue tick bars mark the Bragg positions in the $R\bar{3}m$ space group.

Further, coin-type cells were assembled with the two 2.0 V discharged samples, before and after annealing, to evaluate how the recovery of Mn-migration impacts on the electrochemical properties (Figure III. 24). Galvanostatic tests started directly on charge reveal that the charge profile was restored to its original stair-case shape and its voltage was recovered after the annealing (Figures III. 24 & A. 3. 12), in good agreement with the previous literature.[112] Note that the stair-case charge profile converts back to an S-shaped one during the subsequent discharge, as one can expect that the Mn-migration would occur again when the charge reaching the oxygen redox regime (Figure A. 3. 13). More importantly, the cells started directly on discharge show that the amount of Li^+ (Δx) inserted during the low-voltage discharge process was drastically decreased, by the annealing, from ~ 0.4 Li^+ to ~ 0.07 Li^+. Strikingly, both the degree of Mn-migration (δ) and the low-voltage discharge capacity decrease in a similar manner after annealing, unambiguously confirming that the extra lithiation at low voltages is triggered by the local cation disordering associated with Mn migration.

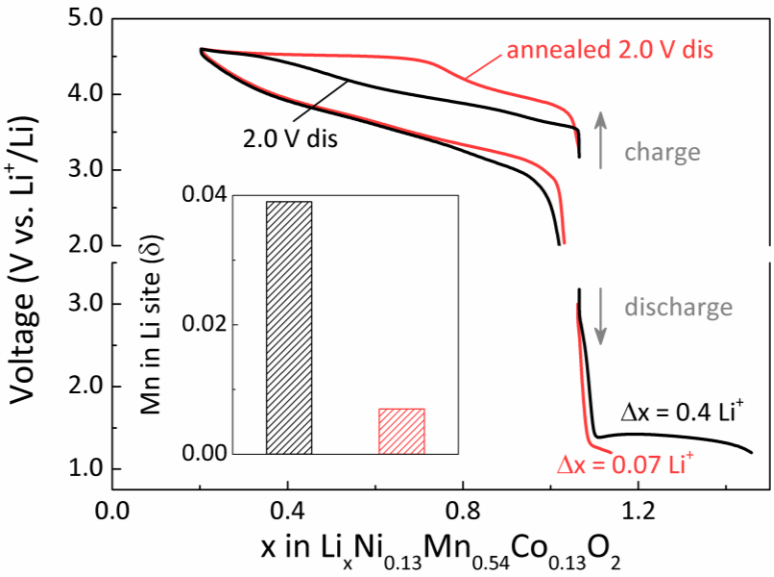

Figure III. 24 Voltage-composition profiles of the 2.0 V discharged sample before (black lines) and after (red lines) annealing. The cells were either directly started on charge to 4.6 V, or on discharge to 1.2 V, as indicated by the grey arrows. The inset shows the amount of Mn-migration (δ) in the 2.0 V discharged sample before (black column) and after (red column) annealing.

Having identified the source of this extra capacity, it pertains now to gain better insights into the origin of the large voltage drop (occurs at ca. x = 1.0) needed to insert the additional Li^+. The

possible electronic limitations across the conductive matrix in the electrode was excluded, since increasing the electrode carbon content from 20 wt.% to 40 wt.% did not alter the amplitude of voltage drop (Figure A. 3. 14). Galvanostatic intermittent titration technique (GITT) measurements, which combine current pulses and open-circuit sequences, were further performed to study the thermodynamic and kinetic features of the low-voltage discharge process (Figure III. 25). A large polarization, concomitant with the increase of Ohmic resistance, occurs before the overshoot (marks with black arrow in Figure III. 25), representing a slow kinetic process. On the contrary, a markedly lower open circuit voltage and small polarization was observed after the overshoot, implying a different reaction. The GITT results are in accordance with the previous *in-situ* XRD study, which demonstrating that the low-voltage discharge process involves two distinct regions separated by the voltage overshooting: first a solid-solution with a continuous evolution of the lattice parameters, followed by the growth of a new phase P" at the expense of the original phase P'. In the P" phase, which possesses higher Li content than that in the pristine material, Li^+ can be inserted into the tetrahedral sites in order to accommodate additional Li^+. This shift of Li^+ insertion site from octahedral to tetrahedral sites can accounts for the lowering of Li^+ insertion voltage.

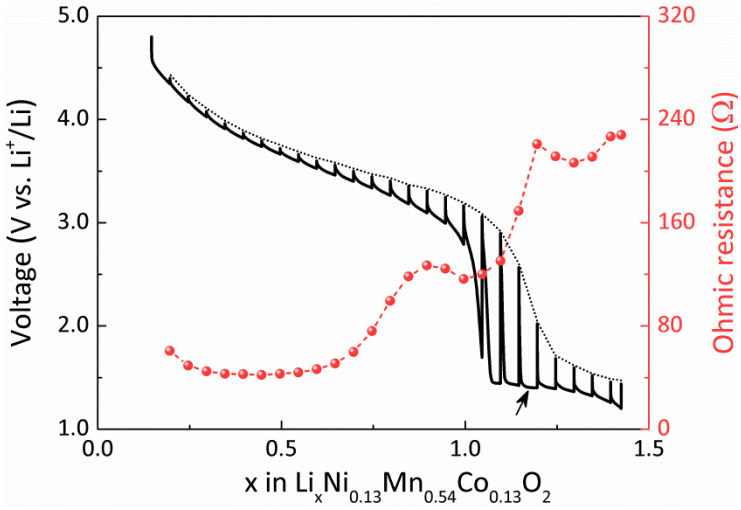

Figure III. 25 Galvanostatic intermittent titration technique (GITT, every Δx = 0.05) test of $Li_{1.2}Ni_{0.13}Mn_{0.54}Co_{0.13}O_2$ during the first discharge to 1.2 V after 4.8 V charge. The cell was cycled at C/5 rate, and the relaxing process was controlled by either $dV/dt \leq 0.01$ mV s^{-1} or time = 4 h. The Ohmic resistance was deduced from the voltage jump in a short time (1 s) after the application of the current pulse. The black arrow marks the voltage overshooting point.

The amplitude of the voltage drop can be reduced by either raising the operation temperature or decreasing the discharge current rate (Figure III. 26a), providing further evidence of the kinetic controlling voltage drop. Given that the part of low-voltage capacity before the overshoot is of kinetic origin, it should be able to be recovered by an additional constant voltage (CV) step. Indeed, by applying the CV hold at 2.0 V over 40 h until the current decays to nearly zero (~ 6 μA), we could succeed in intercalating more Li^+ until the Li content reaches ~ 1.14, the same value at which the voltage overshoot appears (Figure III. 26b). As the possible limitation of electron transport has already been excluded, and no phase transformation was observed by *in-situ* XRD before the overshoot, we can conclude that the voltage drop to be mainly caused by the sluggish Li^+ diffusion. Altogether, these results suggest that the part of low-voltage capacity before the overshoot is due to kinetic hindrance of the lithiation process, whereas the part after the overshoot is predominately of thermodynamic origin.

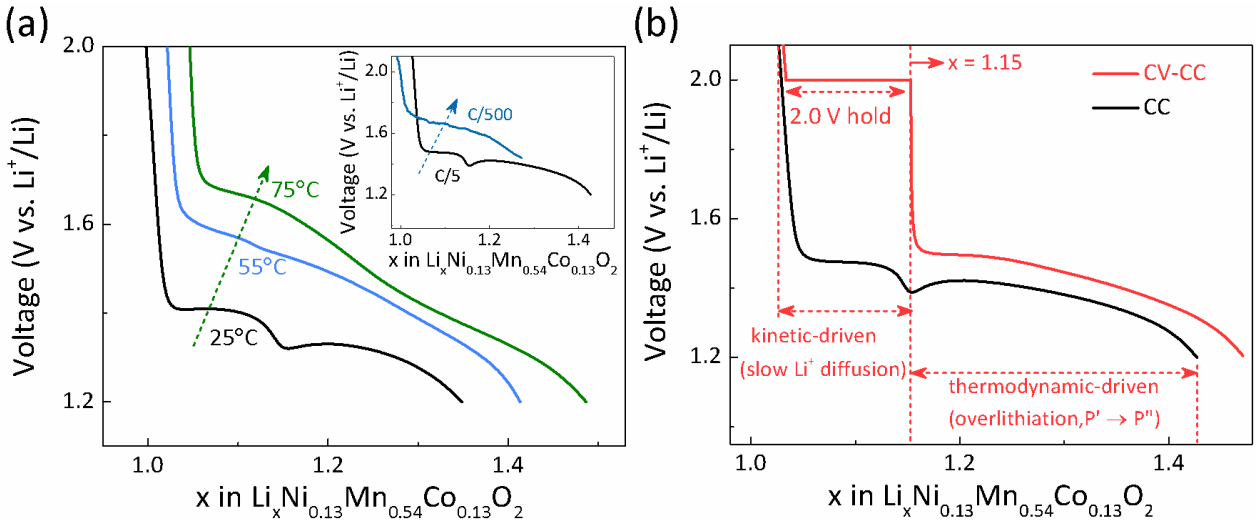

Figure III. 26 Voltage-composition profiles of $Li_{1.2}Ni_{0.13}Mn_{0.54}Co_{0.13}O_2$ in the low-voltage discharge region under various conditions, followed by the first charge to 4.8 V. (a) The cells were discharged with a CC protocol at various temperatures of 25 ℃ (black line), 55 ℃ (blue line) and 75 ℃ (green line). The inset shows the cells discharged at current rates of C/5 (black line) and C/500 (marine blue line). (b) The cells were discharged with either a constant current (CC, black line) protocol, or a constant current-constant voltage (CC-CV) protocol with the CV hold applied at 2.0 V (red line) over 40 h until the current decays to 6 μA.

The part of low-voltage capacity before the overshoot can also be considered in a cell that is cycled under normal condition, i.e., discharged to 2.0 V rather than to a voltage as low as 1.2 V. By applying an additional CV hold at 2.0 V, ~ 0.12 Li^+ could be recovered from the initial apparent Li^+ loss of ~ 0.17 Li^+, suggesting that a major part (ca. 70 %) of the first-cycle irreversible capacity observed in $Li_{1.2}Ni_{0.13}Mn_{0.54}Co_{0.13}O_2$ is due to kinetic inhibition and the 'real' (unrecoverable) irreversible capacity accounts for only ~ 0.05 Li^+ (Figure III. 27).

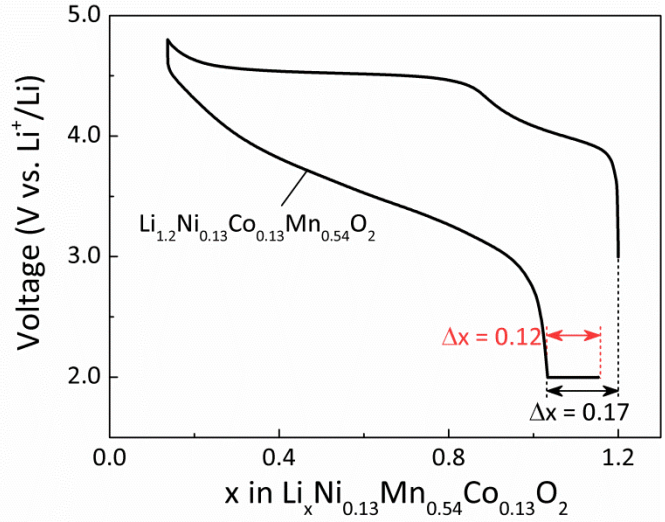

Figure III. 27 The first charge-discharge curves of $Li_{1.2}Ni_{0.13}Mn_{0.54}Co_{0.13}O_2$ cycled between 4.8 V and 2.0 V with an additional CV step at 2.0 V over 40 h until the current decays to 6 μA. During the CV step, ~ 0.12 Li^+ could be recovered from the initial apparent Li^+ loss of ~ 0.17 Li^+.

Next, to examine the change in the oxidation states of Ni, Co, and Mn during the low-voltage discharge process, *ex-situ* XAS measurements were carried out on the Rock beamline of SOLEIL synchrotron, France. The X-ray absorption near edge structure (XANES) spectra was normalized by Dr. A. Iadecola. Figure III. 28 compares the XANES spectra of the samples collected after 2.0 V, 1.4 V and 1.2 V discharge at the three transition-metal (Ni, Co, and Mn) K-edge. Ni K-edge XANES spectra of the three samples show almost no change (Figure III. 28a). In contrast, Mn and Co K-edge XANES spectra for the 1.4 V and 1.2 V discharged sample were observed at lower energies as compared to those for the 2.0 V discharged sample, indicating the concurrent reduction of Mn and Co (Figures III. 28b & 28c). These results unambiguously reveal that the extra lithiation at the low-voltage region is mainly charge compensated by cationic (Co and Mn) redox.

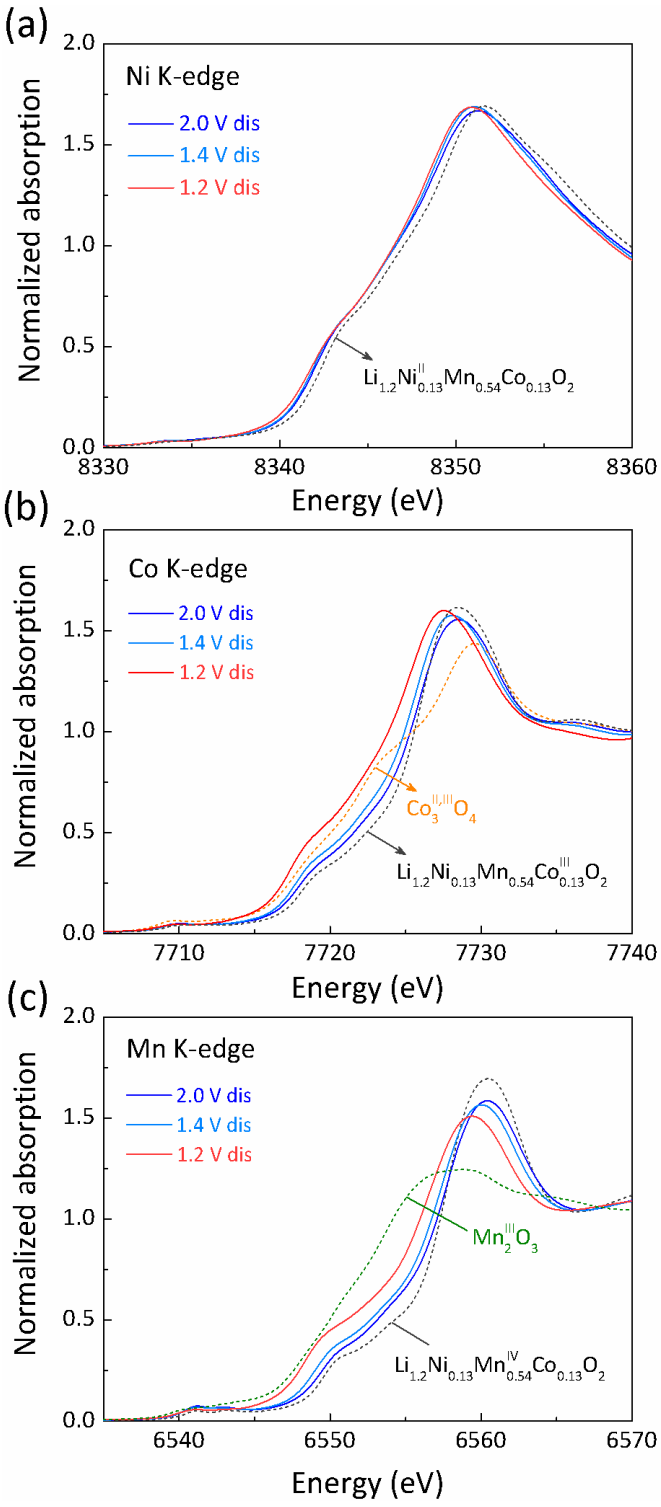

Figure III. 28 Normalized XANES spectra at the (a) Ni K-edge, (b) Co K-edge and (c) Mn K-edge for the samples collected after 2.0 V (blue line), 1.4 V (cyan line) and 1.2 V (red line) discharge. The spectra for $Li_{1.2}Ni_{0.13}Mn_{0.54}Co_{0.13}O_2$, Co_3O_4, and Mn_2O_3 are given as references.

Lastly, the electrochemical performance of $Li_{1.2}Ni_{0.13}Mn_{0.54}Co_{0.13}O_2$ involving the low-voltage discharge process was evaluated by charging several cells identically to 4.8 V, but varying their discharge cutoff voltage from 2.0 V to 1.4 V and to 1.2 V. As shown in Figure III. 29, ~ 1.3 Li^+ (403 mAh g^{-1}) can be reversibly uptaken and released upon discharging to 1.2 V, as compared to ~ 1.0 Li^+ (322 mAh g^{-1}) for 1.4 V discharge, and ~ 0.86 Li^+ (272 mAh g^{-1}) for 2.0 V discharge. Though most of the extra capacity is delivered at low potentials, the 48 % (for 1.2 V discharge) and 18 % (for 1.4 V discharge) gain in the discharge capacity represents 18 % and 7 % increase in the specific energy. Nevertheless, a faster capacity fading was observed during the subsequent cycles when discharging the cell to 1.2 V (Figure III. 30a). After 25 cycles, the discharge capacity decreases to ~ 281 mAh g^{-1} for the 1.2 V discharged cell, as compared to ~ 260 mAh g^{-1} for the 2.0 V discharged cell, leading to a similar value of specific energy (Figure III. 30c). Overall these results suggest that, application-wise, discharging to voltage as low as 1.2 V is not an effective strategy to improve the energy density of $Li_{1.2}Ni_{0.13}Mn_{0.54}Co_{0.13}O_2$ over the long term.

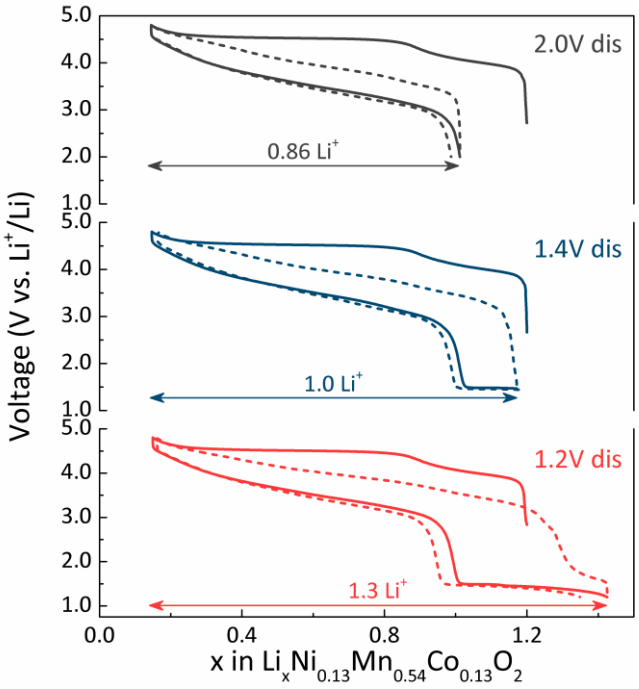

Figure III. 29 The first (solid lines) and second (dash lines) charge-discharge curves of $Li_{1.2}Ni_{0.13}Mn_{0.54}Co_{0.13}O_2$ charged to 4.8 V, while varying the discharge cutoff voltage from 2.0 V (black lines), 1.4 V (blue lines) and 1.2 V (red lines).

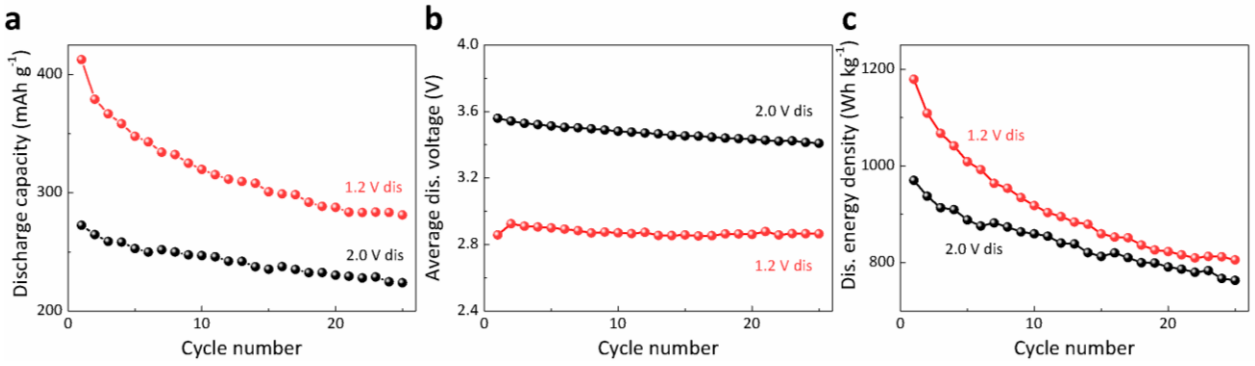

Figure III. 30 Retention profiles of the discharge capacity (a), the average discharge voltage (b), and the discharge energy density (c) of $Li_{1.2}Ni_{0.13}Mn_{0.54}Co_{0.13}O_2$ discharged to 2.0 V (black symbols) and 1.2 V (red symbols).

III. 3 Discussion and chapter conclusion

We have enlarged the cycling potential window for $Li_{1.2}Ni_{0.13}Mn_{0.54}Co_{0.13}O_2$ electrode to both high and low potentials, and unraveled novel structural evolution mechanisms that we discuss next by putting them into the context of numerous literature reports on this topic, to provide a more holistic comprehension of the electrochemically-driven structural evolution in Li-rich NMC materials.

Firstly, by applying a constant voltage step at 4.8 V, we could, for the first time, obtain a single fully charged phase A', thereby enabling its detailed structural characterization. Combing synchrotron X-ray and neutron diffraction, TEM, OEMS and ICP-OES, we have identified phase A' as a densified O3 bulk structure enlisting Mn migration into the interlayer octahedral sites, in contrast to previous reports in stating that it is a densified layer[48,179] or spinel-like structure[157] which grows only at the surface. Moreover, we have revealed that the formation of phase A' is caused by the conjoint removal of Li^+ and oxygen that creates both cationic and anionic vacancies. The cationic vacancies are partially refilled by TM cations causing their appearance in the octahedral interlayer sites and suppressing the "honeycomb" Li-M cation ordering. The anionic vacancies are refilled by their long range migration from the bulk to the surface with subsequent annihilation. Consequently, the M/O ratio increases leading to the structural densification.

Secondly, we demonstrated that a major part of the capacity loss during the first cycle is due to kinetic hindrance, and can be recovered by either applying a constant potential step or discharging to lower voltages. Note that the feasibility of recovering the irreversible capacity by pushing the low-voltage reduction is not specific to $Li_{1.2}Ni_{0.13}Mn_{0.54}Co_{0.13}O_2$. Indeed, by investigating the first-cycle coulombic efficiency of $LiNi_{1/3}Mn_{1/3}Co_{1/3}O_2$, Kasnatscheew *et al.* showed that a main part of the capacity loss is of kinetic origin and linked to sluggish Li^+ diffusion, therefore, they recommended applying a constant voltage step at the end of discharge to fill the remaining Li vacancies.[163] Similar conclusion has been reached by Zhou *et al.* when studying the $LiNi_{0.8}Mn_{0.1}Co_{0.1}O_2$ electrode.[180] Indeed, a drop of Li^+ diffusion coefficient at high state of discharge was commonly observed in many layered oxides,[30,164] and may be explained by i) the contraction of *c* lattice parameter typically occurring at high Li content ($x > 0.6$)[165,181]; and ii) the inhomogeneous lithiation leading to very high Li concentration (not enough vacancy) at the surface of the particles.[182]

Thirdly, using highly reductive conditions, we revealed the formation of a new discharged phase P'' that is responsible for an additional low-voltage capacity. By gradually varying the depth of charge from $\Delta x = 0.0$ (the pristine phase) to 0.4 (cationic redox region), and eventually to 0.6, 0.8 and 1.0 (anionic redox region), we further demonstrated that the appearance of phase P'' is directly linked to the necessity of triggering the oxygen redox activity on charge. The feasibility to inject additional Li^+ at potentials below 2.0 V has been reported in other Li-rich[177,178] and Li-stoichiometric[175,183] layered oxides. The overlithiation usually leads to the formation of a Li_2MO_2-type phase with $P\bar{3}m1$ structure, as confirmed by Robert *et al.*[175] Within the context of this study, we experimentally showed that some additional Li^+ could also be injected into $Li_{1.0}Ni_{0.33}Mn_{0.33}Co_{0.33}O_2$, when discharging directly the pristine material to 1.2 V (Figure A. 3. 15). On the contrary, what is unique about the $Li_{1.2}Ni_{0.13}Mn_{0.54}Co_{0.13}O_2$ phase is that i) extra Li^+ cannot be injected into the pristine phase by lowering the discharge voltage to 1.2 V (Figure A. 3. 16), ii) the low voltage electrochemical activity can only be activated when the compound has been charged sufficiently to trigger the oxygen redox process, and iii) the overlithiation does not lead to a O3 → 1T phase transition. At first, it could be argued that this specific behavior is associated with the presence of Li^+ ions within the MO_2 layers in $Li_{1.2}Ni_{0.13}Mn_{0.54}Co_{0.13}O_2$ that modifies the respective stability of the P' *vs* P'' phase. However, this does not hold as other pristine Li-rich layered oxides have equally shown the feasibility to reversibly uptake extra Li^+ ions ($Li_{2+x}IrO_3$,

$Li_{3+x}IrO_4$),[57,60] through an $R\bar{3}m$ to $P\bar{3}m1$ structural transition that doubles the number of available sites in the Li layers. A more reasonable explanation is rooted in the observed Mn-migration in $Li_{1.2}Ni_{0.13}Mn_{0.54}Co_{0.13}O_2$, triggered by the anionic redox activity, unbalancing the electrostatic interactions between the MO_2 layers together with Li inter-intra layer repartition. In addition, the presence of Mn ions at the interlayer Li sites could act as "pillar" to prevent the gliding of the layered planes which is needed to obtain the 1T structure as previously reported for Li_2NiO_2.[176]

Lastly, we designed a path to retrieve the Mn-migration in the discharged P' phase by mild-temperature annealing (> 250 ℃), as inspired by the work from Singer *et al.*[112] Indeed, the low-voltage discharge capacity vanishes in the same manner as the degree of Mn-migration, further confirming the correlation between the Mn-migration and the low-voltage redox activity. Moreover, the recovery of superstructure and likewise the original stair-case charge profile after the heat treatment, indicate that the cation disordering is decisive in transforming the stair-case charge to an S-shaped sloping discharge during the first electrochemical cycle. An obvious future direction to understand better the role of cation migration (structural disordering) on the electrochemical properties of $Li_{1.2}Ni_{0.13}Mn_{0.54}Co_{0.13}O_2$ resides in assembling solid state Li batteries that can be operated at various high temperatures.

Application-wise, although we have showed the positive effects of recovering part of the first-cycle irreversible capacity loss, neither reaching the full formation of the P' phase nor the exploitation of the low voltage activity provides substantial improvement regarding the energy density, whilst retains the voltage fade and hysteresis pertaining to $Li_{1.2}Ni_{0.13}Mn_{0.54}Co_{0.13}O_2$.

Returning to the electrochemically-driven structural evolution of $Li_{1.2}Ni_{0.13}Mn_{0.54}Co_{0.13}O_2$, we propose the following structure evolution sequence for the first full cycle of $Li_{1.2}Ni_{0.13}Mn_{0.54}Co_{0.13}O_2$ (Figure III. 31). First, the oxidation of the Ni^{2+} and Co^{3+} cations is occurring up to Δx of 0.4, followed by the oxidation of the oxygen anions that triggers Mn-migration until 4.6 V ($\Delta x < 1.0$). Afterwards, some Li^+ can still be removed concomitantly with O_2 evolution to reach nearly the fully delithiated phase, creating both cationic and anionic vacancies that are filled by migrated Mn ions, and eventually leading to a bulk densified phase A' ($\Delta x = 1.15$). Densification implies that the oxygen vacancies formed during the O_2 evolution stage migrate from bulk to the surface with subsequent annihilation that causes increasing of the M/O atomic ratio. A

pure phase A' can only be obtained when sufficient amount of Li^+ is removed and sufficient time is given for the migration of transition metals, which might explain why the phase A' was never reported before in a pure form. Upon discharge, the anionic and cationic network of the phase A' are conjointly reduced with only part of the migrated cations return to their initial positions, explaining that the discharge phase P' differs from the pristine phase, even after reaching a nearly full reduction by either applying a constant voltage step or discharging to lower voltages.

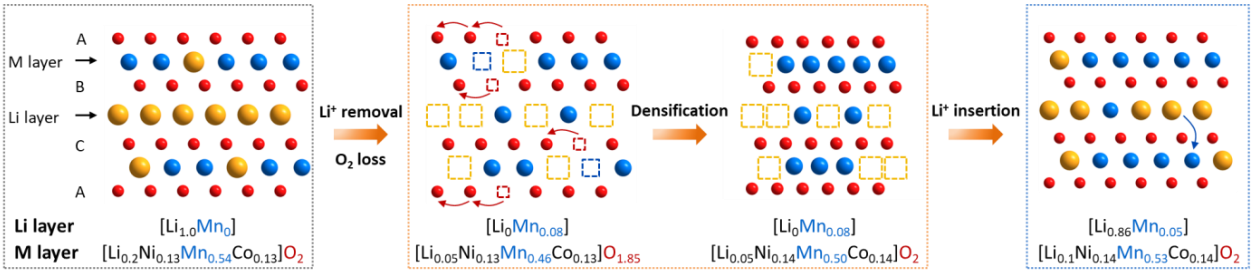

Figure III. 31 **Schematic of the A → A'→ P' phase transition.** Delithiation and oxygen evolution create vacancies in both cationic and anionic sublattices upon first charge above 4.6 V. The oxygen vacancies are refilled implying their long range migration from the bulk to the surface with subsequent annihilation. The vacant Li sites are partially refilled with the TM cations causing their appearance in the octahedral interlayer sites and suppressing the "honeycomb" Li-TM cation ordering. As a result, the TM/O ratio increases that is considered as "densification". During subsequent discharge, the TM cations partially move back to their original positions and the vacant cationic sites are filled with Li^+.

During the subsequent charge, phase P' releases Li^+ through a solid-solution process (Figure A. 3. 17), which differs from the two-phase process (A → A' phase transition) on the first charge, leading to the formation of phase A' at the end of second CC - CV charge. As was demonstrated by OEMS analysis, no O_2 evolves throughout the second CC - CV charge (Figure III. 32b), suggesting that although O_2 evolution is critical to the initial formation of phase A', once it forms, it can reversibly uptake and release Li^+ up to 26 cycles (the maximum number of cycle we have tried, Figure III. 32a) without the need for having more anionic vacancies, hence O_2 release.

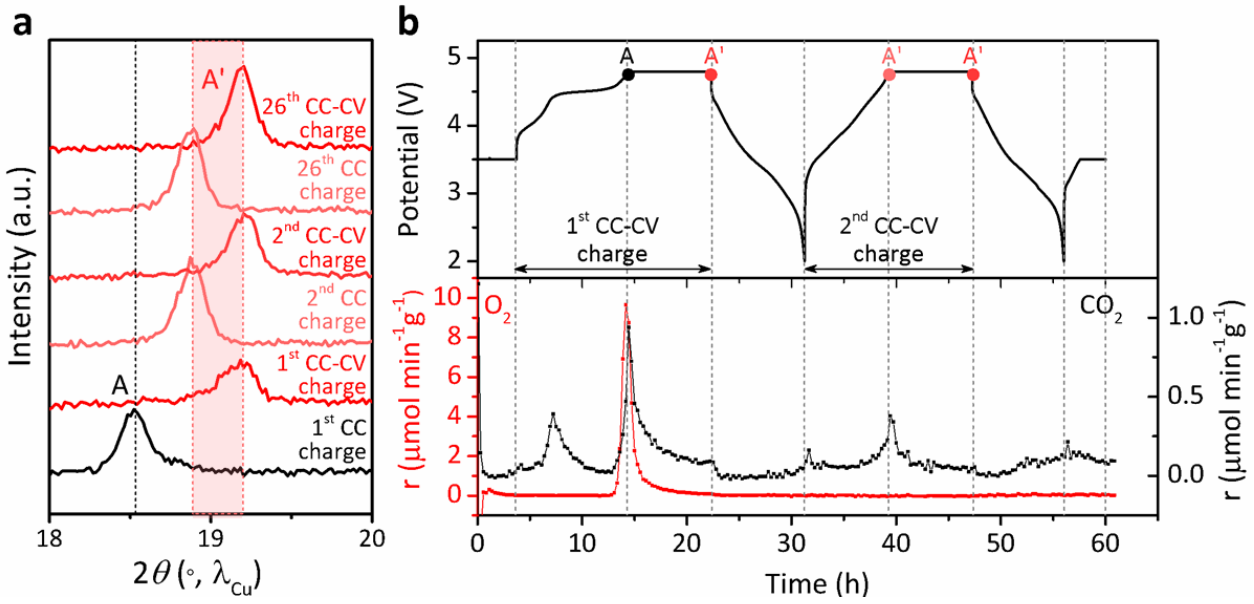

Figure III. 32 (a) Laboratory XRD patterns of $Li_{1.2}Ni_{0.13}Mn_{0.54}Co_{0.13}O_2$ collected at various state of charge in *in-situ* XRD cell which were cycled between 4.8 V and 2.0 V, with an intermediate CV step at 4.8 V for 5 h. The results reveal that phase A' was formed at the end of each CC-CV charge until the 26th cycle (the maximum number of cycle we have tried). (b) OEMS gas analysis during the first and second cycle of $Li_{1.2}Ni_{0.13}Mn_{0.54}Co_{0.13}O_2$. The cell has been cycled between 4.8 V and 2.0 V, with a CV step at 4.8 V for 8 h. O_2 (m/z = 32) and CO_2 (m/z = 44) ion currents were recorded and then converted to gas evolution rates. The voltage *vs* time curves is presented in the upper panel, and the evolved rates of O_2 (red line) and CO_2 (black line) in the units of μmol $min^{-1}g^{-1}$ are shown in the bottom panel. O_2 evolution was only observed at the first charge, whereas CO_2 continues to evolve at the second cycle.

In summary, the results demonstrate the fundamental benefit of operating a cell under harsh electrochemical conditions to deepen our understanding of the Li-rich NMC in terms of O_2 release, phase evolution, cation migration, and oxygen activity with the establishment of a few key correlations that could guide the design of Li-rich phases having greater stability against O_2 release or cation migration. However, a cure to circumvent the voltage decay is still waiting to be found.

Chapter IV Li-CO_2 battery: a new system for energy storage and CO_2 conversion

Chapter IV Li-CO_2 battery: a new system for energy storage and CO_2 conversion

IV. 1 Background and motivation

CO_2 has been recognized as one of the major greenhouse gas (GHG) that responsible for the global temperature increase. To alleviate the carbon emission, research is presently parted between two major focuses: i) CO_2 capture and sequestration in which major findings were obtained by mimicking natural photosynthetic processes or introducing new techniques, such as physical absorption and biological capture by microalgae[184,185] and ii) CO_2 utilization either by electrochemically reducing CO_2 into carbon-based fuels and feedstocks (e.g. carbon monoxide, ethylene and methanol)[186-188] or by transforming CO_2 into other useful compounds via chemical or electrochemical processes (e.g. methane, formic acid, C_2-C_4 olefins, C_5-C_{11} hydrocarbons and oxalate).[189-193] Following the second approach, the activation of CO_2 is unfortunately a challenging task because of the inertness of CO_2. The difficulties thus reside in finding catalysts that are selective and are capable of mediating multiple electron and proton transfer at relatively low overpotentials (i.e., low energy input). Within this context, the battery community has recently proposed an alternative strategy for CO_2 conversion by introducing CO_2 into battery systems, aiming to transform this detrimental greenhouse gas into value-added Li_2CO_3 which can then be used, for instance, as the precursor for synthesizing Li-ion positive electrode materials. The concept of CO_2 battery has the potential not just to mitigate the atmospheric CO_2 concentration back to its pre-industrial level, but more importantly to use CO_2 as a renewable energy carrier. In such a scheme, CO_2 either serves as a gas additive, i.e. Li-O_2/CO_2 battery which involves the chemical reaction between CO_2 and superoxide resulting from the electrochemical reduction of oxygen;[102] or used as the sole reactant, i.e., the "real" Li-CO_2 battery.[194]

On the other hand, as previously mentioned in Chapter I. 3, despite the significant development achieved so far in Li-ion batteries, their energy storage capacities are far from satisfying the energy demands of model society. In fact, even with the state-of-art Li-rich NMC positive electrodes, possibilities for Li-ion battery to achieve the 2025 targets of automotive market rely on further improvements in cyclability, positive electrode loading and negative electrode

performance.[25] Therefore, new energy storage systems such as Li-O_2 battery has been intensively studied since the first report by Jiang *et al.* in 1996, owing to its superior theoretical energy density.[195,196] However, multiple issues still prevent Li-O_2 battery from making substantive progresses. One critical barrier is that Li-O_2 battery is very sensitive to atmospheric pollutions such as CO_2 or moisture traces leading to Li_2CO_3 or LiOH deposition.[81,100,197,198] Another important issue concerns the nucleophilic superoxide radicals, the main intermediates during discharge, which tends to attack organic solvents[199-203] and carbon electrodes[204-206] to form Li_2CO_3, resulting in the passivation of the electrode surface and hence the premature cell death. The decomposition of Li_2CO_3 is incomplete on subsequent charge and only occurs at very high potentials leading to relevant decomposition of cell components ($E° = 3.82$ V *vs* Li/Li^+ for the reaction $Li_2CO_3 \rightarrow CO_2 + ½\ O_2 + 2\ Li^+ + 2\ e^-$, [207,208] and with a practical potential of > 4.3 *vs* Li/Li^+ as observed in the literatures and computed by first-principles calculation).[209,210] Moreover, the CO_2 released from Li_2CO_3 decomposition chemically reacts with Li_2O_2, the ultimate discharge product of Li-O_2 battery, in turn to form more Li_2CO_3 and further deteriorates the cycling performance. Last but not least, the chemical reactivity of superoxide radical with CO_2 dissolved in aprotic solvents has also been reported to potentially alter the discharge products.[211,212] In light of the multifaceted role played by CO_2 on Li-O_2 electrochemistry, it is therefore essential to provide a comprehensive understanding about the interplay between CO_2 and all the intermediates or final products formed in Li-O_2 battery (i.e., Li^+, superoxide radical, Li_2O_2).

This chapter will be divided into two parts. The first part (IV. 2) will focus on the fundamental understanding about the formation mechanism of Li_2CO_3 in Li-O_2/CO_2 batteries and how the electrolyte properties dictate the reaction pathway, the morphology of Li_2CO_3 and the battery performances. The second part (IV. 3) will demonstrate a mediated Li-CO_2 battery based on quinone derivatives. A series of quinone derivatives will be surveyed in order to reveal the correlation between the molecular structure of quinones and their affinity towards CO_2. In addition, the effect of cations and solvents on the catalytic reduction of CO_2 by quinone derivatives will be discussed.

IV. 2 Li−O_2/CO_2 batteries: CO_2 conversion via electrogenerated superoxide ($O_2^{\bullet-}$)

IV. 2. 1 Introduction

Similar to Li-O_2 battery, a typical Li-O_2/CO_2 battery which can also be intuitively viewed as Li-O_2 battery with CO_2 as gas additive consists of a metallic lithium negative electrode, a separator soaked with organic electrolyte and a porous carbon matrix for accommodating the discharge product (Figure IV. 1). As their names suggest, the notable difference between Li-O_2 battery and Li-O_2/CO_2 battery is the gaseous reactant, resulting in different discharge products with Li_2O_2 for the former while Li_2CO_3 is formed for the latter.

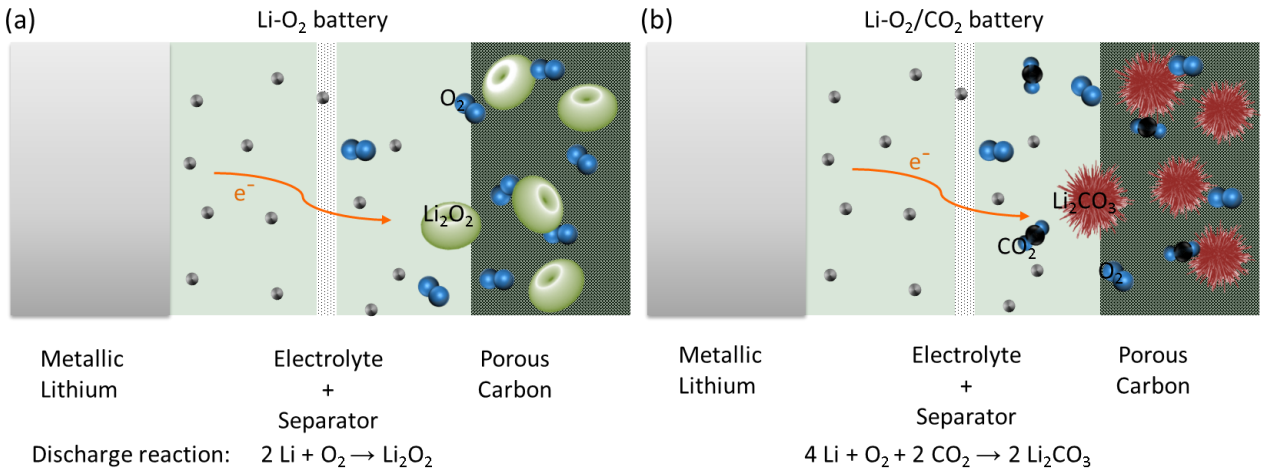

Figure IV. 1 Schematic illustration of (a) Li-O_2 battery and (b) Li-O_2/CO_2 battery.

First proposed by Albertus *et al.* in 2010,[165] the Li-O_2/CO_2 battery is still in its infancy with several fundamental questions remaining unanswered. Primary Li-O_2/CO_2 (1:1 *v*/*v*) batteries were demonstrated using 1 M lithium bis(trifluoromethanesulfonyl)imide (LiTFSI) in a mixture of ethylene carbonate and diethyl carbonate (3:7 *v*/*v*) as electrolytes, while Liu *et al.* argued that Li-O_2/CO_2 (2:1 *v*/*v*) batteries can operate reversibly when lithium triflate-tetraglyme was used as electrolytes.[213] This controversy led to the first question: what is the role of the electrolyte and why is it so critical for the rechargeability of Li-CO_2/O_2 battery? Lim *et al.* further suggested that the solvents can effectively alter the discharge reaction pathways and eventually change the final discharge product from pure Li_2CO_3 in high DN solvent (DMSO) to a mixture of Li_2O_2 and Li_2CO_3

in low DN solvent (DME).[214] Moreover, the solvent seems to affect the discharge capacity of Li-O_2/CO_2 battery. Starting from Takechi *et al.*'s work which showed an increased discharge capacity in the presence of CO_2 using carbonate electrolytes.[102] Different results were later reported with comparable discharge capacity obtained when using DMSO electrolyte while a smaller discharge capacity was obtained using DME electrolyte.[214] Although several possibilities are still largely debated, such as i) the low concentrations of CO_2 which can block the surface-active nucleation sites of Li_2O_2[100], ii) the increased electronic conductivity of Li_2CO_3 through O_2-induced morphology change,[198] and iii) increased electronic conductivity of the discharge product due to the favorable electron polaron hopping within the Li_2O_2 part of the Li_2O_2@Li_2CO_3 interface,[215] these rather contradicting results emphasized the important role played by the solvents.[214] Another critical issue concerns the discharge reaction mechanism, more specifically, whether there is a direct electrochemical reduction of CO_2 in Li-O_2/CO_2 battery. While one may expect a straightforward answer to this question by cycling batteries in pure CO_2 atmosphere (termed as Li-CO_2 battery hereinafter), nevertheless, discrepancy exists in the literatures with Takechi *et al.* showing very limited discharge capacity of 66 mAh g^{-1} for Li-CO_2 battery,[102] whereas Liu *et al.* reported reversible Li-CO_2 battery with a discharge capacity of ~ 1000 mAh g^{-1} and attributed this improvement to the use of glyme electrolyte.[213]

Aware of the important role played by the electrolytes in the electrochemical properties of Li-O_2/CO_2 batteries, we therefore decided to embark into a detailed electrochemical study on the discharge processes for Li-O_2/CO_2 (7:3 *v*/*v*) batteries using various solvents. Doing so, we aim (1) to provide an overall mechanistic image about the discharge reaction mechanism, (2) to identify the dominant electrolyte property which governs the reaction route, (3) to reveal how the capacity and the morphology of final product will be modified depending on the solvent used and also (4) to evaluate the rechargeability of Li-O_2/CO_2 battery. Dimethyl sulfoxide (DMSO), 1, 2-dimethoxyethane (DME) and acetonitrile (MeCN) were chosen for the initial evaluation, since they have different DN but DMSO and MeCN have similar acceptor number (AN) and different dielectric strength (ε) while DME alone has significantly smaller ε (Table IV. 1). Thus comparing the results obtained with these solvents should help us in identifying which parameter of the solvent, DN, AN, or ε, dictates the discharge reaction routes.

Table IV. 1 Summary of the intrinsic physical and chemical properties of all the solvents investigated in this work. Donor number, acceptor number, solubility data and diffusion coefficients of oxygen and carbon dioxide were collected from literatures[84,216-218] and the conductivity values were experimentally determined using 0.1 M $LiClO_4$ as the supporting salt.

	ε (25℃)	DN	AN	O_2 solubility [mmol]	CO_2 solubility [mmol]	10^5*Do_2 [cm^2/s]	10^5*Dco_2 [cm^2/s]	Conductivity [mS/cm]	Viscosity η [217]
DMSO	48.0	29.8	19.3	2.1	125	2.2±0.4	1.02±0.1	2.72	1.948
DME	7.2	24.0	10.2	10.1±0.3	NA	6.0±0.5	NA	0.22	0.46
MeCN	36.64	14.1	18.9	8.1	280	11±1.2	38.3±1.1	9.88	0.361

Considering the complexity of the Li-O_2/CO_2 system with all the possible interactions among its reactants, electrolytes and intermediates, for the sake of clarity, various possible discharge paths based on the previous knowledge in the literatures[102,211,217,219,220] as well as their establishments in this work, are shown in Scheme IV. 1.[151]

Scheme IV. 1 Survey of the most likely reaction paths from the various scenarios formerly proposed in the literatures and their establishment in the present work.

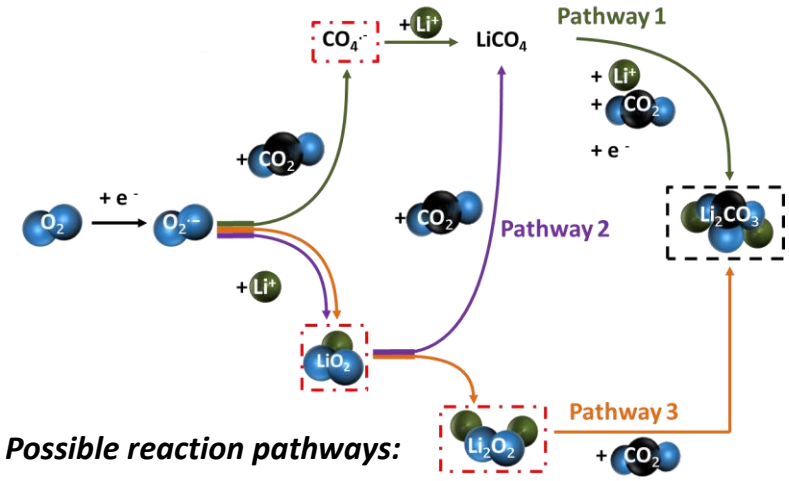

Possible reaction pathways:

Pathway 1:

$O_2 + e^- \longrightarrow O_2^{\cdot-}$ (1.1)

$O_2^{\cdot-} + CO_2 \longrightarrow CO_4^{\cdot-}$ (1.2)

$Li^+ + CO_4^{\cdot-} \longrightarrow LiCO_4$ (1.3)

$LiCO_4 + 3Li^+ + CO_2 + 3e^- \longrightarrow 2Li_2CO_3$ (1.5)

Overall:

$4Li^+ + O_2 + 2CO_2 + 4e^- \longrightarrow 2Li_2CO_3$ (1.6)

Pathway 2:

$O_2 + e^- \longrightarrow O_2^{\cdot-}$

$O_2^{\cdot-} + Li^+ \longrightarrow LiO_2$ (1.4)

$LiO_2 + CO_2 \longrightarrow LiCO_4$ (1.7)

$LiCO_4 + 3Li^+ + CO_2 + 3e^- \longrightarrow 2Li_2CO_3$

Pathway 3:

$O_2 + e^- \longrightarrow O_2^{\cdot-}$

$O_2^{\cdot-} + Li^+ \longrightarrow LiO_2$

$2LiO_2 \longrightarrow 2Li_2O_2 + O_2$ (1.8)

$2Li_2O_2 + 2CO_2 \longrightarrow 2Li_2CO_3 + O_2$ (1.9) (Chemical reaction)

IV. 2. 2 Results and discussion

Aware of the fact that CO_2 is more soluble in organic solvents than O_2 (125 ± 13 mM for CO_2 and 2.1 mM for O_2 in DMSO, for instance),[217] together with the aforementioned controversy over direct electrochemical reduction of CO_2 in Li-CO_2 battery and its possible dependence on the nature of solvents and electrodes used, we therefore first explore the electrochemical activity of Li^+ with CO_2 alone on a glassy carbon electrode (GCE) before to add O_2 to the system. Similar cyclic voltammograms were obtained for CO_2- and with Ar- (inert gas) saturated electrolytes (Figure IV. 2), suggesting that CO_2 cannot be electrochemically reduced in the potential range of Li-CO_2 battery, namely 2 – 4.5 V *vs* Li^+/Li, irrespective of the solvents used (DME, DMSO or MeCN). These results are in good agreement with the fact that, injecting an electron into the lowest unoccupied molecular orbital (LUMO) of the linear CO_2 molecule to form $CO_2^{\bullet-}$ requires a very low potential (high energy) in aprotic solvents without efficient catalyst.[217,221] Hence, the direct

electrochemical reduction of CO_2 can practically be neglected in this work. To further confirm this, Li-CO_2 cells were tested with 0.1 M $LiClO_4$ in both DMSO- and DME- based electrolytes using carbon super P (Csp) electrodes. In agreement with the previous CV results, when using a cut-off voltage of 2 V *vs* Li^+/Li, CO_2 cells delivered very small capacity (Figures IV. 3a & 3c, ~ 100 mAh g^{-1} DMSO, ~ 10 mAh g^{-1} in DME) associated with very limited gas consumption (Figures IV. 3b & 3d). Further decreasing the cut-off voltage to 1 V (a voltage in which DMSO is unstable as can be seen from the cells discharged in argon (Figures A. 4. 1e & 1f) as well as observing the characteristic "yellow" color found in the separators (Figure A. 4. 2)), a gas consumption corresponding to 4 e^- / mole of gas is measured for DMSO under pure CO_2 (Figure A. 4. 1d). Knowing that the S=O double bond of DMSO can be reduced; one can tentatively assign this reaction to the nucleophilic attack of reduced DMSO to CO_2. Moreover, bearing in mind that successful Na-CO_2 cells were also been reported in the literature,[222] we discharged cells in pure CO_2 with various Na^+-based electrolytes in order to examine the cation effect. Once again, a very limited capacity (less than 5 mAh g^{-1}) was obtained, either with Csp or with gas diffusion layer (GDL) electrodes (Figure A. 4. 3). These results are surprisingly in contradiction with previous works[213,222-224] and indicate that, in the absence of O_2 and under the conditions that allows to reversibly cycle Li-O_2 cells at limited capacity of 1000 mAh g^{-1} or to discharge Na-O_2 cells,[127,225] CO_2 cannot be electrochemically reduced and Li-CO_2 cells deliver almost no discharge capacity.

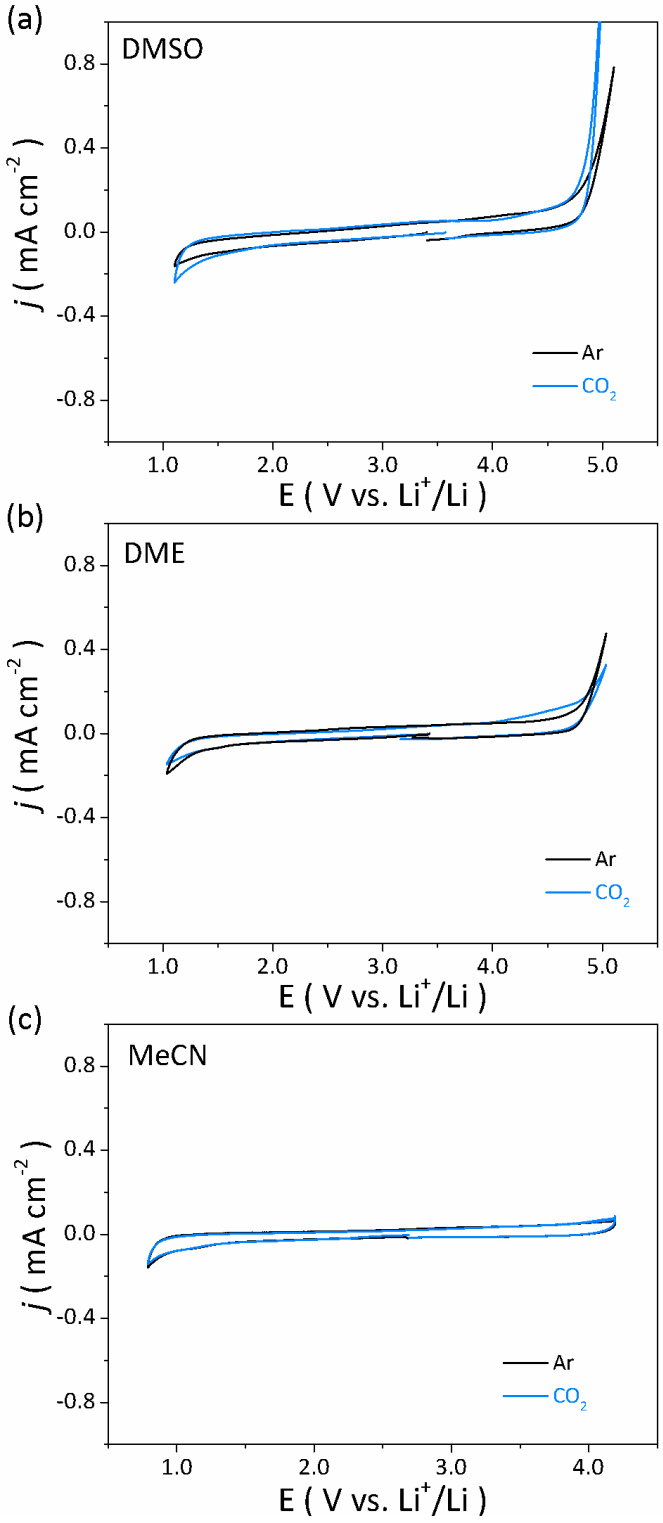

Figure IV. 2 Cyclic voltammograms at 50 mV s^{-1} for CO_2- (blue curves) and Ar- (black curves) saturated (a) DMSO, (b) DME and (c) MeCN. 0.1 M $LiClO_4$ was used as supporting salt in all the solvents to increase the conductivity.

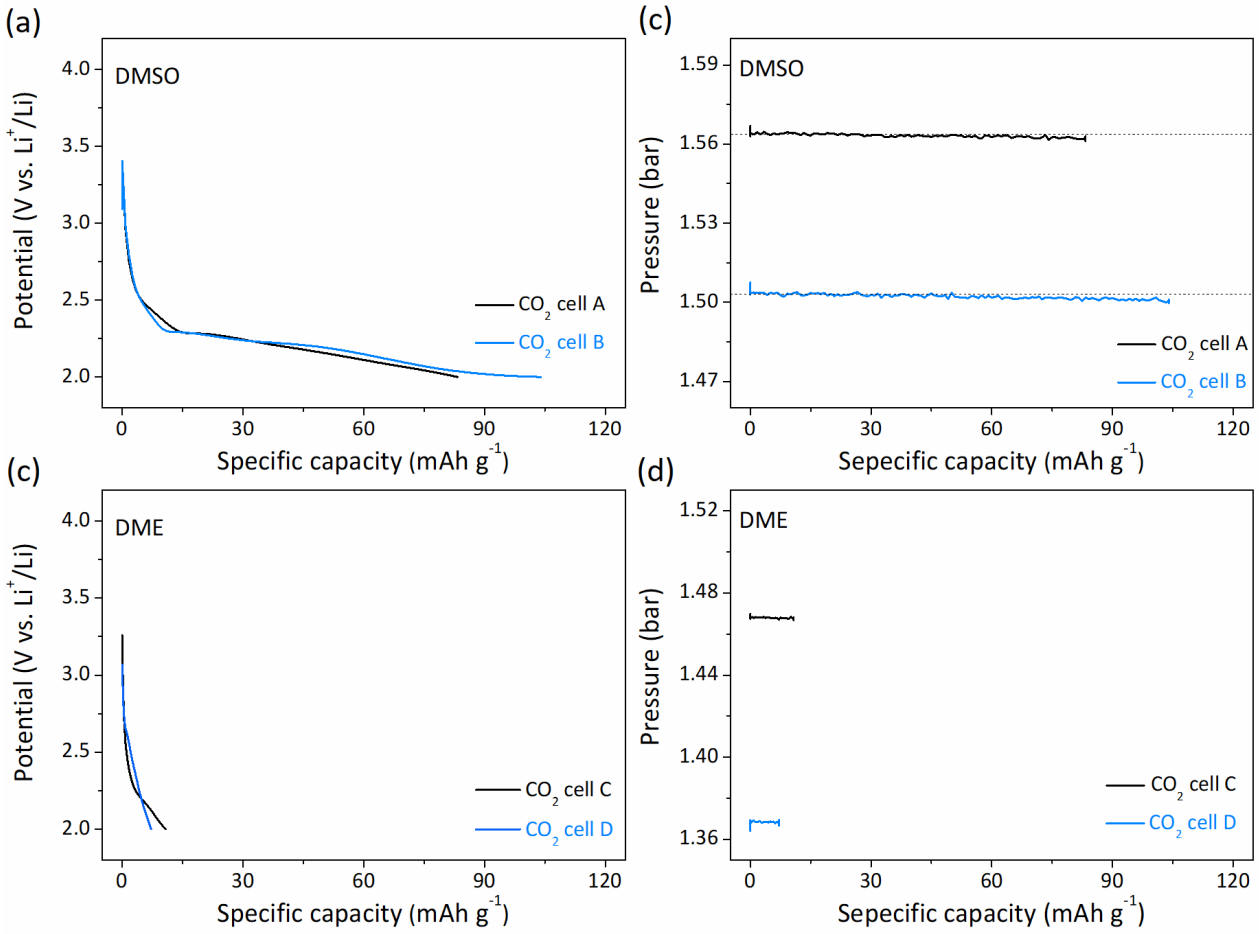

Figure IV. 3 (a) Discharge curves and (b) pressure change of Li-CO_2 batteries using 0.1 M $LiClO_4$/DMSO as electrolyte, at a current density of 100 mA g^{-1}; and using 0.1 M $LiClO_4$/DME as electrolyte, at a current density of 50 mA g^{-1} in (c) and (d); black curve and blue curve are representative of two cells measured under the same condition.

Having established that CO_2 is inert when limiting the potential range and under these conditions, CVs were then performed with TBA^+ salt to explore the electrochemical behavior of O_2/CO_2 gas mixture and compared with pure O_2. As seen in Figure IV. 4, a one electron reduction of oxygen to superoxide species (cathodic scan) followed by the reoxidation of the latter (anodic scan) is observed in pure O_2-saturated DMSO, DME and MeCN (black curves), as already largely reported in the literatures.[82,84,216] Switching to O_2/CO_2-saturated electrolytes, the same reduction peak is observed (blue curves) regardless of the solvents, demonstrating that the first step of the reaction is the formation of superoxide species (Scheme IV. 1, equation (1.1)). It should be noted that the reoxidation peak of superoxide was totally 'suppressed' (titrated) under O_2/CO_2,

demonstrating that all the generated superoxide species had fully reacted with CO_2 to form the $CO_4^{\bullet-}$ intermediates that cannot be oxidized back.[211] It is noteworthy that this strong reactivity between $O_2^{\bullet-}$ and CO_2 was observed in all the three solvents herein studied. This result indicates that the stability of the TBA^+-$O_2^{\bullet-}$ complex formed upon reduction is not sufficient to stabilize the superoxide species and to prevent its nucleophilic attack on CO_2 to form $CO_4^{\bullet-}$.

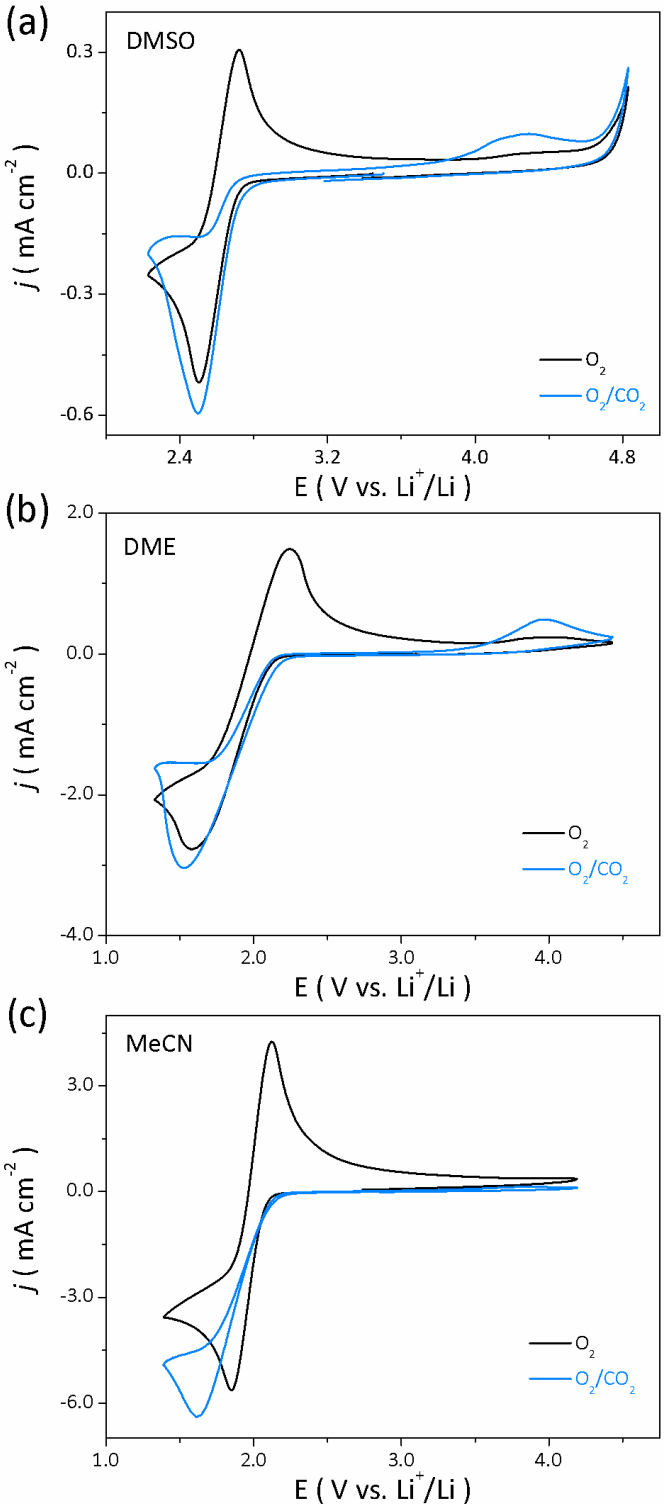

Figure IV. 4 Cyclic voltammetry curves at 50 mV s^{-1} for O_2-saturated (black curves) and O_2/CO_2-saturated (blue curves) (a) 0.1 M $TBAPF_6$/DMSO, (b) 0.1 M TBATFSI/DME and (c) 0.1 M $TBAPF_6$/MeCN.

After observing that all the superoxide species generated during reduction in O_2/CO_2-saturated electrolytes readily react with CO_2 when using TBA^+ as a salt, a legitimate question concerns the relative reactivity of the superoxide species towards Li^+ compared to CO_2. For that, CV measurements were performed with O_2/CO_2-saturated electrolytes using Li^+ salt and were compared with the previously discussed results obtained with TBA^+ salt (Figure IV. 5). This is the first report of O_2/CO_2 interaction in presence of Li^+ to the best of our knowledge. Beginning with DMSO (Figure IV. 5a), the onset reduction potential in O_2/CO_2 mixture is ~ 0.1 V higher than the onset potential measured in pure O_2. This observation indicates that the reaction of $CO_4^{\bullet -}$ with Li^+ forms an intermediate which is thermodynamically more stable than lithium superoxide intermediates in DMSO. Thus it is reasonable to write the first two reaction steps in DMSO as equation (1.2) in Scheme IV. 1 followed by the reaction of $CO_4^{\bullet -}$ with Li^+ (Scheme IV. 1, equation (1.3)). A positive shift was also observed when comparing CV results obtained in O_2/CO_2-saturated Li^+- and TBA^+-based electrolytes (Figure IV. 6a), demonstrating that the formation of $LiCO_4$ is thermodynamically more favorable and governs the reduction potential in DMSO. In light of this observation, it is interesting to reexamine the results obtained in O_2-saturated DMSO where no significant shift from TBA^+ to Li^+ was observed (Figure A. 4. 4). We can therefore conclude that the stabilization of Li^+ by DMSO is sufficiently strong to prevent the early formation of lithium superoxide (Scheme IV. 1, equation (1.4)), hence enabling the formation of $LiCO_4$ which is thermodynamically more favored (Scheme IV. 1, equation (1.3). During the positive scan, no current response was detected until at very high potential in O_2/CO_2-saturated DMSO in contrary to pure O_2 (Figure IV. 5a). This different oxidation behavior suggests that, instead of Li_2O_2, Li_2CO_3 which shows an oxidation potential of about 3.82 V *vs* Li^+/Li is probably formed from a subsequent reduction of the $LiCO_4$ intermediate during the reduction process.[209] Moreover, the greater reactivity of $CO_4^{\bullet -}$ intermediate when compared to $O_2^{\bullet -}$ is further seen by the fact that it cannot be reversibly oxidized in TBA^+-containing solution, indicating a possible reaction with the solvent (Figures IV. 4a & 6a). Therefore, in light of the increasing instability of high DN solvent towards $O_2^{\bullet -}$ as it has been seen for Li-O_2 batteries, one can expect even more limited stability of high DN solvents towards $CO_4^{\bullet -}$ radicals when used in Li-O_2/CO_2 batteries.[226,227] Switching to DME and MeCN, notably similar onset reduction potentials were observed in both Li^+-O_2 and Li^+-O_2/CO_2 systems (Figure IV. 5b & 5c), implying that, unlike for DMSO, the step that governs the onset potential is the same in O_2/CO_2 mixture as in pure O_2, namely the formation of lithium superoxide (Scheme IV. 1, equation (1.4)). Note that significantly different $O_2^{\bullet -}$ reaction pathways were found

for DMSO and MeCN, despite MeCN share the similar values of AN and ε with DMSO, we can therefore excludes AN and ε but identify DN as the most important parameter governing the reaction routes in Li-O_2/CO_2 batteries. The effect of DN is further supported by the fact that similar reduction potentials were measured for other low DN solvents such as diethylene glycol dimethyl ether (DGME, DN = 18) and tetraethylene glycol dimethyl ether (TGME, DN = 12) glymes (Figure A. 4. 5).

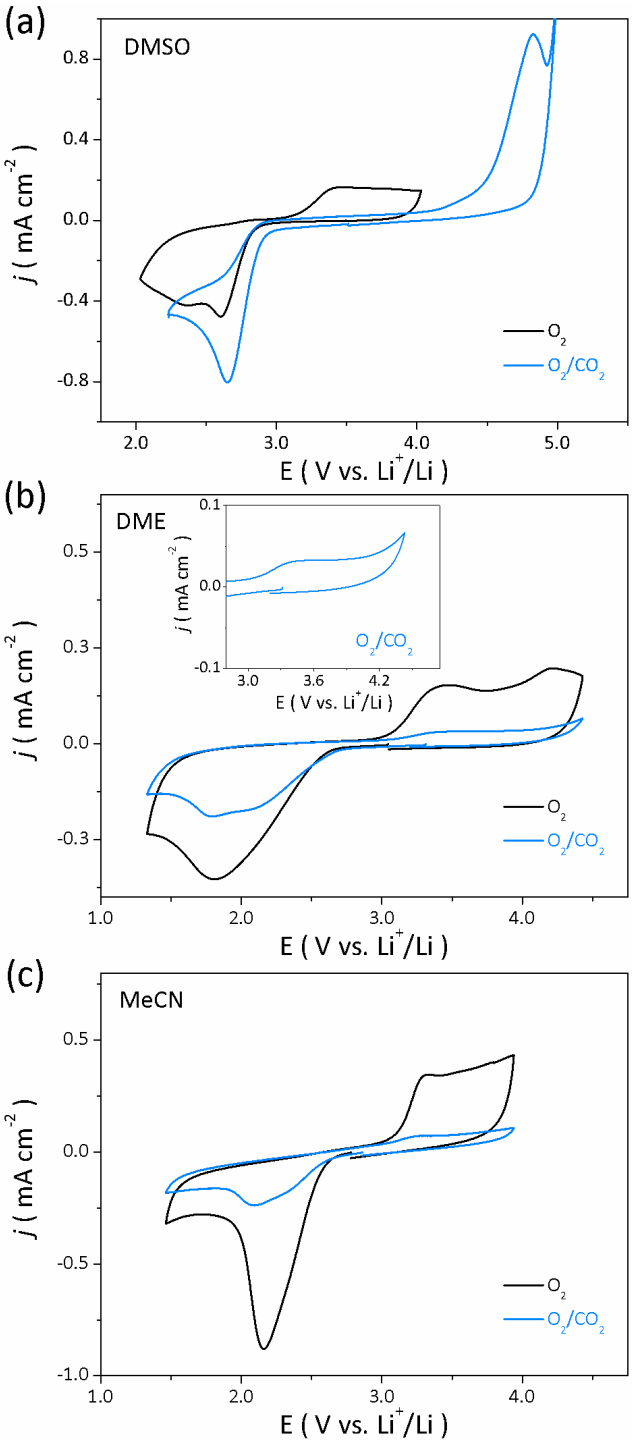

Figure IV. 5 Cyclic voltammetry curves at 50 mV s^{-1} for O_2-saturated (black curves) and O_2/CO_2-saturated (blue curves) (a) 0.1 M $LiClO_4$/DMSO, (b) 0.1 M $LiClO_4$/DME and (c) 0.1 M $LiClO_4$/MeCN. Inset figure in (b) is the zoom image for the cyclic voltammetry curve of O_2/CO_2-saturated 0.1 M $LiClO_4$/DME above 2.8 V *vs* Li/Li^+.

Our results highlight the clear difference in reactivity of $O_2^{\bullet -}$ towards CO_2 and Li^+ in DMSO (Scheme IV. 1, equation (1.2)) and in DME and MeCN (Scheme IV. 1, equation (1.4)), which is consistent with the DFT calculations reported by Lim *et al.*.[214] Specifically, a strong coordination shell will form between Li^+ and the solvent molecules in a high DN solvent like DMSO,[82,85,214,228] pushing the reaction towards the nucleophilic attack of $O_2^{\bullet -}$ with CO_2 instead of Li^+. In contrary, the Li^+ stabilization is weaker for DME and MeCN and therefore $O_2^{\bullet -}$ reacts preferentially with Li^+ rather than with the neutral dissolved CO_2. Finally, even though DMSO possesses large acceptor and donor numbers compared to DME (AN = 19.3 and DN = 29.8 for DMSO, AN = 10.2 and DN = 24 for DME), it is not enough to sufficiently stabilize $CO_4^{\bullet -}$ and to prevent its reaction with Li^+. These different pathways are summarized in Scheme IV. 1. However, at this stage of the study, one cannot distinguish for DME between two different pathways: one involving the electrochemical formation of Li_2CO_3 from lithium superoxide (pathway 2 in Scheme IV. 1) and one involving the chemical reaction of Li_2O_2 with CO_2 (pathway 3 in Scheme IV. 1), this will be discussed later.

Another interesting result was obtained when comparing the reduction currents measured in O_2/CO_2-saturated Li^+- and TBA^+-based electrolytes. For DMSO, only slightly smaller reduction currents were measured in Li^+- with respect to TBA^+ - based electrolyte (Figure IV. 6a). On the contrary, significantly smaller reduction currents were measured in Li^+-based DME and MeCN electrolytes compared to their TBA^+ counterparts (Figure IV. 6b & 6c), suggesting a faster blockage of electrode surface in Li^+-containing electrolytes of DME and MeCN than in DMSO. This point will also be discussed in more details later on in this chapter.

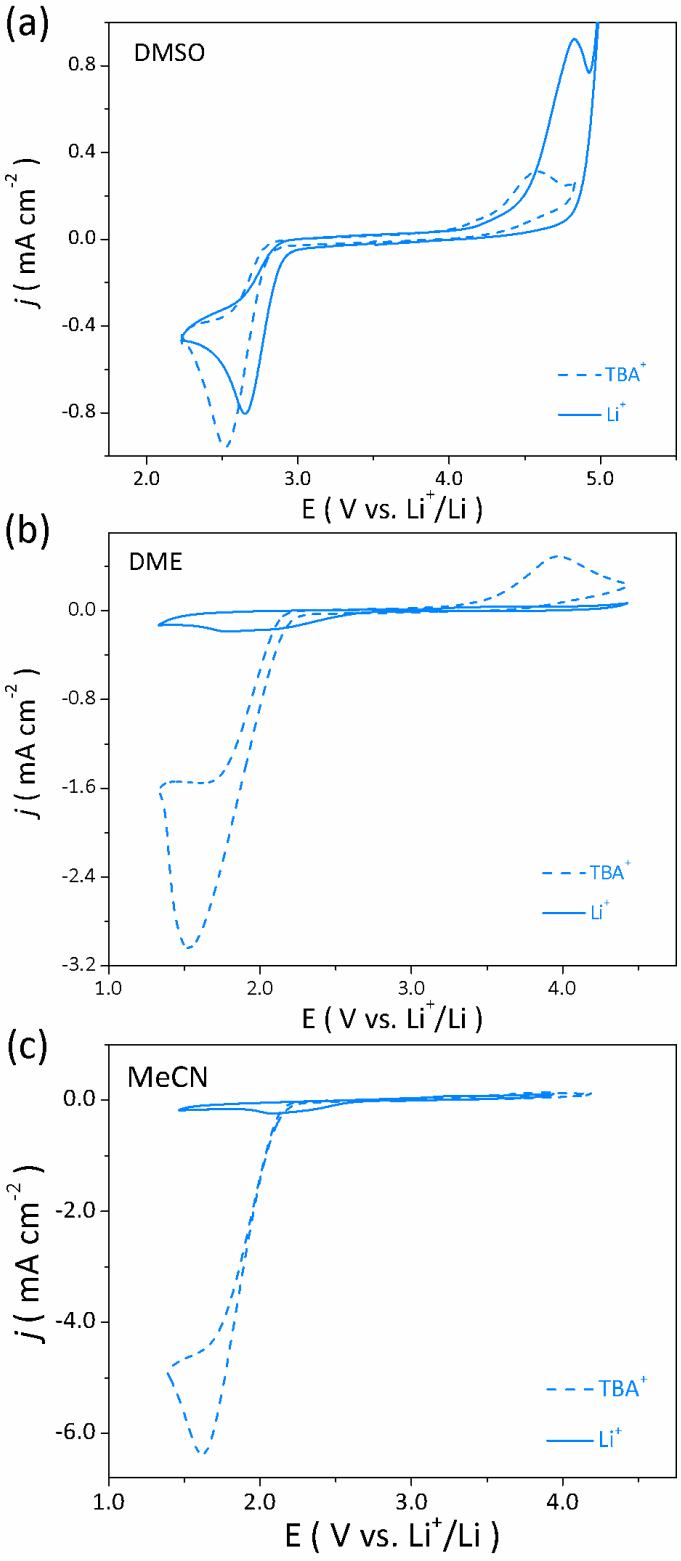

Figure IV. 6 Cyclic voltammetry curves at 50 mV s^{-1} for O_2/CO_2-saturated TBA^+- (dash curves) and Li^+- (solid curves) based (a) DMSO, (b) DME and (c) MeCN.

To definitively conclude on the discharge reaction mechanisms, cells were discharged at various current densities using 0.1 M $LiClO_4$ in DMSO and DME as electrolytes in both pure O_2 and O_2/CO_2 mixture and their resulting discharge products were analyzed (Figures IV. 7 & 8). In agreement with our cyclic voltammetry results previously discussed in Figure IV. 5a, the discharge potential for O_2/CO_2 cells with DMSO is consistently higher (> 0.1 V) than the discharge potential measured for O_2 cells at all investigated current densities (Figures IV. 7a, 7c & 7e), which confirms a different electrochemical pathway for O_2/CO_2 cells from O_2 cells. The electrode fully discharged in O_2/CO_2-saturated electrolyte showed by XRD the formation of highly crystalline Li_2CO_3, while no Li_2O_2 was detected (Figure IV. 8a), indicating that Li_2CO_3 was the ultimate discharge product as expected from the mechanism uncovered by our CV study. Since there can be numerous complex intermediate steps to form Li_2CO_3 from $LiCO_4$ and which cannot be distinguished by CVs , we simply wrote the overall reaction as equation (1.5) (Scheme IV. 1). Overall, we can conclude that the discharge reaction of Li-O_2/CO_2 battery in DMSO-based electrolyte is following the equation (1.6) (Scheme IV. 1). This conclusion was further confirmed by measuring the number of electrons consumed per mol of gas deduced from pressure measurements (Figures IV. 7b, 7d & 7f). Independently of the current density, every O_2/CO_2 cell consumed $\sim 1.33 \pm 0.1$ e^- per mole of gas during discharge compared to $\sim 2 \pm 0.3$ e^- per mole of gas measured for O_2 cells, in agreement with the overall reaction $4\ Li^+ + 4\ e^- + O_2 + 2\ CO_2 \rightarrow 2\ Li_2CO_3$ (Scheme IV. 1, equation (1.6)). This assumption is also further supported by the fact that Li_2CO_3 formed in DMSO cells shows a sea urchin-like shape (Figure IV. 8b), very different from that of Li_2O_2 particles formed under the same conditions in pure O_2 systems (Figure A. 4. 6a).[229-232] Another interesting observation is that O_2/CO_2 cells delivered larger capacity than O_2 cells at lower current densities of 50 mA g^{-1} and 100 mA g^{-1} (Figures IV. 7a, 7c), while the reverse trend being observed at higher current density of 200 mA g^{-1} (Figures IV. 7e). Even though the physical origin for this capacity difference is not fully understood, based on previous reports on the impact of discharge product morphology on the Li-O_2 cells capacity, [229,230,233] we can suspect at this point that morphology can also play a role for Li-O_2/CO_2 cells. At higher current density, the nucleation rate will be faster than the growth rate, [234] leading to the formation of smaller Li_2CO_3 particles (Figure A. 4. 6d) and eventually to the formation of a film covering the electrode, alike what has been observed for Li-O_2 cells. Also considering that Li_2CO_3 is a wider band gap insulator than Li_2O_2 (5.03 eV for Li_2O_2 and 8.01 eV for Li_2CO_3, as calculated previously),[215] we can postulate that a shorter electron tunneling distance is expected for Li_2CO_3 film compared to Li_2O_2, hence leading to a premature cell death.

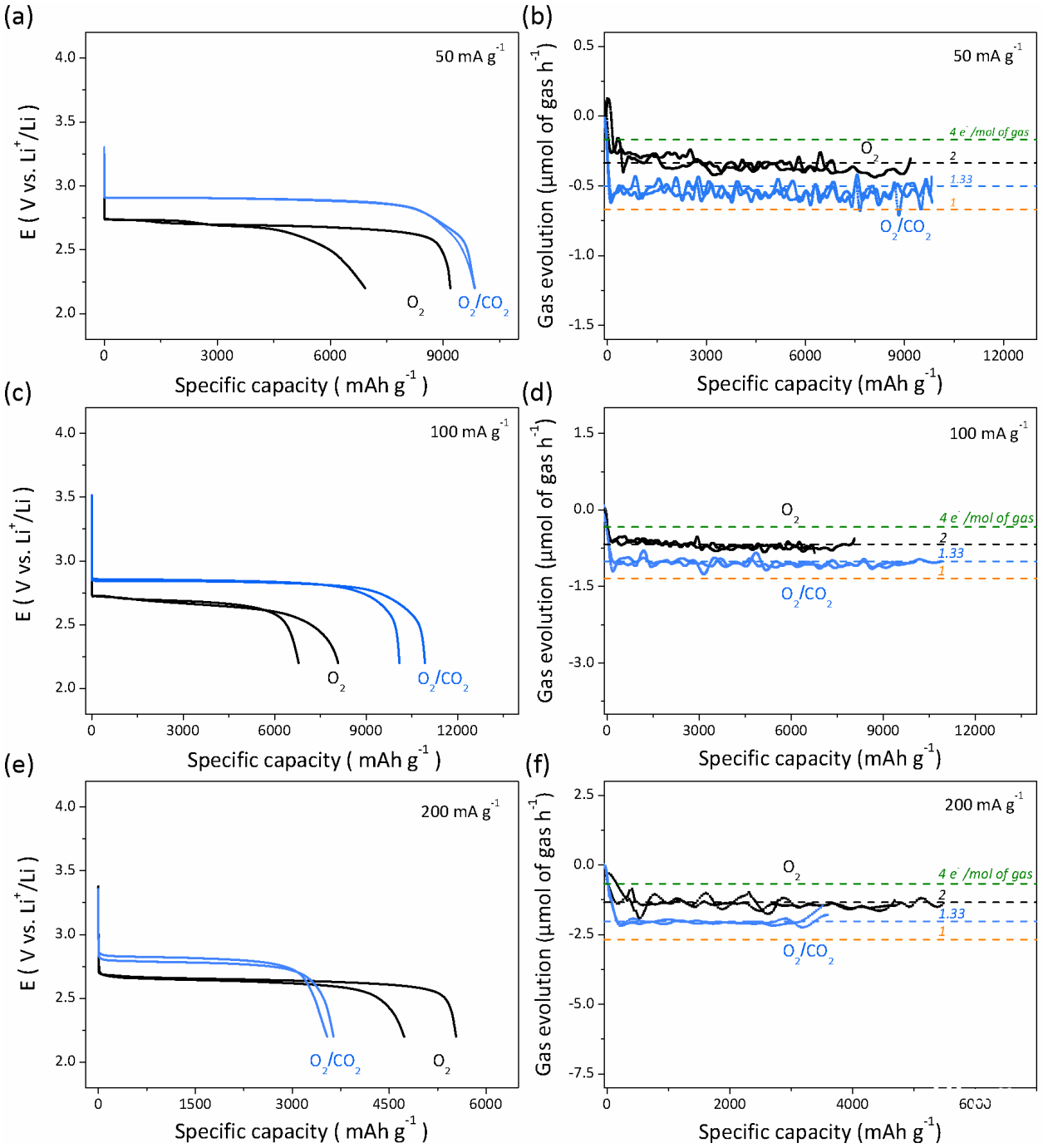

Figure IV. 7 (a, c, e) Galvanostatic discharge curves and (b, d, f) the corresponding pressure changes in 0.1 M $LiClO_4$/DMSO electrolyte under pure O_2 (black curves) and under O_2/CO_2 (blue curves) at various current densities of 50 mA g^{-1} (a, b); 100 mA g^{-1} (c, d) and 200 mA g^{-1} (e, f). For each measurement, two cells measured under the same conditions are reported to show the data reproducibility.

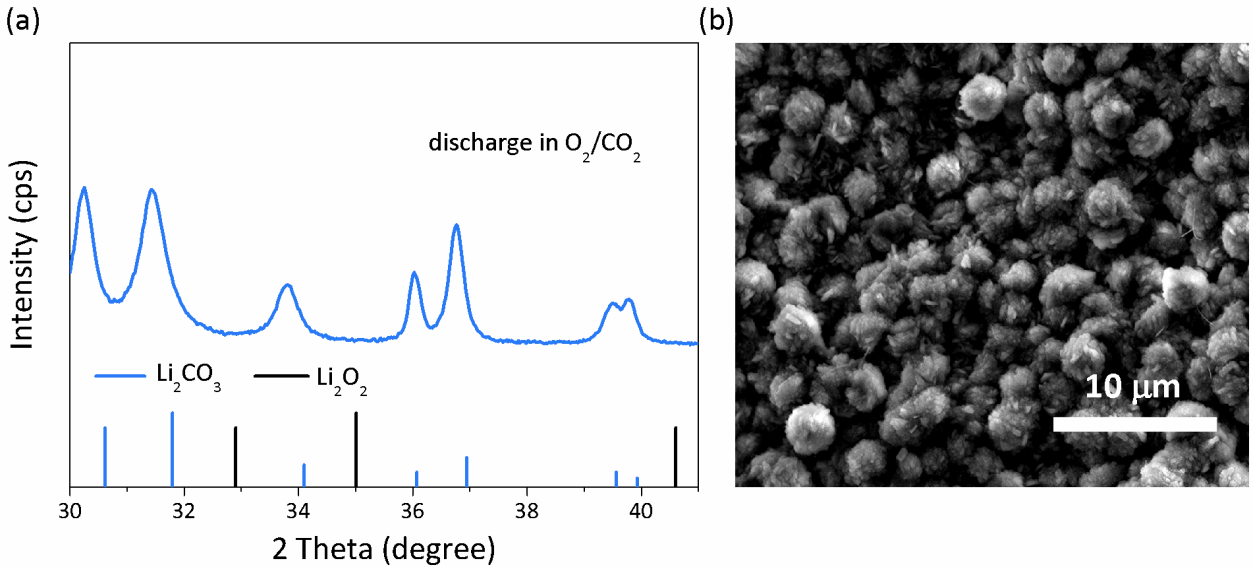

Figure IV. 8 (a) X-ray diffraction pattern and (b) SEM image of electrode after fully discharged under O_2/CO_2 using 0.1 M $LiClO_4$/DMSO electrolyte at a current density of 50 mA g^{-1}.

As we observed by CVs , $O_2^{\bullet -}$ reacts first with Li^+ in DME in O_2/CO_2 atmosphere, in a similar way to what is observed in pure O_2. To further test and verify this observation, Li-O_2/CO_2 cells were assembled and discharged in DME-based electrolyte (Figure IV. 9). In agreement with the aforementioned CV results (Figure IV. 5b), the same discharge potential is measured in O_2 and O_2/CO_2 at all studied current densities (Figures IV. 9a, 9c & 9e), indicating that the potential is governed by the same equilibrium corresponding to the lithium superoxide formation (Scheme IV. 1, equation (1.4)). Interestingly, the pressure analysis shows that the e^- / mole of gas consumption is ~ 1.33 ± 0.2 during discharge for O_2/CO_2 cells, compared to ~ 2 ± 0.8 e^- / mole of gas for O_2 cells (Figures IV. 9b, 9d & 9f). This strongly suggests that Li_2CO_3 is the discharge product, which is confirmed by XRD (Figure IV. 10a). SEM images show that similar morphology of particles was found in both O_2 and O_2/CO_2 cells (Figures IV. 10b & A. 4. 6b). Reexamining the CV results in Li^+-O_2/CO_2 system in DME in the potential range of 2.8 - 4.5 V vs Li/Li^+, an oxidation peak, although very weak, can be noticed at the same potential as the oxidation peak measured in pure O_2 (inset figure of Figure IV. 5b). As previously discussed, while our CV study clearly demonstrates that equation (1.1) and equation (1.4) (Scheme IV. 1) initially occurred, two subsequent pathways for the Li_2CO_3 formation can be envisioned: pathway 2 (equations (1.7) and (1.5)) and pathway 3 (equations (1.8) and (1.9)) (Scheme IV. 1). At this stage, the question is to know if the chemical reaction of lithium superoxide with CO_2 is faster than its disproportionation into Li_2O_2. Knowing

that the Li_2O_2 morphology observed after discharge in Li-O_2 cells was found to be influenced by the lithium superoxide stability,[37] we examined the morphology of Li_2CO_3 formed under electrochemical or chemical conditions to determine which pathway is the most likely to occur in DME-based Li-O_2/CO_2 cells. Comparing the SEM images obtained by chemical reaction of Li_2O_2 with CO_2 with those obtained after discharge in O_2/CO_2 atmosphere (Figure A. 4. 7), a similar morphology with small and round shaped particles was observed in both cases. Besides, based on the findings by Lim *et al.* suggesting that Li_2O_2 tends to primarily form in DME[30] and on the observation by McCloskey's group that DME-based cells discharged in CO_2-O_2 with a 10-90 ration show a discharge potential and a e^- / mole of gas ratio similar to O_2 cells, [25] we postulate that lithium superoxide first disproportionates to form Li_2O_2, and then spontaneously reacts with CO_2 to form Li_2CO_3, following the pathway 3 (Scheme IV. 1, equations (1.8) and (1.9)). However, since lithium superoxide is known to be very reactive, we should not neglect the possibility for pathway 2 (Scheme IV. 1, equations (1.7) and (1.5)) to occur. Another observation that can be made from the discharge curves is that the O_2/CO_2 cells deliver larger capacity than O_2 cells at lower current densities (50 mA g^{-1} and 100 mA g^{-1}, Figures IV. 9a & 9c); but the trend was reversed when increasing the current density to 200 mA g^{-1} (Figure IV. 9e). From the SEM images obtained for electrodes discharged at different current densities in O_2/CO_2 (Figures IV. 10b, 10c & 10d), we noticed that particles grow bigger in size and number when decreasing the current density from 100 mA g^{-1} to 50 mA g^{-1} (Figures IV. 10b & 10c). However, at relatively high current density of 200 mA g^{-1}, a continuous film covering the Super P electrode surface was found in agreement with an enhanced nucleation rate at high current density (Figure 10d). This change in morphology could be attributed to the previously discussed conductivity difference between Li_2CO_3 and Li_2O_2 films and which might be the reason for the current density dependence of the discharge capacity measured for DME-based O_2/CO_2 cells when compared with pure O_2 cells.

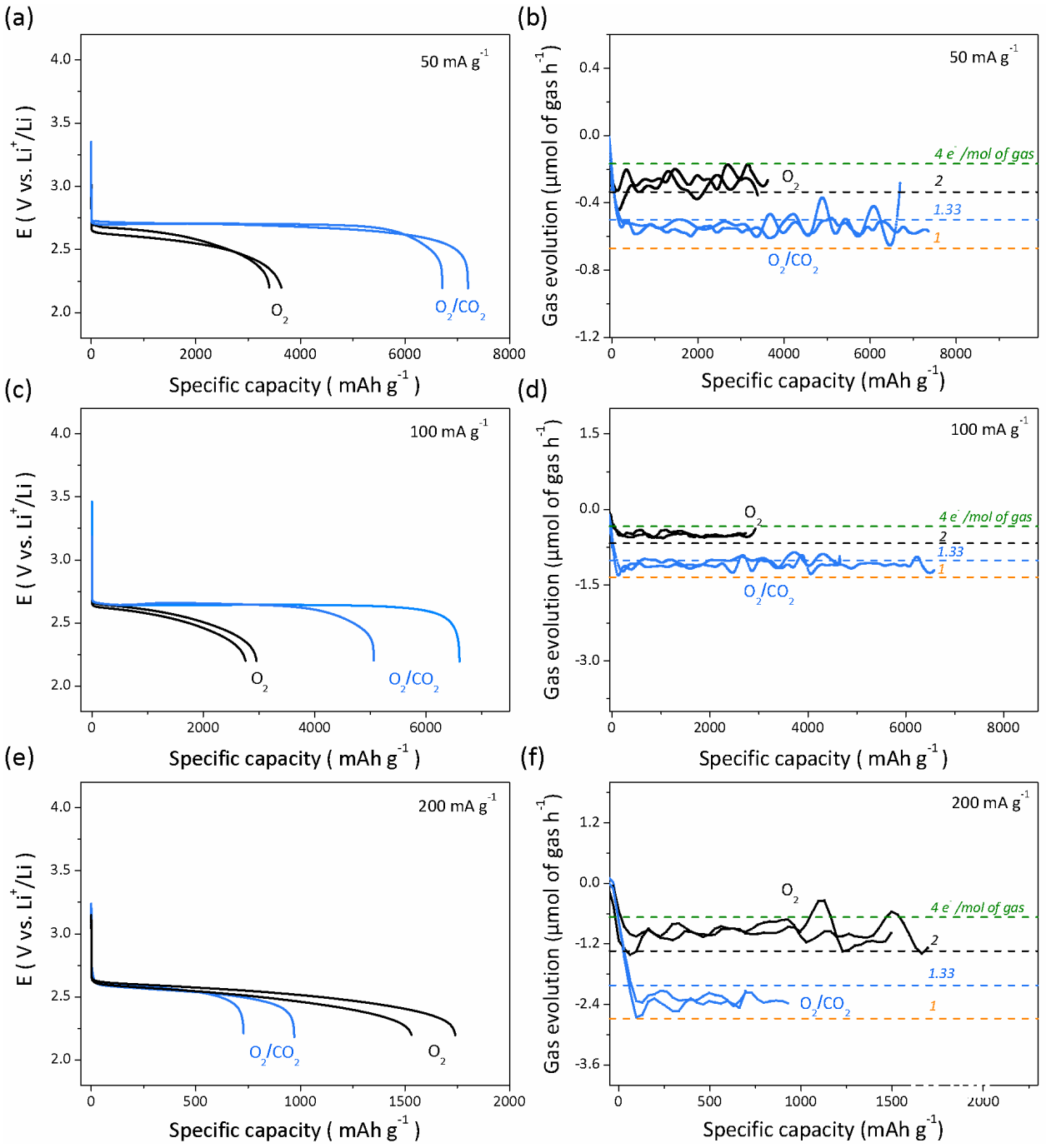

Figure IV. 9 (a, c, e) Galvanostatic discharge curves and (b, d, f) the corresponding pressure changes in 0.1 M $LiClO_4$/DME electrolyte under pure O_2 (black curves) and under O_2/CO_2 (blue curves) at various current densities of 50 mA g^{-1} (a, b); 100 mA g^{-1} (c, d) and 200 mA g^{-1} (e, f). For each measurement, two cells measured under the same conditions are reported to show the data reproducibility.

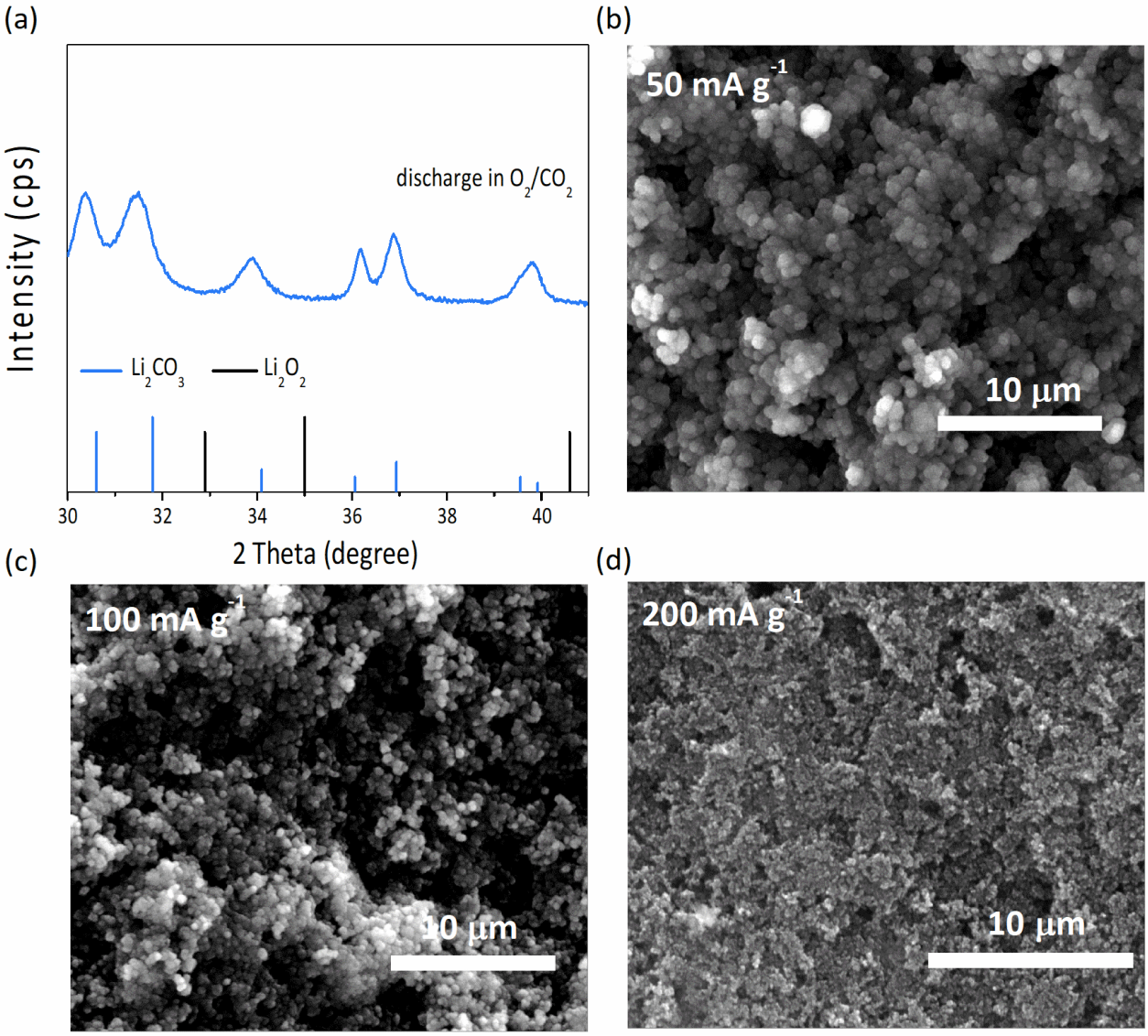

Figure IV. 10 (a) X-ray diffraction pattern of electrode after fully discharged under O_2/CO_2 using 0.1 M $LiClO_4$/DME electrolyte at current densities of 50 mA g^{-1}. SEM images of electrodes after fully discharged under O_2/CO_2 using 0.1 M $LiClO_4$/DME electrolyte at current densities of 50 mA g^{-1} (b), 100 mA g^{-1} (c) and 200 mA g^{-1} (d).

Finally, bearing in mind that previous works reported rechargeable Li-O_2/CO_2 batteries, [27, 30] we investigated the cycling behavior of Li-O_2/CO_2 cells. For that, we compared two cells: one with a capacity limitation of 1000 mA g^{-1} (corresponding to an absolute capacity of 0.36 mAh) and one without capacity limitation. At first glance, our results could naively lead us to conclude that Li-O_2/CO_2 cells are rechargeable, but it is not the case (Figure IV. 11a & 11b). Indeed, the gas evolution measurements for both cells clearly indicate drastic side reactions (dashed areas in Figure

IV. 11c and in inset of Figure IV. 11d). More specifically, the gas evolution in charge doesn't exhibit the ratio of ~ 1.33 e^- / mol of gas which is measured in discharge, instead, a much higher value of ~ 2.26 ± 0.3 e^- / mol of gas was observed from the very beginning of the charge process for both cells (stage I in Figure IV. 11c and inset of Figure IV. 11d). This observation evidences that although a Li-O_2/CO_2 cell can be cycled for few tens of cycles when drastically limiting the capacity, a similar situation that has been encountered for many years and erroneously associated to the reversibility of Li_2O_2 rather than electrolyte decomposition in Li-O_2 cells. Therefore, cycling cells with limited capacity and decreasing the electrode loading so as to obtain cycling performances are not ways to achieve cleaner chemistry, and one can conclude that Li-O_2/CO_2 cells are not rechargeable under these conditions (electrode, electrolyte, and current density) owing to the very high potential needed to oxidize Li_2CO_3. Efforts must be made to find redox mediators or solid catalysts so as to decrease the oxidation potential closer to its theoretical value of 3.82 V *vs* Li/Li^+.[18, 19] However, as the discharge potential is pinned in DMSO by the formation of $LiCO_4$ at about 2.8 V *vs* Li/Li^+ that governs the discharge potential, a poor round trip efficiency can already be foreseen for this system, which should therefore be more certainly seen as a primary battery. Moreover, looking in details to the cell cycled with no capacity limitation (Figure IV. 11c), a negative pressure evolution of ~ 3.26 e^- / mol of gas at high potential range (stage II) was observed following the positive gas evolution of 2.26 ± 0.3 e^- / mol of gas measured at stage I. Knowing that the capacity corresponding to stage I matches with the discharge capacity of about 10000 mAh g^{-1}, one can postulate that the reaction in stage I is associated with the oxidation of Li_2CO_3 discharge product which presumably forms solid products instead of releasing gaseous O_2 and CO_2 as expected from equation (1.6). Using gas analysis carried out with online electrochemical mass spectrometry (Figure IV. 12) as well as previous report,[52] we found that CO_2 is released upon charge while almost no gaseous O_2 is evolved, explaining the ratio of ~ 2.26 ± 0.3 e^- / mol of gas found by pressure measurements in Figure IV. 11c. Moreover, knowing that no gas corresponding to DMSO decomposition was found by mass spectrometry, we therefore suspected that oxidized oxygen species react with DMSO and/or the electrode to form a solid product. Moreover, this reactivity certainly leads to different product formation than the direct oxidation of the electrolyte measured at stage II, as seen by the different pressure evolutions measured for both processes in Figure IV. 11c as well as the different CO_2 evolution rates found by mass spectroscopy (Figure IV. 12).

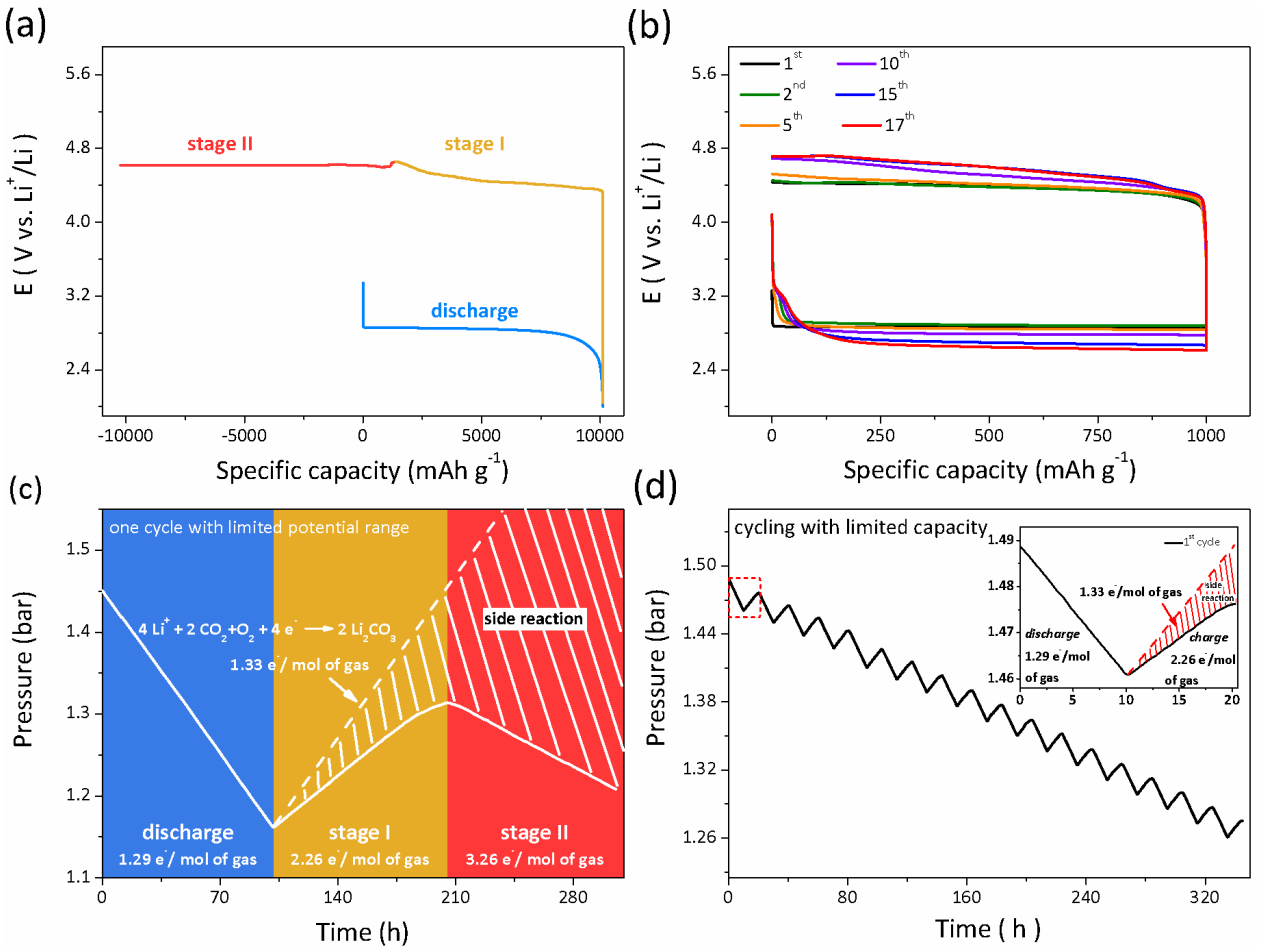

Figure IV. 11 (a) Galvanostatic discharge-charge profiles and (c) the corresponding pressure changes of Li-O_2/CO_2 cells with a limited potential range, and with a limited capacity of 1000 mAh g^{-1} in (b) and (d). Both cells are cycled at a current density of 100 mA g^{-1}, using 0.1 M $LiClO_4$/DMSO as electrolyte.

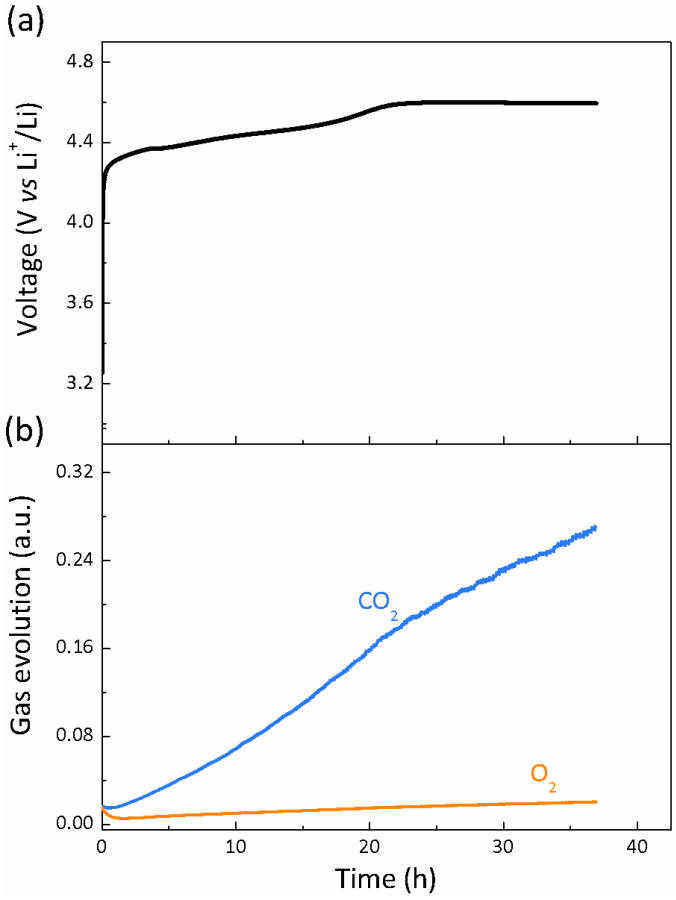

Figure IV. 12 (a) Charge profile of a Li-O_2/CO_2 cell at 25 ℃ using 0.1 M $LiClO_4$/DMSO at a current density of 100 mA g^{-1}; and (b) partial pressure curve for CO_2 (m/z = 44) and O_2 (m/z = 32) during charge, the cell was vacuumed and refilled with argon before mass spectroscopy measurement.

IV. 2. 3 Discussion and conclusion

Firstly, our findings reveal that CO_2 cannot be directly reduced in aprotic solvents within their electrochemical window (DME, DMSO and MeCN are investigated in this work) using carbon Super P as positive electrode. Correspondingly, no electrochemical activity in Li-CO_2 batteries was observed in contrasts with many literatures. Worth mentioning is a recent study which demonstrated that, despite Li-CO_2 battery exhibiting negligible discharge capacity (with positive electrodes of bare and monodispersed Ru nanoparticles functionalized graphene nanosheet), the introduction of 2 % O_2 (at volume ratio) can lead to a high capacity of 4742 mAh g^{-1} (termed as O_2-assisted Li-CO_2

battery).[235] In general, Li-CO_2 battery is still in its infancy, and new insights are necessary to explain this discrepancy in electrochemical activity.

Secondly, we demonstrate that different discharge reaction mechanisms in Li-O_2/CO_2 batteries are indeed at play, depending on the Li^+ solvation strength by the electrolyte solvents. As depicted in Scheme IV. 2, although the initial discharge step either in DMSO or DME, is the electrochemical reduction of oxygen into superoxide, afterwards, superoxide favorably reacts with CO_2 in high DN solvent DMSO due to the strong solvation of Li^+ by DMSO while it reacts with Li^+ in low DN solvent DME to form lithium superoxide. Consequently, Li_2CO_3 is electrochemically formed in DMSO (denoted as the electrochemical pathway). Whereas in DME, Li_2O_2 is first formed alike in Li-O_2 batteries before to chemically react with CO_2 to form Li_2CO_3 (denoted as the chemical reaction pathway). Despite the different superoxide reactivity that was highlighted in this work, Li_2CO_3 is the only final product for Li-O_2/CO_2 batteries, regardless of the solvents. Note that, following our work, similar reaction scenario was also established in trace O_2-assisted Li-CO_2 battery (which can be intuitively viewed as Li-O_2/CO_2 battery with very high CO_2/O_2 ratio) based on *in-situ* surface enhanced Raman spectroscopy.[236] Although the abovementioned scenario rationalizes the major difference in the discharge of Li-O_2/CO_2 batteries, the following reaction steps in DMSO, i.e., after the superoxide reaction with CO_2, remain to be identified (the reaction paths from superoxide to form Li_2O_2 in DME have already been investigated in detail within the context of Li-O_2 batteries). Along this line, Qiao *et al.* later on emphasized the importance of CO_2/O_2 ratio in dictating the reaction of superoxide and CO_2 based on fitted Raman spectra.[237] Specifically, peroxodicarbonate ($C_2O_6^{2-}$) tends to form under conditions with a high CO_2/O_2 ratio while peroxomonocarbonate (CO_4^{2-}) is the dominant reaction intermediate at low CO_2/O_2 ratio.

Scheme IV. 2 Schematic illustration of the Li_2CO_3 formation in Li-O_2/CO_2 batteries with DMSO- and DME-based electrolytes, following either the electrochemical pathway or the chemical pathway.

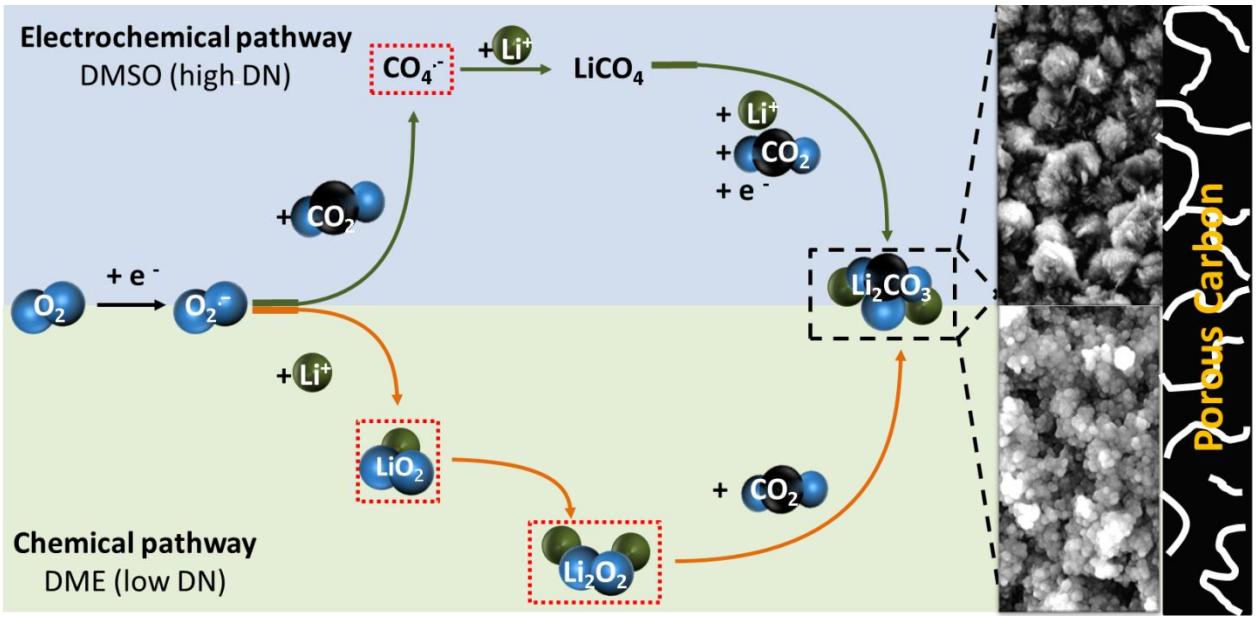

Thirdly, different reaction pathways result in significantly different Li_2CO_3 morphology (sea urchin-like shape in DMSO compared to particle shape in DME). In addition, the capacity difference between Li-O_2/CO_2 batteries and Li-O_2 batteries depends on the discharge current density, possibly resulting from the competition between nucleation and growth, as well as the charge-transfer difference between Li_2CO_3 and Li_2O_2.

Finally, we demonstrate that Li-O_2/CO_2 batteries may not be rechargeable batteries based on two facts: i) only CO_2 is evolved but not O_2 during the oxidation of Li_2CO_3 on charge; and ii) the very high potentials required for Li_2CO_3 oxidation lead to drastic side reactions. To overcome these limitations, one interesting future direction is to alter the discharge reaction thus to avoid the "troublemaker" Li_2CO_3. Following this strategy, Qiao *et al.* demonstrated a Li-O_2/CO_2 battery which operates based on peroxodicarbonate at a low charge potential of 3.5 V by stabilizing the peroxodicarbonate intermediates in concentrated electrolytes.[237]

IV. 3 Li−CO_2 batteries: CO_2 conversion mediated by quinone derivatives

IV. 3. 1 Introduction

In contrast to the O_2-based battery systems, where the electrochemical reduction of O_2 into $O_2^{\bullet-}$ in aprotic solvents is thermodynamically more favored (-0.85 V *vs* SCE in DMF),[238] the electrochemical reduction of CO_2 into $CO_2^{\bullet-}$ requires a highly negative potential (-2.21 V *vs* SCE in DMF),[239,240] because of the energy required to rearrange a linear molecule into a bent radical anion. This realization i) adds difficulty to trigger the electrochemical activity in Li-CO_2 battery (as discussed in Chapter IV. 2) and ii) induces copious parasitic reactions (e.g., electrolytes and other cell components are generally unstable at such low potentials). It is therefore essential to promote the electrochemical reduction of CO_2 so as to improve the electrochemical performance of Li-CO_2 battery. Starting from the first report on Li-CO_2 battery, Archer *et al.* showed that the electrochemical reduction of CO_2 can be thermally activated at elevated temperatures based on the reaction of 4 Li + 3 CO_2 → 2 Li_2CO_3 + C.[241] Later on, research efforts have been placed in exploring heterogeneous electrocatalysts (e.g., carboneous materials with improved electronic conductivity,[194,223,224,242,243] noble metals, [207,208] etc.), seeking to facilitate the electron transfer to CO_2 at room temperature. Nevertheless, the efficiency of this research direction remains limited since the surface deposition of Li_2CO_3 will block the catalytic sites. Alternatively, an electron can be injected into the CO_2 molecule indirectly via a solution chemical reaction, with the hope to evoke solution formation of Li_2CO_3. Another fascinating aspect of this approach is to avoid the energy-hungry step in classical electrochemical reduction of CO_2, namely the formation of $CO_2^{\bullet-}$, thereby effectively increasing the discharge voltage of Li-CO_2 battery. One example supporting this view is provided by introducing O_2 into Li-CO_2 battery system (denoted as Li-O_2/CO_2 battery, as detailed investigated in Chapter IV. 2). Consequently, CO_2 reduction is preceded through an initial electrochemical reduction of O_2 to $O_2^{\bullet-}$ which then chemically reacts with CO_2 to eventually form Li_2CO_3.[102,151,214] Therefore, the discharge voltage of Li-O_2/CO_2 battery is now given by the electrochemical reduction of O_2 rather than that of CO_2, a process thermodynamically more favorable than the latter. Nevertheless, the major issue of this system resides in charge where the oxidation of Li_2CO_3 is irreversible,[101,151] namely CO_2 is released but almost no O_2 is given back,[102,151] entailing O_2 as a scavenger instead of a catalyst.

Aside from the battery community, the electrochemical reduction of CO_2 in aprotic solvents is also heavily investigated by the electrocatalysis community. Numerous chemical catalysts were proposed aiming to bypass the formation of $CO_2^{\bullet-}$ intermediate along the reaction pathway to final products.[244,245] Note that, in contrast to redox catalysts (also referred as "soluble catalyst" or "redox mediator") which only shuttle electrons from the electrode surface to the target reactant,[74,214-218] chemical catalysts involve multi-step CO_2 reduction through the formation/ decomposition of adducts formed between CO_2 and the catalyst in their reduced form. More specifically, the catalyst first undergoes electrochemical reduction prior to chemically react with CO_2 to give the final products and to regenerate the parent catalyst.[246-248] Worth mentioning is that the concept of chemical catalyst has also been extended to Li-O_2 battery field to promote the electrochemical reduction of O_2 and the solution growth of Li_2O_2.[89]

Quinones are well-known for their high binding affinities toward CO_2 in their reduced form and were used to concentrate and selectively separate CO_2.[249-251] In addition, the synergistic effect of Lewis acid cation such as Li^+ on the electrochemical reduction of CO_2 by chemical catalyst, i.e., iron(0) porphyrins, has been previously identified.[252] Encouraged by the aforementioned findings, we decided to investigate quinones as potential chemical catalysts for the CO_2 in Li-CO_2 batteries.

IV. 3. 2 Results and discussion

Quinones represent a class of organic compounds with versatile chemical/electronic structures, redox potentials and affinities toward CO_2 as well as Li^+.[253-255] Therefore, three quinones with different chemical structures ─ 9, 10-anthraquinone (AQ), 9, 10-phenanthrenequinone (PAQ), and 2, 5-di-tert-butyl-1, 4-benzoquinone (DBBQ) ─ have been surveyed aiming to examine the possible correlation between structure and catalytic properties (Figure IV. 13).

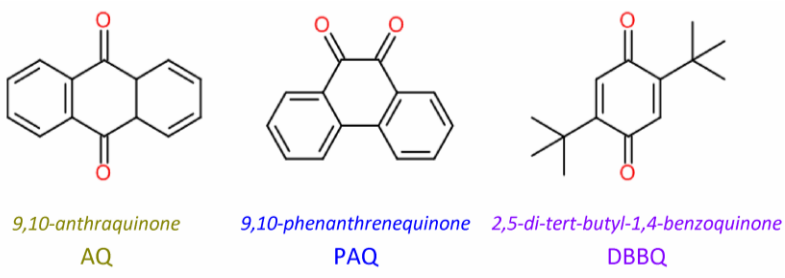

Figure IV. 13 Chemical structures of the herein investigated quinones.

To spot the electrochemical behavior of quinones in the absence of CO_2 and Li^+, voltammetry studies were first carried out in argon-saturated electrolytes using tetrabutylammonium (TBA^+) as the supporting cation. Compared to the voltammograms recorded without quinone showing almost no current response (green curves in Figure IV. 14), two well-defined redox waves was observed in the presence of quinone, irrespective of the solvent (orange curves in Figure IV. 14) as well as their chemical structures (red curves in Figure IV. 15a).

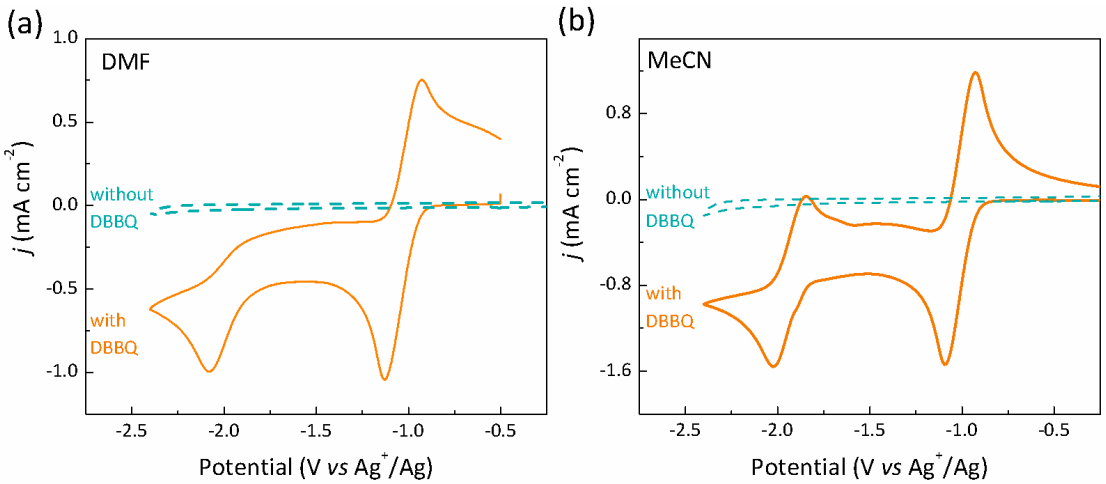

Figure IV. 14 Cyclic voltammograms recorded under argon atmosphere in solutions of 0.1 M $LiClO_4$ in DMF (a) and MeCN (b) with (orange curves) and without (green curves) DBBQ. Scan rate: 100 mV s^{-1}.

Consistent with previous findings, these two waves correspond successively to the formation/oxidation of quinone anion radicals $Q^{\bullet -}$ and dianions Q^{2-} (Q stands for quinones):[251,256]

$$Q + e^- \leftrightarrow Q^{\bullet -} \qquad (1)$$

$$Q^{\bullet -} + e^- \leftrightarrow Q^{2-} \qquad (2)$$

The reactivity of quinones towards CO_2 was then studied (Figure IV. 15a), and no substantial change in both the onset potentials and peak currents of the first reduction waves was observed, indicating no CO_2 reactivity of $Q^{\bullet -}$ independent of the chemistry of quinones. Instead, all the second reduction waves shifted to more positive voltages in the presence of CO_2, suggesting a strong interaction between CO_2 and Q^{2-}. Note that similar voltammetric behavior was previously

reported and indeed these positive shifts were attributed to the coupling of CO_2 to Q^{2-} following the reactions:[257]

$$Q + e^- \rightarrow Q^{\bullet -} \qquad (3)$$

$$Q^{\bullet -} + e^- \rightarrow Q^{2-} \qquad (4)$$

$$Q^{2-} + pCO_2 \rightarrow Q(CO_2)_p^{2-} \qquad (5)$$

The reaction of Q^{2-} with CO_2 (eqn. (5)) is further supported by the disappearance of the Q^{2-} oxidation peak, indicating the formation of a different reduction product rather than Q^{2-}. Overall, the observed voltammogram is similar to that of an EC reaction, i.e., electrochemical reduction followed by a fast chemical step.[258]

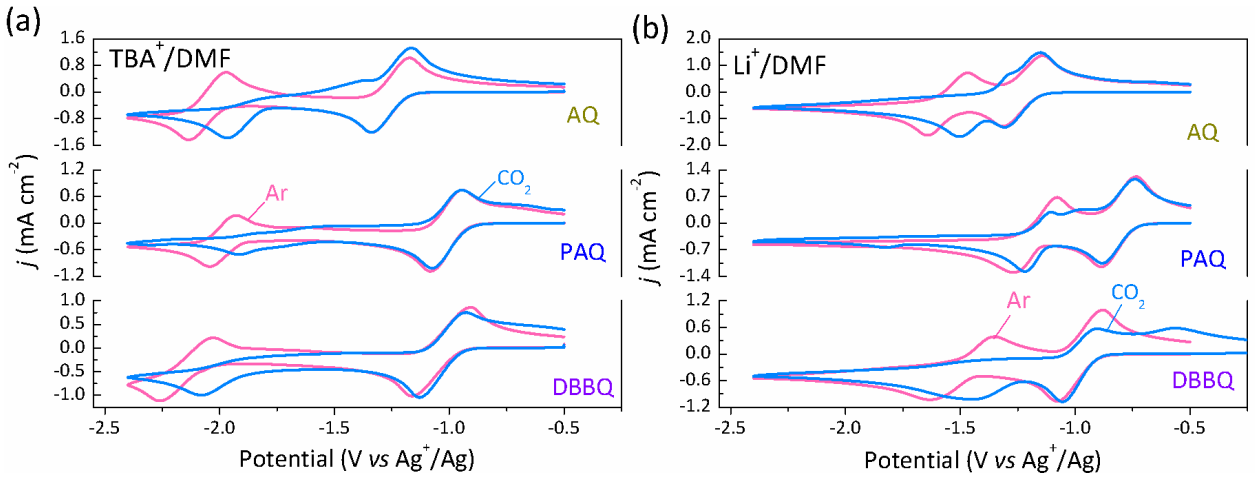

Figure IV. 15 Cyclic voltammograms of quinones (2.5 mM AQ (top), 5 mM PAQ (middle) and 5 mM DBBQ (bottom)) in Ar - (red curves) and CO_2 - (blue curves) saturated DMF containing 0.1 M $TBAClO_4$ (a), and 0.1 M $LiClO_4$ (b), respectively. Scan rate: 100 mV s^{-1}. 2.5 mM AQ was used due to the solubility limit.

The positive shifts measured for the second reduction waves (ΔE_2) following the chemical reactions of Q^{2-} with CO_2 (eqn. (5)) are reported in Table A. 4. 1. As previously established, a higher ΔE_2 value is associated with greater association constant and stoichiometric constant (p) for CO_2 reaction.[257] Among all the three quinones studied in this work, the highest ΔE_2 value is measured for DBBQ, indicating its greatest CO_2 reactivity (affinity) which can be explained by the

better stability of DBBQ-CO_2 adduct (the term DBBQ-CO_2 adduct was used here for the sake of simplicity, although it was formed from DBBQ dianion and CO_2) and its high aromaticity. Moreover, the ΔE_2 value for PAQ (*ortho*-quinone) was smaller than those for AQ and DBBQ (*para*-quinones) possibly due to steric hindrance and/or coulombic repulsion induced by the two oxygens in *ortho* positions of PAQ dianion.

To gain deeper insights into the reaction rate of Q^{2-} and CO_2, voltammetry measurements at various scan rates were performed (Figure IV. 16). Even at scan rate as high as 20 V s^{-1}, no oxidation peak could be recovered for the reverse reaction of $Q^{\bullet-} + e^- \rightarrow Q^{2-}$ (eqn. (4)), indicating a very fast chemical reaction between Q^{2-} and CO_2. Unfortunately, the very fast nature of this step prevents the estimation of its kinetic rate constant.

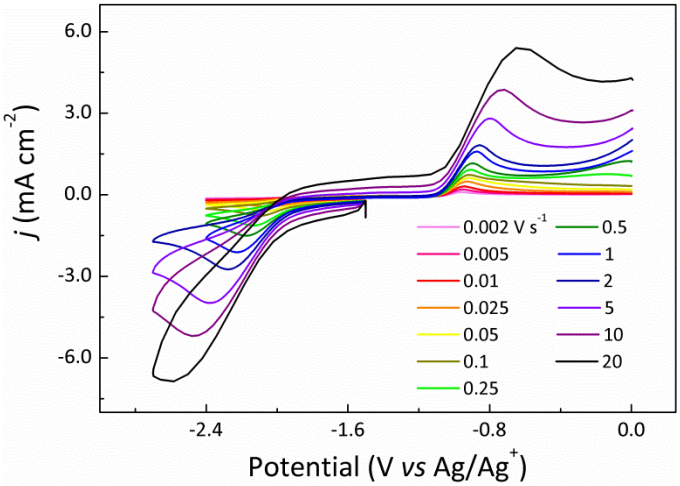

Figure IV. 16 Cyclic voltammograms in the presence of CO_2 at various sweep rates for 5 mM DBBQ in 0.1 M TBAClO_4/DMF. For all the measurements, the potential was held at -1.5 V vs Ag/Ag^+ for 20 s to intentionally produce the same amount of $Q^{\bullet-}$.

Next, we went on to investigate the effects of adding a Lewis acid, namely Li^+, on the reduction of quinones. Let us first recall that Li^+ was demonstrated, both experimentally and theoretically, to form ion-pairs with both $Q^{\bullet-}$ and Q^{2-} as evidenced by shifting their redox potentials to more positive values.[259,260] Therefore, we first compared the voltammograms obtained with argon-saturated electrolytes containing Li^+ and TBA^+, as bulky TBA^+ does not form stable chelates with organic compounds upon reduction. Similar to what is observed in TBA^+-based electrolytes, all quinones exhibit successively two reduction waves in the presence of Li^+ (Figure IV.

17). However, when comparing their reduction potentials (Table A. 4. 2), positive shifts were observed for the first redox waves for DBBQ and PAQ, whereas little change was found for AQ. The difference in the extent of positive shift is related to the different strengths of ion-ion interactions between Li^+ and $Q^{\bullet -}$.[259,261] Indeed, the most pronounced positive shift measured for PAQ is in agreement with its high Li-binding energy, as computationally studied elsewhere.[253] Turning to the second reduction waves, positive shifts were found for all three quinones (Figure IV. 17). The extent of this shift is in general greater than those for the first waves, suggesting a stronger Li^+ interaction with Q^{2-} than with $Q^{\bullet -}$. Alike what was observed for the first reduction wave, PAQ dianion shows the strongest interaction with Li^+ (Table A. 4. 2). Overall, we have shown that Li^+ shifts the reduction potentials of quinones for each electron transfer via ion-ion interactions, following the reactions:

$$Q + e^- + Li^+ \leftrightarrow QLi \qquad (6)$$

$$QLi + e^- + Li^+ \leftrightarrow QLi_2 \qquad (7)$$

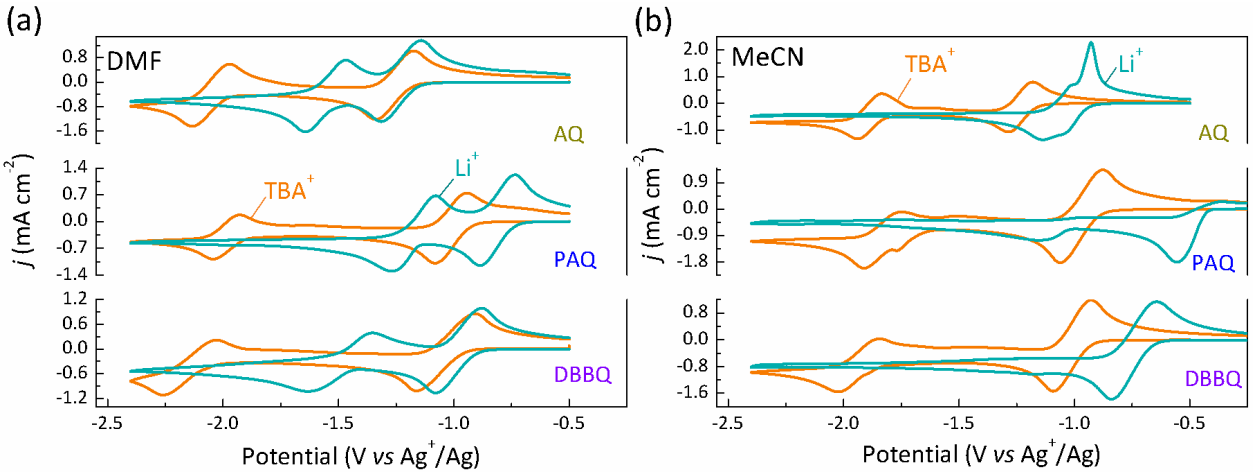

Figure IV. 17 Cyclic voltammograms of quinones (2.5 mM AQ (top), 5 mM PAQ (middle) and 5 mM DBBQ (bottom)) in Ar- saturated DMF (a) and MeCN (b) containing 0.1 M $TBAClO_4$ (orange curves), and 0.1 M $LiClO_4$ (green curves). Scan rate: 100 mV s^{-1}.

Having understood the interaction of Li^+ and quinones, we finally explored the CO_2 reaction with quinones in the presence of Li^+ (Figure IV. 15b). The onset reduction potentials and the peak currents for the first reduction waves remained unaltered as compared to the results obtained under argon, suggesting that CO_2 does not react with $Q^{\bullet -}$ even with the addition of a Lewis acid.

Nevertheless, positive shifts were found for the second reduction waves for AQ and DBBQ, alike what have been observed in TBA^+-based electrolyte (Figure IV. 15a). After demonstrating that no direct CO_2 reduction occurs in the presence of Li^+ without quinone (Figure A. 4. 8), we can conclude that such positive shifts are indeed related to the chemical reaction between Q^{2-}-Li^+ complex and CO_2. This reaction led to the formation of a new stable adduct, as suggested by the disappearance of the oxidation peak for Q^{2-}-Li^+ complex and the appearance of an oxidation peak at more positive potential (especially in the case of DBBQ). Step-wise voltammetry further confirmed that the new oxidation peak appeared at -0.55 V *vs* Ag^+/Ag (in the case of DBBQ) was indeed related to the reaction between Q^{2-}-Li^+ complex and CO_2 (Figure IV. 18). Notably, very little change in the voltammogram was observed for PAQ after adding CO_2 (Figure IV. 15b), indicating a weak interaction between PAQ^{2-}-Li^+ complex and CO_2, likely due to the very strong interaction between PAQ^{2-} and Li^+.

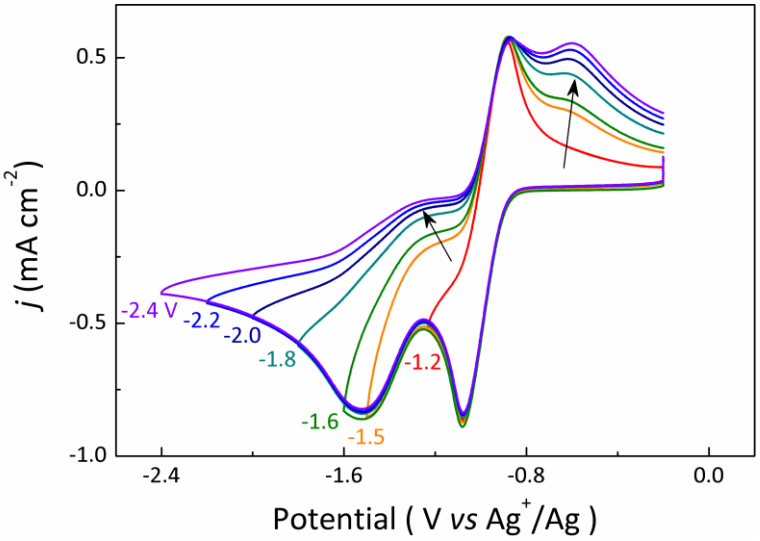

Figure IV. 18 Stepwise cyclic voltammograms of 5 mM DBBQ in 0.1 M $LiClO_4$/ DMF in the presence of CO_2. Scan rate: 100 mV s^{-1}.

Until now, we have demonstrated that AQ and DBBQ are capable to react with Li^+ and CO_2 during their second electron transfer and results in a new adduct formation. Worth mentioning is that similar reductive currents were measured at the end of anodic scan in both CO_2- and argon-saturated electrolytes, suggesting negligible "surface blocking" effect (negligible surface deposition of insulating products).

In light of the important role played by the interaction between Li^+ and quinone dianions on the CO_2 reaction, we carried out similar study in MeCN, which is known to have weaker Li^+ and slightly stronger anion solvation ability (Table IV. 2), as suggested from their donor number (DN) and acceptor number (AN), respectively.

Table IV. 2 Summary of the intrinsic properties of DMF and MeCN.

Solvent	DN (Kcal mol^{-1})[84]	AN (Kcal mol^{-1})[84]	ε 25 ℃	CO_2 solubility (mM)[217]	$10^5 * D_{CO2}$ (cm^2 s^{-1})[217]	Viscosity ŋ (cP)
DMF	26.6	16	36.7	198	3.56±0.2	0.92
MeCN	14.1	18.9	36.64[216]	280	38.3±1.1	0.361[216]

We first considered the influence of the solvents on the reduction of quinones in TBA^+-based electrolytes (Figure IV. 19a). A shift towards more positive potentials for the two reduction waves typical for quinones were observed in MeCN as compared to DMF (Table A. 4. 3), which can likely be explained by the fact that MeCN solvates stronger, and therefore stabilize more, the anions.[262] In CO_2-saturated solutions (blue curves in Figure IV. 19a), little change was found for the onset reduction potentials and peak intensities for the first reduction waves, but positive shifts were observed for the second reduction waves, revealing the chemical reaction of Q^{2-} with CO_2. The extent of positive shifts were in general more pronounced in MeCN than in DMF, indicating that a more stable adduct of Q^{2-} and CO_2 was formed in MeCN (Table A. 4. 3). Notably for PAQ and DBBQ, the addition of CO_2 causes the disappearance of the oxidation peaks for Q^{2-} and the growth of new oxidation peaks at more positive potentials, suggesting the formation of quinone─CO_2 adducts. By comparing the potential of such new oxidation peaks, which can be seen as an indicator of the stability of the quinone─CO_2 adducts, DBBQ dianion was determined to exhibit the strongest interaction with CO_2 as deduced from its highest oxidation potential. Whereas for AQ, the constant existence of Q^{2-} oxidation peak at a more positive potential implies that the interaction of AQ dianion with CO_2 is the weakest.

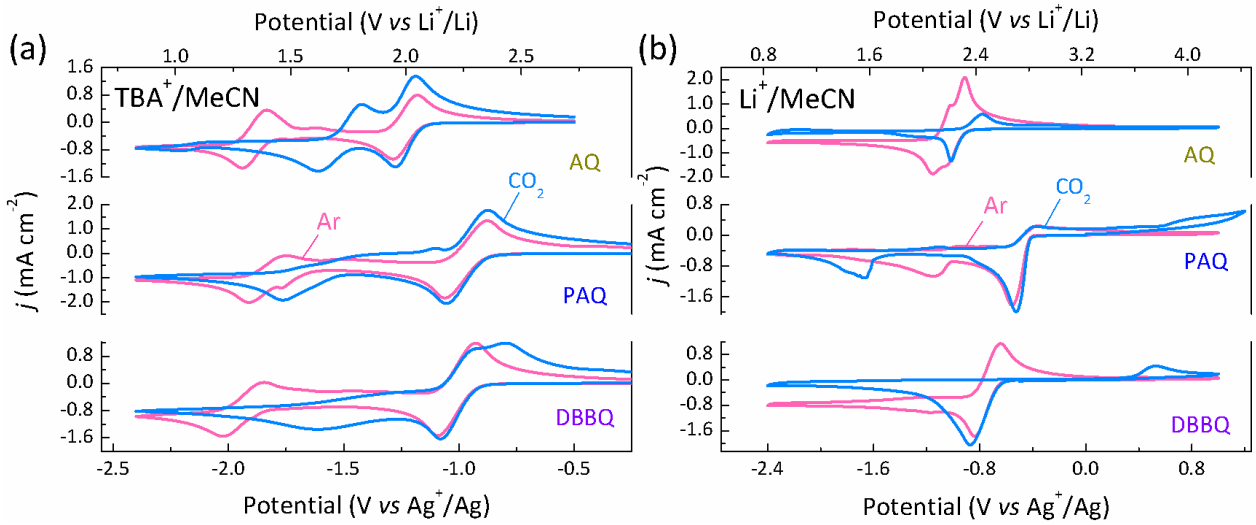

Figure IV. 19 Cyclic voltammograms of quinones (2.5 mM AQ (top), 5 mM PAQ (middle) and 5 mM DBBQ (bottom)) in Ar- (red curves) and CO_2- (blue curves) saturated MeCN containing 0.1 M $TBAClO_4$ (a), and 0.1 M $LiClO_4$ (b), respectively. Scan rate: 100 mV s^{-1}.

When comparing our results with those previously reported by Wrighton *et al.* for PAQ in MeCN/0.1 M $TBABF_4$ solution after the addition of 0.24 M CO_2, differences arise. That is, only one redox wave with increased reduction current density was observed in their study, which was interpreted as the change from two successive one-electron processes to a two-electron process in the presence of CO_2.[250] However, we found that such variations might result from the presence of water in the electrolyte (Figure IV. 20), as similar results were obtained when MeCN was not further dried and in which the water content is relatively high (without drying: 400 ppm, after drying: < 20 ppm). The presence of water as a proton source shifts the second reduction wave to a potential identical to that for the first electron transfer because of the strong interaction of Q^{2-} with proton, i.e., strong H-bonding, as established elsewhere.[263]

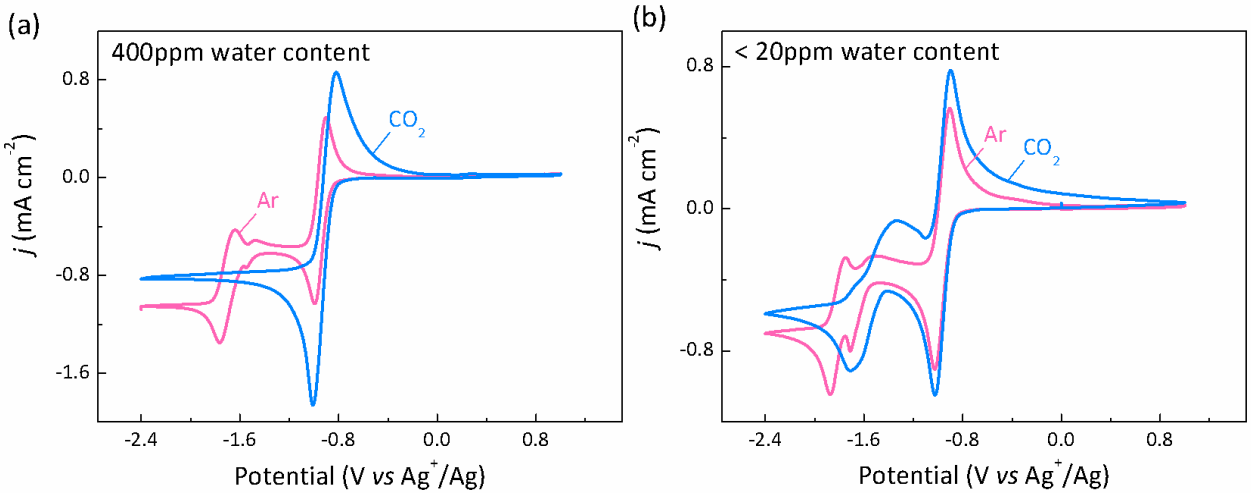

Figure IV. 20 Cyclic voltammograms of 5 mM PAQ under Ar (red curves) and CO_2 (blue curves) in MeCN with a water content of 400 ppm (a) and below 20 ppm (b), respectively. Scan rate: 20 mV s^{-1}.

As previously stated, Li^+ tends to interact with quinone anions through ion-ion pairing. Given the weaker Li^+ solvation strength by MeCN, a stronger Li^+ pairing with quinone anions can already be foreseen. Indeed, we observed in MeCN a greater influence of Li^+ on the redox behavior of quinones (green lines in Figure IV. 17b). In DMF-based electrolytes, the two successive reduction waves preserved with only their onset potentials shifting to more positive values (green lines in Figure IV. 17a). In contrary, in MeCN-based electrolytes, all quinones lost their typical feature of two well-defined redox waves. More specifically, the second reduction wave for AQ shifted positively to such a large extent that the two redox waves became nearly indistinguishable; only one redox wave at more positive potentials was observed for DBBQ; whereas PAQ exhibited two reduction waves but almost no oxidation wave were found. PAQ will therefore not be further studied because of its irreversible nature. Turning eventually to CO_2-saturated electrolytes (blue lines in Figure IV. 19b), one reduction wave was observed for both AQ and DBBQ with its onset potential remain unchanged, suggesting that CO_2 does not participate in the initial electrochemical step. Interestingly, unlike for DMF electrolytes, a typical passivation behavior, i.e., the current drops to nearly zero at the end of reduction, is observed in MeCN electrolytes suggesting the precipitation of a solid product.

Li-CO_2 cells were then assembled using *in-situ* pressure cells to gain more insights into the reactions among Li^+, quinone anions and CO_2 in MeCN-based electrolytes. In the absence of

DBBQ, Li-CO_2 cell exhibited negligible discharge capacity (black line in Figure IV. 21a), consistent with the negligible current response previously measured with cyclic voltammetry (Figure A. 4. 8b). In contrary, Li-CO_2 cell with DBBQ discharged under the same condition delivered a notably greater capacity of ~ 6300 mAh g^{-1} at a voltage plateau of 2.69 V *vs* Li^+/Li (blue curve in Figure IV. 21a), along with a clear pressure drop (blue curve in Figure IV. 21b), confirming that the reduction of DBBQ in Li^+-containing MeCN electrolyte is associated with the consumption of CO_2. At first glance, our results could naively lead us to conclude that DBBQ significantly promotes the discharge in Li-CO_2 battery. However, a capacity of ~ 7900 mAh g^{-1} was obtained (red curve in Figure IV. 21a) when discharging the cell under argon, which is ~ 36 times higher than the theoretical capacity for the reduction of DBBQ itself (~ 216 mAh g^{-1}). This discrepancy could be explained by the use of $Li_{1-x}FePO_4$ negative electrode (metallic Li was not used because of its reactivity with MeCN). Indeed, given the high redox potential of $Li_{1-x}FePO_4$ (~ 3.45 V *vs* Li^+/Li), the reduced form of DBBQ generated at the positive electrode upon discharge can diffuse to the negative electrode side to be reoxidized. Therefore, to avoid such "shuttle effect" of quinones, a two compartment "Ohara" cell that integrates a lithium ion conductive glass ceramic membrane was thereby implemented. Correspondingly, a capacity of ~ 34 mAh g^{-1} was obtained in the cell discharged under argon (red curve in Figure IV. 21c), indicating that the crossover of DBBQ was effectively avoided. In contrast, a greater capacity of ~ 160 mAh g^{-1} was achieved when discharging the cell under CO_2 (blue curve in Figure IV. 21c). A slight pressure drop corresponding to the consumption of CO_2 by DBBQ anions was detected (blue curve in Figure IV. 21d), while the pressure was found constant in argon cell (red curve in Figure IV. 21d). Nevertheless, the small discharge capacity delivered by this Li-CO_2 cell does not allow for a reliable quantification of the amount of CO_2 consumed. Nevertheless, we could demonstrate the formation of Li_2CO_3 at the end of discharge by XRD (Figure IV. 22). Accordingly, a high potential (above 4.2 V *vs* Li^+/Li) typical for the oxidation of Li_2CO_3 was observed on charge (Figure A. 4. 9). For Li-CO_2 cell using AQ, a lower discharge voltage associated with a small pressure drop were obtained compared to those measured for DBBQ (Figures IV. 21e & 21f), in agreement with previous voltammetry study showing smaller reduction current response (Figure IV. 19b), and no crystalline phase could be assigned as the ultimate discharge product by means of XRD (Figure IV. 22).

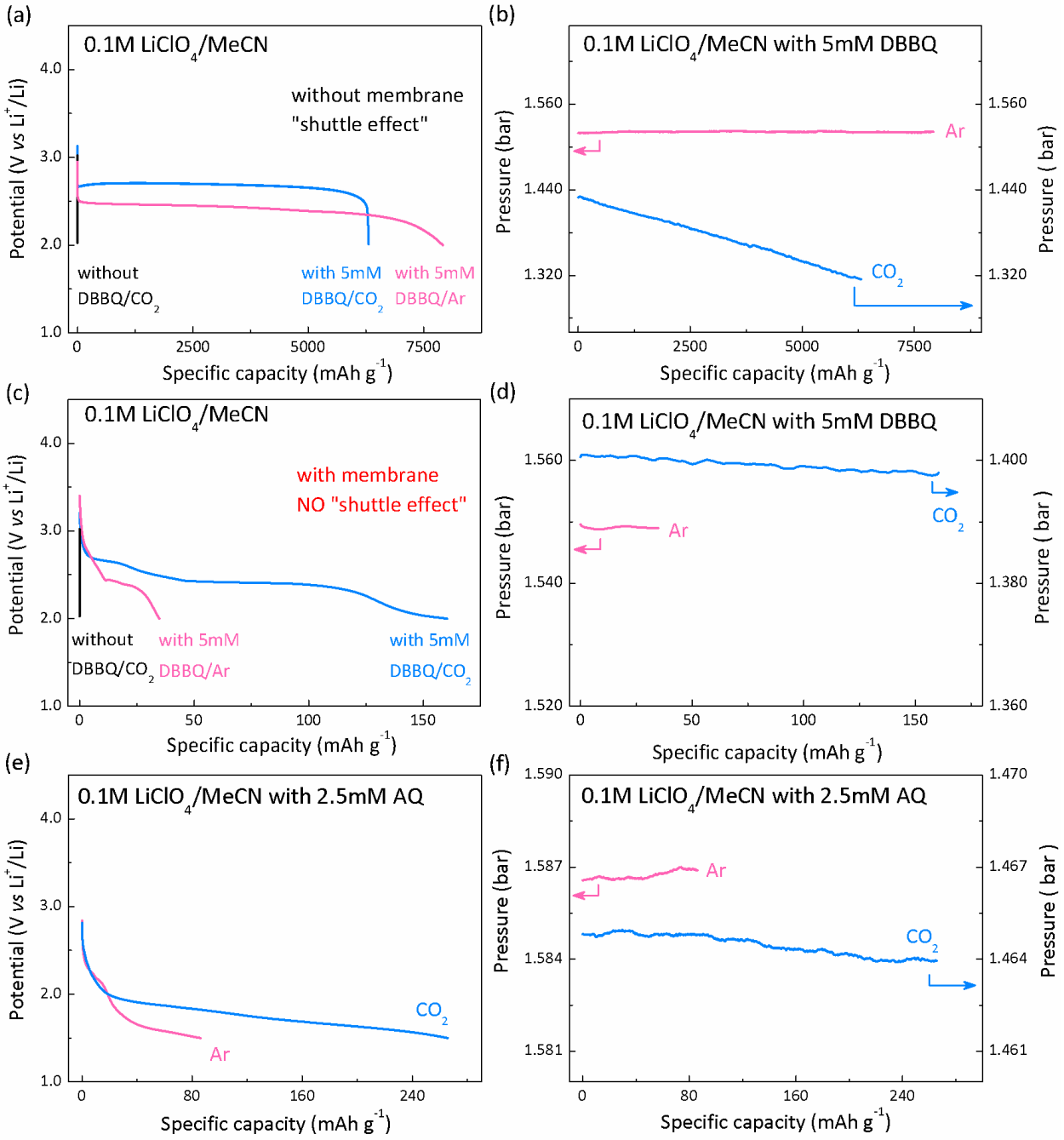

Figure IV. 21 Galvanostatic discharge curves (a) and their corresponding pressure changes (b) of Li batteries discharged in 0.1 M $LiClO_4$ /MeCN without DBBQ under CO_2 (black curve), and with 5 mM DBBQ under Ar (red curves) and CO_2 (blue curves) using a classical *in-situ* pressure cell. Galvanostatic discharge curves (c, e) and their corresponding pressure changes (d, f) of Li batteries discharged in 0.1 M $LiClO_4$ /MeCN with 5 mM DBBQ (c, d) and 2.5 mM AQ (e , f) under Ar (red curves) and CO_2 (blue curves) using a two-compartment "oraha" cell with a ceramic membrane to prevent the crossover of quinones.

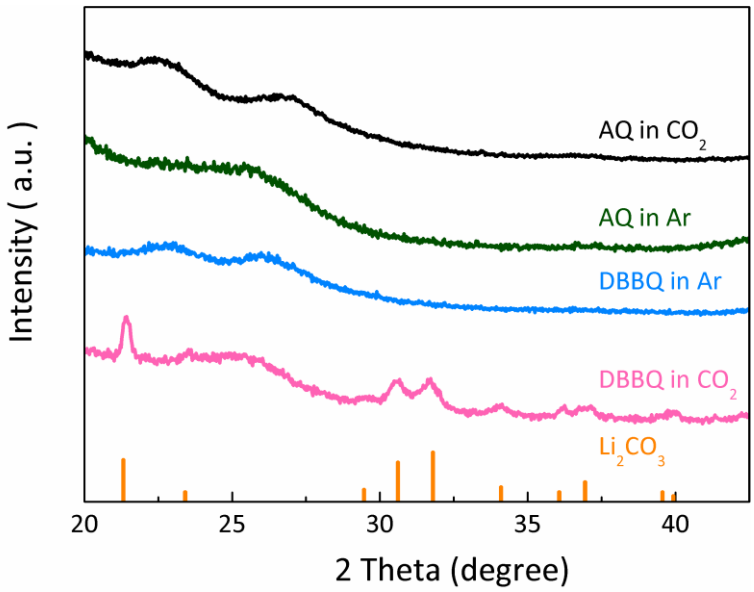

Figure IV. 22 X-ray diffraction of electrodes after discharging in MeCN with 5mM DBBQ under CO_2 (red line) and Ar (blue line); and with 2.5 mM AQ under CO_2 (black line) and Ar (green line). The broad peak at around 26 °is referred to carbon Super P.

In light of the fairly small discharge capacity obtained from the Li-CO_2 cell using DBBQ as a mediator, ^{1}H NMR was therefore employed to understand i) if soluble products are formed and ii) if degradation of electrolyte and/or DBBQ occurs (Figure IV. 23). Two signals at 6.47 ppm and 1.24 ppm were observed for the solution before discharge, corresponding to the aromatic protons and the protons in the methyl groups of the *tert*-butyl in DBBQ, respectively (Figure IV. 23a). After reduction (Figure IV. 23b), two distinct sets of ^{1}H NMR signals were detected in the regions of 6.1 - 6.7 ppm (shaded blue and labeled *a*) and 2.8 - 4.5 ppm (shaded grey and labeled *b*). The two peaks in region *a* around the signal for the aromatic protons of DBBQ can be assigned to the aromatic protons of the reduced form of DBBQ. Nevertheless, one cannot rule out that one of these two signals might arise from the aromatic protons of degradation products arising from the decomposition of DBBQ. The three new peaks in region *b* were not observed in the solution before reduction, indicating the formation of products with very different proton environment. Although we failed to successfully assign these species using 2D correlation NMR spectroscopy (not shown here), the use of liquid mass spectrometry suggested a quinone degradation mechanism associated with a dimerization phenomenon coupled with the loss of oxygen and tert-butyl groups (Figure IV. 24). Moreover, knowledge from Li-O_2 battery can be used to tentatively explain the formation of these peaks. Indeed, redox-active electrolyte additives are susceptible to degrade during battery

operation and in some cases can induce degradation of other battery components (e.g., solvents).[264] Hence, bearing in mind that reactive radical species, i.e., DBBQ anion radical, was formed after the initial electron transfer, we can suspect at this stage that these species in region *b* are likely originate from either the degradation of DBBQ itself or the nucleophilic attack of MeCN by DBBQ anion radical. Finally, the singlet at 1.31 ppm was assigned to the protons in the methyl groups of the *tert*-butyl group of the reduced DBBQ. Looking in more detail at the peaks at 6.47 ppm and at 1.24 ppm which were still present after reduction, one can deduce that a small amount of DBBQ remain unreacted. More importantly, the relative intensity measured for these two peaks clearly increased after bubbling the solution with CO_2 (Figure IV. 23c), which can be explained by the regeneration of DBBQ after CO_2 reaction, in a manner similar to the quinone mediated O_2 reduction.[89] No extra distinct signal and little change for the three peaks in region *b* were observed after CO_2 reaction, likely suggesting that the parasitic reactions are related to the initial electrochemical reduction step. To conclude, NMR analysis revealed the formation of side products during discharge which can possibly explain the limited capacity delivered in DBBQ mediated Li-CO_2 battery. This result further emphasizes the importance of the stability for both organic electrolyte solvents and their additives in harsh electrochemical environments for potential Li-gas battery technologies.

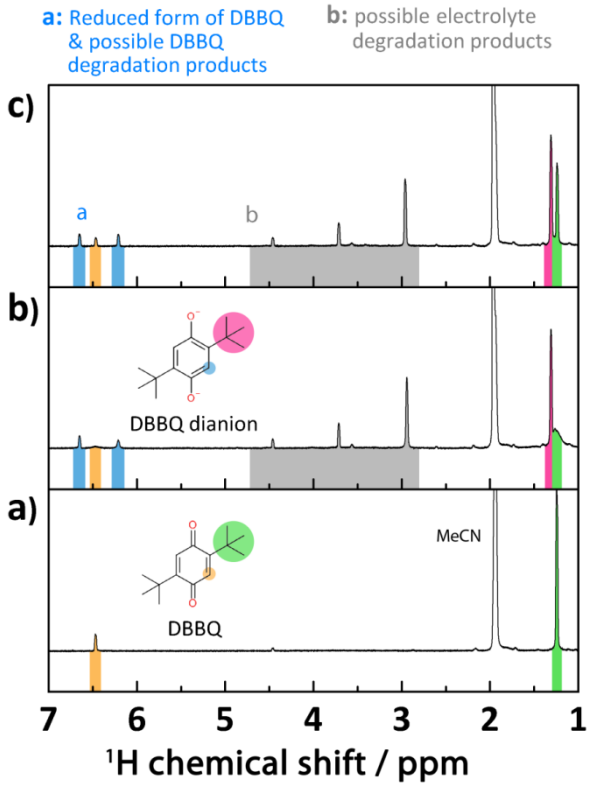

Figure IV. 23 ^{1}H NMR spectra of (a) d_3-MeCN + $LiClO_4$ + DBBQ, (b) d_3-MeCN + $LiClO_4$ + DBBQ after reduction and (c) d_3-MeCN + $LiClO_4$ + DBBQ after reduction and CO_2 reaction.

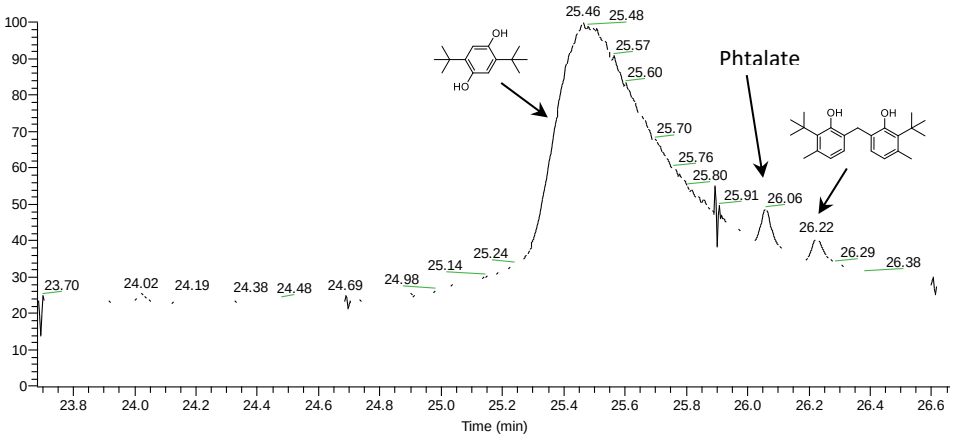

Figure IV. 24 Possible degradation products detected by liquid mass spectrometry in the solution of d_3-MeCN with DBBQ after reduction and reaction with CO_2. The solution was tested after a short exposure to the air, hence the formation of hydroxides.

IV. 3. 3 Conclusion

Firstly, we revealed an intimate chemical interaction between CO_2 and quinone dianions based on a push-pull mechanism. The effects of the chemical structure of quinones, the addition of Lewis acid cation (i.e., Li^+), and the electrolyte solvents on such interaction have also been considered. More specifically, weaker CO_2 interaction is observed for *ortho*-quinones than *para*-quinones because of the steric hindrance and coulombic repulsion induced by the two oxygens in *ortho* positions. Li^+ might impede the interactions between quinone and CO_2 when strong ion pairings are formed between Li^+ and quinone anions. The interaction of quinone and CO_2 can be altered via tuning the solvation strength of quinone anions by the electrolyte solvent, e.g., a stronger quinone interaction with CO_2 is observed in MeCN than in DMF.

Secondly, by adding DBBQ into the MeCN electrolyte, we evaluated the concept of quinone-mediated CO_2 reduction in Li-CO_2 batteries. The discharge voltage was found to be dictated by the reduction potential of DBBQ, which is more positive than that of CO_2 reduction. Moreover, Li_2CO_3 was identified as the ultimate discharge product. Nevertheless, the limited discharge capacity together with NMR results suggested parasitic reactions involving DBBQ itself and/or other cell components.

To conclude, the use of chemical catalysts is an effective approach to facilitate the electrochemical reduction of CO_2 in Li-CO_2 batteries. However, to take advantage of such approach, the catalyst should be properly selected to provide appropriate redox potential, proper catalytic activity towards CO_2 reduction, along with good electrochemical and chemical stability. Also of importance is the anode side, which needs to be protected by a solid electrolyte membrane to avoid the undesirable “shuttle effect”.

Chapter V General conclusion and outlook

Chapter V General conclusion and outlook

The ever-growing energy demands of modern society have instigated intensive researches in i) continuously pushing the energy limits of Li-ion batteries, especially at the positive electrode side, and ii) exploring new battery chemistries with potentially higher energy storage. Li-rich layered oxides are among the most promising positive electrode materials for high-energy Li-ion batteries, provided their superior capacities due to the cumulative cationic and anionic redox processes. Nevertheless, the activation of anionic redox generally induces structural instabilities associated with irreversible O_2 loss and cation migration, resulting in unfavorable performance decay upon cycling. In this work, an electrochemical method, i.e., rotating ring disk electrode (RRDE) voltammetry, was first introduced to follow the O_2 evolution phenomenon in Li-rich layered oxides. The dynamic structural evolutions linked with oxygen redox activities (both irreversible O_2 evolution and reversible oxygen redox), along with their influence on the electrochemical properties, were further investigated for a practically important $Li_{1.2}Ni_{0.13}Mn_{0.54}Co_{0.13}O_2$ phase. At last, the fundamental aspects of Li-CO_2 battery, an alternative to the conventional Li-ion battery, was explored.

The main contents and conclusions of this work include:

i) RRDE voltammetry was successfully developed as an alternative technique for monitoring the O_2 gas evolution from Li-rich layered oxides during high-potential charge process. In a typical RRDE measurement, the oxide of interest was deposited onto the disk electrode where its delithiation was controlled by cyclic voltammetry or galvanostatic cycling, whilst the ring electrode was fixed at a potential at which the reduction of O_2 could effectively takes place. Thanks to the rotation of the whole RRDE assembly, the evolved O_2 gas from the oxide can be transported to and reduced (detected) at the ring electrode. As a proof of concept, we conducted RRDE measurements using various Li-rich layered oxides, and the results were systematically compared with those obtained by two other well-established gas/pressure analysis techniques, i.e., OEMS and *in-situ* pressure cell. Through this comparative study, we could demonstrate that the proposed RRDE method can reliably detect O_2 while it has the advantage of being more sensitive, making it suitable for determining the onset of O_2 evolution and examining oxides that release a reduced amount of O_2. Moreover, owing to the simplicity of this approach, and the widespread of RRDE in

the fields of battery and electrocatalysis, we believe that it can be used for routine O_2 analysis when designing new materials that are prone to O_2 release. Despite of its positive attributes, an obvious optimization of RRDE method lies in the quantification of the total O_2 amount generated from the oxide. For that purpose, a calibration curve of the increase of reductive ring current as a function of the O_2 concentration at the disk surface may be obtained to deduce the "detection efficiency". RRDE voltammetry can also be extended to detect other type of gases such as CO_2, provided that the adequate ring electrode is selected.

ii) In light of previous works, O_2 loss from Li-rich layered oxides may facilitate cation migration and result in structure transformation. Therefore, we carried out a detailed study using a stellar Li-rich compound with nominal composition of $Li_{1.2}Ni_{0.13}Mn_{0.54}Co_{0.13}O_2$, in order to provide more in-depth insights into the coupling between structural dynamics and oxygen redox. By pushing the high-voltage oxidation as well as enlarging the discharge voltage window, we could propose a more holistic scenario for the structural evolution of $Li_{1.2}Ni_{0.13}Mn_{0.54}Co_{0.13}O_2$ during the first electrochemical cycle.

Starting on oxidation, the delithiation occurs first through the oxidation of the Ni^{2+} and Co^{3+} cations until the removal of 0.4 Li^+, followed by the oxidation of oxygen anions that triggers Mn-migration until 4.6 V (ca. $\Delta x < 1.0$). Afterwards, the delithiation further proceeds concomitantly with O_2 evolution, creating both cationic and anionic vacancies that are filled by migrated Mn ions, and eventually leading to the fully delithiated phase A' ($\Delta x = 1.15$). Through an arsenal of techniques including synchrotron X-ray and neutron diffraction, TEM, OEMS and ICP-OES, we identified phase A' as a densified O3 bulk structure enlisting Mn migration into the interlayer octahedral sites, in contrast to previous literatures proposing it as a densified layer[48,179] or spinel-like structure[157] which grows only at the surface. Combing *in-situ* laboratory XRD, OEMS and RRDE voltammetry, we revealed the conjoint removal of Li^+ and oxygen as the primary cause for the formation of phase A'. In terms of electrochemical properties, pushing the high-voltage oxidation to obtain the phase A' induces a drop in both the voltage and capacity on the subsequent discharge, which thus does not improve the long-term voltage fading. Several factors could contribute to such performance decay, including Mn-migration, the presence of O1-like defects, cation reduction (e.g., Co) driven by O_2 loss etc. However, further investigations are needed to

understand better their correlation, which will also provide useful guidance for designing Li-rich oxides with improved cycling performance.

Turning to the discharge (until 2.0 V), the anionic and cationic network of the phase A' are conjointly reduced along with only part of the migrated Mn ions returning to their initial positions, forming a discharge phase P' that differs from the pristine phase (ca. x = 1.03). By applying a constant voltage step at 2.0 V or discharging to lower voltages (ca. 1.4 V), additional Li^+ can be inserted through a solid-solution process to reach the nearly fully lithiated phase P' (ca. x = 1.15) enlisting substantial amount of Mn-migration. This result reveals that a major part of the capacity loss during the first cycle is actually of kinetic origin and linked to the sluggish Li^+ diffusion at high degree of lithiation. Upon further discharging to 1.2 V, the Li content of phase P' exceeds that of the pristine phase (ca. x = 1.43), leading to the growth of a new discharged phase P". Phase P" remains in the $R\bar{3}m$ space group with the same (*ccp*) oxygen stacking sequence pertaining to the pristine phase, but with some of the interlayer tetrahedral sites filled by Li^+. By gradually increasing the depth of charge, as well as designing a path to restore the migrated Mn ions in the phase P', we demonstrated that the formation of phase P'' is directly linked to the necessity of triggering the oxygen redox activity on charge, more specifically, the Mn-migration triggered by the oxygen redox. The cation mixing in the phase P" likely favors the stabilization of the oxygen sublattice, preventing the layered to 1T phase transition upon overlithiation. Although we have showed the positive effects of obtaining the fully lithiated phase P' in recovering the first-cycle irreversible capacity loss, application-wise, the exploitation of the low-voltage activity does not provide substantial improvement regarding the energy density, whilst retains the voltage fade and hysteresis pertaining to $Li_{1.2}Ni_{0.13}Mn_{0.54}Co_{0.13}O_2$. In light of the recovery of voltage and the original stair-case charge profile after restoring the cation ordering by the heat treatment, future research directions could therefore be explored regarding the impact of cation disordering on the electrochemical characteristics, and to design materials with reversible cation migration.

During the subsequent charge, phase P' releases Li^+ through a solid-solution process, which differs from the two-phase process (A → A' phase transition) on the first charge, leading to the formation of phase A' at the end of 2nd CC-CV charge. This finding suggests that although O_2 evolution is critical to the initial formation of phase A', once it forms, it can reversibly uptake and release Li^+ without the need for having more anionic vacancies.

iii) We investigated the fundamentals of Li-CO_2 chemistries which were explored in the battery community as an alternative end-use of CO_2. Firstly, the electrolyte solvents were found to be very crucial in dictating the reaction mechanisms of Li-O_2/CO_2 batteries. Two distinct discharge reaction pathways were identified herein. Following the initial discharge step, which is the electrochemical reduction of O_2 into superoxide, the superoxide intermediate can either react with Li^+ to form Li_2O_2 that further chemically reacts with CO_2 to give Li_2CO_3 (denoted as the chemical pathway), or first react with CO_2 and then Li^+ to electrochemically form Li_2CO_3 (denoted as the electrochemical pathway). Through a comparative study using three electrolyte solvents with various physico-chemical parameters, we revealed that the competition between the two reaction pathways depends strongly on the Li^+ solvation, which is reflected by the donor number (DN) of the solvent. In high DN solvent like DMSO, due to the strong solvation of Li^+, the superoxide tends to react with CO_2; consequently, Li_2CO_3 is mainly formed through the electrochemical pathway. Whereas in low DN solvent like DME, the reaction between superoxide and Li^+ is more favored and Li_2CO_3 is predominantly formed through the chemical pathway. Although the abovementioned scenario rationalizes the major difference in the discharge processes of Li-O_2/CO_2 batteries, further investigation into the electrochemical pathway are necessary to identify the reaction steps following the reaction between the superoxide and CO_2. Concerning the charge, Li-O_2/CO_2 batteries are not rechargeable in their present form, as we found that only CO_2 is evolved during the oxidation of Li_2CO_3, and no O_2. To overcome this limitation, interesting future directions might be i) tuning the oxidation of Li_2CO_3 into a reversible manner; and ii) altering the discharge reaction so as to avoid the formation of "troublemaker" Li_2CO_3.

Secondly, in contrasts with many literatures, our findings reveal that CO_2 cannot be directly reduced in aprotic solvents within their electrochemical window using carbon electrodes (DME, DMSO and MeCN were investigated herein). Correspondingly, no electrochemical activity was observed in pure Li-CO_2 batteries. Future investigations are therefore necessary to explain such discrepancy in electrochemical activity.

Finally, bearing in mind the inertness of CO_2 in these solvents, we evaluated the use of quinones as solution catalysts, aiming to facilitate the electrochemical reduction of CO_2 in Li-CO_2 battery. The concept was validated by the demonstration of a DBBQ-mediated Li-CO_2 battery with Li_2CO_3 as the ultimate discharge product. Nevertheless, the limited discharge capacity together with

NMR analysis highlights the degradation of DBBQ itself and/or other cell components under operative conditions. These results emphasize that the choice of catalyst is critical. Hence, a suitable solution catalyst should provide appropriate redox potential, proper catalytic activity towards CO_2 reduction, along with good electrochemical and chemical stability. To take advantage of this mediator approach, it is also essential to protect the anode side by a solid electrolyte membrane to avoid the undesirable “shuttle effect”.

Appendix

Appendix

A. 1 Design of experimental equipment

A. 1.1 Gas filling station

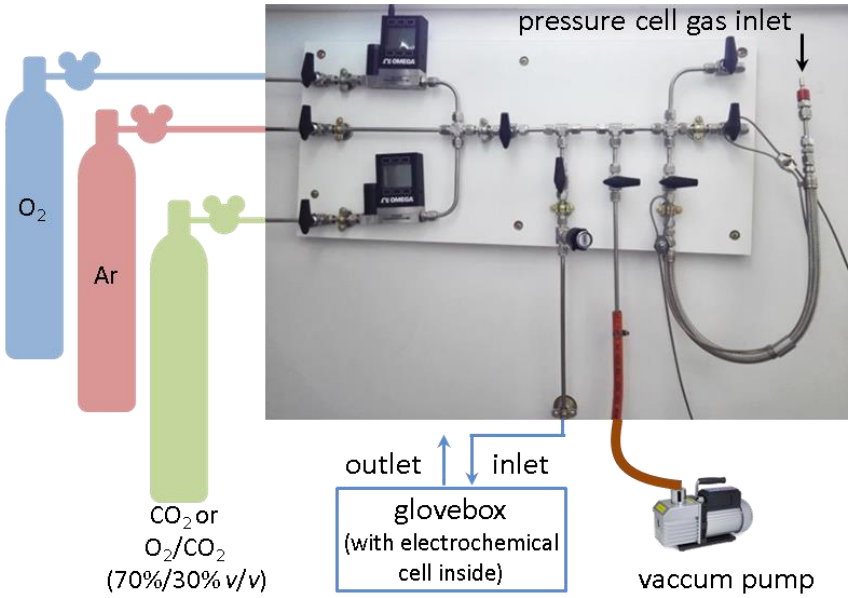

Figure A. 1. 1 Schematic of the gas filling station developed in this Ph.D. work which enables a purging/refilling of the *in-situ* pressure cell and the electrochemical cell located inside the glovebox with desired gases.

A. 1. 2 Description of OEMS systems

The closed OEMS system used in this work comprises an electrochemical cell (with a detailed description in Chapter II. 2. 2), a BioLogic galvanostat /potentiostat and an ExQ gas analysis system (Hiden Analytical, USA). The ExQ system is composed of a HAL series quadrupole mass spectrometer, an Ultra-High Vacuum (UHV) mass spectrometer vacuum chamber, a vacuum pumping system and a QIC series capillary inlet. The whole system is controlled by a MASsoft 7 professional software.

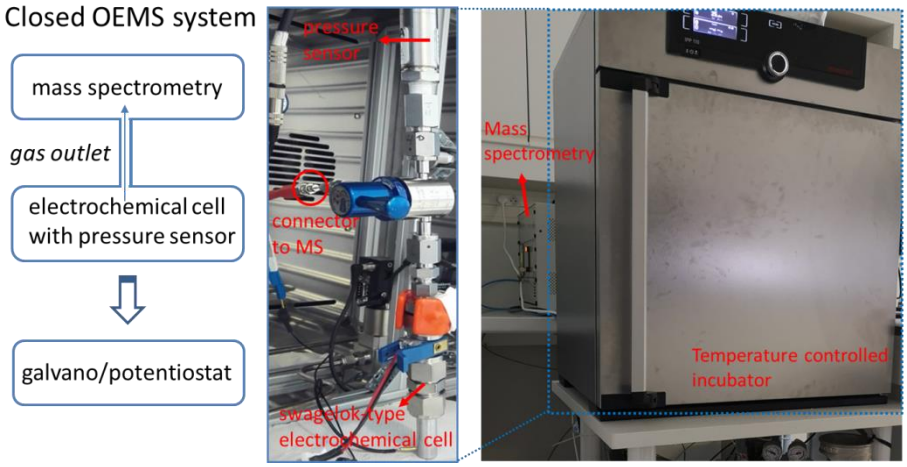

Figure A. 1. 2 Schematic and photograph of the closed OEMS system.

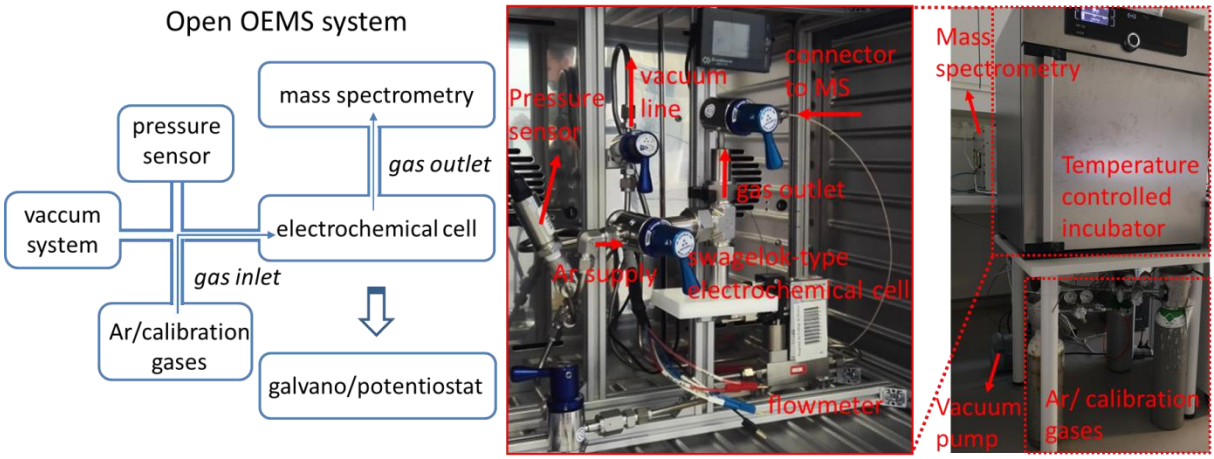

Figure A. 1. 3 Schematic and photograph of the open OEMS system developed in this Ph.D. work.

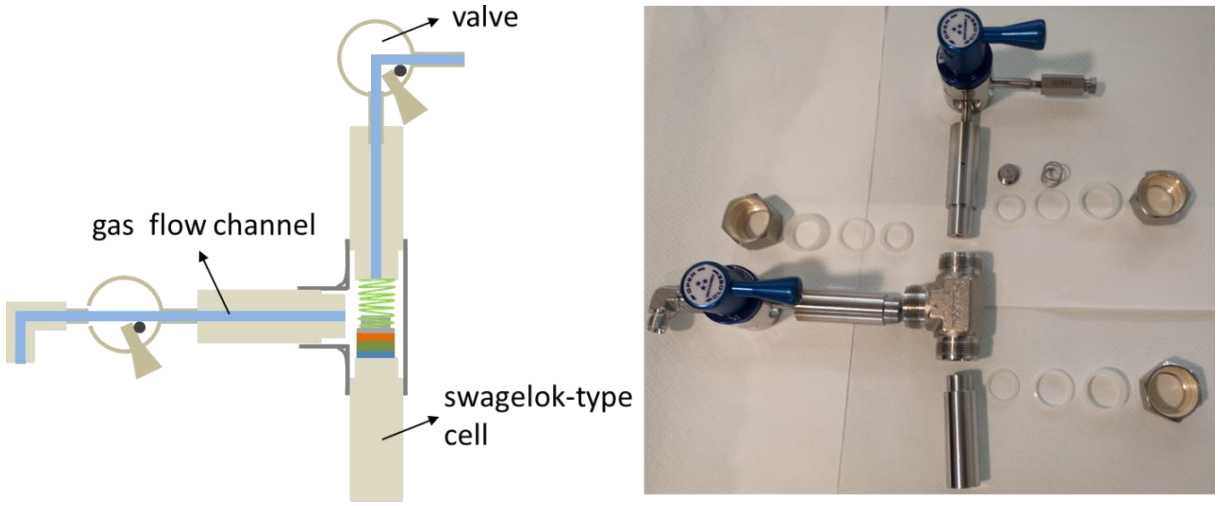

Figure A. 1. 4 Schematic and photograph of the electrochemical cell dedicated to the open OEMS system.

A. 2 Supporting information for Chapter II

A. 2. 1 Methods

Materials. $Li_{1.2}Ni_{0.13}Mn_{0.54}Co_{0.13}O_2$ was prepared by co-precipitation combined with solid-state synthesis,[43] $Li_2Ru_{0.75}Ti_{0.25}O_3$ and $Li_2Ru_{0.5}Ti_{0.5}O_3$ were prepared by classical solid-state synthesis, as described in details elsewhere.[154] $LiNi_{1/3}Mn_{1/3}Co_{1/3}O_2$ (> 98%) and Carbon Super P (Csp) were purchased from Sigma-Aldrich and MTI Corporation, respectively. LP30 electrolyte (99.9 %) made of 1 M $LiPF_6$ dissolved in 1:1 *v*/*v* Ethylene carbonate/Dimethyl carbonate was purchased from Solvionic, France.

Preparation of self-standing $Li_{1-x}FePO_4$ film. Self-standing $Li_{1-x}FePO_4$ film is composed of 85 wt.% (by weight) $LiFePO_4$, 10 wt.% Csp and 5 wt.% polytetrafluoroethylene (PTFE).[151] A blend of $LiFePO_4$ and Csp was first mix in a SPEX 8000M ball-miller for 15 min before adding PTFE (60 wt.% dispersion in H_2O, Sigma-Aldrich). After several minutes' hand grinding, a few drops of isopropanol (Sigma-Aldrich) were gradually added into the mixture and further hand grinded before obtaining one piece of elastic dough. This dough was tape-casted into a 0.5 mm thick film and further punched into 11 mm diameter self-standing disks which were washed with a water/ethanol solution before being dried overnight at 80 ℃ under vacuum in BÜCHI oven and

transferred into the glovebox. Every single as-prepared LFP electrode (60 to 65 mg per cm^2) was then pre-charged in a Swagelok-type cell with metallic lithium as counter electrode and LP30 as electrolyte until it reached a constant plateau with a stable potential of 3.45 V *vs* Li/Li^+. To recover the pre-charged $Li_{1-x}FePO_4$ electrode, the Swagelok cell was disassembled in the glovebox, washed with dimethylcarbonate at least three times and dried under vacuum.

RRDE setup. All RRDE experiments were performed in an argon filled glovebox (water content < 0.5 ppm, oxygen content < 0.1 ppm) with a five-neck glass cell sealed with rubber stoppers, except a bubbler which was connected to a gas line that allows feeding the cell with dry argon (5.0 quality, Linde France), and a needle which was inserted into the cell as a gas outlet. The RRDE tip consists of an inter-changeable glassy carbon disc of 5.0 mm in diameter and a platinum ring with an internal diameter of 6.5 mm and an external diameter of 7.5 mm (E6 series, Pine Research Instrumentation, USA). Prior to its use, both platinum ring and glassy carbon disk were polished sequentially with alumina suspensions of 0.5, 0.3, 0.05 μm (Allied Tech Products Inc., USA), followed by sonication with DI water and an electrochemical cleaning procedure in 0.5 M H_2SO_4 solution until typical characteristic cyclic voltammograms were obtained.[265,266] The reference electrode (Ag^+/Ag, RE-7, ALS Co., Ltd) consists of a silver wire, a glass tube filled with a MeCN/0.1 M $TBAClO_4$/0.01 M $AgNO_3$ solution (ALS Co., Ltd) and sealed with a Vycor 7930 frit (ALS Co., Ltd). The reference electrode was assembled in the glovebox at least 24 hours before use and was stored partially immersed in a MeCN/0.1 M $TBAClO_4$ solution. Self-standing $Li_{1-x}FePO_4$ film was used as the counter electrode. The LP30 electrolyte with water content less than 10 ppm, as deduced by Karl Fischer titration (Coulometric KF titration, Metrohm), was first purged with argon. The typical volume of electrolyte used was 10 mL for each experiment. The potential difference between Ag^+/Ag reference electrode and Li^+/Li redox potential was measured to be 3.19 V in LP30, and all potentials in this work were corrected using this potential difference. All the experiments were operated on an AFMSRCE rotator (PINE Research Instrumentation, USA) and a VMP3 Bipotentiostat (BioLogic Science Instruments, France).

Fabrication of layered oxide casted disk electrodes. A blend of active material and Csp at a 4:1 mass ratio was hand-grinded with N-methyl pyrrolidine (NMP)/poly (vinylidene fluoride) (PVDF) solution for 10 minutes and then stirred for another 1 hour, yielding a slurry with the final concentrations of 10 mg_{oxide} mL_{slurry}^{-1}, 2.5 mg_{Csp} mL_{slurry}^{-1} and 1.25 mg_{PVDF} mL_{slurry}^{-1}. Next, 10 μL of

as-prepared slurry was drop-casted onto a 0.196 cm^2 glassy carbon disk. The oxide layer on the glassy carbon disk was dried under vacuum at room temperature for 1 hour prior to be dried further for 6 hours at 55 °C under vacuum in BÜCHI oven. The electrode had a final composition of 100 μg_{oxide}, 25 μg_{Csp}, and 12.5 μg_{pvdf}. The uniformity of such as-prepared electrodes was verified by scanning electron microscopy (SEM) (Figure A. 2. 1). The Csp electrode was prepared in a similar manner, except that the slurry was obtained with a mixture of Csp and PVDF at a 6:4 mass ratio. The collection efficiency, N, of the RRDE geometry remained unchanged on a Csp supported disk at 25.05% ± 0.15 as evaluated by the redox reaction of ferrocene/ferrocenium ($K_3Fe(CN)_6$ was not used here due to solubility limitation in LP30 electrolyte) (Figure A. 2. 2). Similar collection efficiencies were obtained on both bare and Csp-supported disk electrodes which 1) justify the electrode preparation method proposed here and 2) demonstrate that the low collection efficiency found in the present work is originating from gas solubility issues and not from a modification of the laminar flow by the particles.

Electrochemical cycling of *in-situ* pressure cell and OEMS cell. All electrochemical tests were performed with BioLogic galvanostat/potentiostats (BioLogic Science Instruments, France). A typical electrochemical cell is made with metallic lithium foil counter electrode (Sigma-Aldrich), two layers of glass fiber separators (Whatman GF/D, United Kingdom) soaked with LP30 electrolyte and positive electrode in powder form. The positive electrode is composed of active materials and Csp at a 4:1 mass ratio. Prior to be cycled, the pressure cells were kept under open-circuit voltage at 25 °C for at least 10 h in a temperature-controlled incubator (IPP260, Memmert) in order to stabilize the internal cell pressure. After assembly, the OEMS cells were flushed and pressurized with pure argon to avoid any contamination from the glove box atmosphere. Prior to perform the galvanostatic cycling, the OEMS cells were typically held at open circuit voltage for approximately 1.5 hours to reach a gas-liquid equilibrium phase inside the cell, and therefore to obtain a stable baseline value for all the partial pressure signals. During the OEMS measurements, the internal cell pressure was continuously measured by the pressure sensor and the produced gaseous species were continuously sampled from the cell head space to the mass spectrometer via a thin capillary (1/16″ diameter) at a leak rate of 12.5 $\mu L\ min^{-1}$. The partial pressures are eventually determined for each gas based on their mass to charge ratio (m/z). After ionization in the ionization source of the MS, separation in the mass analyzer and further detection in the ion detector, the partial pressures at m/z = 32, m/z = 44 were used to determine the evolution of O_2 and CO_2,

respectively. All the partial pressure signals were normalized to the partial pressure of the ^{36}Ar isotope to correct for fluctuations of pressure. The specific gas evolution rate is obtained by processing the first order derivative of the normalized partial pressure *vs* time profile.

A. 2. 2 Supporting figures

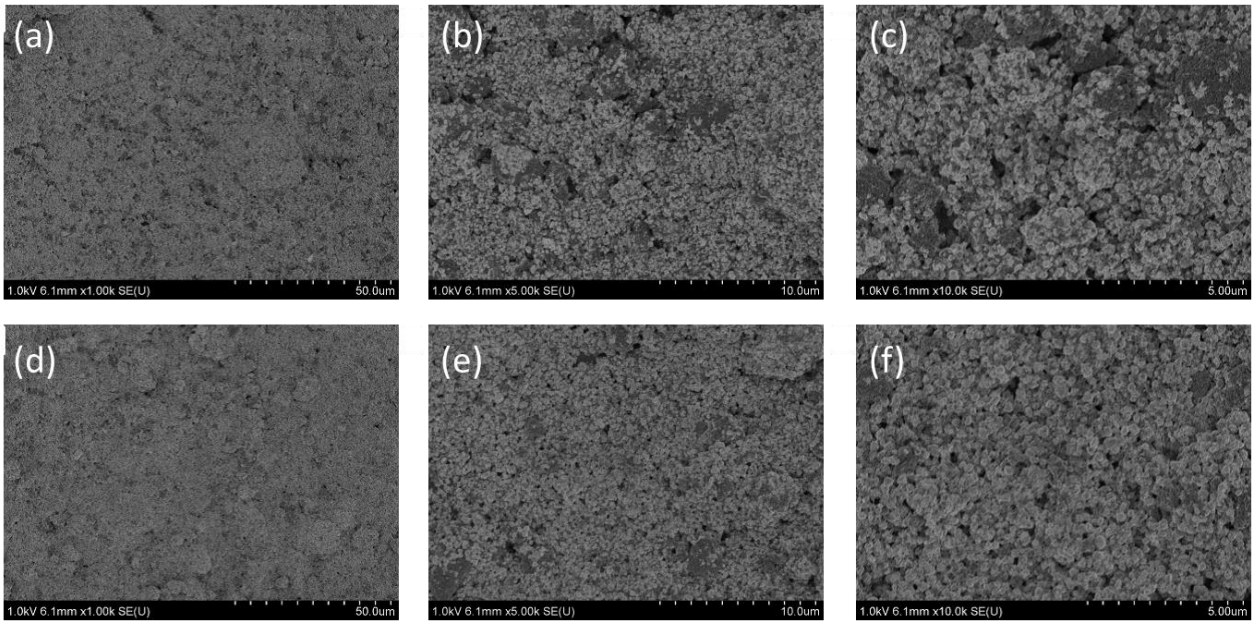

Figure A. 2. 1 Scanning electron microscopy (SEM) images of $Li_2Ru_{0.5}Ti_{0.5}O_3$-casted disk electrode at various resolutions, images of two electrodes were presented to show the reproducibility: electrode 1 (a ~ c), electrode 2 (d ~ f).

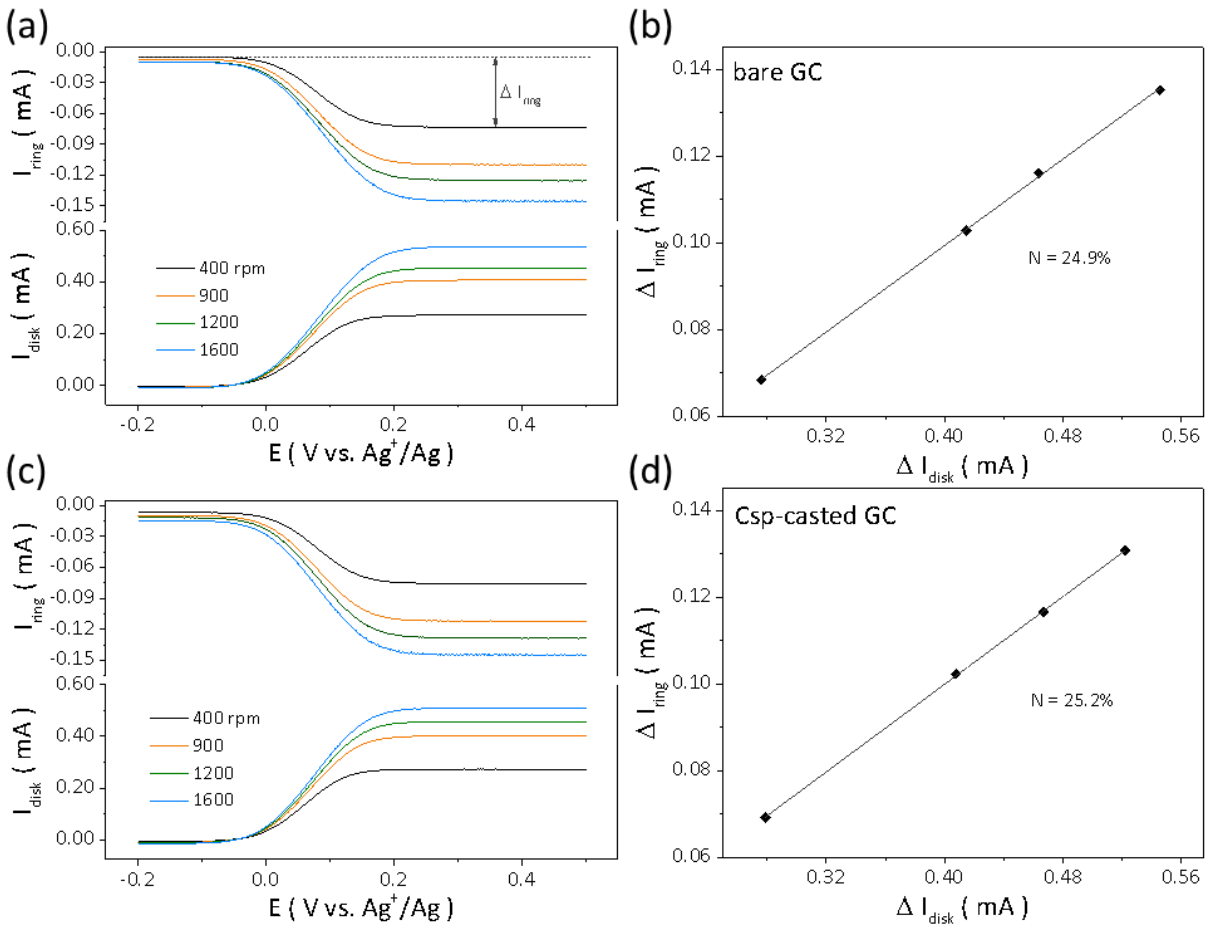

Figure A. 2. 2 Ring and disk currents for the determination of the collection efficiency, N, on bare (a) and Csp-casted (c) glassy carbon disk electrodes in LP30 electrolytes with 10mM Ferrocene, positive scan at 10 mV s^{-1}, E_{ring} = -0.4 V *vs* Ag^+/Ag. Ring currents as a function of disk currents and the N value of RRDE tips with bare (b) and Csp-casted (d) glassy carbon disk electrodes, respectively.

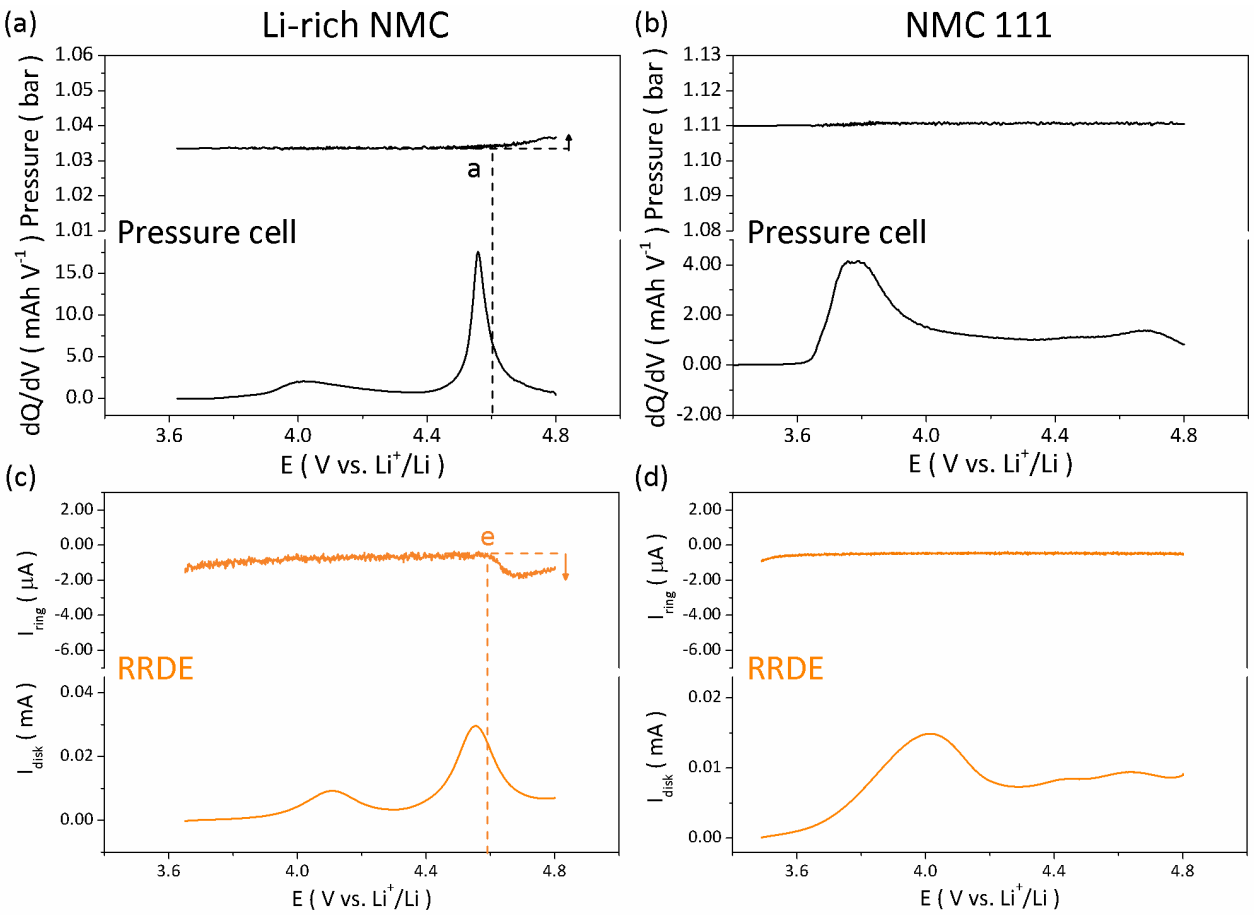

Figure A. 2. 3 Differential capacity (*dQ/dV*) *vs* V plots (bottom panels) and their respective pressure changes (top panels) for Li-rich NMC (a) and NMC 111 (b) derived from the galvanostatic charging curves in pressure cells charged at a current rate of 0.3 C to 4.8 V *vs* Li^+/Li. RRDE profiles for Li-rich NMC (c) and NMC 111 (d) measured in LP30 electrolyte. Bottom panels present the linear scan voltammograms obtained in the disk electrodes at a scan rate of 0.1 mV s^{-1} to 4.8 V *vs* Li^+/Li. Top panels illustrate their corresponding ring current responses.

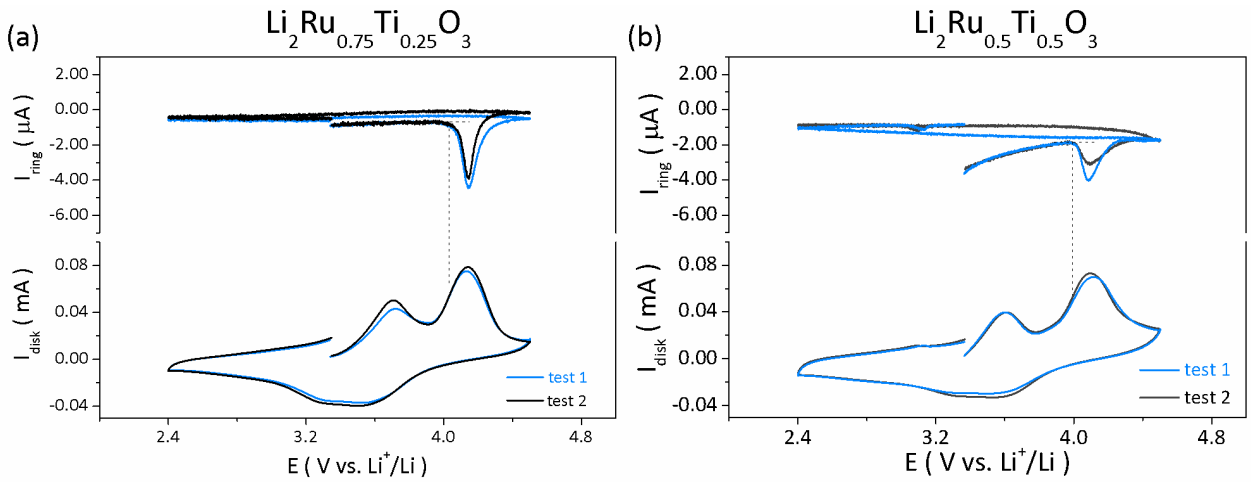

Figure A. 2. 4 Two identical RRDE experiments for (a) $Li_2Ru_{0.75}Ti_{0.25}O_3$ and (b) $Li_2Ru_{0.5}Ti_{0.5}O_3$, showing fairly reproducible electrochemical performance in the disk (bottom panel), and ring current response (top panel, corresponding to O_2 detection).

A. 2. 3 Calculation of the quantity of released O_2 gas

1, $Li_2Ru_{0.5}Ti_{0.5}O_3 \rightarrow Li_{2-x}Ru_{0.5}Ti_{0.5}O_{3-2y} + x\ e^- + x\ Li^+ + y\ O_2$

Total charge detected in the ring: 3.04177 e^{-4} mAh

Collection efficiency: 25 %

Total charge compensated by oxygen redox: 12.16708 e^{-4} mAh

Total amounts of O atoms loss: 0.0227 µmol

Total O atoms in the material: 2.2 µmol

Percentage of O loss from $Li_2Ru_{0.5}Ti_{0.5}O_3$: 1.036 %

2, $Li_2Ru_{0.75}Ti_{0.25}O_3 \rightarrow Li_{2-x}Ru_{0.75}Ti_{0.25}O_{3-2y} + x\ e^- + x\ Li^+ + y\ O_2$

Total charge detected in the ring: 1.66337 e^{-4} mAh

Collection efficiency: 25 %

Total charge compensated by oxygen redox: 6.65348 e^{-4} mAh

Total amounts of O atoms loss: 0.0123135 μmol

Total O atoms in the material: 2 μmol

Percentage of O loss from $Li_2Ru_{0.75}Ti_{0.25}O_3$: 0.62 %

Table A. 2. 1 The final composition for Li-rich compounds after the initial charge calculated based on RRDE and pressure measurements

oxides	RRDE				Pressure cell
	25%	20%	10%	5%	
$Li_2Ru_{0.5}Ti_{0.5}O_3$	$LiRu_{0.5}Ti_{0.5}O_{2.97}$	$LiRu_{0.5}Ti_{0.5}O_{2.96}$	$LiRu_{0.5}Ti_{0.5}O_{2.94}$	$LiRu_{0.5}Ti_{0.5}O_{2.88}$	$Li_{0.65}Ru_{0.5}Ti_{0.5}O_{2.74}$
$Li_2Ru_{0.75}Ti_{0.25}O_3$	$Li_{0.5}Ru_{0.75}Ti_{0.25}O_{2.98}$	$Li_{0.5}Ru_{0.75}Ti_{0.25}O_{2.97}$	$Li_{0.5}Ru_{0.75}Ti_{0.25}O_{2.95}$	$Li_{0.5}Ru_{0.75}Ti_{0.25}O_{2.9}$	$Li_{0.25}Ru_{0.75}Ti_{0.25}O_{2.69}$
Li-rich NMC	$Li_{0.262}(NMC)O_{1.954}$	$Li_{0.262}(NMC)O_{1.94}$	$Li_{0.262}(NMC)O_{1.88}$	$Li_{0.262}(NMC)O_{1.76}$	$Li_{0.215}(NMC)O_{1.76}$

A. 3 Supporting information for Chapter III

A. 3. 1 Methods

Material synthesis and characterization. $Li_{1.2}Ni_{0.13}Mn_{0.54}Co_{0.13}O_2$ powder was synthesized by a two-step process involving the co-precipitation of carbonate precursor followed by two annealing steps.[43] Synchrotron X-ray diffraction (XRD) measurements were performed on the 11-BM beamline of the Advanced Photon Source at Argonne National Laboratory, with a wavelength of 0.4128 Å. Neutron powder diffraction pattern was collected with the high resolution powder diffractometer SPODI in Forschungs-Neutronenquelle Heinz Maier-Leibnitz (FRM II) at Technical University of Munich with a wavelength of 1.5482 Å. *In-situ* XRD measurements were carried out using an airtight electrochemical cell equipped with a Beryllium window in a BRUKER D8 Advance diffractometer with Cu Kα radiation source ($\lambda_{K\alpha1}$ = 1.54056 Å, $\lambda_{K\alpha2}$ = 1.54439 Å). Electron diffraction (ED) patterns, high angle annular dark field scanning transmission electron microscopy (HAADF-STEM) images, annular bright field scanning transmission electron microscopy (ABF-STEM) images were obtained with an aberration-corrected Titan G3 electron microscope operated at 200 kV. TEM sample was prepared in an Ar-filled glove box by crushing the crystals in a mortar with dimethyl carbonate and depositing drops of suspension onto holey carbon grids. A specialized Gatan vacuum transfer holder was also used for the TEM analysis.

Electrochemical tests. All the electrochemical characterization was performed in CR2032-type coin cells, which were assembled in Ar-filled glovebox with metallic lithium as negative electrode and two glass-fiber separators (Whatman, United Kingdom) soaked with LP30 electrolyte (1 M $LiPF_6$ dissolved in 1:1 *v*/*v* ethylene carbonate/dimethyl carbonate, Solvionic, France). A blend of $Li_{1.2}Ni_{0.13}Mn_{0.54}Co_{0.13}O_2$ and carbon super P loose powder at a 4:1 mass ratio was hand-ground for 15 min before using as the positive electrode. Galvanostatic cycling tests were performed at C/5, unless specified otherwise. All the *ex-situ* samples were prepared using Swagelok-type cells with similar cell stacking described above. The as-recovered samples were washed with dimethyl carbonate for at least three times before being dried under vacuum. The near - equilibrium voltage profiles of the first discharge were obtained using galvanostatic intermittent titration technique (GITT, every $\Delta x = 0.05$) with the relaxation process controlled by either $dV/dt \leq 0.01$ mV s^{-1} or

time = 4 h. The Ohmic resistance was deduced from the voltage jump in a short time (1 s) after the application of the current pulse.

Gas analyses. A homemade cell was developed for **online electrochemical mass spectrometry (OEMS)** experiments as described elsewhere.[267] A slurry consisting of 72 wt.% of cathode active material, 18 wt.% of carbon Super P, and 10 wt.% of Polyvinylidene fluoride or polyvinylidene difluoride (PVDF) binder was coated on one side of a Celgard 2400 separator (22 mm in diameter) with a wet thickness of 200 µm. Lithium discs with 20 mm in diameter were used as the counter and reference electrode with 120 µL of LP30 electrolyte. **Rotating ring disk electrode (RRDE)** measurements were performed with a four-electrode cell configuration as described in Chapter A. 2. 1.[145] The glassy carbon disk electrode was coated by slurry with the final concentrations of 10 mg_{oxide} mL_{slurry}^{-1}, 2.5 mg_{Csp} mL_{slurry}^{-1} and 1.25 mg_{PVDF} mL_{slurry}^{-1}. The platinum ring electrode was kept at a potential sufficient for oxygen reduction reaction (i.e., 2.5 V). The reference electrode (Ag^{+}/Ag, RE-7, ALS Co., Ltd) consists of a silver wire, a glass tube filled with a MeCN/0.1 M $TBAClO_4$/0.01 M $AgNO_3$ solution (ALS Co., Ltd) and sealed with a Vycor 7930 frit (ALS Co., Ltd). Self-standing $Li_{1-x}FePO_4$ film was used as the counter electrode following a preparation method as described in Chapter A. 2. 1.[151]

X-ray absorption spectroscopy (XAS). Self-standing films consisting of 74 wt.% of $Li_{1.2}Ni_{0.13}Mn_{0.54}Co_{0.13}O_2$, 18 wt.% of carbon Super P, and 8 wt.% of Polytetrafluoroethylene (PTFE) were used and cycled to the desired state of charge or discharge. After washing with dimethyl carbonate and drying under vacuum, the cycled electrodes were then placed between two layers of Kapton tape and sealed under argon atmosphere in an air-tight transparent plastic bag. *Ex-situ* XAS measurements at the three transition-metal (Ni, Co, Mn) K-edge were performed in transmission mode at the ROCK beamline of synchrotron SOLEIL (France).

X-ray photoelectron spectroscopy (XPS). Loose powder consisting of 90 % of $Li_{1.2}Ni_{0.13}Mn_{0.54}Co_{0.13}O_2$ and 10 % of carbon Super P was used and cycled to the desired state of charge. XPS measurements were carried out with a Kratos Axis Ultra spectrometer, using focused monochromatic Al Kα radiation source ($h\nu$ = 1486.6 eV). The XPS spectrometer was directly connected through a transfer chamber to an argon dry box, to avoidmoisture/air exposure of the samples. The analyzed area of the samples was 300 × 700 μm^2. Peaks were recorded with constant

pass energy of 20 eV. For the Ag $3d_{5/2}$ line, the full width at half maximum (FWHM) was 0.58 eV under the recording conditions.

Mild-temperature annealing of the cycled $Li_{1.2}Ni_{0.13}Mn_{0.54}Co_{0.13}O_2$ electrodes. Loose powder of $Li_{1.2}Ni_{0.13}Mn_{0.54}Co_{0.13}O_2$ and carbon super P at a 4:1 mass ratio was used as positive electrode, and charged to 4.6 V prior to be discharged 2.0 V in a Swagelok-type cell. The cycled samples were recovered in Ar-filled glovebox, washed with dimethyl carbonate for three times and dried under vacuum before annealing under Ar atmosphere at 250°C for 1 h. After the annealing, the as-obtained powders were assembled in a CR-2032 type coin cell against metallic lithium to evaluate the impact of annealing on their electrochemical properties.

A. 3. 2 Supporting figures

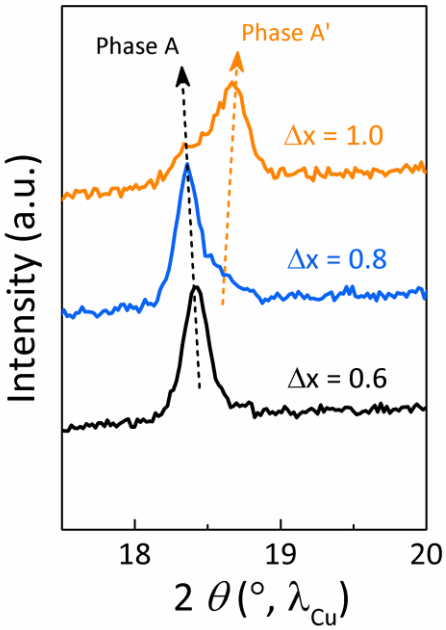

Figure A. 3. 1 Selective region of the laboratory XRD patterns for *ex-situ* samples charged to various states (i.e., the amount of Li removal Δx = 0.6 (black curve), 0.8 (blue curve), and 1.0 (yellow curve)) and followed with an OCV step for 120 h. The more $Li_{1.2}Ni_{0.13}Mn_{0.54}Co_{0.13}O_2$ is delithiated, the more growth of phase A'.

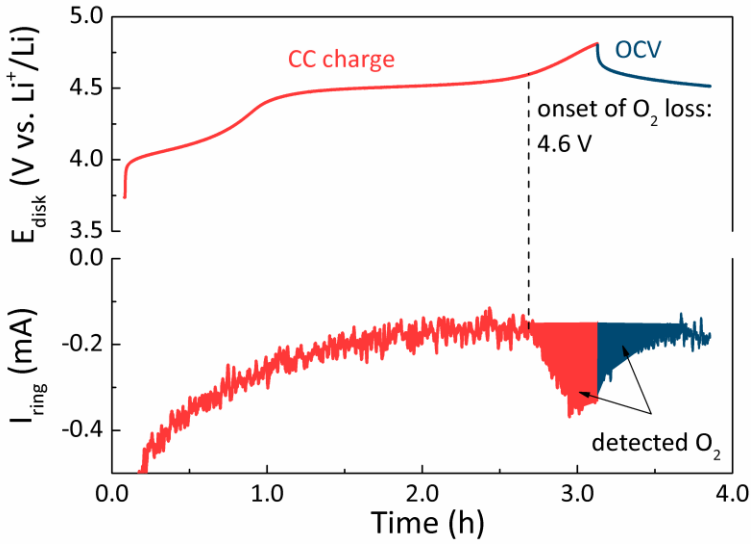

Figure A. 3. 2 RRDE profiles measured for the first charge of $Li_{1.2}Ni_{0.13}Mn_{0.54}Co_{0.13}O_2$ to 4.8 V, following with an OCV step. Top panel presents the galvanostatic charge curves obtained in the disk electrode. Bottom panel illustrates the corresponding ring current responses. Dash black line marks the onset of O_2 loss that is located at the end of charge (ca. 4.6 V). Filled blue area in the bottom panel reveals that O_2 continues to evolve during the OCV.

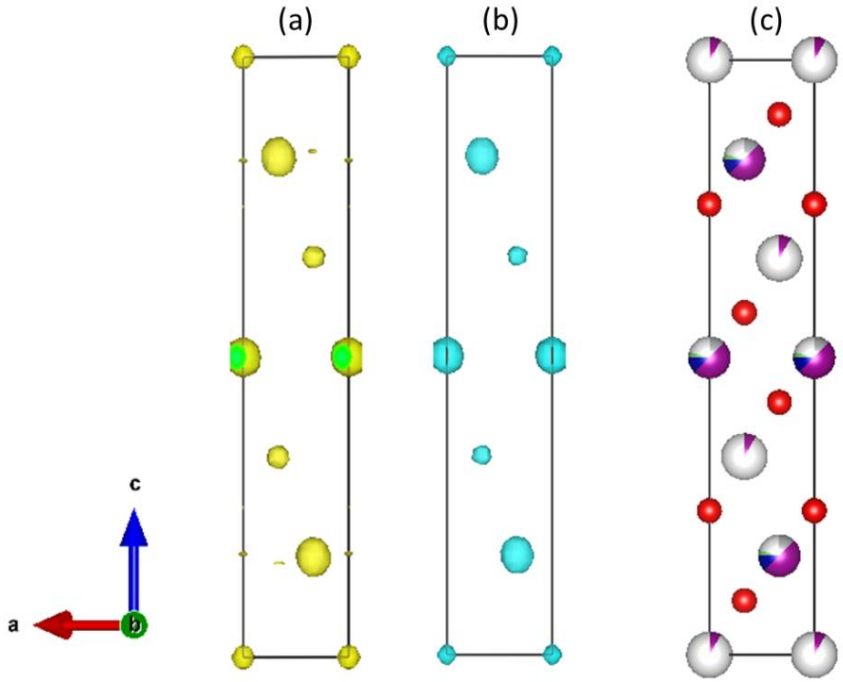

Figure A. 3. 3 Difference-Fourier Maps generated from the neutron (a) and synchrotron (b) XRD patterns of the A' phase. The difference was calculated after having removed all the transition metals from the structure (Ni, Mn and Co), clearly showing density on the octahedral sites, and not on the tetrahedral sites. Panel (c) presents a view of the structure as deduced from the combined refinement of the neutron and XRD patterns (oxygen is red, Mn is purple, Li is green, Ni is gray, Co is dark blue).

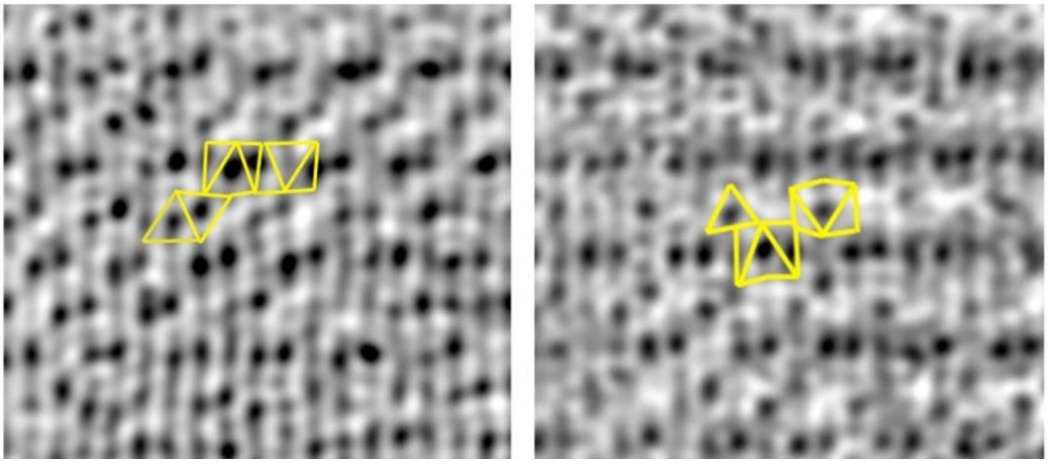

Figure A. 3. 4 ABF-STEM images demonstrating local oxygen environment of the TM cations in the tetrahedral and octahedral positions.

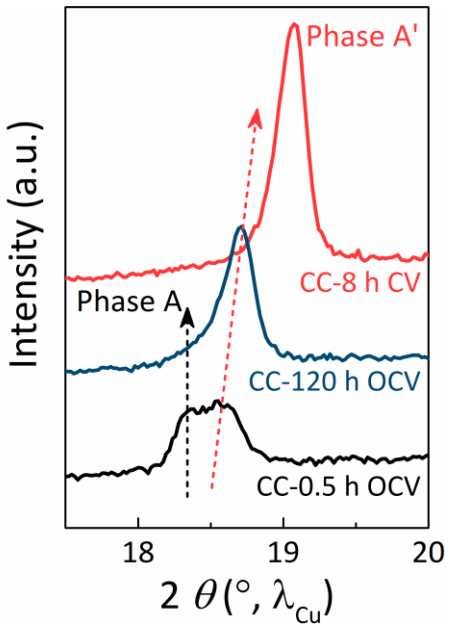

Figure A. 3. 5 Selective region of the laboratory XRD patterns for *ex-situ* samples charged to 4.8 V with an OCV step for 0.5 h (black line, denoted as CC - 0.5 h OCV) and 120 h (blue line, denoted CC - 120 h OCV), or a CV hold for 8 h (red line, denoted as CC-8 h CV). A mixture of phase A and phase A' are obtained after 0.5 h OCV, whereas phase A' is the dominate phase after 120 h OCV storage or 8 h CV hold. Rietveld refinement of the synchrotron XRD pattern of CC - 120 h OCV charged phase is shown in Figure A. 3. 7d, with corresponding crystallographic parameters reported in Table A. 3. 1.

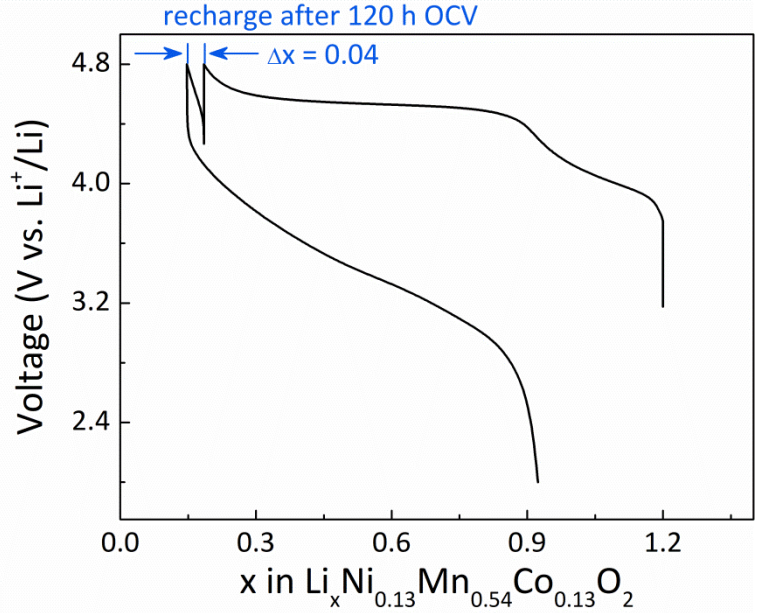

Figure A. 3. 6 Galvanostatic charge-discharge voltage curves of $Li_{1.2}Ni_{0.13}Mn_{0.54}Co_{0.13}O_2$. The cell has been firstly charged to 4.8 V followed by an OCV step for 120 h, then recharged to 4.8 V. Very small amount of Li^+ (~ 0.04 Li^+) was extracted after 120 h OCV, suggesting the reinsertion of Li^+ during the OCV period is negligible.

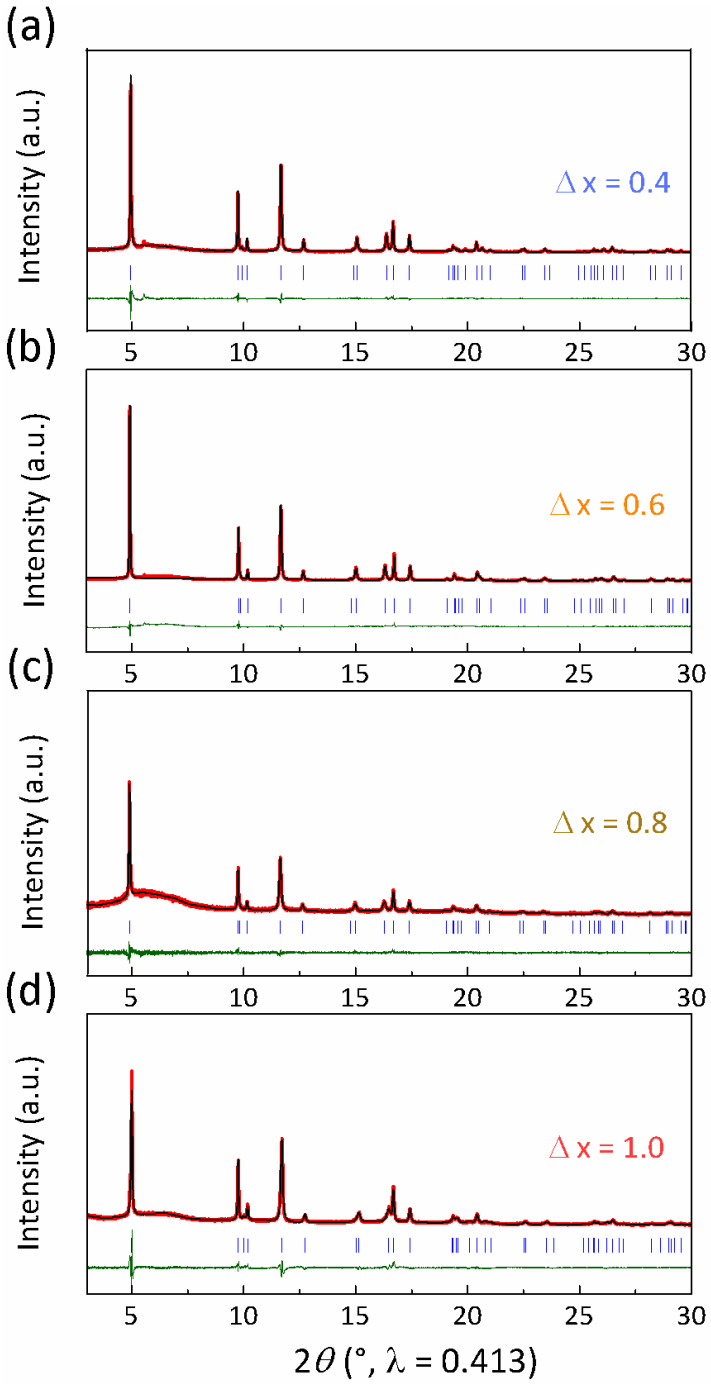

Figure A. 3. 7 Rietveld refinements of the synchrotron XRD patterns of $Li_{1.2}Ni_{0.13}Mn_{0.54}Co_{0.13}O_2$ collected at their charged states with the amount of Li^+ removal (Δx) ranging from 0.4 (a), 0.6 (b), 0.8 (c), and 1.0 (d), followed by 120 h OCV. The red line, black line and bottom green line represent the observed, calculated XRD patterns and the difference, respectively. Vertical blue tick bars mark the Bragg positions in the $R\bar{3}m$ space group.

Table A. 3. 1 Crystallographic data and atomic positions of the Δx = 1.0 (CC - 120 h OCV) charged phase determined from Rietveld refinement of the synchrotron XRD pattern.

Δx = 1.0 charged Li-rich NMC phase ($O3 - Li_{0.2}Ni_{0.13}Mn_{0.56}Co_{0.13}O_2$)						
Space group: $R\bar{3}m$	a (Å)		b (Å)	c (Å)		V (Å^3)
SXRD	2.84525(3)		2.84525(3)	14.2057(4)		99.595(3)
χ^2 = 1.76, Bragg R-factor = 10.1 %						
Atom	Site	x/a	y/b	z/c	Occupancy	B_{iso} (Å^2)
Li	3a	0	0	0	0.2	0.449(8)
Mn	3a	0	0	0	0.081(2)	0.449(8)
Ni/Mn/ Co/Li	3b	0	0	0.5	0.13/0.46/ 0.13/0	0.449(8)
O	6c	0	0	0.24034(10)	1	2.11(3)

Table A. 3. 2 Crystallographic data and atomic positions of the Δx = 0.4 charged phase determined from Rietveld refinement of the synchrotron XRD pattern.

Δx = 0.4 charged Li-rich NMC phase ($O3 - Li_{0.8}Ni_{0.13}Mn_{0.54}Co_{0.13}O_2$)						
Space group: $R\bar{3}m$	a (Å)		b (Å)	c (Å)		V (Å^3)
SXRD	2.84702(2)		2.84702(2)	14.32683(17)		100.568(2)
χ^2 = 1.48, Bragg R-factor = 5.11 %						
Atom	Site	x/a	y/b	z/c	Occupancy	B_{iso} (Å^2)
Li	3a	0	0	0	0.8	0.320(8)
Ni/Mn/ Co/Li	3b	0	0	0.5	0.13/0.54/ 0.13/0	0.320(8)
O	6c	0	0	0.23932(7)	1	0.766(19)

Table A. 3. 3 Crystallographic data and atomic positions of the Δx = 0.6 charged phase determined from Rietveld refinement of the synchrotron XRD pattern.

Δx = 0.6 charged Li-rich NMC phase (O3 – $Li_{0.6}Ni_{0.13}Mn_{0.54}Co_{0.13}O_2$)						
Space group: $R\bar{3}m$	*a* (Å)		*b* (Å)	*c* (Å)		*V* (Å^3)
SXRD	2.83878(2)		2.83878(2)	14.4306(3)		100.711(2)
χ^2 = 1.76, Bragg R-factor = 10.1 %						
Atom	Site	*x/a*	*y/b*	*z/c*	Occupancy	B_{iso} (Å^2)
Li	3*a*	0	0	0	0.6	0.9(2)
Mn	3*a*	0	0	0	0.019(2)	0.9(2)
Ni/Mn/ Co/Li	3*b*	0	0	0.5	0.13/0.52/ 0.13/0	0.293(12)
O	6*c*	0	0	0.23793(10)	1	0.98(3)

Table A. 3. 4 Crystallographic data and atomic positions of the Δx = 0.8 charged phase determined from Rietveld refinement of the synchrotron XRD pattern.

Δx = 0.8 charged Li-rich NMC phase (O3 – $Li_{0.4}Ni_{0.13}Mn_{0.54}Co_{0.13}O_2$)						
Space group: $R\bar{3}m$	*a* (Å)		*b* (Å)	*c* (Å)		*V* (Å^3)
SXRD	2.84452(4)		2.84452(4)	14.4666(6)		101.371(4)
χ^2 = 0.833, Bragg R-factor = 8.72 %						
Atom	Site	*x/a*	*y/b*	*z/c*	Occupancy	B_{iso} (Å^2)
Li	3*a*	0	0	0	0.4	0.319(13)
Mn	3*a*	0	0	0	0.045(2)	0.319(13)
Ni/Mn/ Co/Li	3*b*	0	0	0.5	0.13/0.495/ 0.13/0	0.319(13)
O	6*c*	0	0	0.23886(16)	1	1.62(6)

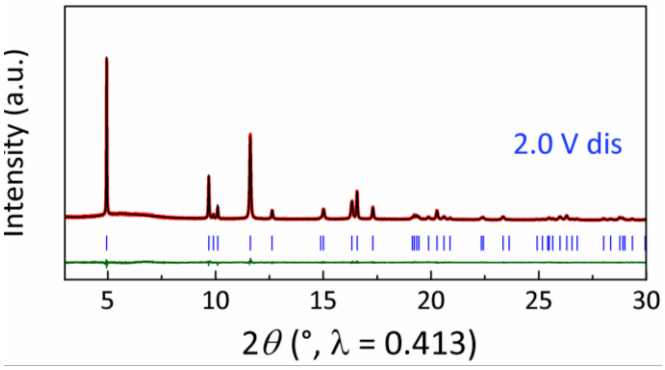

Figure A. 3. 8 Rietveld refinement of the synchrotron XRD pattern of $Li_{1.2}Ni_{0.13}Mn_{0.54}Co_{0.13}O_2$ charged to 4.8 V and then discharged to 2.0 V. The red line, black line and bottom green line represent the observed, calculated XRD patterns and the difference, respectively. Vertical blue tick bars mark the Bragg positions in the $R\bar{3}m$ space group.

Table A. 3. 5 Crystallographic data and atomic positions of the sample collected at 2.0 V discharge state after 4.8 V charge determined from Rietveld refinement of the synchrotron XRD pattern.

2.0 V discharged Li-rich NMC phase (O3 - $Li_{1.08}Ni_{0.13}Mn_{0.54}Co_{0.13}O_{1.95}$)						
Space group: $R\bar{3}m$	a (Å)		b (Å)	c (Å)		V (Å^3)
SXRD	2.86457(2)		2.86457(2)	14.34441(14)		101.937(2)
χ^2 = 0.963, Bragg R-factor = 3.91 %						
Atom	Site	x/a	y/b	z/c	Occupancy	B_{iso} (Å^2)
Li	3a	0	0	0	1	0.333(7)
Mn	3a	0	0	0	0.0349(3)	0.333(7)
Ni/Mn/ Co/Li	3b	0	0	0.5	0.13/0.51/ 0.13/0.03	0.333(7)
O	6c	0	0	0.24100(6)	0.975	0.878(16)

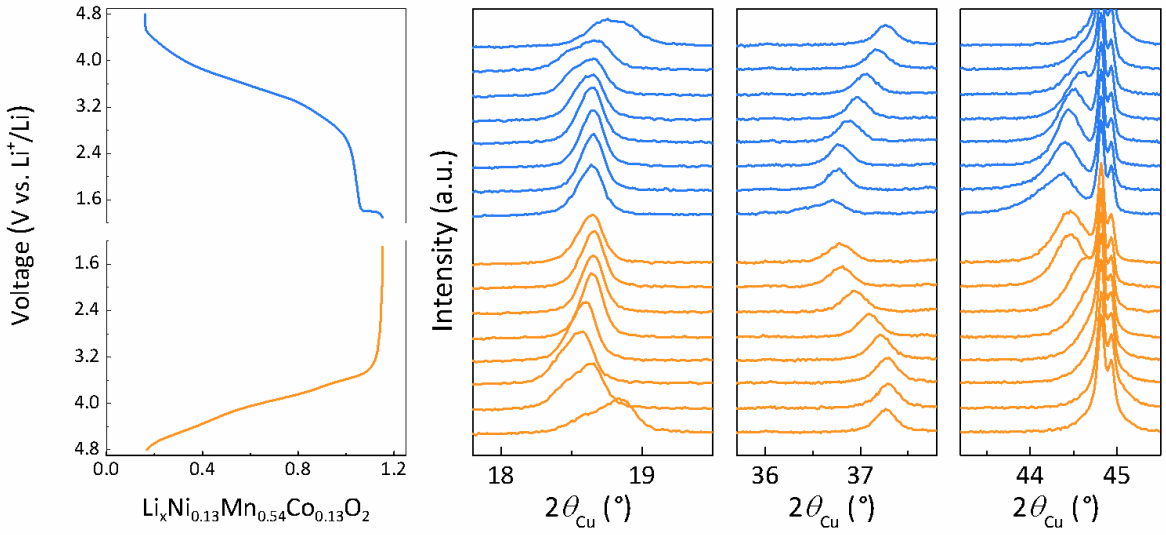

Figure A. 3. 9 Galvanostatic discharge-charge curves collected during the first discharge (down to 1.4 V) and 2nd charge of $Li_{1.2}Ni_{0.13}Mn_{0.54}Co_{0.13}O_2$/Li cell after the initial 4.8 V charge and the corresponding *in-situ* X-ray diffraction patterns.

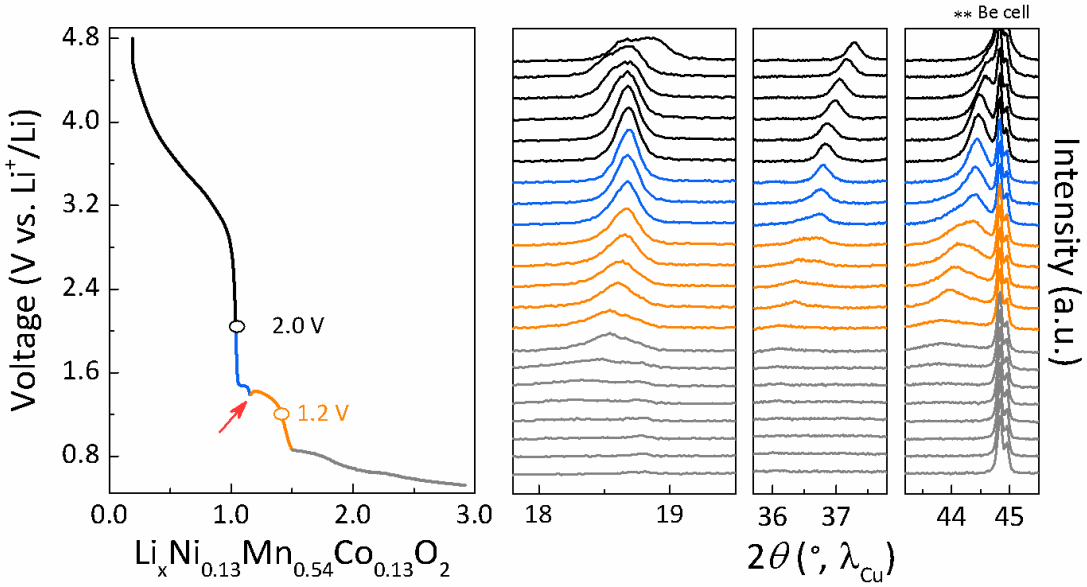

Figure A. 3. 10 Galvanostaic discharge curve collected on discharging $Li_{1.2}Ni_{0.13}Mn_{0.54}Co_{0.13}O_2$ down to 0.5 V after 4.8 V charge (left side) and the corresponding *in-situ* X-ray diffraction patterns. Blue and yellow lines show the results before and after the overshooting point (marked by red arrow), respectively. Grey lines reveal that further pushing the discharge down to 0.5 V results in a material amorphization.

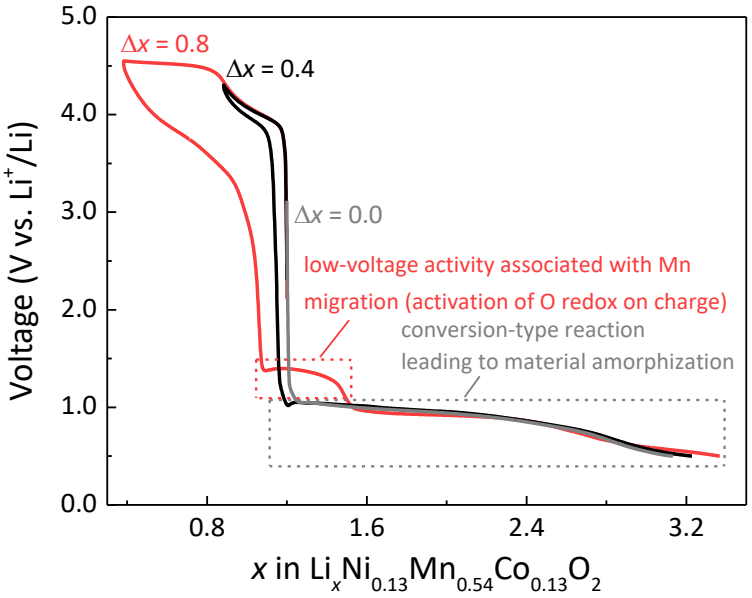

Figure A. 3. 11 Voltage-composition profiles of $Li_{1.2}Ni_{0.13}Mn_{0.54}Co_{0.13}O_2$ while varying the lithium removal during charge (Δx) from 0.0 (pristine, grey line) to 0.4 (black line), and 0.8 (red line), but fixing the discharge cutoff voltage at 0.5 V.

Table A. 3. 6 Crystallographic data and atomic positions of the 1.4 V discharged phase (P') determined from Rietveld refinement of the synchrotron XRD pattern.

1.4 V discharged Li-rich NMC phase (O3 - $Li_{1.14}Ni_{0.13}Mn_{0.54}Co_{0.13}O_{1.95}$)						
Space group: $R\bar{3}m$	a (Å)		b (Å)	c (Å)		V (Å^3)
SXRD	2.87386(2)		2.87386(2)	14.3442(2)		102.598(2)
χ^2 = 0.792, Bragg R-factor = 4.43 %						
Atom	Site	x/a	y/b	z/c	Occupancy	B_{iso} (Å^2)
Li	3a	0	0	0	0.93	0.90(8)
Mn	3a	0	0	0	0.057(1)	0.90(8)
Ni/Mn/ Co/Li	3b	0	0	0.5	0.13/0.48/ 0.13/0.2	0.410(8)
O	6c	0	0	0.24161(9)	0.975	0.87(3)

Table A. 3. 7 Crystallographic data and atomic positions of the 1.2 V discharged phase (P") determined from Rietveld refinement of the synchrotron XRD pattern.

1.2 V discharged Li-rich NMC phase (O3 - $Li_{1.44}Ni_{0.13}Mn_{0.54}Co_{0.13}O_{1.95}$)						
Space group: $R\bar{3}m$	a (Å)		b (Å)	c (Å)		V (Å^3)
SXRD	2.90026(5)		2.90026(5)	14.3783(5)		104.739(4)
χ^2 = 0.871, Bragg R-factor = 7.95 %						
Atom	Site	x/a	y/b	z/c	Occupancy	B_{iso} (Å^2)
Li	3a	0	0	0	0.914	1.6(1)
Mn	3a	0	0	0	0.084(2)	1.6(1)
Ni/Mn/ Co/Li	3b	0	0	0.5	0.13/0.46/ 0.13/0.284	0.547(13)
O	6c	0	0	0.24376(14)	0.975	1.53(4)

Table A. 3. 8 Crystallographic data and atomic positions of the 4.6 V charged – 2.0 V discharged phase determined from Rietveld refinement of the synchrotron XRD pattern.

4.6 V charged – 2.0 V discharged Li-rich NMC phase (O3 – $Li_{1.07}Ni_{0.13}Mn_{0.54}Co_{0.13}O_2$)						
Space group: $R\bar{3}m$	a (Å)		b (Å)	c (Å)		V (Å^3)
SXRD	2.86520(2)		2.86520(2)	14.35258(12)		102.04(2)
χ^2 = 0.992, Bragg R-factor = 4.76 %						
Atom	Site	x/a	y/b	z/c	Occupancy	B_{iso} (Å^2)
Li	3a	0	0	0	0.961	1.23(7)
Mn	3a	0	0	0	0.038(2)	1.23(7)
Ni/Mn/ Co/Li	3b	0	0	0.5	0.13/0.50/ 0.13/0.045	0.290(8)
O	6c	0	0	0.25890(6)	1	0.948(18)

Table A. 3. 9 Crystallographic data and atomic positions of the annealed 4.6 V charged – 2.0 V discharged phase determined from Rietveld refinement of the synchrotron XRD pattern.

Annealed 4.6 V charged – 2.0 V discharged Li-rich NMC phase ($O3 – Li_{1.07}Ni_{0.13}Mn_{0.54}Co_{0.13}O_2$)						
Space group: $R\bar{3}m$	a (Å)		b (Å)	c (Å)		V (Å^3)
SXRD	2.85448(2)		2.85448(2)	14.29207(13)		100.851(2)
χ^2 = 1.04, Bragg R-factor = 5.44 %						
Atom	Site	x/a	y/b	z/c	Occupancy	B_{iso} (Å^2)
Li	3a	0	0	0	0.993	1.19(9)
Mn	3a	0	0	0	0.007(2)	1.19(9)
Ni/Mn/ Co/Li	3b	0	0	0.5	0.13/0.53/ 0.13/0.013	0.222(8)
O	6c	0	0	0.25939(7)	1	0.77(2)

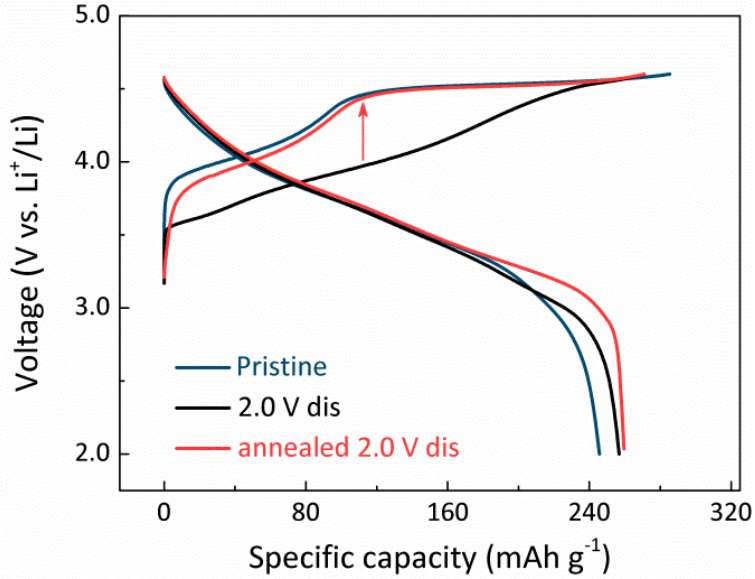

Figure A. 3. 12 Charge-discharge voltage profiles of the pristine $Li_{1.2}Ni_{0.13}Mn_{0.54}Co_{0.13}O_2$ phase (first cycle, marine line), the 2.0 V discharged phase (second cycle, black line) and the annealed 2.0 V discharged phase (second cycle, red line). All the cells were cycled at a current rate of C/5.

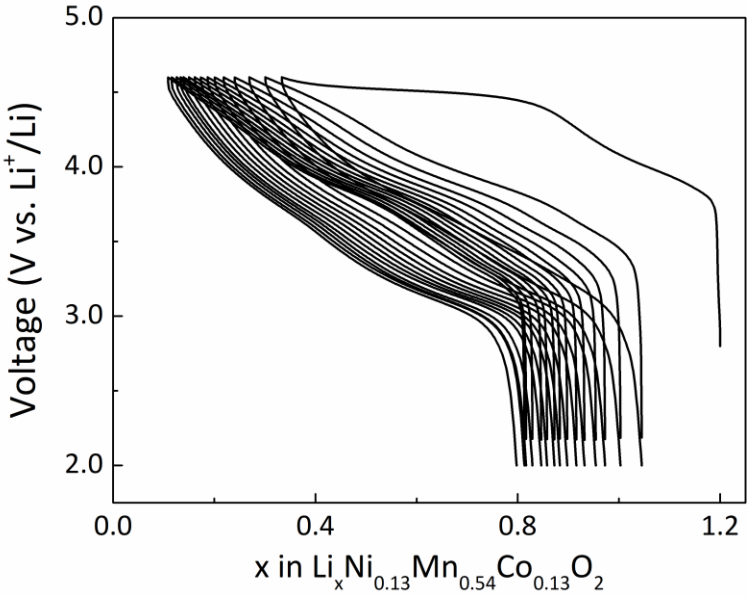

Figure A. 3. 13 Voltage-composition profiles of the annealed 2.0 V CV discharged sample cycled between 4.6 V and 2.0 V.

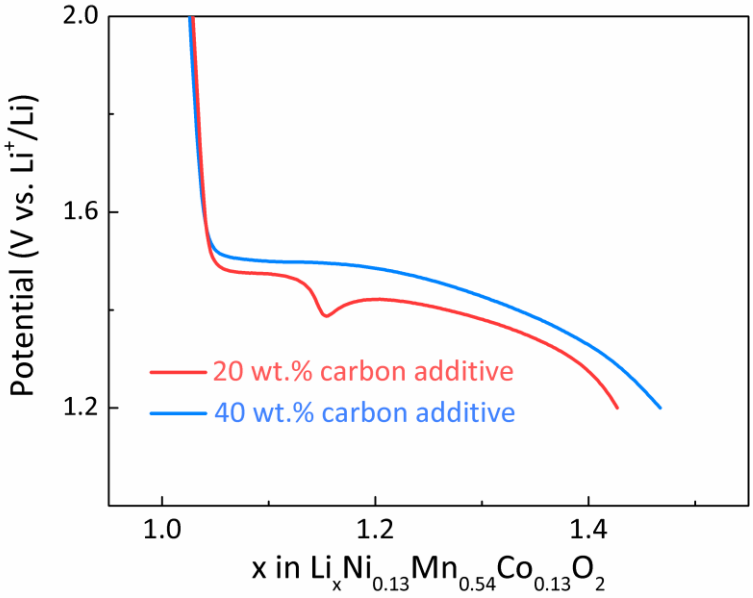

Figure A. 3. 14 The initial charge-discharge curves of $Li_{1.2}Ni_{0.13}Mn_{0.54}Co_{0.13}O_2$ mixed with 20 wt.% (red line) and 40 wt.% (blue line) carbon super P within a voltage window of 4.8 – 1.2 V at a current rate of C/5.

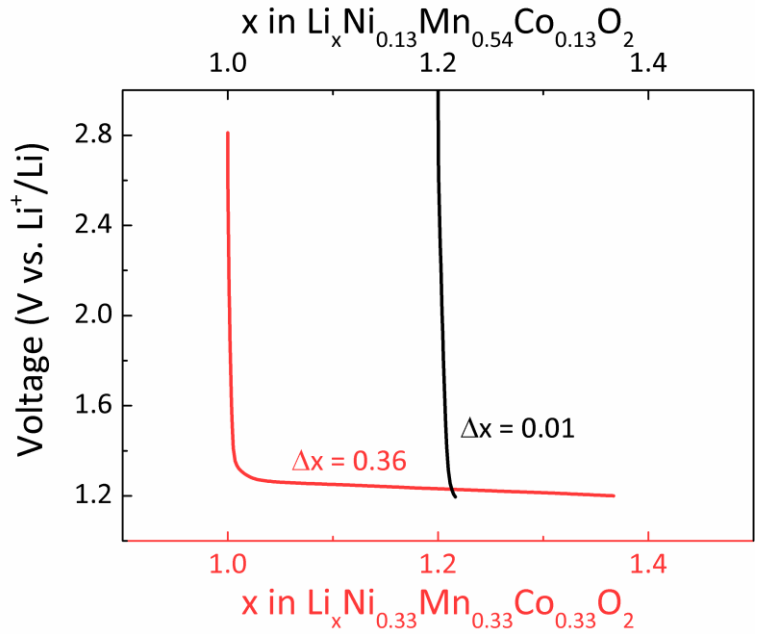

Figure A. 3. 15 Voltage-composition profiles of $Li_{1.2}Ni_{0.13}Mn_{0.54}Co_{0.13}O_2$ (black line) and $Li_{1.0}Ni_{0.33}Mn_{0.33}Co_{0.33}O_2$ (red line) discharge to 1.2 V at C/5.

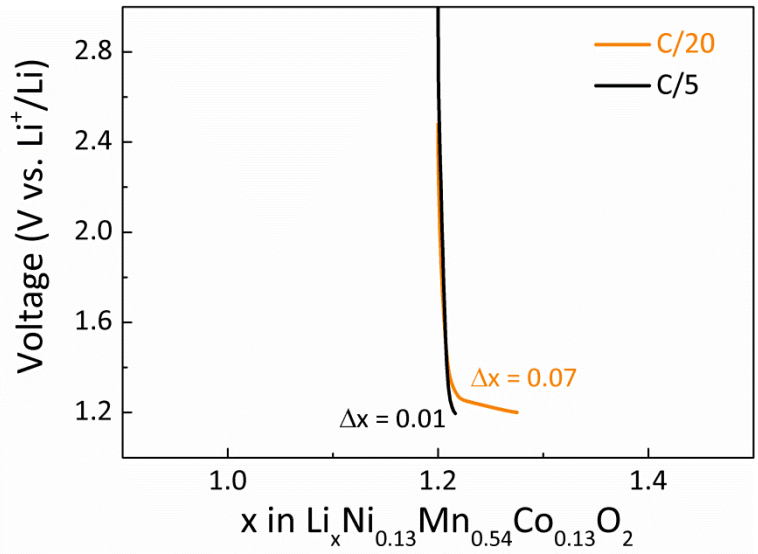

Figure A. 3. 16 Voltage-composition profiles of $Li_{1.2}Ni_{0.13}Mn_{0.54}Co_{0.13}O_2$ discharge to 1.2 V at C/5 (black line) and C/20 (yellow line).

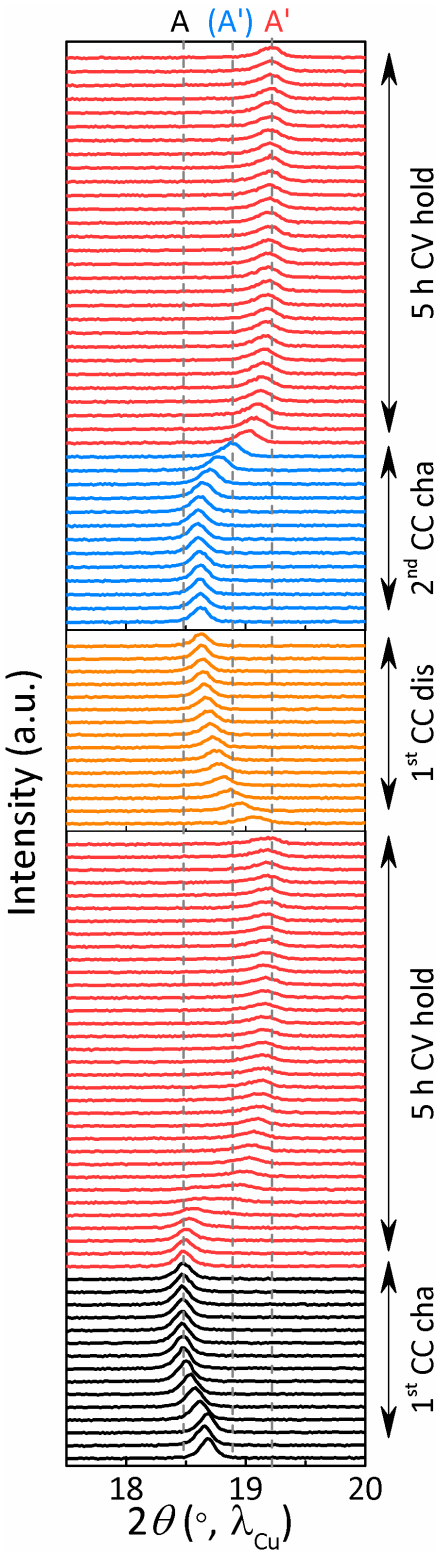

Figure A. 3. 17 *In-situ* XRD study of the first cycle and the second charge of $Li_{1.2}Ni_{0.13}Mn_{0.54}Co_{0.13}O_2$.

A. 4 Supporting information for Chapter IV

A. 4. 1 Methods

Chemicals. 1, 2-Dimethoxyethane (DME, 99.9 %, Sigma-Aldrich), dimethyl sulfoxide (DMSO, ≥ 99.9 %, Sigma-Aldrich), diethylene glycol dimethyl ether (DGME, 99.5 %, Sigma-Aldrich), tetraethylene glycol dimethyl ether (TGME, ≥ 99 %, Sigma-Aldrich), acetonitrile (MeCN, anhydrous, 99.8 %, Sigma-Aldrich), deuterated acetonitrile (d_3-MeCN, ≥ 99.8 %, Eurisotop) and N, N-dimethylformamide (DMF, 99.8 %, sigma Aldrich) were dried with activated molecular sieves (4 Å, Sigma-Aldrich) for at least 2 days before use. Lithium perchlorate ($LiClO_4$, 99.99 %, Sigma-Aldrich), tetrabutylammonium bis-trifluoromethanesulfonimidate (TBATFSi, ≥ 99.0 %, Sigma-Aldrich) tetrabutylammonium hexafluorophosphate($TBAPF_6$, ≥ 99.0 %, Sigma-Aldrich), tetrabutylammonium perchlorate ($TBAClO_4$, ≥ 98.0 %, Sigma-Aldrich), 9, 10 anthraquinone (AQ, analytical standard, sigma Aldrich), 9,10-phenanthrenequinone (PAQ, ≥ 99 %, Sigma Aldrich) and 2,5-di-tert-butyl-1,4-benzoquinone (DBBQ, 99 %, sigma Aldrich) were dried overnight at 80 ℃ under vacuum in BÜCHI oven, so as to decrease the water content of the as-prepared electrolytes (solvents and salts) < 20 ppm as deduced by Karl Fischer titration (Coulometric KF titration, Metrohm). Glass microfiber filters (Whatman) were dried under vacuum at 220 ℃ overnight.

Cyclic voltammetry measurements. A PTFE embedded glassy carbon disk (5.0 mm diam, Pine Research Instrumentation) was used as the working electrode unless otherwise specified and a platinum wire was used as the counter electrode. The reference electrode (Ag/Ag^+, RE-7, ALS Co., Ltd) consists of a silver wire, a glass tube filled with a MeCN/0.1 M $TBAClO_4$/0.01 M $AgNO_3$ solution (ALS Co., Ltd) and sealed with a Vycor 7930 frit (BioLogic Science Instruments).The reference electrode was always assembled in the glovebox at least 24 hours before use and was partially immersed in an MeCN/0.1 M $TBAClO_4$ solution. All measurements were performed in a glove box with water content < 0.5 ppm. The electrochemical cell was well sealed with rubber stoppers except a bubbler which was connected to a gas line able to feed with dry Ar (5.0 quality, Linde France), O_2 (5.6 quality, Linde France), CO_2 (5.3 quality, Linde France) or 70 % O_2 / 30 % CO_2 mixture (Linde France). The water content of electrolytes is found to be < 40 ppm after cyclic voltammetry measurements.

Preparation of carbon positive electrodes. 90 wt.% Carbon Super P (C_{sp}, Timcal Ltd) and 10 wt.% polytetrafluorethylene (PTFE, 60 wt.% dispersion in water, Sigma-Aldrich) were firstly well mixed with an electrical blender in certain amount of isopropanol (≥ 99.9 %, Sigma-Aldrich) to prepare a slurry. The as-prepared slurry was then drop-casted onto 11 mm diameter stainless steel meshes (AISI 316, 325 mesh, 0.036 mm diam wire, Alfa Aesar). After being dried in ambient air and washed with a water/ethanol (1:2 *v*/*v*) solution to remove the surfactants in the PTFE dispersion, these positive electrodes were further dried overnight at 80 ℃ under vacuum in BÜCHI oven and stored in glove box. Carbon Super P loading of the resulting electrodes is 0.36 (± 0.02) mg on a surface of 0.4 (± 0.04) cm^2.

Preparation of $Li_{1-x}FePO_4$ negative electrodes. Self-standing composite $Li_{1-x}FePO_4$ (LFP) electrodes (LFP: Super P: PTFE = 85:10:5) were used as lithium source for both electrolytes. Detailed preparation method can be found in A. 2. 1. Every single as-prepared LFP electrode (60 to 65 mg per cm^2) was then pre-charged in a Swagelok cell with metallic lithium as counter electrode and LP30 as electrolyte until it reached a constant plateau before serving as an excess lithium source with a stable potential of 3.45 V vs Li/Li^+ for Li-O_2, Li-CO_2, Li-O_2/CO_2 or Li-Ar cells.

Cell testing. Li-O_2/CO_2 cells were tested with *in-situ* pressure cell so as to monitor uninterruptedly the pressure change during discharge/charge. Li─CO_2 cells were tested with a two compartment "Ohara" *in-situ* pressure cell that integrates an additional ceramic membrane (Lithium ion conductive glass ceramics (LICGC), $Li_{1+x+y}Al_xTi_{2-x}Si_yP_{3-y}O_{12}$, 200 µm thick, Ohara Inc) in order to prevent the crossover of quinones. All the cells were assembled in an argon-filled glove box (water content < 1 ppm, oxygen content < 1 ppm) with carbon positive electrode and $Li_{1-x}FePO_4$ negative electrode. Two layers of glass fibers wetted with 450 ± 20 µL electrolytes were used as separators. After assembly, the cells were quickly vacuumed and refilled with O_2, CO_2, O_2/CO_2 mixture or Ar at a constant pressure of 1.55 ± 0.05 bars. Electrochemical tests were performed with a VMP3 multichannel potentiostat (BioLogic Science Instruments) in a temperature-controlled oven at 25.0 ± 0.05 ℃. The current density and specific capacity are normalized based on the mass of Carbon Super P.

Online electrochemical mass spectrometry (OEMS). The OEMS cell was first fully discharged under O_2/CO_2 mixture before to be quickly vacuumed to remove all residual O_2/CO_2

inside and refilled with pure Ar. Detailed description of the routine OEMS measurement can be found in A. 2. 1.

Nuclear magnetic resonance (NMR). For NMR analyses, deuterated acetonitrile (d_3-MeCN) was used as the supporting solvent for the sake of better sensitivity. In order to generate exclusively the reduced form of DBBQ, one cell was discharged in pure argon by first decreasing its potential down to 2 V *vs* Li^+/Li where the reduction takes place, and then hold this potential until the reduction current gradually decreases close to zero. To differentiate the conditions of electrolyte solutions after the initial electrochemical reduction of DBBQ and the follow-up CO_2 chemical reaction, NMR analyses were performed with the solutions collected right after the discharge and after further bubbling with CO_2, respectively. All NMR spectra were recorded on a Bruker 300 MHz spectrometer.

A. 4. 2 Supporting figures

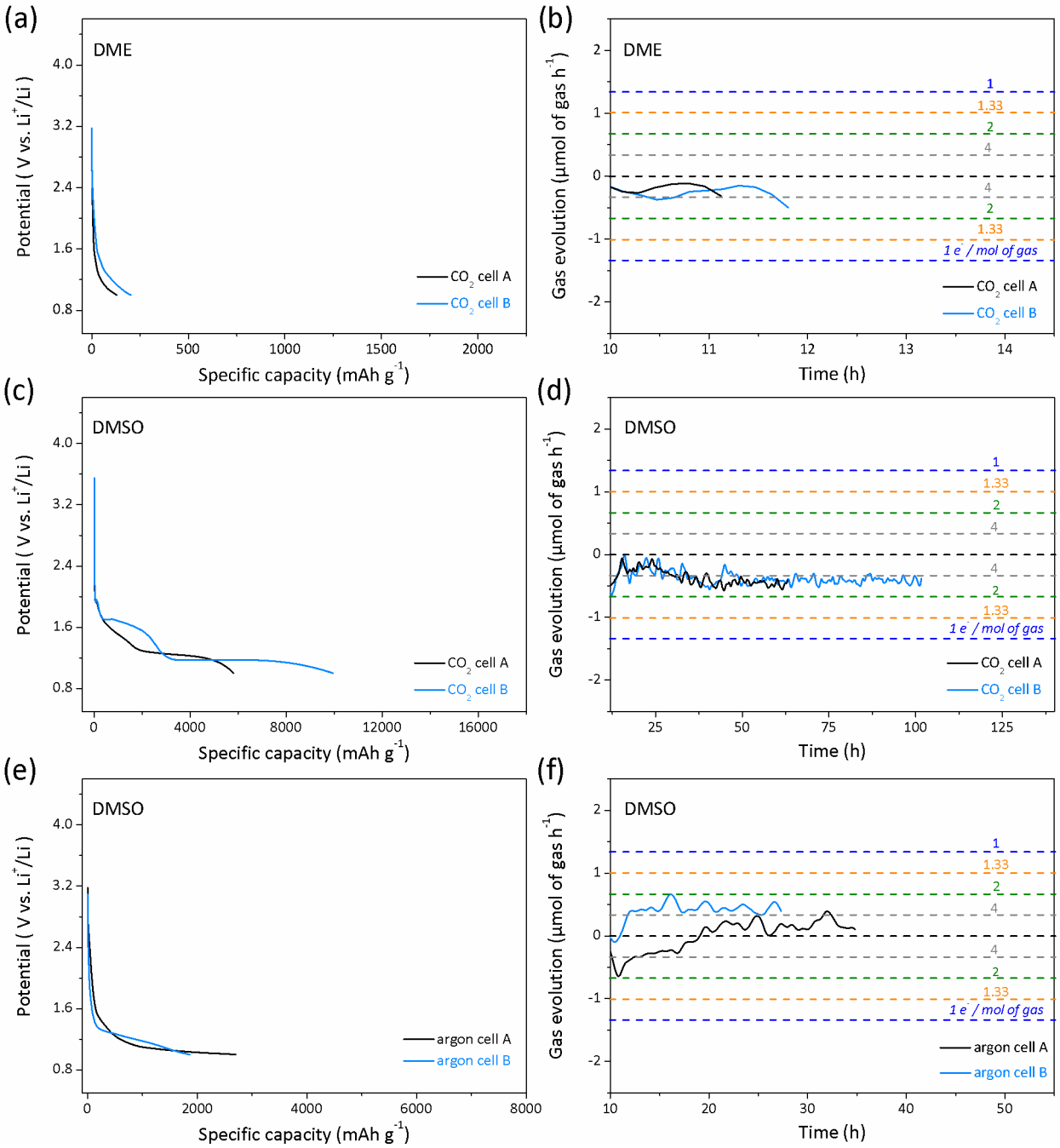

Figure A. 4. 1 Galvanostatic discharge curves and pressure change of Li-CO_2 batteries using 0.1 M $LiClO_4$/DME in (a) and (b), 0.1 M $LiClO_4$/DMSO in (c) and (d).Galvanostatic discharge curves (e) and (f) pressure change of Li-argon batteries using 0.1 M $LiClO_4$/DMSO as electrolyte. The discharge current density is 100 mA g^{-1}. Blue curve and red curve are representative of two cells measured under the same condition.

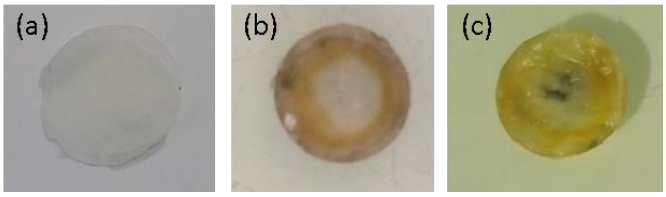

Figure A. 4. 2 Photos of separators after discharged in (a) Li-O_2/CO_2 battery down to 2 V vs Li/Li^+, (b) Li-CO_2 battery down to 1 V vs Li^+/Li and (c) Li-argon battery down to 1 V vs Li^+/Li, using 0.1 M $LiClO_4$/DMSO as electrolytes, at a current density of 100 mA g^{-1}.

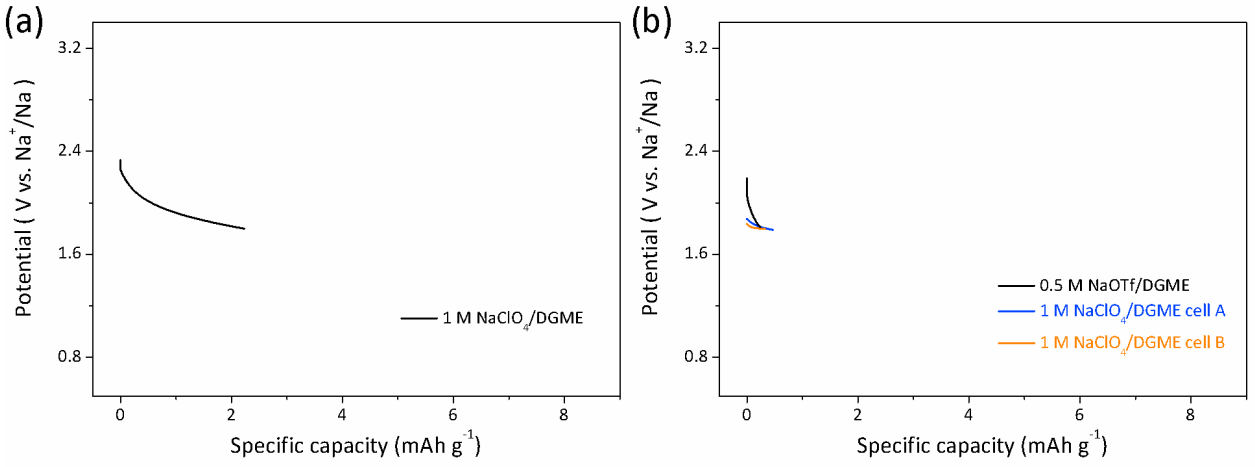

Figure A. 4. 3 Galvanostatic discharge curves for Na-CO_2 batteries with (a) 1 M $NaClO_4$/DGME and (b) 1 M $NaClO_4$/TGME (blue curve and yellow curve are two cells measured under the same condition) as electrolytes, using carbon super p as electrode; and with (b) 0.5 M NaOTf /DGME as electrolyte, using GDL as electrode (black curve). The discharge current density is 100 mA g^{-1}.

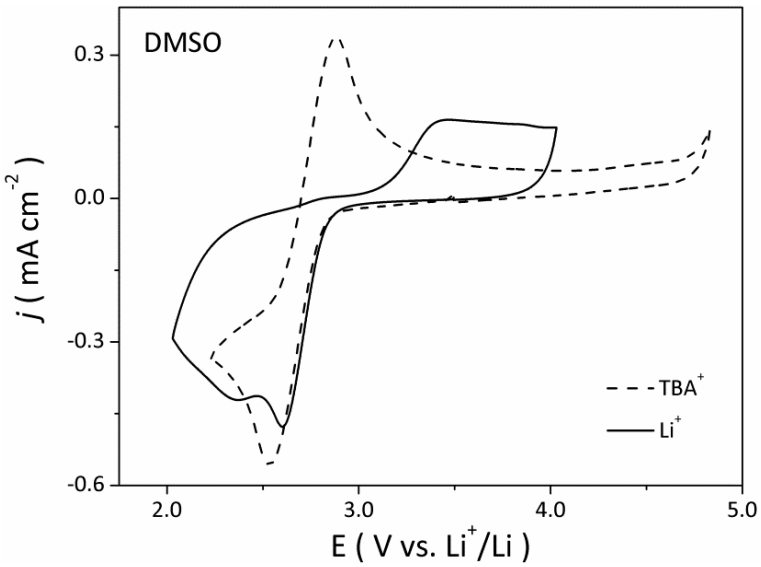

Figure A. 4. 4 Cyclic voltammograms at 50 mV s^{-1} with O_2-saturated electrolytes of 0.1 M $TBAPF_6$/DMSO (dash curve) and 0.1 M $LiClO_4$/DMSO (solid curve).

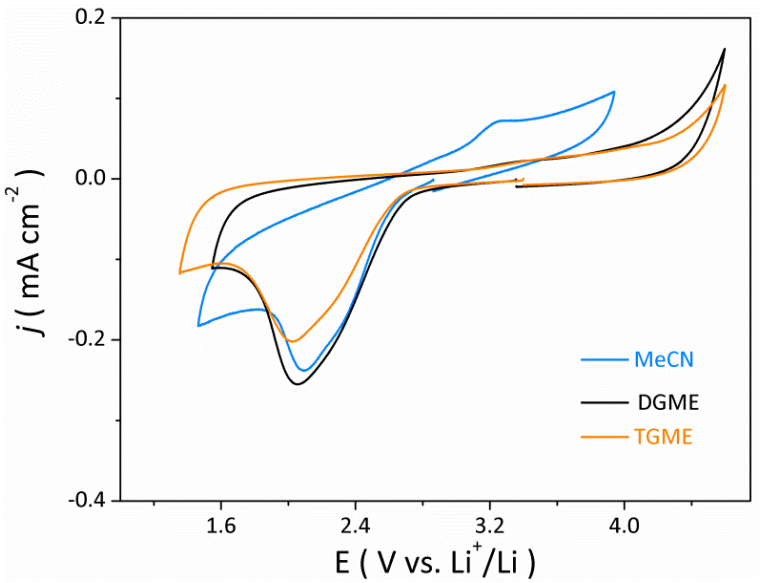

Figure A. 4. 5 (a) Cyclic voltammograms at 50 mV s^{-1} with various O_2/CO_2-saturated solvents: 0.1 M $LiClO_4$/MeCN (blue curve), 0.1 M $LiClO_4$/DGME (black curve), and 0.1 M $LiClO_4$/TGME (yellow curve).

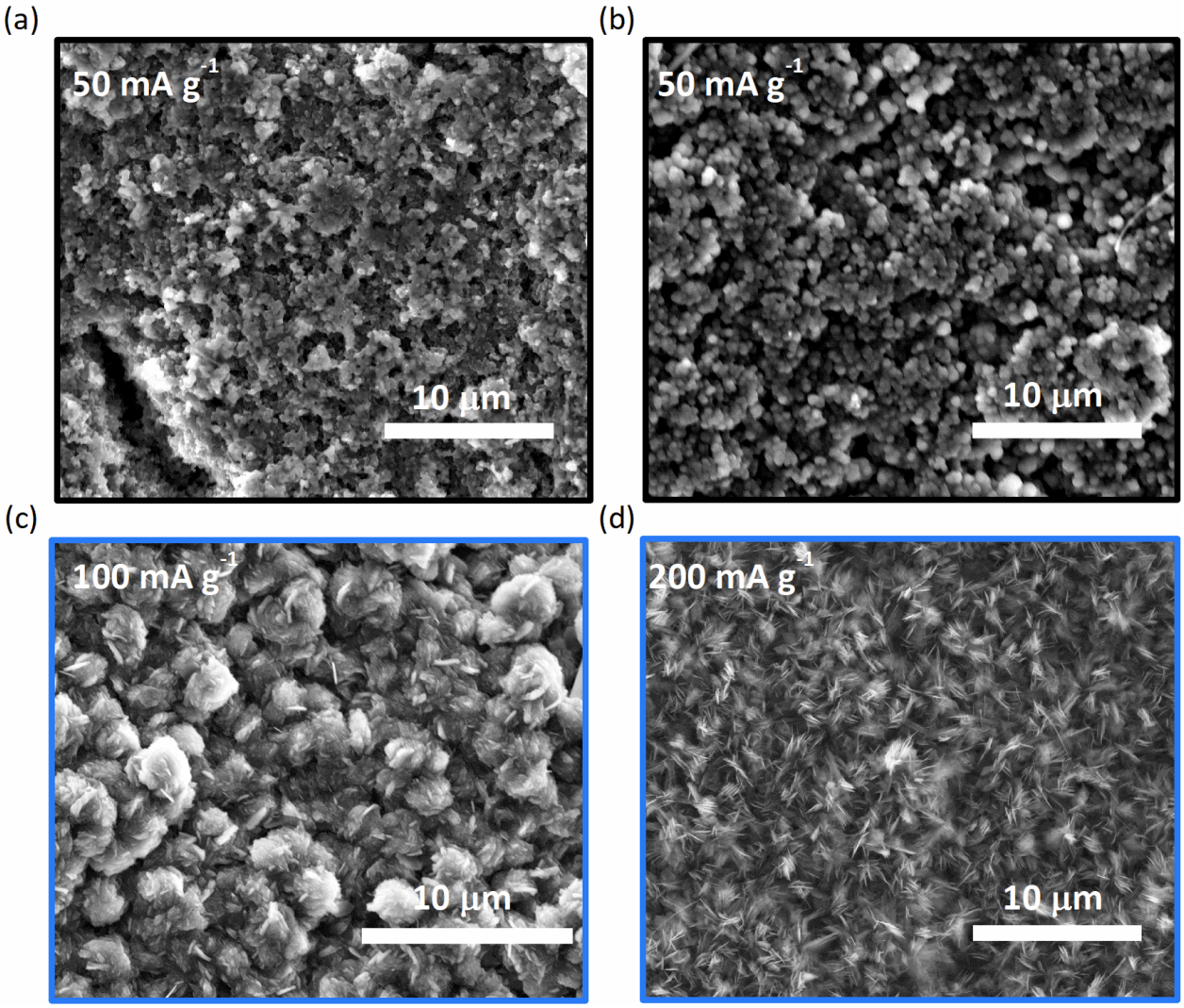

Figure A. 4. 6 SEM images of electrodes fully discharged in pure O_2 with an electrolyte of (a) 0.1 M $LiClO_4$/DMSO and (b) 0.1 M $LiClO_4$/DME, at a current density of 50 mA g^{-1}. SEM images of electrodes fully discharged in O_2/CO_2 mixture, with 0.1 M $LiClO_4$/DMSO as electrolyte, at current densities of (c) 100 mA g^{-1} and (d) 200 mA g^{-1}.

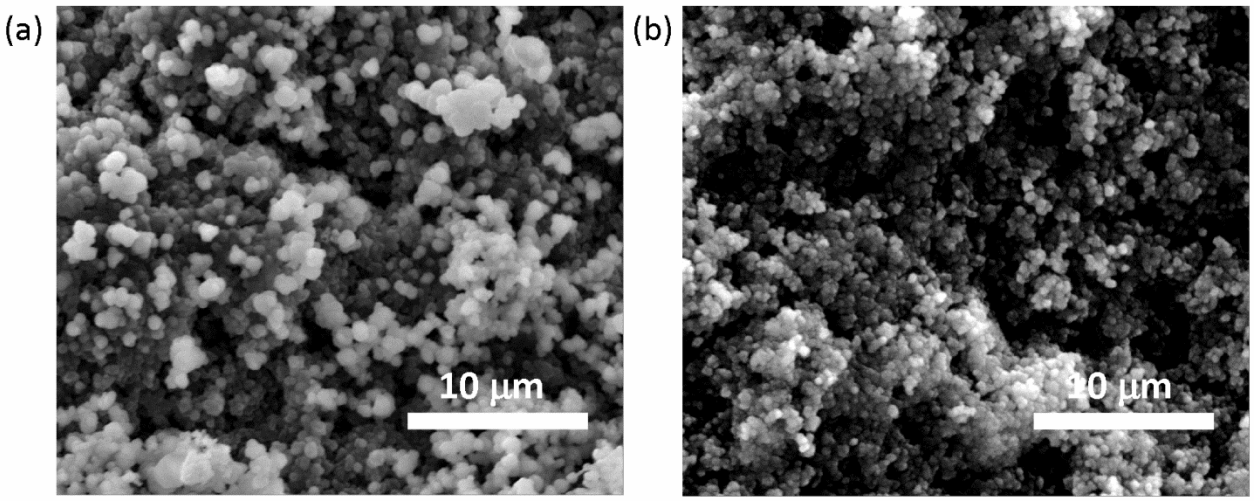

Figure A. 4. 7 SEM images of electrodes after fully discharged in (a) pure O_2 and then exposed in pure CO_2; and (b) O_2/CO_2 mixture.

Table A. 4. 1 Positive shifts of the second reduction waves (ΔE_2) due to chemical reactions of CO_2 and Q^{2-} in DMF and MeCN, respectively. ΔE_2 were obtained by comparing the peak positions of the second reduction waves in presence of argon and CO_2, respectively.

		ΔE_2 (mV)
AQ	DMF	167
	MeCN	331
PAQ	DMF	131
	MeCN	147
DBBQ	DMF	180
	MeCN	408

Table A. 4. 2 Positive shifts of the reduction potentials for the first and second reduction waves (ΔE_1 and ΔE_2, respectively) in presence of Li^+ in DMF and in MeCN, respectively.

		ΔE_1 (mV)	ΔE_2 (mV)
AQ	DMF	32	498
	MeCN	215	NA
PAQ	DMF	205	810
	MeCN	408	NA
DBBQ	DMF	57	659
	MeCN	271	NA

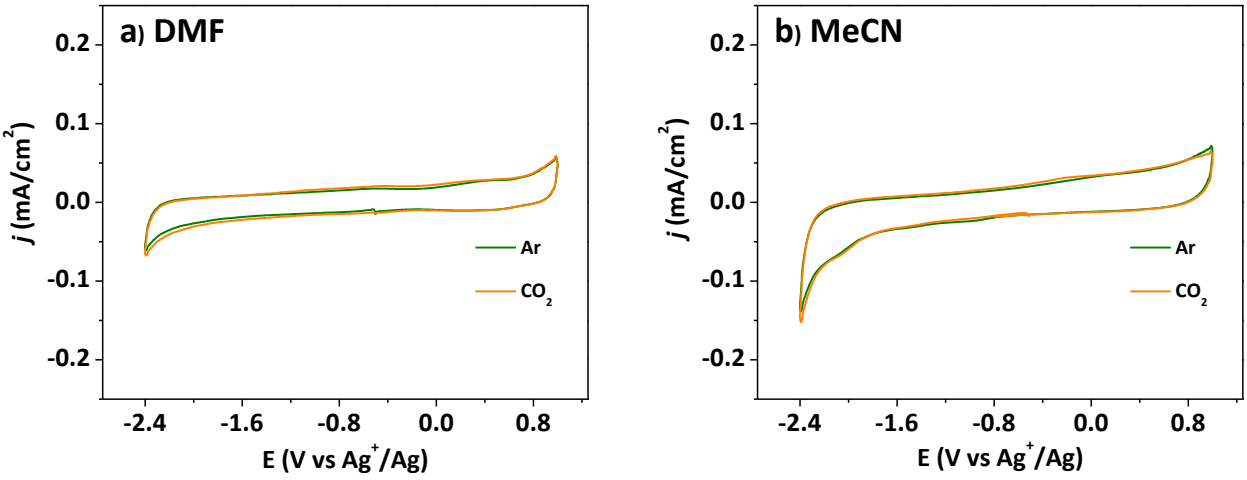

Figure A. 4. 8 Cyclic voltammograms at electrolytes with 0.1 M $LiClO_4$ in DMF (a) and MeCN (b) under argon (green curves) and CO_2 (orange curves). Scan rate: 100 mV s^{-1}.

Table A. 4. 3 Half-wave potentials of the first and second reduction waves (E_1 and E_2, respectively) for quinones in DMF and MeCN.

		E_1 (V)	E_2 (V)
AQ	DMF	-1.25	-2.05
	MeCN	-1.23	-1.88
PAQ	DMF	-1.01	-1.98
	MeCN	-0.97	-1.83
DBBQ	DMF	-1.03	-2.14
	MeCN	-1.01	-1.93

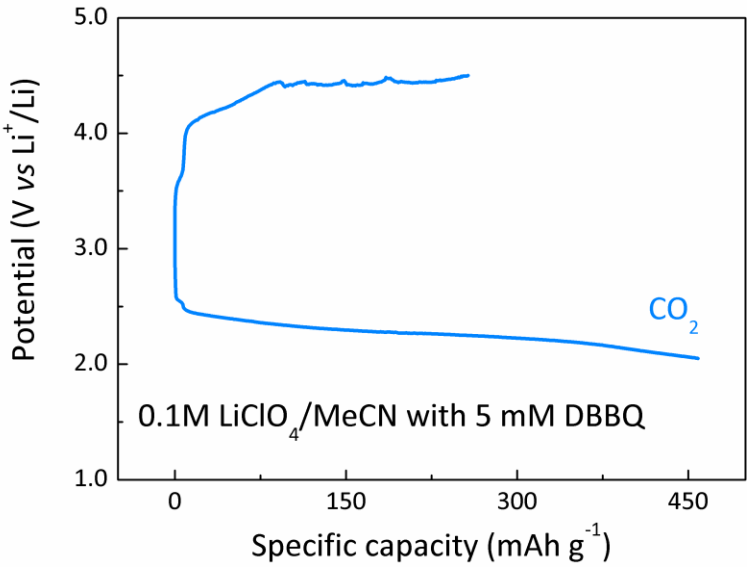

Figure A. 4. 9 Galvanostatic discharge-charge curve in 0.1 M $LiClO_4$ /MeCN with the addition of 5 mM DBBQ under CO_2 in a two-compartment "oraha" cell with a ceramic membrane to prevent the crossover of quinones.

Bibliography

Bibliography

1 International Energy Agency, O. IEA World Energy Outlook 2017. (2017).

2 Whittingham, M. S. & Jr., F. R. G. The Lithium Intercalates of the Transition Metal Dichalcogenides. *Mater. Res. Bull.* **10**, 363-371 (1975).

3 Whittingham, M. S. Electrical Energy Storage and Intercalation Chemistry. *Science* **192**, 1126-1127 (1976).

4 Rao, B. M. I., Francis, R. W. & Christopher, H. A. Lithium-Aluminum Electrode. *J. Electrochem. Soc.* **124**, 1490-1492 (1977).

5 Wang, J., Raistrick, I. D. & Huggins, R. A. Behavior of Some Binary Lithium Alloys as Negative Electrodes in Organic Solvent-Based Electrolytes. *J. Electrochem. Soc.* **123**, 457-460 (1986).

6 Buiel, E. & Dahn, J. R. Reduction of the Irreversible Capacity in Hard-Carbon Anode Materials Prepared from Sucrose for Li-Ion Batteries. *J. Electrochem. Soc.* **145**, 1977-1981 (1998).

7 Han, Y. S., Yu, J. S., Park, G. S. & Lee, J. Y. Effects of Synthesis Temperature on the Electrochemical Characteristics of Pyrolytic Carbon for Anodes of Lithium-Ion Secondary Batteries. *J. Electrochem. Soc.* **146**, 3999-4004 (1999).

8 Magasinski, A. *et al.* High-Performance Lithium-Ion Anodes Using a Hierarchical Bottom-Up Approach. *Nat. Mater.* **9**, 353-358 (2010).

9 Poizot, P., Laruelle, S., Grugeon, S., Dupont, L. & Tarascon, J.-M. Nano-Sized Transition-Metal Oxides as Negative-Electrode Materials for Lithium-Ion Batteries. *Nature* **407**, 496-499 (2000).

10 Chang, H. J. *et al.* Investigating Li Microstructure Formation on Li Anodes for Lithium Batteries by in Situ ^{6}Li/^{7}Li NMR and SEM. *J. Phys. Chem. C* **119**, 16443-16451 (2015).

11 Wang, X. *et al.* New Insights on the Structure of Electrochemically Deposited Lithium Metal and Its Solid Electrolyte Interphases via Cryogenic TEM. *Nano Lett.* **17**, 7606-7612 (2017).

12 Ding, F. *et al.* Dendrite-Free Lithium Deposition via Self-Healing Electrostatic Shield Mechanism. *J. Am. Chem. Soc.* **135**, 4450-4456 (2013).

13 Monroe, C. & Newman, J. Dendrite Growth in Lithium/Polymer Systems A Propagation Model for Liquid Electrolytes under Galvanostatic Conditions. *J. Electrochem. Soc.* **150**, A1377-A1384 (2003).

14 Lin, D., Liu, Y. & Cui, Y. Reviving the Lithium Metal Anode for High-Energy Batteries. *Nat. Nanotechnology* **12**, 194-206 (2017).

15 Liang, X. *et al.* A Facile Surface Chemistry Route to a Stabilized Lithium Metal Anode. *Nat. Energy* **2**, 17119-17125 (2017).

16 Zhao, J. *et al.* Surface Fluorination of Reactive Battery Anode Materials for Enhanced Stability. *J. Am. Chem. Soc.* **139**, 1550-11558 (2017).

17 Li, L. *et al.* Self-Heating–Induced Healing of Lithium Dendrites. *Science* **359**, 1513–1516 (2018).

18 Mizushima, K., Jones, P. C., Wiseman, P. J. & Goodenough, J. B. Li_xCoO_2 ($0 < x < 1$): A New Cathode Material for Batteries of High Energy Density. *Mater. Res. Bull.* **15**, 783-789 (1980).

19 Amatucci, G. G., Tarascon, J. M. & Kleinb, L. C. CoO_2, The End Member of the Li_xCoO_2 Solid Solution. *J. Electrochem. Soc.* **143**, 1114-1123 (1996).

20 Delmas, C., Fouassier, C. & Hagenmuller, P. Structural Classification and Properties of the Layered Oxides. *Physica B+C* **99**, 81-85 (1980).

21 Delmas, C. *et al.* An Overview of the $Li(Ni,M)O_2$ Systems: Syntheses, Structures and Properties. *Electrochim. Acta.* **45**, 243-253 (1999).

22 Dahn, J. R., Fuller, E. W., Obrovac, M. & Sacken, U. v. Thermal Stability of Li_xCoO_2, Li_xNiO_2 and λ-MnO_2 and Consequences for the Safety of Li-ion Cells. *Solid State Ion.* **69**, 265-270 (1994).

23 Shao-Horn, Y. *et al.* Structural Characterization of Layered $LiMnO_2$ Electrodes by Electron Diffraction and Lattice Imaging. *J. Electrochem. Soc.* **146**, 2404-2412 (1999).

24 Nitta, N., Wu, F., Lee, J. T. & Yushin, G. Li-Ion Battery Materials: Present and Future. *Mater. Today* **18**, 252-264 (2015).

25 Andre, D. *et al.* Future Generations of Cathode Materials: An Automotive Industry Perspective. *J. Mater. Chem. A* **3**, 6709-6732 (2015).

26 Choi, J. & Manthiram, A. Role of Chemical and Structural Stabilities on the Electrochemical Properties of Layered $LiNi_{1/3}Mn_{1/3}Co_{1/3}O_2$ Cathodes. *J. Electrochem. Soc.* **152**, A1714-A1718 (2005).

27 Yoon, C. S. *et al.* High-Energy Ni-Rich $Li[Ni_xCo_yMn_{1-x-y}]O_2$ Cathodes via Compositional Partitioning for Next-Generation Electric Vehicles. *Chem. Mater.* **29**, 10436-10445 (2017).

28 Jung, R., Metzger, M., Maglia, F., Stinner, C. & Gasteiger, H. A. Oxygen Release and Its Effect on the Cycling Stability of $LiNi_xMn_yCo_zO_2$(NMC) Cathode Materials for Li-Ion Batteries. *J. Electrochem. Soc.* **164**, A1361-A1377 (2017).

29 Xu, J., Lin, F., Doeff, M. M. & Tong, W. A Review of Ni-Based Layered Oxides for Rechargeable Li-Ion Batteries. *J. Mater. Chem. A* **5**, 874-901 (2017).

30 Radin, M. D. *et al.* Narrowing the Gap between Theoretical and Practical Capacities in Li-Ion Layered Oxide Cathode Materials. *Adv. Energy Mater.* **7**, 1602888-1602920 (2017).

31 Rozier, P. & Tarascon, J. M. Review—Li-Rich Layered Oxide Cathodes for Next-Generation Li-Ion Batteries: Chances and Challenges. *J. Electrochem. Soc.* **162**, A2490-A2499 (2015).

32 James, A. C. W. P. & Goodenough, J. B. Structure and Bonding in Li_2MoO_3 and $Li_{2-x}MoO_3$ ($0 \leq x \leq 1.7$). *J. Solid State Chem.* **76**, 87-96 (1988).

33 Rossouw, M. H. & Thackeray, M. M. Lithium Manganese Oxides from Li_2MnO_3 for Rechargeable Lithium Battery Applications. *Mater. Res. Bull.* **26**, 463-473 (1991).

34 Thackeray, M. M. *et al.* Li_2MnO_3-Stabilized $LiMO_2$ (M = Mn, Ni, Co) Electrodes for Lithium-Ion Batteries. *J. Mater. Chem.* **17**, 3112–3125 (2007).

35 Jiang, J., Eberman, K. W., Krause, L. J. & Dahn, J. R. Structure, Electrochemical Properties, and Thermal Stability Studies of Cathode Materials in the $x\text{Li}[Mn_{1/2}Ni_{1/2}]O_2 \cdot y\text{LiCoO}_2 \cdot z\text{Li}[Li_{1/3}Mn_{2/3}]O_2$ Pseudoternary System ($x + y + z = 1$). *J. Electrochem. Soc.* **152**, A1879-A1889 (2005).

36 Kalyani, P., Chitra, S., Mohan, T. & Gopukumar, S. Lithium Metal Rechargeable Cells Using Li_2MnO_3 as the Positive Electrode. *J. Power Sources* **80**, 103-106 (1999).

37 Park, Y. Structural and Electrochemical Properties of $Li[Co_xLi_{1/3-x/3}Mn_{2/3-2x/3}]O_2$ Cathode Materials. *Solid State Ion.* **175**, 305-309 (2004).

38 Numata, K., Sakaki, C. & Yamanaka, S. Synthesis and Characterization of Layer Structured Solid Solutions in the System of $LiCoO_2$–Li_2MnO_3. *Solid State Ion.* **117**, 257–263 (1999).

39 Numata, K., Sakaki, C., Yamanaka, S. & Synthesis of Solid Solutions in a System of $LiCoO_2$-Li_2MnO_3 for Cathode Materials of Secondary Lithium Batteries. *Chem. Lett.* **26**, 725-726 (1997).

40 Lu, Z., MacNeil, D. D. & Dahn, J. R. Layered Cathode Materials $Li[Ni_xLi_{1/3-2x/3}Mn_{2/3-x/3}]O_2$ for Lithium-Ion Batteries. *Electrochem. Solid State Lett.* **4**, A191-A194 (2001).

41 Lu, Z. & Dahn, J. R. Understanding the Anomalous Capacity of $Li/Li[Ni_xLi_{1/3-2/3x}Mn_{2/3-x/3}]O_2$ Cells Using In Situ X-Ray Diffraction and Electrochemical Studies. *J. Electrochem. Soc.* **149**, A815-A822 (2002).

42 Kim, J. Synthesis and Electrochemical Behavior of $Li[Li_{0.1}Ni_{0.35-x/2}Co_xMn_{0.55-x/2}]O_2$ Cathode Materials. *Solid State Ion.* **164**, 43-49 (2003).

43 Pimenta, V. *et al.* Synthesis of Li-Rich NMC: A Comprehensive Study. *Chem. Mater.* **29**, 9923-9936 (2017).

44 Armstrong, A. R. *et al.* Demonstrating Oxygen Loss and Associated Structural Reorganization in the Lithium Battery Cathode $Li[Ni_{0.2}Li_{0.2}Mn_{0.6}]O_2$. *J. Am. Chem. Soc.* **128**, 8694-8698 (2006).

45 Tran, N. *et al.* Mechanisms Associated with the "Plateau" Observed at High Voltage for the Overlithiated $Li_{1.12}(Ni_{0.425}Mn_{0.425}Co_{0.15})_{0.88}O_2$ System. *Chem. Mater.* **20**, 4815–4825 (2008).

46 Luo, K. *et al.* Charge-Compensation in 3*d*-Transition-Metal-Oxide Intercalation Cathodes Through the Generation of Localized Electron Holes on Oxygen. *Nat. Chem.* **8**, 684-691 (2016).

47 Strehle, B. *et al.* The Role of Oxygen Release from Li- and Mn-Rich Layered Oxides During the First Cycles Investigated by On-Line Electrochemical Mass Spectrometry. *J. Electrochem. Soc.* **164**, A400-A406 (2017).

48 Koga, H. *et al.* Different Oxygen Redox Participation for Bulk and Surface: A Possible Global Explanation for the Cycling Mechanism of $Li_{1.20}Mn_{0.54}Co_{0.13}Ni_{0.13}O_2$. *J. Power Sources* **236**, 250-258 (2013).

49 Boulineau, A., Simonin, L., Colin, J. F., Bourbon, C. & Patoux, S. First Evidence of Manganese-Nickel Segregation and Densification upon Cycling in Li-rich Layered Oxides for Lithium Batteries. *Nano Lett.* **13**, 3857-3863 (2013).

50 Teufl, T., Strehle, B., Müller, P., Gasteiger, H. A. & Mendez, M. A. Oxygen Release and Surface Degradation of Li- and Mn-Rich Layered Oxides in Variation of the Li_2MnO_3 Content. *J. Electrochem. Soc.* **165**, A2718-A2731 (2018).

51 Sathiya, M. *et al.* Reversible Anionic Redox Chemistry in High-Capacity Layered-Oxide Electrodes. *Nat. Mater.* **12**, 827-835 (2013).

52 Xie, Y., Saubanère, M. & Doublet, M. L. Requirements for Reversible Extra-Capacity in Li-Rich Layered Oxides for Li-Ion Batteries. *Energy Environ. Sci.* **10**, 266-274 (2017).

53 Saubanère, M., McCalla, E., Tarascon, J. M. & Doublet, M. L. The Intriguing Question of Anionic Redox in High-Energy Density Cathodes for Li-Ion Batteries. *Energy Environ. Sci.* **9**, 984-991 (2016).

54 Seo, D.-H., Urban, A. & Ceder, G. The Structural and Chemical Origin of the Oxygen Redox Activity in Layered and Cation-Disordered Li-Excess Cathode Materials. *Nat. Chem.* **8**, 692-697 (2016).

55 Maitra, U. *et al.* Oxygen Redox Chemistry without Excess Alkali-Metal Ions in $Na_{2/3}[Mg_{0.28}Mn_{0.72}]O_2$. *Nat. Chem.* **10**, 288–295 (2018).

56 Mortemard de Boisse, B. *et al.* Highly Reversible Oxygen-Redox Chemistry at 4.1 V in $Na_{4/7-x}[\square_{1/7}Mn_{6/7}]O_2$ (□: Mn Vacancy). *Adv. Energy Mater.* **8**, 1800409-1800415 (2018).

57 Perez, A. J. *et al.* Approaching the Limits of Cationic and Anionic Electrochemical Activity with the Li-Rich Layered Rocksalt Li_3IrO_4. *Nat. Energy* **2**, 954-962 (2017).

58 Yabuuchi, N. *et al.* High-Capacity Electrode Materials for Rechargeable Lithium Batteries: Li_3NbO_4-Based System with Cation-Disordered Rocksalt Structure. *Proc. Natl. Acad. Sci.* **112**, 7650-7655 (2015).

59 McCalla, E. *et al.* Visualization of O-O Peroxo-Like Dimers in High-Capacity Layered Oxides for Li-ion Batteries. *Science* **350**, 1516-1521 (2015).

60 Pearce, P. E. *et al.* Evidence for Anionic Redox Activity in a Tridimensional-Ordered Li-Rich Positive Electrode β-Li_2IrO_3. *Nat. Mater.* **16**, 580–586 (2017).

61 Yahia, M. B., Vergnet, J., Saubanère, M. & Doublet, M.-L. Unified Picture of Anionic Redox in Li/Na-Ion Batteries. *Nat. Mater.* **18**, 496–502 (2019).

62 Manthiram, A. & Goodenough, J. B. Lithium Insertion into $Fe_2(SO_4)_3$ Frameworks. *J. Power Sources* **26**, 403-408 (1989).

63 Goodenough, J. B. & Kim, Y. Challenges for Rechargeable Li Batteries. *Chem. Mater.* **22**, 587-603 (2010).

64 De Dompablo, M. E. A. y., Amador, U. & Tarascon, J. M. A Computational Investigation on Fluorinated-Polyanionic Compounds as Positive Electrode for Lithium Batteries. *J. Power Sources* **174**, 1251-1257 (2007).

65 Nagahama, M., Hasegawa, N. & Okada, S. High Voltage Performances of Li_2NiPO_4F Cathode with Dinitrile-Based Electrolytes. *J. Electrochem. Soc.* **157**, A748-A752 (2010).

66 Goodenough, J. B. Evolution of Strategies for Modern Rechargeable Batteries. *Acc. Chem. Res.* **46**, 1053-1061 (2013).

67 Gao, J., Shi, S.-Q. & Li, H. Brief Overview of Electrochemical Potential in Lithium Ion Batteries. *Chin. Phys. B* **25**, 018210-018224 (2016).

68 Wang, H., Xia, H., Lai, M. O. & Lu, L. Enhancements of Rate Capability and Cyclic Performance of Spinel $LiNi_{0.5}Mn_{1.5}O_4$ by Trace Ru-Doping. *Electrochem. Commun.* **11**, 1539-1542 (2009).

69 Amatucci, G., Pasquier, A. D., A. Blyra, T. Z. & Tarascon, J.-M. The Elevated Temperature Performance of the $LiMn_2O_4$/C System: Failure and Solutions. *Electrochim. Acta* **45**, 255-271 (1999).

70 Yang, L., Ravdel, B. & Lucht, B. L. Electrolyte Reactions with the Surface of High Voltage $LiNi_{0.5}Mn_{1.5}O_4$ Cathodes for Lithium-Ion Batteries. *Electrochem. Solid State Lett.* **13**, A95-A97 (2010).

71 Pieczonka, N. P. W. *et al.* Understanding Transition-Metal Dissolution Behavior in $LiNi_{0.5}Mn_{1.5}O_4$ High-Voltage Spinel for Lithium Ion Batteries. *J. Phys. Chem. C* **117**, 15947-15957 (2013).

72 Dedryvère, R. *et al.* Electrode/Electrolyte Interface Reactivity in High-Voltage Spinel $LiMn_{1.6}Ni_{0.4}O_4/Li_4Ti_5O_{12}$ Lithium-Ion Battery. *J. Phys. Chem. C* **114**, 10999-11008 (2010).

73 Amatucci, G. G., Blyrc, A., Sigala, C., Alfonse, P. & Tarascon, J.-M. Surface Treatments of $Li_{1+x}Mn_{2-x}O_4$ Spinels for Improved Elevated Temperature Performance. *Solid State Ion.* **104**, 13-25 (1997).

74 Zhang, Z. *et al.* Fluorinated Electrolytes for 5 V Lithium-Ion Battery Chemistry. *Energy Environ. Sci.* **6**, 1806-1811 (2013).

75 Pieczonka, N. P. W. *et al.* Impact of Lithium Bis(oxalate)borate Electrolyte Additive on the Performance of High-Voltage Spinel/Graphite Li-Ion Batteries. *J. Phys. Chem. C* **117**, 22603-22612 (2013).

76 Kang, H.-B., Myung, S.-T., Amine, K., Lee, S.-M. & Sun, Y.-K. Improved Electrochemical Properties of BiOF-Coated 5V Spinel $Li[Ni_{0.5}Mn_{1.5}]O_4$ for Rechargeable Lithium Batteries. *J. Power Sources* **195**, 2023-2028 (2010).

77 Xu, K., Zhang, S. S., Lee, U., Allen, J. L. & Jow, T. R. LiBOB: Is It an Alternative Salt for Lithium Ion Chemistry? *J. Power Sources* **146**, 79-85 (2005).

78 Wang, J. *et al.* Superconcentrated Electrolytes for a High-Voltage Lithium-Ion Battery. *Nat. Commun.* **7**, 12032-12040 (2016).

79 Jung, S.-K. *et al.* Lithium-Free Transition Metal Monoxides for Positive Electrodes in Lithium-Ion Batteries. *Nat. Energy* **2**, 16208, doi:10.1038/nenergy.2016.208 (2017).

80 Zhang, L., Chen, G., Berg, E. J. & Tarascon, J.-M. Triggering the *In Situ* Electrochemical Formation of High Capacity Cathode Material from MnO. *Adv. Energy Mater.* **7**, 1602200-1602205 (2017).

81 Liu, T. *et al.* Cycling Li-O_2 Batteries via LiOH Formation and Decomposition. *Science* **350**, 530-533 (2015).

82 Johnson, L. *et al.* The Role of LiO_2 Solubility in O_2 Reduction in Aprotic Solvents and Its Consequences for Li–O_2 Batteries. *Nat. Chem.*, 1091–1099 (2014).

83 Knudsen, K. B., Vegge, T., McCloskey, B. D. & Hjelm, J. An Electrochemical Impedance Spectroscopy Study on the Effects of the Surface- and Solution-Based Mechanisms in Li-O_2 Cells. *J. Electrochem. Soc.* **163**, A2065-A2071 (2016).

84 Kwabi, D. G. *et al.* Experimental and Computational Analysis of the Solvent-Dependent O_2 /Li^+-O_2^- Redox Couple: Standard Potentials, Coupling Strength, and Implications for Lithium-Oxygen Batteries. *Angew. Chem. Int. Ed. Engl.* **55**, 3129-3134 (2016).

85 Burke, C. M., Pande, V., Khetan, A., Viswanathan, V. & McCloskey, B. D. Enhancing Electrochemical Intermediate Solvation Through Electrolyte Anion Selection to Increase Nonaqueous Li–O_2 Battery Capacity. *Proc. Natl. Acad. Sci.* **112**, 9293-9298 (2015).

86 Aetukuri, N. B. *et al.* Solvating Additives Drive Solution-Mediated Electrochemistry and Enhance Toroid Growth in Non-aqueous Li-O_2 Batteries. *Nat. Chem.* **7**, 50-56 (2015).

87 Yao, W. *et al.* Tuning Li_2O_2 Formation Routes by Facet-Engineering of MnO_2 Cathode Catalysts. *J. Am. Chem. Soc.* **141**, 12832-12838 (2019).

88 Khetan, A., Luntz, A. & Viswanathan, V. Trade-Offs in Capacity and Rechargeability in Nonaqueous Li-O_2 Batteries: Solution-Driven Growth versus Nucleophilic Stability. *J. Phys. Chem. Lett.* **6**, 1254-1259 (2015).

89 Gao, X., Chen, Y., Johnson, L. & Bruce, P. G. Promoting Solution Phase Discharge in Li-O_2 Batteries Containing Weakly Solvating Electrolyte Solutions. *Nat. Mater.* **15**, 882-888 (2016).

90 Dai, W. *et al.* Defect Chemistry in Discharge Products of Li–O_2 Batteries. *Small Methods* **3**, 1800358-1800375 (2018).

91 Kang, S., Mo, Y., Ong, S. P. & Ceder, G. A Facile Mechanism for Recharging Li_2O_2 in Li–O_2 Batteries. *Chem. Mater.* **25**, 3328-3336 (2013).

92 Geng, W. T., He, B. L. & Ohno, T. Grain Boundary Induced Conductivity in Li_2O_2. *J. Phys. Chem. C* **117**, 25222-25228 (2013).

93 Yang, Y. *et al.* Tuning the Morphology and Crystal Structure of Li_2O_2: A Graphene Model Electrode Study for Li-O_2 Battery. *ACS Appl. Mater. Interfaces* **8**, 21350-21357 (2016).

94 Zhang, Y. *et al.* Amorphous Li_2O_2 Chemical Synthesis and Electrochemical Properties. *Angew. Chem. Int. Ed.* **55**, 1-6 (2016).

95 Gallagher, K. G. *et al.* Quantifying the Promise of Lithium–Air Batteries for Electric Vehicles. *Energy Environ. Sci.* **7**, 1555-1563 (2014).

96 Kwabi, D. G. *et al.* The Effect of Water on Discharge Product Growth and Chemistry in Li-O_2 Batteries. *Phys. Chem. Chem. Phys.* **18**, 24944-24953 (2016).

97 Tułodziecki, M. *et al.* The Role of Iodide on the Formation of Lithium Hydroxide in Lithium-Oxygen Batteries. *Energy Environ. Sci.* **10**, 1828-1842 (2017).

98 Qiao, Y. *et al.* From O^{2-} to HO_2^-: Reducing By-Products and Overpotential in Li-O_2 Batteries by Water Addition. *Angew. Chem. Int. Ed. Engl.* **56**, 4960-4964 (2017).

99 Liu, T. *et al.* The Effect of Water on Quinone Redox Mediators in Nonaqueous Li-O_2 Batteries. *J. Am. Chem. Soc.* **140**, 1428-1437 (2018).

100 Mekonnen, Y. S. *et al.* The Influence of CO_2 Poisoning on Overvoltages and Discharge Capacity in Non-Aqueous Li-Air Batteries. *J. Chem. Phys.* **140**, 121101-121106 (2014).

101 Yang, S., He, P. & Zhou, H. Exploring the Electrochemical Reaction Mechanism of Carbonate Oxidation in Li-Air/CO_2 Battery Through Tracing Missing Oxygen. *Energy Environ. Sci.* **9**, 1650-1654 (2016).

102 Takechi, K., Shiga, T. & Asaoka, T. A Li-O_2/CO_2 Battery. *Chem. Commun.* **47**, 3463-3465 (2011).

103 Okuoka, S.-i. *et al.* A New Sealed Lithium-Peroxide Battery with a Co-Doped Li_2O Cathode in a Superconcentrated Lithium Bis(fluorosulfonyl)amide Electrolyte. *Sci. Rep.* **4**, 5684-5689 (2014).

104 Zhu, Z. *et al.* Anion-Redox Nanolithia Cathodes for Li-Ion Batteries. *Nat. Energy* **1**, 16111-16127 (2016).

105 Shimada, Y. *et al.* Fluorine and Copper Codoping for High Performance Li_2O-Based Cathode Utilizing Solid-State Oxygen Redox. *ACS Appl. Energy Mater.* **2**, 4389-4394 (2019).

106 McCalla, E. *et al.* Understanding the Roles of Anionic Redox and Oxygen Release During Electrochemical Cycling of Lithium-Rich Layered Li_4FeSbO_6. *J. Am. Chem. Soc.* **137**, 4804-4814 (2015).

107 La Mantia, F., Rosciano, F., Tran, N. & Novák, P. Quantification of Oxygen Loss from $Li_{1+x}(Ni_{1/3}Mn_{1/3}Co_{1/3})_{1-x}O_2$ at High Potentials by Differential Electrochemical Mass Spectrometry. *J. Electrochem. Soc.* **156**, A823-A827 (2009).

108 La Mantia, F., Rosciano, F., Tran, N. & Novâk, P. Direct Evidence of Oxygen Evolution from $Li_{1+x}(Ni_{1/3}Mn_{1/3}Co_{1/3})_{1-x}O_2$ at High Potentials. *J. Appl. Electrochem.* **38**, 893-896 (2008).

109 Lanz, P., Sommer, H., Schulz-Dobrick, M. & Novâk, P. Oxygen Release from High-energy $xLi_2MnO_3{\cdot}(1-x)LiMO_2$ (M=Mn, Ni, Co): Electrochemical, Differential Electrochemical

Mass Spectrometric, In Situ Pressure, and In Situ Temperature Characterization. *Electrochim. Acta* **93**, 114-119 (2013).

110 Michalak, B. *et al.* Gas Evolution in $LiNi_{0.5}Mn_{1.5}O_4$/Graphite Cells Studied *In Operando* by a Combination of Differential Electrochemical Mass Spectrometry, Neutron Imaging, and Pressure Measurements. *Anal. Chem.* **88**, 2877-2883 (2016).

111 Castel, E., Berg, E. J., El Kazzi, M., Novák, P. & Villevieille, C. Differential Electrochemical Mass Spectrometry Study of the Interface of $xLi_2MnO_3 \cdot (1-x)LiMO_2$ (M = Ni, Co, and Mn) Material as a Positive Electrode in Li-Ion Batteries. *Chem. Mater.* **26**, 5051-5057 (2014).

112 Singer, A. *et al.* Nucleation of Dislocations and Their Dynamics in Layered Oxide Cathode Materials during Battery Charging. *Nat. Energy* **3**, 641-647 (2018).

113 Xiong, D. J. *et al.* Measuring Oxygen Release from Delithiated $LiNi_xMn_yCo_{1-x-y}O_2$ and Its Effects on the Performance of High Voltage Li-Ion Cells. *J. Electrochem. Soc.* **164**, A3025-A3037 (2017).

114 Shin, Y. & Persson, K. A. Surface Morphology and Surface Stability against Oxygen Loss of the Lithium-Excess Li_2MnO_3 Cathode Material as a Function of Lithium Concentration. *ACS Appl. Mater. Interfaces* **8**, 25595-25602 (2016).

115 Lee, J. *et al.* Mitigating Oxygen Loss to Improve the Cycling Performance of High Capacity Cation-Disordered Cathode Materials. *Nat. Commun.* **8**, 981-990 (2017).

116 Peng, Z., Freunberger, S. A., Chen, Y. & Bruce, P. G. A Reversible and Higher-Rate Li-O_2 Battery. *Science* **337**, 563-566 (2012).

117 Barile, C. J. & Gewirth, A. A. Investigating the Li-O_2 Battery in an Ether-Based Electrolyte Using Differential Electrochemical Mass Spectrometry. *J. Electrochem. Soc.* **160**, A549-A552 (2013).

118 Tsiouvaras, N., Meini, S., Buchberger, I. & Gasteiger, H. A. A Novel On-Line Mass Spectrometer Design for the Study of Multiple Charging Cycles of a Li-O_2 Battery. *J. Electrochem. Soc.* **160**, A471-A477 (2013).

119 Eggert, G. & Heitbaum, J. Electrochemical Reactions of Propylenecarbonate and Electrolytes Solved Therein—A DEMS Study. *Electrochim. Acta* **31**, 1443-1448 (1986).

120 Imhof, R. & Novák, P. In Situ Investigation of the Electrochemical Reduction of Carbonate Electrolyte Solutions at Graphite Electrodes. *J. Electrochem. Soc.* **145**, 1081-1087 (1998).

121 Vetter, J. *et al.* In Situ Study on CO_2 Evolution at Lithium-Ion Battery Cathodes. *J. Power Sources* **159**, 277-281 (2006).

122 Holzapfel, M., Würsig, A., Scheifele, W., Vetter, J. & Novák, P. Oxygen, Hydrogen, Ethylene and CO_2 Development in Lithium-Ion Batteries. *J. Power Sources* **174**, 1156-1160 (2007).

123 He, M. *et al.* In Situ Gas Analysis of $Li_4Ti_5O_{12}$ Based Electrodes at Elevated Temperatures. *J. Electrochem. Soc.* **162**, A870-A876 (2015).

124 Guéguen, A. *et al.* Decomposition of $LiPF_6$ in High Energy Lithium-Ion Batteries Studied with Online Electrochemical Mass Spectrometry. *J. Electrochem. Soc.* **163**, A1095-A1100 (2016).

125 Uddin, J. *et al.* Lithium Nitrate As Regenerable SEI Stabilizing Agent for Rechargeable Li/O_2 Batteries. *J. Phys. Chem. Lett.* **4**, 3760-3765 (2013).

126 Giordani, V. *et al.* A Molten Salt Lithium-Oxygen Battery. *J. Am. Chem. Soc.* **138**, 2656-2663 (2016).

127 Lepoivre, F., Grimaud, A., Larcher, D. & Tarascon, J. M. Long-Time and Reliable Gas Monitoring in Li-O_2 Batteries via a Swagelok Derived Electrochemical Cell. *J. Electrochem. Soc.* **163**, A923-A929 (2016).

128 Jia, Z., Yin, G. & Zhang, J. Rotating Ring-Disk Electrode Method. 199-229 (2014).

129 Albery, W. J. & Drur, J. S. Ring-Disc Electrodes Part 1.-A New Approach to the Theory. *Trans. Faraday Soc.* **62**, 1915-1919 (1966).

130 Dalton, F. Historical Origins of the Rotating Ring-Disk Electrode. *Electrochem. Soc. Interface* **25**, 50-59 (2016).

131 Zoski, C. G. Review—Advances in Scanning Electrochemical Microscopy (SECM). *J. Electrochem. Soc.* **163**, H3088-H3100 (2015).

132 Wang, Y. *et al.* A Solvent-Controlled Oxidation Mechanism of Li_2O_2 in Lithium-Oxygen Batteries. *Joule* **2**, 2364-2380 (2018).

133 Wang, W., Lai, N. C., Liang, Z., Wang, Y. & Lu, Y. C. Superoxide Stabilization and a Universal KO_2 Growth Mechanism in Potassium-Oxygen Batteries. *Angew. Chem. Int. Ed.* **57**, 5042-5046 (2018).

134 Behm, R. J., Paulus, U. A., Schmidt, T. J. & Gasteiger, H. A. Oxygen Reduction on a High-Surface Area Pt/Vulcan Carbon Catalyst: a Thin-Film Rotating Ring-Disk Electrode Study. *J. Electroanal. Chem.* **495**, 134–145 (2001).

135 Jaouen, F. d. r. & Dodelet, J.-P. O_2 Reduction Mechanism on Non-Noble Metal Catalysts for PEM Fuel Cells. Part II: A Porous-Electrode Model To Predict the Quantity of H_2O_2 Detected by Rotating Ring-Disk Electrode. *J. Phys. Chem. C* **113**, 15422-15432 (2009).

136 Herranz, J., Garsuch, A. & Gasteiger, H. A. Using Rotating Ring Disc Electrode Voltammetry to Quantify the Superoxide Radical Stability of Aprotic Li–Air Battery Electrolytes. *J. Phys. Chem. C* **116**, 19084-19094 (2012).

137 Xia, C., Black, R., Fernandes, R., Adams, B. & Nazar, L. F. The Critical Role of Phase-Transfer Catalysis in Aprotic Sodium Oxygen Batteries. *Nat. Chem.* **7**, 496-501 (2015).

138 Sankarasubramanian, S., Seo, J., Mizuno, F., Singh, N. & Prakash, J. Elucidating the Oxygen Reduction Reaction Kinetics and the Origins of the Anomalous Tafel Behavior at the Lithium–Oxygen Cell Cathode. *J. Phys. Chem. C* **121**, 4789-4798 (2017).

139 Lu, Y.-C., He, Q. & Gasteiger, H. A. Probing the Lithium–Sulfur Redox Reactions: A Rotating-Ring Disk Electrode Study. *J. Phys. Chem. C* **118**, 5733-5741 (2014).

140 Wang, L.-F., Ou, C.-C., Striebel, K. A. & Chen, J.-S. Study of Mn Dissolution from $LiMn_2O_4$ Spinel Electrodes Using Rotating Ring-Disk Collection Experiments. *J. Electrochem. Soc.* **150**, A905-A911 (2003).

141 Buchheit, R. G., Martinez, M. A. & Montes, L. P. Evidence for Cu Ion Formation by Dissolution and Dealloying the Al2CuMg Intermetallic Compound in Rotating Ring-Disk Collection Experiments. *J. Electrochem. Soc.* **147**, 119-124 (2000).

142 Li, J., Sun, W., Hurley, B., Luo, A. A. & Buchheit, R. G. Cu Redistribution Study during the Corrosion of AZ91 using a Rotating Ring-Disk Collection Experiment. *Corros. Sci.* **112**, 760-764 (2016).

143 McCrory, C. C., Jung, S., Peters, J. C. & Jaramillo, T. F. Benchmarking Heterogeneous Electrocatalysts for the Oxygen Evolution Reaction. *J. Am. Chem. Soc.* **135**, 16977-16987 (2013).

144 Scholz, J. *et al.* Rotating Ring–Disk Electrode Study of Oxygen Evolution at a Perovskite Surface: Correlating Activity to Manganese Concentration. *J. Phys. Chem. C* **120**, 27746-27756 (2016).

145 Yin, W., Mariyappan, S., Grimaud, A. & Tarascon, J. M. Rotating Ring Disk Electrode for Monitoring the Oxygen Release at High Potentials in Li-Rich Layered Oxides. *J. Electrochem. Soc.* **165**, A3326-A3333 (2018).

146 Lepoivre, F. Study and Improvement of Non-Aqueous Lithium-Air Batteries via the Development of a Silicon-Based Anode. *Ph.D Thesis*, Université Pierre et Marie Curie - Paris VI (2016).

147 Ashton, S. J. Design, Construction and Research Application of a Differential Electrochemical Mass Spectrometer (DEMS). *Springer* **8**, 9-27 (2012).

148 Lu, Y. C., Gasteiger, H. A. & Shao-Horn, Y. Catalytic Activity Trends of Oxygen Reduction Reaction for Nonaqueous Li-Air Batteries. *J. Am. Chem. Soc.* **133**, 19048-19051 (2011).

149 Strmcnik, D. *et al.* The Role of Non-Covalent Interactions in Electrocatalytic Fuel-Cell Reactions on Platinum. *Nat. Chem.* **1**, 466-472 (2009).

150 Bard, A. J. & Faulkner, L. R. Electrochemical Methods,Fundamentals and Applications. *Wiley* **New York** (2001).

151 Yin, W., Grimaud, A., Lepoivre, F., Yang, C. & Tarascon, J.-M. Chemical *vs* Electrochemical Formation of Li_2CO_3 as a Discharge Product in Li-O_2/CO_2 Batteries by Controlling the Superoxide Intermediate. *J. Phys. Chem. Lett.* **8**, 214−222 (2017).

152 Chen, H. & Islam, M. S. Lithium Extraction Mechanism in Li-Rich Li_2MnO_3 Involving Oxygen Hole Formation and Dimerization. *Chem. Mater.* **28**, 6656-6663 (2016).

153 Li, B. *et al.* Understanding the Stability for Li-Rich Layered Oxide Li_2RuO_3 Cathode. *Adv. Funct. Mater.* **26**, 1330-1337 (2016).

154 Sathiya, M. *et al.* Origin of Voltage Decay in High-Capacity Layered Oxide Electrodes. *Nat. Mater.* **14**, 230-238 (2014).

155 Gao, Q., Ranjan, C., Pavlovic, Z., Blume, R. & Schlögl, R. Enhancement of Stability and Activity of MnO_x/Au Electrocatalysts for Oxygen Evolution Through Adequate Electrolyte Composition. *ACS Catal.* **5**, 7265-7275 (2015).

156 Zhang, X. *et al.* Structural and Electrochemical Study of Al_2O_3 and TiO_2 Coated $Li_{1.2}Ni_{0.13}Mn_{0.54}Co_{0.13}O_2$ Cathode Material Using ALD. *Adv. Energy Mater.* **3**, 1299-1307 (2013).

157 Yu, H. *et al.* Temperature-Sensitive Structure Evolution of Lithium-Manganese-Rich Layered Oxides for Lithium-Ion Batteries. *J. Am. Chem. Soc.* **140**, 15279-15289 (2018).

158 Xu, B., Fell, C. R., Chi, M. & Meng, Y. S. Identifying Surface Structural Changes in Layered Li-Excess Nickel Manganese Oxides in High Voltage Lithium Ion Batteries: A Joint Experimental and Theoretical Study. *Energy Environ. Sci.* **4**, 2223-2233 (2011).

159 Fell, C. R. *et al.* Correlation Between Oxygen Vacancy, Microstrain, and Cation Distribution in Lithium-Excess Layered Oxides During the First Electrochemical Cycle. *Chem. Mater.* **25**, 1621-1629 (2013).

160 Jiang, M., Key, B., Meng, Y. S. & Grey, C. P. Electrochemical and Structural Study of the Layered, "Li-Excess" Lithium-Ion Battery Electrode Material $Li[Li_{1/9}Ni_{1/3}Mn_{5/9}]O_2$. *Chem. Mater.* **21**, 2733-2745 (2009).

161 Van Bommel, A., Krause, L. J. & Dahn, J. R. Investigation of the Irreversible Capacity Loss in the Lithium-Rich Oxide $Li[Li_{1/5}Ni_{1/5}Mn_{3/5}]O_2$. *J. Electrochem. Soc.* **158**, A731-A735 (2011).

162 Shunmugasundaram, R., Senthil Arumugam, R. & Dahn, J. R. High Capacity Li-Rich Positive Electrode Materials with Reduced First-Cycle Irreversible Capacity Loss. *Chem. Mater.* **27**, 757-767 (2015).

163 Kasnatscheew, J. *et al.* The Truth about the 1st Cycle Coulombic Efficiency of $LiNi_{1/3}Co_{1/3}Mn_{1/3}O_2$ (NCM) Cathodes. *Phys. Chem. Chem. Phys.* **18**, 3956-3965 (2016).

164 Zhou, H., Xin, F., Pei, B. & Whittingham, M. S. What Limits the Capacity of Layered Oxide Cathodes in Lithium Batteries? *ACS Energy Lett.* **4**, 1902-1906 (2019).

165 Song, B. *et al.* Mitigated Phase Transition during First Cycle of a Li-Rich Layered Cathode Studied by In Operando Synchrotron X-Ray Powder Diffraction. *Phys. Chem. Chem. Phys.* **18**, 4745-4752 (2016).

166 Yabuuchi, N., Yoshii, K., Myung, S. T., Nakai, I. & Komaba, S. Detailed Studies of a High-Capacity Electrode Material for Rechargeable Batteries, Li_2MnO_3-$LiCo_{1/3}Ni_{1/3}Mn_{1/3}O_2$. *J. Am. Chem. Soc.* **133**, 4404-4419 (2011).

167 Mohanty, D. *et al.* Structural Transformation of a Lithium-Rich $Li_{1.2}Co_{0.1}Mn_{0.55}Ni_{0.15}O_2$ Cathode During High Voltage Cycling Resolved by In Situ X-Ray Diffraction. *J. Power Sources* **229**, 239-248 (2013).

168 Hatsukade, T., Schiele, A., Hartmann, P., Brezesinski, T. & Janek, J. The Origin of Carbon Dioxide Evolved during Cycling of Nickel-Rich Layered NCM Cathodes. *ACS Appl. Mater. Interfaces* **10**, 38892-38899 (2018).

169 Renfrew, S. E. & McCloskey, B. D. Residual Lithium Carbonate Predominantly Accounts for First Cycle CO_2 and CO Outgassing of Li-Stoichiometric and Li-Rich Layered Transition Metal Oxides. *J. Am. Chem. Soc.* **139**, 17853-17960 (2017).

170 Jung, R., Metzger, M., Maglia, F., Stinner, C. & Gasteiger, H. A. Chemical *versus* Electrochemical Electrolyte Oxidation on NMC111, NMC622, NMC811, LNMO, and Conductive Carbon. *J. Phys. Chem. Lett.* **8**, 4820-4825 (2017).

171 Mohanty, D. *et al.* Unraveling the Voltage-Fade Mechanism in High-Energy-Density Lithium-Ion Batteries: Origin of the Tetrahedral Cations for Spinel Conversion. *Chem. Mater.* **26**, 6272-6280 (2014).

172 Dogan, F. *et al.* Reentrant Lithium Local Environments and Defect Driven Electrochemistry of Li- and Mn-rich Li-ion Battery Cathodes. *J. Am. Chem. Soc.* **137**, 2328-2335 (2015).

173 Croy, J. R. *et al.* First-charge Instabilities of Layered-Layered Lithium-Ion-Battery Materials. *Phys. Chem. Chem. Phys.* **17**, 24382-24391 (2015).

174 Benedek, R. & Iddir, H. Simulation of First-Charge Oxygen-Dimerization and Mn-Migration in Li-Rich Layered Oxides $x\mathrm{Li_2MnO_3}\cdot(1-x)\mathrm{LiMO_2}$ and Implications for Voltage Fade. *J. Phy. Chem. C* **121**, 6492-6499 (2017).

175 Robert, R. & Novák, P. Switch of the Charge Storage Mechanism of $\mathrm{Li}_x\mathrm{Ni}_{0.80}\mathrm{Co}_{0.15}\mathrm{Al}_{0.05}\mathrm{O}_2$ at Overdischarge Conditions. *Chem. Mater.* **30**, 1907-1911 (2018).

176 Davidson, I., Greedan, J. E., Sacken, U. v., Michal, C. A. & Dahn, J. R. Structure of 1T-$\mathrm{Li_2NiO_2}$ from Powder Neutron Diffraction. *Solid State Ion.* **46** 243-247 (1991).

177 Lyu, Y. *et al.* Correlations between Transition-Metal Chemistry, Local Structure, and Global Structure in $\mathrm{Li_2Ru_{0.5}Mn_{0.5}O_3}$ Investigated in a Wide Voltage Window. *Chem. Mater.* **29**, 9053-9065 (2017).

178 Lyu, Y. *et al.* Probing Reversible Multi-electron Transfer and Structure Evolution of $\mathrm{Li_{1.2}Cr_{0.4}Mn_{0.4}O_2}$ Cathode Material for Li-ion Batteries in a Voltage Range of 1.0 - 4.8 V. *Chem. Mater.* **27**, 5238-5252 (2015).

179 Genevois, C. *et al.* Insight into the Atomic Structure of Cycled Lithium-Rich Layered Oxide $\mathrm{Li_{1.20}Mn_{0.54}Co_{0.13}Ni_{0.13}O_2}$ Using HAADF STEM and Electron Nanodiffraction. *J. Phys. Chem. C* **119**, 75-83 (2014).

180 Bridges, N. J., Gutowski, K. E. & Rogers, R. D. Investigation of Aqueous Biphasic Systems Formed from Solutions of Chaotropic Salts with Kosmotropic Salts (salt–salt ABS). *Green Chem.* **9**, 177-183 (2007).

181 Yin, S.-C., Rho, Y.-H., Swainson, I. & Nazar, L. F. X-ray/Neutron Diffraction and Electrochemical Studies of Lithium De/Re-Intercalation in $\mathrm{Li}_{1-x}\mathrm{Co_{1/3}Ni_{1/3}Mn_{1/3}O_2}$ ($x = 0 \rightarrow 1$). *Chem. Mater.* **18**, 1901-1910 (2006).

182 Mueller-Neuhaus, J. R., Dunlap, R. A. & Dahn, J. R. Understanding Irreversible Capacity in $\mathrm{Li}_x\mathrm{Ni}_{1-y}\mathrm{Fe}_y\mathrm{O_2}$ Cathode Materials. *J. Electrochem. Soc.* **147**, 3598-3605 (2000).

183 Kang, S.-H., Yoon, W.-S., Nam, K.-W., Yang, X.-Q. & Abraham, D. P. Investigating the First-Cycle Irreversibility of Lithium Metal Oxide Cathodes for Li Batteries. *Journal of Materials Science* **43**, 4701-4706 (2008).

184 Mondal, M., Khanra, S., Tiwari, O. N., Gayen, K. & Halder, G. N. Role of Carbonic Anhydrase on the Way to Biological Carbon Capture Through Microalgae-A Mini Review. *Enrivon. Prog. Sustain.* **35**, 1605-1615 (2016).

185 Nugent, P. *et al.* Porous Materials with Optimal Adsorption Thermodynamics and Kinetics for $\mathrm{CO_2}$ Separation. *Nature* **495**, 80-84 (2013).

186 Mistry, H. *et al.* Highly Selective Plasma-Activated Copper Catalysts for Carbon Dioxide Reduction to Ethylene. *Nat. Commun.* **7**, 12123-12131 (2016).

187 Studt, F. *et al.* Discovery of a Ni-Ga Catalyst for Carbon Dioxide Reduction to Methanol. *Nat. Chem.* **6**, 320–324 (2014).

188 Chen, Y., Li, C. W. & Kanan, M. W. Aqueous CO_2 Reduction at Very Low Overpotential on Oxide-Derived Au Nanoparticles. *J. Am. Chem. Soc.* **134**, 19969-19972 (2012).

189 Wei, J. *et al.* New Insights Into the Effect of Sodium on Fe_3O_4- Based Nanocatalysts for CO_2 Hydrogenation to Light Olefins. *Catal. Sci. Technol.* **6**, 4786-4793 (2016).

190 Wei, J. *et al.* Directly Converting CO_2 into a Gasoline Fuel. *Nat. Commun.* **8**, 15174-15181 (2017).

191 Zhu, Y. *et al.* Catalytic Conversion of Carbon Dioxide to Methane on Ruthenium–Cobalt Bimetallic Nanocatalysts and Correlation between Surface Chemistry of Catalysts under Reaction Conditions and Catalytic Performances. *ACS Catal.* **2**, 2403-2408 (2012).

192 Moret, S., Dyson, P. J. & Laurenczy, G. Direct Synthesis of Formic Acid from Carbon Dioxide by Hydrogenation in Acidic Media. *Nat. Commun.* **5**, 4017-4023 (2014).

193 Angamuthu, R., Byers, P., Lutz, M., Spek, A. L. & Bouwman, E. Electrocatalytic CO_2 Conversion to Oxalate by a Copper Complex. *Science* **327**, 313-315 (2010).

194 Qiao, Y. *et al.* Li-CO_2 Electrochemistry: A New Strategy for CO_2 Fixation and Energy Storage. *Joule* **1**, 1-12 (2017).

195 Abraham, K. M. & Jiang, Z. A Polymer Electrolyte-Based Rechargeable lithium/Oxygen Battery. *J. Electrochem. Soc.* **143**, 1-5 (1996).

196 Bruce, P. G., Freunberger, S. A., Hardwick, L. J. & Tarascon, J. M. Li-O_2 and Li-S Batteries with High Energy Storage. *Nat. Mater.* **11**, 19-29 (2012).

197 Cho, M. H. *et al.* The Effects of Moisture Contamination in the Li-O_2 Battery. *J. Power Sources* **268**, 565-574 (2014).

198 Gowda, S. R., Brunet, A., Wallraff, G. M. & McCloskey, B. D. Implications of CO_2 Contamination in Rechargeable Nonaqueous Li-O_2 Batteries. *J. Phys. Chem. Lett.* **4**, 276-279 (2013).

199 Freunberger, S. A. *et al.* The Lithium-Oxygen Battery with Ether-Based Electrolytes. *Angew. Chem. Int. Ed. Engl.* **50**, 8609-8613 (2011).

200 Chen, Y., Freunberger, S. A., Peng, Z., Barde, F. & Bruce, P. G. Li-O_2 Battery with a Dimethylformamide Electrolyte. *J. Am. Chem. Soc.* **134**, 7952-7957 (2012).

201 Freunberger, S. A. *et al.* Reactions in the Rechargeable Lithium-O_2 Battery with Alkyl Carbonate Electrolytes. *J. Am. Chem. Soc.* **133**, 8040-8047 (2011).

202 McCloskey, B. D., Bethune, D. S., Shelby, R. M., Girishkumar, G. & Luntz, A. C. Solvents' Critical Role in Nonaqueous Lithium-Oxygen Battery Electrochemistry. *J. Phys. Chem. Lett.* **2**, 1161-1166 (2011).

203 McCloskey, B. D. *et al.* Limitations in Rechargeability of Li-O_2 Batteries and Possible Origins. *J. Phys. Chem. Lett.* **3**, 3043-3047 (2012).

204 Ottakam Thotiyl, M. M., Freunberger, S. A., Peng, Z. & Bruce, P. G. The Carbon Electrode in Nonaqueous Li-O_2 Cells. *J. Am. Chem. Soc.* **135**, 494-500 (2013).

205 McCloskey, B. D. *et al.* Twin Problems of Interfacial Carbonate Formation in Nonaqueous Li-O_2 Batteries. *J. Phys. Chem. Lett.* **3**, 997-1001 (2012).

206 Gallant, B. M. *et al.* Chemical and Morphological Changes of Li–O_2 Battery Electrodes upon Cycling. *J. Phys. Chem. C* **116**, 20800-20805 (2012).

207 Lu, Y.-C. *et al.* Influence of Hydrocarbon and CO_2 on the Reversibility of Li–O_2 Chemistry Using In Situ Ambient Pressure X-ray Photoelectron Spectroscopy. *J. Phys. Chem. C* **117**, 25948-25954 (2013).

208 Liu, J. *et al.* Pathways for Practical High-Energy Long-Cycling Lithium Metal Batteries. *Nat. Energy* **4**, 180–186 (2019).

209 Ling, C., Zhang, R., Takechi, K. & Mizuno, F. Intrinsic Barrier to Electrochemically Decompose Li_2CO_3 and LiOH. *J. Phys. Chem. C* **118**, 26591-26598 (2014).

210 Meini, S. *et al.* Rechargeability of Li-Air Cathodes Pre-Filled with Discharge Products Using an Ether-Based Electrolyte Solution: Implications for Cycle-Life of Li-Air Cells. *Phys. Chem. Chem. Phys.* **15**, 11478-11493 (2013).

211 Julian L. Roberts, J., Calderwood, T. S. & Sawyer, D. T. Nucleophilic Oxygenation of Carbon Dioxide by Superoxide Ion in Aprotic Media To Form the $C_2O_6^{2-}$ Species. *J. Am. Chem. Soc.* **106**, 4667-4670 (1984).

212 Buzzeo, M. C. *et al.* Kinetic Analysis of the Reaction between Electrogenerated Superoxide and Carbon Dioxide in the Room Temperature Ionic Liquids 1-Ethyl-3-methylimidazolium Bis(trifluoromethylsulfonyl)imide and Hexyltriethylammonium Bis(trifluoromethylsulfonyl)imide. *J. Phys. Chem. B* **108**, 3947-3954 (2004).

213 Liu, Y., Wang, R., Lyu, Y., Li, H. & Chen, L. Rechargeable Li/CO_2–O_2 (2 : 1) Battery and Li/CO_2 Battery. *Energy Environ. Sci.* **7**, 677-681 (2014).

214 Lim, H. K. *et al.* Toward a Lithium-"Air" Battery: the Effect of CO_2 on the Chemistry of a Lithium-Oxygen Cell. *J. Am. Chem. Soc.* **135**, 9733-9742 (2013).

215 Mekonnen, Y. S., Garcia-Lastra, J. M., Hummelshøj, J. S., Jin, C. & Vegge, T. Role of Li_2O_2@Li_2CO_3 Interfaces on Charge Transport in Nonaqueous Li–Air Batteries. *J. Phys. Chem. C* **119**, 18066-18073 (2015).

216 Laoire, C. O., Mukerjee, S., Abraham, K. M., Plichta, E. J. & Hendrickson, M. A. Influence of Nonaqueous Solvents on the Electrochemistry of Oxygen in the Rechargeable Lithium−Air Battery. *J. Phys. Chem. C* **114**, 9178-9186 (2010).

217 Wadhawan, J. D., Welford, P. J., McPeak, H. B., Hahn, C. E. W. & Compton, R. G. The Simultaneous Voltammetric Determination and Detection of Oxygen and Carbon Dioxide A Study of the Kinetics of the Reaction Between Superoxide and Carbon Dioxide in Non-Aqueous Media using Membrane-Free Gold Disc Microelectrodes. *Sens. Actuator B* **88**, 40-52 (2003).

218 Hartmann, P. *et al.* Pressure Dynamics in Metal–Oxygen (Metal–Air) Batteries: A Case Study on Sodium Superoxide Cells. *J. Phys. Chem. C* **118**, 1461-1471 (2014).

219 Wadhawan, J. D. *et al.* Microelectrode Studies of the Reaction of Superoxide with Carbon Dioxide in DimethylSulfoxide. *J. Phys. Chem. B* **105**, 10659-10668 (2001).

220 Casadei, M. A., Cesa, S. & Moracci, F. M. Activation of Carbon Dioxide by Electrogenerated Superoxide Ion: A New Carboxylating Reagent. *J. Org. Chem.* **61**, 380-383 (1996).

221 Vassiliev, Y. B., Bagotzky, V. S., Khazova, O. A. & Mayorova, N. A. Electroreduction of Carbon Dioxide: Part II. The Mechanism of Reduction in Aprotic Solvents. *J. Electroanal. Chem. Interfacial Electrochem.* **189**, 295-309 (1985).

222 Hu, X. *et al.* Rechargeable Room-Temperature Na–CO_2 Batteries. *Angew. Chem. Int. Ed.* **55**, 6482-6486 (2016).

223 Zhang, Z. *et al.* The First Introduction of Graphene to Rechargeable Li-CO_2 Batteries. *Angew. Chem. Int. Ed.* **54**, 6550-6553 (2015).

224 Zhang, X. *et al.* Rechargeable Li–CO_2 Batteries with Carbon Nanotubes as Air Cathodes. *Chem. Commun.* **51**, 14636-14639 (2015).

225 Lutz, L. *et al.* High Capacity Na–O_2 Batteries: Key Parameters for Solution-Mediated Discharge. *J. Phys. Chem. C* **120**, 20068-20076 (2016).

226 Sharon, D. *et al.* Oxidation of Dimethyl Sulfoxide Solutions by Electrochemical Reduction of Oxygen. *J. Phys. Chem. Lett.* **4**, 3115-3119 (2013).

227 Kwabi, D. G. *et al.* Chemical Instability of Dimethyl Sulfoxide in Lithium-Air Batteries. *J. Phys. Chem. Lett.* **5**, 2850-2856 (2014).

228 Abraham, K. M. Electrolyte-Directed Reactions of the Oxygen Electrode in Lithium-Air Batteries. *J. Electrochem. Soc.* **162**, A3021-A3031 (2014).

229 Adams, B. D. *et al.* Current Density Dependence of Peroxide Formation in the Li–O_2 Battery and Its Effect on Charge. *Energy Environ. Sci.* **6**, 1772-1778 (2013).

230 Gallant, B. M. *et al.* Influence of Li2O2 Morphology on Oxygen Reduction and Evolution Kinetics in Li–O_2 Batteries. *Energy Environ. Sci.* **6**, 2518-2528 (2013).

231 Zhai, D. *et al.* Raman Evidence for Late Stage Disproportionation in a Li-O_2 Battery. *J. Phys. Chem. Lett.* **5**, 2705-2710 (2014).

232 Mitchell, R. R., Gallant, B. M., Thompson, C. V. & Shao-Horn, Y. All-Carbon-Nanofiber Electrodes for High-Energy Rechargeable Li–O_2 Batteries. *Energy Environ. Sci.* **4**, 2952-2958 (2011).

233 Lau, S. & Archer, L. A. Nucleation and Growth of Lithium Peroxide in the Li–O_2 Battery. *Nano Lett.* **15**, 5995-6002 (2015).

234 Horstmann, B. *et al.* Rate-Dependent Morphology of Li_2O_2 Growth in Li-O_2 Batteries. *J. Phys. Chem. Lett.* **4**, 4217-4122 (2013).

235 Wang, L. *et al.* Monodispersed Ru Nanoparticles Functionalized Graphene Nanosheets as Efficient Cathode Catalysts for O_2-Assisted Li–CO_2 Battery. *ACS Omega* **2**, 9280-9286 (2017).

236 Zhao, Z., Su, Y. & Peng, Z. Probing Lithium Carbonate Formation in Trace O_2-Assisted Aprotic Li-CO_2 Batteries Using In-Situ Surface Enhanced Raman Spectroscopy. *J. Phys. Chem. Lett.* **10**, 322-328 (2019).

237 Qiao, Y. *et al.* A Li_2CO_3-Free Li-O_2/CO_2 Battery with Peroxide Discharge Product. *Energy Environ. Sci.* **11**, 1211-1217 (2018).

238 Jain, P. S. & Lal, S. Electrolytic Reduction of Oxygen at Solid Electrodes in Aprotic Solvents- the Superoxide Ion. *Electrochim. Acta* **27**, 759-763 (1982).

239 Sullivan, B. P. Electrochemical and Electrocatalytic Reactions of Carbon Dioxide. *Elsevier*, Laramie, WY, USZ (1993).

240 Lamy, E., Nadjo, L. & Saveant, J. M. Standard Potential and Kinetic Parameters of the Electrochemical Reduciton of Carbon Dioxide in Dimethyformamide. *J. Electroanal. Chem.* **78**, 403-407 (1977).

241 Xu, S., Das, S. K. & Archer, L. A. The Li–CO_2 Battery: A Novel Method for CO_2 Capture and Utilization. *RSC Adv.* **3**, 6656-6660 (2013).

242 Qie, L., Lin, Y., Connell, J. W., Xu, J. & Liming, D. Highly Rechargeable Lithium-CO_2 Batteries with a Boron- and Nitrogen-Codoped Holey-Graphene Cathode. *Angew. Chem. Int. Ed.* **56**, 6970–6974 (2017).

243 Yang, S. *et al.* A Reversible Lithium–CO_2 Battery with Ru Nanoparticles as a Cathode Catalyst. *Energy Environ. Sci.* **10**, 972-978 (2017).

244 Costentin, C., Robert, M. & Saveant, J. M. Catalysis of the Electrochemical Reduction of Carbon Dioxide. *Chem. Soc. Rev.* **42**, 2423-2436 (2013).

245 Savéant, J. M. Molecular Catalysis of Electrochemical Reactions. Mechanistic Aspects. *Chem. Rev.* **208**, 2348–2378 (2008).

246 Andrieux, C. P., Dumas-Bouchiat, J. M. & Saveant, J. M. Homogeneous Redox Catalysis of Electrochemical Reactions: Part I. Introduction. *J. Electroanal. Chem. Interfacial Electrochem.* **87**, 39-53 (1978).

247 Bhugun, I., Lexa, D. & Saveant, J.-M. Ultraefficient Selective Homogeneous Catalysis of the Electrochemical Reduction of Carbon Dioxide by an Iron(0) Porphyrin Associated with a Weak Bronsted Acid Cocatalyst. *J. Am. Chem. Soc.* **116**, 5015-5016 (1994).

248 Costentin, C., Drouet, S., Robert, M. & Saveant, J. M. A Local Proton Source Enhances CO_2 Electroreduction to CO by a Molecular Fe Catalyst. *Science* **338**, 90-94 (2012).

249 Rheinhardt, J. H., Singh, P., Tarakeshwar, P. & Buttry, D. A. Electrochemical Capture and Release of Carbon Dioxide. *ACS Energy Lett.* **2**, 454-461 (2017).

250 Mizen, M. B. & Wrighton, M. S. Reductive Addition of CO_2 to 9, 10-Phenanthrenequinone. *J. Electrochem. Soc.* **136**, 941-946 (1989).

251 Gurkan, B., Simeon, F. & Hatton, T. A. Quinone Reduction in Ionic Liquids for Electrochemical CO_2 Separation. *ACS Sustain. Chem. Eng.* **3**, 1394-1405 (2015).

252 Bhugun, I., Lexa, D. & Saveant, J. M. Catalysis of the Electrochemical Reduction of Carbon Dioxide by Iron(0) Porphyrins. Synergistic Effect of Lewis Acid Cations. *J. Phys. Chem.* **100**, 19981-19985 (1996).

253 Ding, Y., Li, Y. & Yu, G. Exploring Bio-inspired Quinone-Based Organic Redox Flow Batteries: A Combined Experimental and Computational Study. *Chem* **1**, 790-801 (2016).

254 Wilfrod, J. H. & Archer, M. D. Solvent Effects on the Redox Potentials of Benzoquinone. *J. Electroanal. Chem.* **190**, 271-277 (1985).

255 Neeraj, G. & Henry, L. Hydrogen-Bonding and Protonation Effects in Electrochemistry of Quinones in Aprotic Solvents. *J. Am. Chem. Soc.* **119**, 6384-6391 (1997).

256 Guin, P. S., Das, S. & Mandal, P. C. Electrochemical Reduction of Quinones in Different Media: A Review. *Int. J. Electrochem.* **2011**, 1-22 (2011).

257 Tsutomu, N., Nobuyuki, N., Koji, F. & Kotaro, O. Mechanisms of Reductive Addition of CO_2 to Quinones in Acetonitrile. *J. Electroanal. Chem.* **322**, 383-389 (1992).

258 Saveant, J. M. Elements of Molecular and Biomolecular Electrochemistry. *Wiley*, Paris, France (2006).

259 Fujinaga, T., Izutsu, K. & Nomura, T. Effect of Metal Ions on the Polarographic Reduction of Organic Compounds in Dipolar Aprotic Solvents. *J. Electroanal. Chem.* **29**, 203-209 (1971).

260 Kim, K. C., Liu, T., Lee, S. W. & Jang, S. S. First-Principles Density Functional Theory Modeling of Li Binding: Thermodynamics and Redox Properties of Quinone Derivatives for Lithium-Ion Batteries. *J. Am. Chem. Soc.* **138**, 2374-2382 (2016).

261 Marek, K. K. & Barbara, T. G. Ion-pair Effects in the Electrochemistry of Aromatic Compounds Effects of Metal Ions and Solvents on the Polarographic Reduction of Quinones. *J. Electroana. Chem. Interfacial Electrochem.* **55**, 277-286 (1974).

262 Jaworski, J. S., Lesniewska, E. & Kalinowski, M. K. Solvent Effect on the Redox Potential of Quinone-Semiquinone Systems. *J. Electroanal. Chem.* **105**, 329-334 (1979).

263 Staley, P. A. The Electrochemistry of Quinones in Aprotic Solvents. *Ph.D Thesis*, University of California, San Diego, San Diego State University (2016).

264 McCloskey, B. D. & Addison, D. A Viewpoint on Heterogeneous Electrocatalysis and Redox Mediation in Nonaqueous Li-O_2 Batteries. *ACS Catal.* **7**, 772-778 (2017).

265 Markovic, N. M., Gasteiger, H. A. & Philip N. Ross, J. Oxygen Reduction on Platinum Low-Index Single-Crystal Surfaces in Sulfuric Acid Solution: Rotating Ring-Pt(hkl) Disk Studies. *J. Phys. Chem.* **99**, 3411-3415 (1995).

266 Solla-Gullo ́n, J., Montiel, V., Aldaz, A. & Clavilier, J. Electrochemical Characterisation of Platinum Nanoparticles Prepared by Microemulsion: How to Clean Them Without Loss of Crystalline Surface Structure. *J. Electroanal. Chem.* **491**, 69-77 (2000).

267 Berg, E. J. & P. Nov ́ak. Recent Progress on Li-O_2 Batteries at PSI. *ECL Annual Report, Paul Scherrer Institut, Villigen, Switzerland* (2012).

Abstract/Résumé

Fundamental understanding of high-energy-density Li-ion batteries and beyond: structure-property relationships and reaction chemistries

Abstract:

The increasing energy demands placed on energy storage devices for both transportation and mobile applications have stimulated the development of high-capacity positive materials for Li-ion batteries. Li-rich layered oxides are among the leading candidates provided their staggering capacities, owing to the participation of anionic redox in the charge compensation mechanism aside from the conventional transition metal redox. Nevertheless, Li-rich layered oxides are yet to reach commercial success since the extra capacities offered by oxygen anions generally come with structural instability, leading to significant first-cycle irreversibility and performance deterioration upon cycling. Understanding the structural evolution in these materials and its effect on their electrochemical properties are therefore of vital importance. This work addressed the major degradation phenomenon in Li-rich layered oxides, i.e., irreversible oxygen release, by introducing a simple while sensitive oxygen gas detection technique. The strong coupling between the structural evolution and the electrochemical behaviors was further investigated using a practically important $Li_{1.2}Ni_{0.13}Mn_{0.54}Co_{0.13}O_2$ compound. Other than Li-ion batteries based on intercalation chemistry, numerous alternative battery chemistries are undergoing intensive research in the battery community, seeking to move beyond the limits of Li-ion technology. Within this context, the fundamental aspects of Li-CO_2 batteries, which include the reaction mechanisms and the catalytic CO_2 reduction, were explored in the second part of this work.

Keywords: Li-ion batteries; Anionic redox; Li-rich layered oxides; Li-CO_2 batteries; Reaction mechanisms; Homogeneous catalysis

Compréhension fondamentale des batteries Li-ion à haute densité d'énergie et au-delà: relations structure-propriété et chimies de réaction

Résumé:

La recherche de dispositifs de stockage d'énergie plus denses en énergie pour les applications de transport et d'électronique portable a stimulé le développement de matériaux de cathode de grande capacité pour les batteries Li-ion. Les oxydes lamellaires riches en lithium figurent ainsi parmi les principaux candidats. Leur capacité importante résulte de la participation, en plus de la rédox cationique conventionnel, de la rédox anionique lors de l'insertion/désinsertion du lithium. Néanmoins, ils n'ont pas encore rencontré de succès commercial car la capacité supplémentaire offerte par la rédox anionique s'accompagne généralement d'une instabilité structurelle, ce qui entraîne une irréversibilité significative au premier cycle et une dégradation des performances lors du cyclage. Comprendre l'évolution structurelle de ces matériaux et son effet sur leurs propriétés électrochimiques revêt donc une importance vitale. Les travaux réalisés lors de cette thèse ont porté sur le phénomène de dégradation prédominant dans les oxydes lamellaires riches en lithium, à savoir la libération irréversible d'oxygène, en introduisant une technique de détection simple mais sensible à l'oxygène gazeux. Le couplage fort entre l'évolution de la structure et les comportements électrochimiques a été étudié plus en détail pour $Li_{1.2}Ni_{0.13}Mn_{0.54}Co_{0.13}O_2$ qui présente un grand intérêt industriel. Afin de dépasser les limites de la technologie Li-ion, de nombreuses chimies alternatives font actuellement l'objet de recherches approfondies. Dans ce contexte, les aspects fondamentaux des batteries Li-CO_2, qui incluent les mécanismes de réaction et la réduction catalytique de CO_2, ont aussi été explorés.

Mot clés: Batteries Li-ion; Redox anionique; Oxydes lamellaires riches en lithium; Batteries Li-CO_2; Mécanismes de réaction; Catalyseurs homogènes

Résumé

Résumé Compréhension fondamentale des batteries Li-ion à haute densité d'énergie et au-delà: relations structure-propriété et chimies de réaction

Les demandes énergétiques croissantes de la société moderne ont entraîné des recherches intensives afin de i) repousser sans cesse les limites de densité d'énergie des batteries Li-ion, en particulier du côté des électrodes positives, et ii) d'explorer de nouvelles chimies permettant de stocker plus d'énergie. Les oxydes lamellaires riches en Li sont parmi les matériaux d'électrodes positives les plus prometteurs pour les batteries Li-ion à haute densité d'énergie. En effet, les capacités de stockage de ces matériaux sont très élevées et ce grâce à la participation du réseau d'oxygène dans les mécanismes de compensation de charge lors du cyclage. Néanmoins, l'activation du rédox anionique induit généralement des instabilités structurelles associées à une perte irréversible d'oxygène et à une migration des cations, entraînant une dégradation des performances lors du cycle. Dans ce travail, une méthode électrochimique, i.e. la voltampérométrie cyclique utilisant une électrode à disque et à anneau tournante (RRDE), a été introduite pour la première fois pour suivre le phénomène de dégagement d'oxygène dans les oxydes lamellaires riches en Li. Les évolutions structurelles dynamiques liées aux activités redox de l'oxygène (l'évolution irréversible de l'oxygène et redox de l'oxygène réversible), ainsi que leur influence sur les propriétés électrochimiques ont été étudiées plus en détail en utilisant un matériau d'intérêt pratique de formule chimique $Li_{1.2}Ni_{0.13}Mn_{0.54}Co_{0.13}O_2$. Enfin, les aspects fondamentaux de la batterie Li-CO_2, une alternative à la batterie conventionnelle Li-ion, ont été explorés.

Le contenu principal et les conclusions de ce travail incluent:

i) La voltampérométrie RRDE a été développée avec succès en tant que technique alternative pour surveiller le dégagement d'oxygène gazeux à partir d'oxydes lamellaires riches en Li au cours d'un processus de charge à hauts potentiels. La Figure 1 présente un schéma du système RRDE proposé. Dans une mesure RRDE typique, l'oxyde d'intérêt a été déposé sur l'électrode à disque où sa délithiation était contrôlée par voltampérométrie cyclique ou par

cyclage galvanostatique, tandis que l'électrode anneau était fixée à un potentiel permettant la réduction de l'oxygène. Grâce à la rotation de l'ensemble de la RRDE, l'oxygène dégagé de l'oxyde peut être transporté et réduit (détecté) au niveau de l'électrode anneau. Comme preuve de concept, nous avons effectué des mesures RRDE en utilisant divers oxydes lamellaires riches en Li, et les résultats ont été systématiquement comparés à ceux obtenus par deux autres techniques bien établies d'analyse de gaz/pression, i.e. la spectrométrie de masse électrochimique en ligne (OEMS) et le suivi *operando* de la pression grâce à un capteur monté sur une cellule électrochimique. Grâce à cette étude comparative, nous avons démontré que la méthode RRDE proposée peut détecter de manière fiable l'oxygène avec une précision supérieure aux autres techniques. Cette technique est donc appropriée pour déterminer le début de l'évolution de l'oxygène et examiner les oxydes libérant une quantité faible d'oxygène. De plus, grâce à la simplicité de cette approche et de la généralisation de la RRDE dans les domaines de la batterie et de l'électrocatalyse, nous pensons qu'elle peut être utilisée pour les analyses de routine de l'oxygène lors de la conception de nouveaux matériaux susceptibles de dégager de l'oxygène. Malgré ses attributs positifs, une optimisation évidente de la méthode RRDE réside dans la quantification de la quantité totale d'oxygène générée à partir de l'oxyde. Dans ce but, une courbe d'étalonnage de l'augmentation des courants de réduction annulaires en fonction des concentrations en oxygène à la surface du disque peut être obtenue pour déduire "l'efficacité de détection". La voltampérométrie RRDE peut également être étendue pour détecter d'autres types de gaz tels que le CO_2, à condition qu'une électrode anneau adéquate soit sélectionnée.

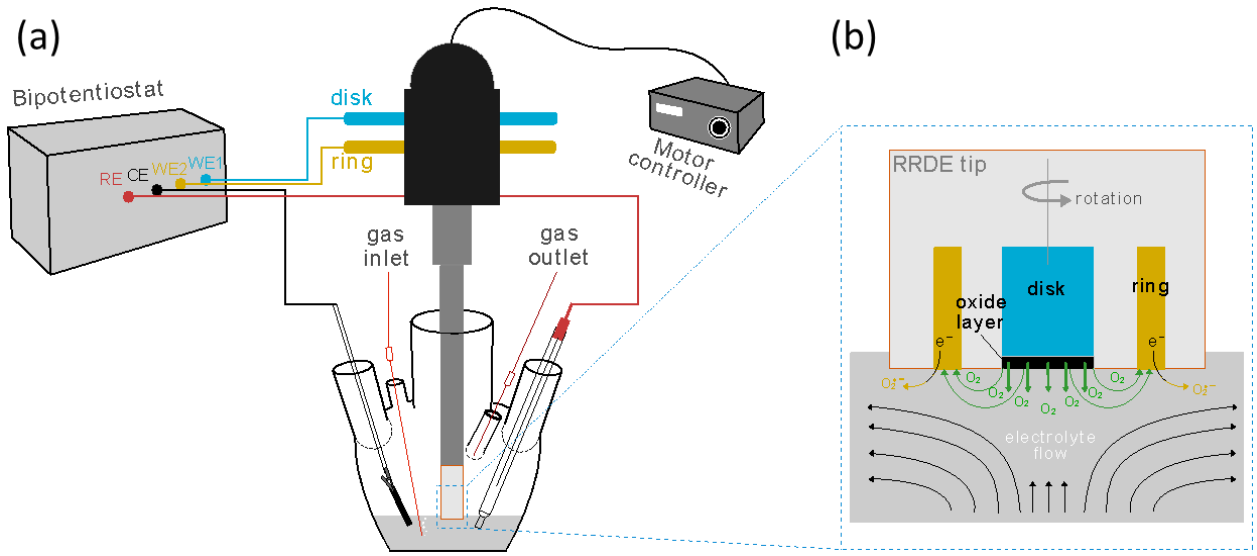

Figure 1 (a) Schéma du système RRDE et de la configuration de cellule à quatre électrodes, WE1, WE2, CE et RE représentent respectivement l'électrode de travail 1 (électrode à disque), l'électrode de travail 2 (électrode à anneau), la contre-électrode et l'électrode de référence. (b) Une vue agrandie de la pointe RRDE et de sa région proche de l'électrolyte décrit les processus de transport et redox se produisant dans le système RRDE conçu pour évaluer le phénomène de libération d'oxygène dans les oxydes lamellaires riches en Li.

ii) À la lumière des travaux précédents, une perte irréversible en oxygène des oxydes lamellaires riches en Li pourrait faciliter la migration des cations et entraîner une transformation de la structure. Par conséquent, nous avons effectué une étude détaillée en utilisant un composé riche en Li de composition nominale en $Li_{1.2}Ni_{0.13}Mn_{0.54}Co_{0.13}O_2$, afin de fournir des informations plus approfondies sur le couplage fort entre les changements structuraux et le redox de l'oxygène. En élargissant la fenêtre de potentiel lors du cyclage nous avons proposé un scénario plus holistique pour l'évolution structurale de $Li_{1.2}Ni_{0.13}Mn_{0.54}Co_{0.13}O_2$ au cours du premier cycle électrochimique.

Premièrement, en appliquant une tension constante à 4,8 V, nous avons obtenu pour la première fois une seule phase complètement chargée A', permettant ainsi sa caractérisation structurale détaillée. En combinant la diffraction des rayons X synchrotron, la diffraction des neutrons sur poudre, la microscopie électronique à transmission (TEM), l'OEMS et le Spectrométrie optique à plasma à couplage inductif (ICP-OES), nous avons identifié la phase A'

comme ayant une structure de type O3 densifiée impliquant la migration de Mn dans les sites octaédriques inter-lamellaires, contrairement aux rapports précédents qui déclaraient qu'il s'agissait d'une couche densifiée[1,2] ou d'une structure en forme de spinelle[3] présente qu'à la surface des particules. De plus, nous avons révélé que sa formation est causée par l'élimination conjointe de Li^+ et d'oxygène, ce qui crée des lacunes cationiques et anioniques. Les lacunes cationiques sont partiellement comblées par des métaux de transition par migration dans les sites octaédriques inter-lamellaires, ainsi supprimant arrangement cationique Li-M "en nid d'abeille" (M étant un métal de transition). Les lacunes anioniques migrent à la surface et sont ainsi comblées. Les lacunes anioniques migrent à la surface et sont ainsi comblées. En conséquence, le ratio M/O augmente et de fait la structure se densifie.

Deuxièmement, nous avons démontré qu'une grande partie de la perte de capacité au cours du premier cycle est due à une barrière cinétique et peut être récupérées en appliquant une étape de potentiel constant ou en abaissant la limite basse de potentiel. Notez que cette dernière méthode n'est pas spécifique à $Li_{1.2}Ni_{0.13}Mn_{0.54}Co_{0.13}O_2$. En effet, en étudiant l'efficacité coulombique de $LiNi_{1/3}Mn_{1/3}Co_{1/3}O_2$ au premier cycle, Kasnatscheew *et al.* ont montré qu'une partie importante de la perte de capacité est d'origine cinétique et est liée à une diffusion lente de Li^+; par conséquent, ils ont recommandé d'appliquer une étape de potentiel constant à la fin de la décharge pour combler les lacunes de Li.[4] Une conclusion similaire a été tirée par Zhou *et al*. lors de l'étude de l'électrode $LiNi_{0,8}Mn_{0,1}Co_{0,1}O_2$.[5] En effet, une baisse du coefficient de diffusion du Li^+ à un état de décharge élevé a été observée pour de nombreux oxydes lamellaires,[5,6] et peut s'expliquer par i) la contraction du paramètre maille *c* se produisant généralement à une teneur élevée en Li ($x > 0,6$, x étant la quantité de Li);[7,8] et ii) la lithiation inhomogène conduisant à une très forte concentration de Li (manque de lacunes) à la surface des particules.[9]

Troisièmement, en utilisant des conditions très réductrices, nous avons révélé la formation d'une nouvelle phase déchargée P", responsable d'une capacité supplémentaire à bas potentiel. En faisant varier progressivement la profondeur de charge de $\Delta x = 0.0$ (Δx étant la quantité de Li extraite pendant la charge) à $\Delta x = 0.4$ (région impliquant les métaux de transition uniquement, redox cationique), et finalement à $\Delta x = 0,6$, 0,8 et 1,0 (région impliquant le réseau d'oxygène, rédox anionique), nous avons en outre démontré que l'apparition de la phase P" est directement

liée à l'activité redox de l'oxygène pendant la charge. L'insertion de Li^+ supplémentaire à des potentiels inférieurs à 2,0 V a été rapportée pour d'autres oxydes lamellaires riches en Li[10,11] et Li-stœchiométrique.[12,13] La sur-lithiation conduit généralement à la formation d'une phase de type Li_2MO_2 avec une structure $P\bar{3}m1$, confirmée par Robert *et al.*[13] Dans le cadre de cette étude, nous avons montré expérimentalement que du Li^+ supplémentaire pouvait également être inséré dans $Li_{1.0}Ni_{0.33}Mn_{0.33}Co_{0.33}O_2$, lors de la décharge du matériau non cyclé à 1,2 V. Par ailleurs, nous avons montré que le composé $Li_{1.2}Ni_{0.13}Mn_{0.54}Co_{0.13}O_2$ non cyclé ne peut pas être sur-lithiée et ce même lorsque la tension limite de décharge est abaissée à 1,2 V. Cependant, une fois le processus redox de l'oxygène activé à haut potentiel, il est possible d'insérer du Li supplémentaire à bas potentiel mais cela ne conduit pas à une transition de phase O3 → 1T comme observé pour d'autres matériaux lamellaires. Ce comportement pourrait être associé à la présence d'ions Li^+ dans les couches de métaux de transition dans $Li_{1.2}Ni_{0.13}Mn_{0.54}Co_{0.13}O_2$, ce qui modifie la stabilité respective de la phase P' *vs* P''. Toutefois, il a été montré que d'autres oxydes lamellaires riches en Li étaient capables d'insérer de manière réversible des ions Li^+ supplémentaires ($Li_{2+x}IrO_3$, $Li_{3+x}IrO_4$)[14,15] entrainant une transition structurale de $R\bar{3}m$ à $P\bar{3}m1$ doublant ainsi le nombre de sites disponibles dans les couches de Li. Une explication plus raisonnable réside dans la migration de Mn observée dans $Li_{1.2}Ni_{0.13}Mn_{0.54}Co_{0.13}O_2$, déclenchée par l'activité redox anionique, déséquilibrant les interactions électrostatiques entre les couches de MO_2 ainsi que la répartition intra-inter des couches de Li. De plus, la présence d'ions Mn dans l'inter-feuillet pourrait servir de "pilier" pour empêcher le glissement des plans, ce qui est nécessaire pour obtenir la structure 1T décrite précédemment pour Li_2NiO_2.[16]

Enfin, nous avons conçu un protocole inspiré des travaux de Singer *et al*,[17] permettant de restaurer les migrations de Mn dans la phase P' déchargée par recuit à température modérée (> 250 °C). En effet, le processus redox observé à bas potentiel ainsi que le Mn dans l'inter-feuillet disparaissent après traitement thermique, confirmant la corrélation entre la migration de Mn et l'activité redox à bas potentiel. De plus, la récupération de la superstructure et des plateaux de potentiel en charge après le traitement indiquent que le désordre cationique est responsable du changement de comportement électrochimique après la première charge. L'assemblage de batteries tout solide pouvant fonctionner dans une large fenêtre de température permettrait de

mieux évaluer l'impact des migrations cationiques sur les propriétés électrochimiques de ce matériau.

Bien que ce nouveau protocole permet une récupération partielle de la capacité perdu après la première charge, la densité énergétique n'a pas pu être augmentée ni par l'exploitation des processus redox a bas potentiel ni par l'insertion de Li^+ supplémentaire. De plus, la chute progressive de potentiel au cours du cyclage persiste.

L'évolution structurale de $Li_{1.2}Ni_{0.13}Mn_{0.54}Co_{0.13}O_2$ au cours du premier cycle a été élucidée et est décrite dans la Figure 2. Premièrement, l'oxydation des cations Ni^{2+} et Co^{3+} a lieu jusqu'à $\Delta x = 0,4$, suivie par l'oxydation de O^{2-} qui déclenche la migration du Mn jusqu'à 4,6 V ($\Delta x < 1,0$). Ensuite, une partie de Li^+ peut encore être extraite de manière concomitante avec le dégagement d'oxygène pour atteindre la phase presque complétement délithiée, laissant des lacunes d'oxygène dans la structure qui sont compensées par la migration de Mn dans l'inter-feuillet. La phase ainsi obtenue après charge jusqu'à 4.8 V correspond à la phase "densifiée" nommée A' ($\Delta x = 1.15$). La densification implique que les lacunes d'oxygène formées au cours de l'étape du dégagement d'oxygène migrent du cœur vers la surface, avec l'augmente de ratio atomique M/O. Une phase pure A' ne peut être obtenue que si une quantité suffisante de Li^+ est éliminée et qu'on dispose d'un délai suffisant pour la migration des métaux de transition, ce qui pourrait expliquer pourquoi la phase A' n'a jamais été reportée pure. Lors de la décharge, les réseaux anioniques et cationiques de la phase A' sont conjointement réduits et seule une partie des cations migrés recouvre sa position initiale, ce qui explique que la phase déchargé P' diffère de la phase initiale. Ces mécanismes sont réversibles au cours du cyclage (dans la présente étude jusqu'à 26 cycles) mais le dégagement d'oxygène n'est observé qu'au cours de la première charge.

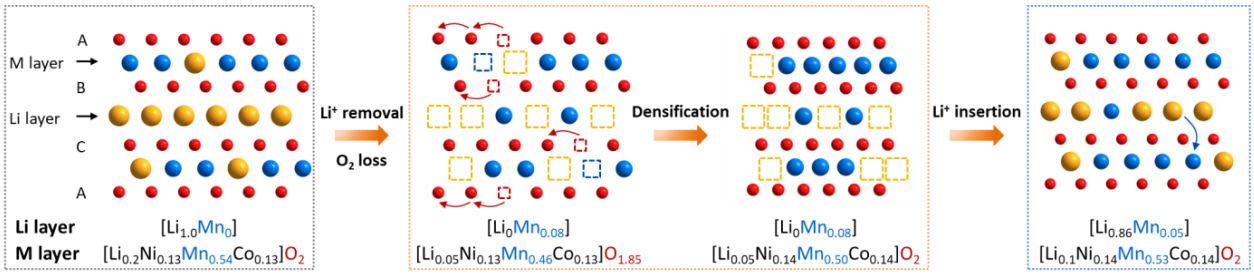

Figure 2 **Schéma de la transition de phase A → A' → P'.**

iii) Nous avons étudié les principes fondamentaux liés à la chimie Li-CO_2 qui a été explorée par la communauté des batteries comme une valorisation du dioxyde de carbone.

Premièrement, nous avons démontré que différents mécanismes réactionnels sont mis effectivement en jeu lors de la décharge dans les batteries Li-O_2/CO_2. Ces mécanismes dépendent de la force de solvatation des solvants de l'électrolyte sur les ions Li^+. Comme décrit dans le Schéma 1, l'étape initiale lors de la décharge est la réduction électrochimique de l'oxygène en superoxyde qu'elle est lieue en diméthylsulfoxyde (DMSO) ou en 1,2-diméthoxyéthane (DME). Ensuite, le superoxyde réagit favorablement avec le CO_2 dans le DMSO, solvant à nombre élevé de donneurs, en raison de la forte solvatation du Li^+ par le DMSO alors qu'il réagit préférentiellement avec le Li^+ dans le DME, solvant à faible nombre de donneurs, pour former du superoxyde de lithium. En conséquence, Li_2CO_3 est formé électrochimiquement dans du DMSO (désigné par voie électrochimique). Alors que dans le DME, Li_2O_2 est formé en premier de la même manière que dans les batteries Li-O_2 avant de réagir chimiquement avec le CO_2 pour former Li_2CO_3 (désigné comme voie chimique). Malgré la réactivité différente des superoxydes mise en évidence dans ce travail, le carbonate de lithium est le seul produit final pour les batteries Li-O_2/CO_2, indépendamment des solvants. Il convient de noter que, à la suite de nos travaux, un scénario similaire a également été établi pour une batterie Li-CO_2 assistée par des traces d'O_2 (ce qui peut être vue intuitivement comme une batterie Li-O_2/CO_2 avec un ratio CO_2/O_2 très élevé) basée sur la spectroscopie Raman *in-situ*.[18] Bien que le scénario susmentionné rationalise la principale différence entre les mécanismes de décharges des batteries Li-O_2/CO_2, les étapes réactionnelles suivant la réaction du superoxyde avec le CO_2 dans le DMSO, restent à identifier (les voies de réaction du superoxyde donnant lieu à la formation de Li_2O_2 dans le DME ont déjà été étudiées en détail dans le contexte des batteries Li-O_2). Dans le même sens, Qiao *et al.* ont

mis l'accent, plus tard, sur l'importance du ratio CO_2/O_2 dans la détermination du mécansime réactionnel du superoxyde avec le CO_2 sur la base de mesures Raman.[19] Plus précisément, le peroxodicarbonate ($C_2O_6^{2-}$) tend à se former dans des conditions avec un ratio CO_2/O_2 élevé, tandis que le peroxomonocarbonate (CO_4^{2-}) est l'intermédiaire de réaction dominant à faible ratio CO_2/O_2.

Deuxièmement, ces multiples voies de réaction entraînent des morphologies du Li_2CO_3 très différentes les unes des autres (forme d'oursin dans le DMSO contrairement à des particule dans le DME). De plus, la différence de capacité entre les batteries Li-O_2/CO_2 et les batteries Li-O_2 dépend de la densité de courant de décharge, pouvant résulter de la compétition entre nucléation et croissance, ainsi que de la différence de transfert de charge entre Li_2CO_3 et Li_2O_2.

Schéma 1 Illustration schématique de la formation de Li_2CO_3 dans des batteries Li-O_2/CO_2 avec des électrolytes à base de DMSO et de DME, suivant la voie électrochimique ou la voie chimique.

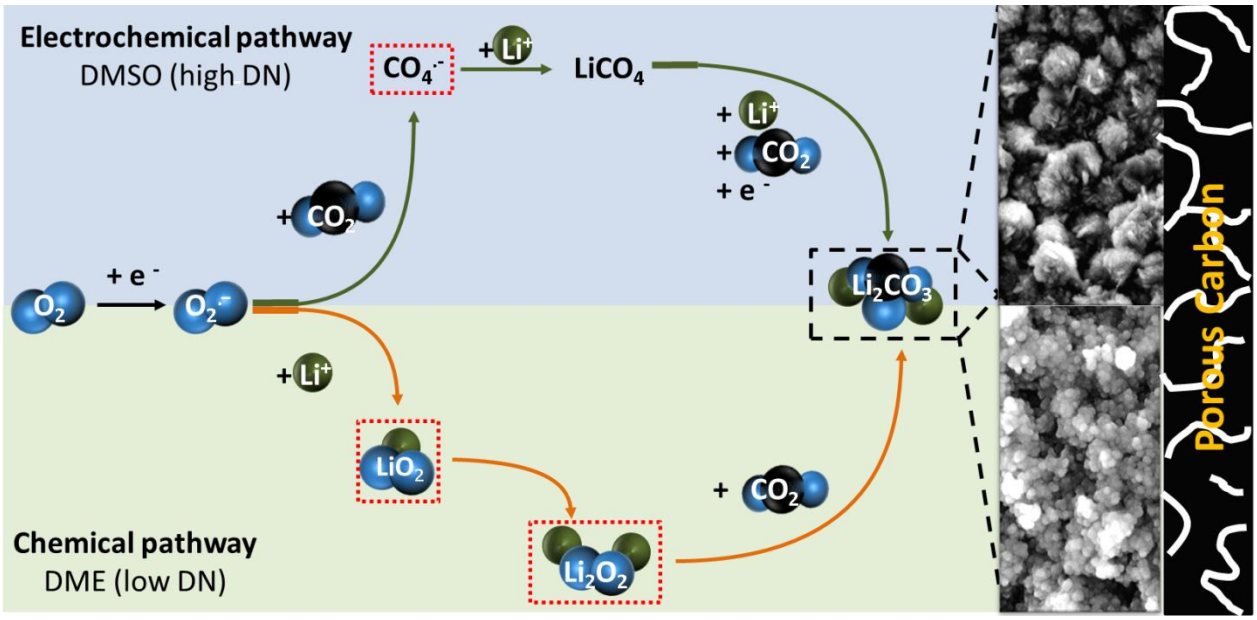

Troisièmement, nous avons démontré que les batteries Li-O_2/CO_2 ne peuvent pas être des batteries rechargeables à cause de ces deux raisonss: i) seul le CO_2 est dégagé mais pas d'O_2 lors de l'oxydation du Li_2CO_3 en charge et ii) les très hauts potentiels requis pour l'oxydation de Li_2CO_3 conduisent à des réactions parasitiques dramatiques. Pour surmonter ces limitations, une

future direction intéressante consisterait à modifier la réaction de décharge de manière à éviter le "fauteur de troubles" qu'est le Li_2CO_3.

Enfin, nos résultats ont révélé que le CO_2 ne peut pas être directement réduit dans les solvants aprotiques dans leur fenêtre électrochimique (DME, DMSO et MeCN ont été étudiés dans ce travail) en utilisant du carbone Super P comme électrode positive. De même, aucune activité électrochimique dans les batteries Li-CO_2 n'a été observée, contrairement à de nombreuses publications. Il convient de mentionner une étude récente qui a démontré que, bien que la batterie Li-CO_2 présente une capacité de décharge négligeable (en utlisant des électrodes positives de graphène nues ou avec nanoparticules de Ru monodispersées à leur surface), l'introduction de 2 % d'O_2 (ratio volumique) peut conduire à une capacité élevée de 4742 mAh g^{-1} (appelée batterie Li-CO_2 assistée par O_2).[20] En général, la batterie Li-CO_2 en est encore à ses balbutiements et de nouvelles connaissances sont nécessaires pour expliquer cette différence d'activité électrochimique.

iv) Compte tenu de la non réactivité du CO_2 dans les solvants non aqueux utilisé dans cette étude, nous avons évalué l'utilisation de quinones en tant que catalyseurs en solution, dans le but de faciliter la réduction électrochimique du CO_2 dans les batteries Li-CO_2.

Tout d'abord, nous avons mis en évidence une complexation entre le CO_2 et les dianions de quinone. Aussi, nous avons étudié l'influence de la nature de la quinone, de la présence d'un cation acide de Lewis (i.e. Li^+) ou du solvant sur cette interaction. Plus spécifiquement, une interaction plus faible avec le CO_2 est observée pour les *ortho*-quinones que pour les *para*-quinones en raison de l'empêchement stérique et de la répulsion coulombique induite par les deux oxygènes en position *ortho*. Le cation lithium pourrait entraver les interactions entre la quinone et le CO_2 lorsque de forts appariements d'ions se forment entre le Li^+ et les anions de quinone. L'interaction de la quinone et du CO_2 peut être modifiée en ajustant la force de solvatation des anions de quinone par le solvant, par exemple, une interaction de quinone plus forte avec le CO_2 est observée dans le MeCN que dans le DMF.

Deuxièmement, en ajoutant du 2,5-di-tert-butyl-1,4-benzoquinone (DBBQ) à l'électrolyte dans l'acétonitrile (MeCN), nous avons évalué le concept de réduction du CO_2 induite par la

quinone dans une batterie Li-CO_2. Le potentiel de décharge est dicté par le potentiel de réduction du DBBQ, qui est plus positif que celui de la réduction de CO_2. De plus, le Li_2CO_3 a été identifié comme le produit de décharge finale. Néanmoins, la capacité de décharge limitée ainsi que les résultats de résonance magnétique nucléaire suggéraient des réactions parasites impliquant le DBBQ lui-même et/ou d'autres composants de la cellule.

Dans l'ensemble, l'utilisation de catalyseurs chimiques est une approche efficace pour faciliter la réduction électrochimique du CO_2 dans les batteries Li-CO_2. Cependant, pour tirer parti de cette approche, le catalyseur doit être correctement choisi pour fournir le potentiel rédox approprié, une activité catalytique appropriée pour la réduction du CO_2, ainsi qu'une bonne stabilité électrochimique et chimique. Le côté de l'anode est également important et doit être protégé par une membrane en électrolyte solide afin d'éviter l'effet "navette" (shuttle effect) indésirable.

Références:

1 Koga, H. *et al.* Different Oxygen Redox Participation for Bulk and Surface: A Possible Global Explanation for the Cycling Mechanism of $Li_{1.20}Mn_{0.54}Co_{0.13}Ni_{0.13}O_2$. *J. Power Sources* **236**, 250-258 (2013).

2 Genevois, C. *et al.* Insight into the Atomic Structure of Cycled Lithium-Rich Layered Oxide $Li_{1.20}Mn_{0.54}Co_{0.13}Ni_{0.13}O_2$ Using HAADF STEM and Electron Nanodiffraction. *J. Phys. Chem. C* **119**, 75-83 (2014).

3 Yu, H. *et al.* Temperature-Sensitive Structure Evolution of Lithium-Manganese-Rich Layered Oxides for Lithium-Ion Batteries. *J. Am. Chem. Soc.* **140**, 15279-15289 (2018).

4 Kasnatscheew, J. *et al.* The Truth about the 1st Cycle Coulombic Efficiency of $LiNi_{1/3}Co_{1/3}Mn_{1/3}O_2$ (NCM) Cathodes. *Phys. Chem. Chem. Phys.* **18**, 3956-3965 (2016).

5 Zhou, H., Xin, F., Pei, B. & Whittingham, M. S. What Limits the Capacity of Layered Oxide Cathodes in Lithium Batteries? *ACS Energy Lett.* **4**, 1902-1906 (2019).

6 Radin, M. D. *et al.* Narrowing the Gap between Theoretical and Practical Capacities in Li-Ion Layered Oxide Cathode Materials. *Adv. Energy Mater.* **7**, 1602888-1602920 (2017).

7 Song, B. *et al.* Mitigated Phase Transition during First Cycle of a Li-Rich Layered Cathode Studied by In Operando Synchrotron X-Ray Powder Diffraction. *Phys. Chem. Chem. Phys.* **18**, 4745-4752 (2016).

8 Yin, S.-C., Rho, Y.-H., Swainson, I. & Nazar, L. F. X-ray/Neutron Diffraction and Electrochemical Studies of Lithium De/Re-Intercalation in $Li_{1-x}Co_{1/3}Ni_{1/3}Mn_{1/3}O_2$ ($x = 0 \rightarrow 1$). *Chem. Mater.* **18**, 1901-1910 (2006).

9 Mueller-Neuhaus, J. R., Dunlap, R. A. & Dahn, J. R. Understanding Irreversible Capacity in $Li_xNi_{1-y}Fe_yO_2$ Cathode Materials. *J. Electrochem. Soc.* **147**, 3598-3605 (2000).

10 Lyu, Y. *et al.* Correlations between Transition-Metal Chemistry, Local Structure, and Global Structure in $Li_2Ru_{0.5}Mn_{0.5}O_3$ Investigated in a Wide Voltage Window. *Chem. Mater.* **29**, 9053-9065 (2017).

11 Lyu, Y. *et al.* Probing Reversible Multi-electron Transfer and Structure Evolution of $Li_{1.2}Cr_{0.4}Mn_{0.4}O_2$ Cathode Material for Li-ion Batteries in a Voltage Range of 1.0 - 4.8 V. *Chem. Mater.* **27**, 5238-5252 (2015).

12 Kang, S.-H., Yoon, W.-S., Nam, K.-W., Yang, X.-Q. & Abraham, D. P. Investigating the first-cycle irreversibility of lithium metal oxide cathodes for Li batteries. *Journal of Materials Science* **43**, 4701-4706 (2008).

13 Robert, R. & Novák, P. Switch of the Charge Storage Mechanism of $Li_xNi_{0.80}Co_{0.15}Al_{0.05}O_2$ at Overdischarge Conditions. *Chem. Mater.* **30**, 1907-1911 (2018).

14 Perez, A. J. *et al.* Approaching the Limits of Cationic and Anionic Electrochemical Activity with the Li-Rich Layered Rocksalt Li_3IrO_4. *Nat. Energy* **2**, 954-962 (2017).

15 Pearce, P. E. *et al.* Evidence for Anionic Redox Activity in a Tridimensional-Ordered Li-Rich Positive Electrode β-Li_2IrO_3. *Nat. Mater.* **16**, 580–586 (2017).

16 Davidson, I., Greedan, J. E., Sacken, U. v., Michal, C. A. & Dahn, J. R. Structure of 1T-Li_2NiO_2 from Powder Neutron Diffraction. *Solid State Ion.* **46** 243-247 (1991).

17 Singer, A. *et al.* Nucleation of Dislocations and Their Dynamics in Layered Oxide Cathode Materials during Battery Charging. *Nat. Energy* **3**, 641-647 (2018).

18 Zhao, Z., Su, Y. & Peng, Z. Probing Lithium Carbonate Formation in Trace O_2-Assisted Aprotic Li-CO_2 Batteries Using *In-Situ* Surface Enhanced Raman Spectroscopy. *J. Phys. Chem. Lett.* **10**, 322-328 (2019).

19 Qiao, Y. *et al.* A Li_2CO_3-Free Li-O_2/CO_2 Battery with Peroxide Discharge Product. *Energy Environ. Sci.* **11**, 1211-1217 (2018).

20 Wang, L. *et al.* Monodispersed Ru Nanoparticles Functionalized Graphene Nanosheets as Efficient Cathode Catalysts for O_2-Assisted Li–CO_2 Battery. *ACS Omega* **2**, 9280-9286 (2017).